Crystallisation of nano-quartz and nano-graphite from microemulsions under ambient conditions.

NATASHA JAYNE HARGREAVES

HARGREAVES, NATASHA JAYNE (2016) Crystallisation of nano-quartz and nano-graphite from microemulsions under ambient conditions. Doctoral thesis, Durham University.

Synthesis of nano-quartz and nano-graphite from microemulsions under ambient conditions

Natasha Hargreaves

A thesis submitted for the degree of Doctor of Philosophy at the University of Durham

Durham University

Department of Chemistry

March 2016

Acknowledgements

A short statement to show my gratitude to all those you have made this possible.

First and foremost, I would like to thank my parents for their undivided support, belief and encouragement throughout the bright and the dark days and John for reawakening my belief in myself.

Dr. Sharon Cooper for her support, guidance, patience and belief over the past 6 years. Dr Kate Nicholson, Dr Cen Chen and Dr Mehrin Chowdhury for maintaining a sense of sanity. All other lab colleagues, past and present for collaborations and discussions.

Dr. Budhika Mendis for foremost – patience during training and discussions regarding TEM analysis. Prof. Andy Beeby and Dr. Kate Nicholson for their patience and kindness in both training myself and running many Raman spectra. Helen Riggs for running and training myself on the SAXS and WAXS machines. Dr. Richard Thompson for training on the AFM.

Statement of copyright

Publication list

The following publications have arisen from the work presented:

Cooper. S.J, Cook. O and Loines. N.J, *‘Crystallization/Book 1: Crystallization in Microemulsions:* A Generic Route to Thermodynamic Control and the Estimation of Critical Nucleus Size’, Chapter 5. 2012

Loines. N.J and Cooper. S.J, ‘Nanographite synthesised from acidified sucrose microemulsions under ambient conditions’, ’Crystal Growth and design’. Due to be published ASAP 2016.

Abstract

The principal basis for the following work is to demonstrate the importance of controllable crystallisation and consequential applications for both silica-based significant inorganic materials and carbonaceous materials. Microemulsions have been employed as a vector to explore the possibility of thermodynamically controlling the crystallisation process, utilising the 3D confinement of crystallisable material within nano-scale droplets. This opens a route to circumvent Ostwald's Rule of Stages, for a multitude of potential applications. We show here that both quartz and nanographite can be synthesised at room temperature and pressure using this methodology.

Previous attempts at silica synthesis from within the microemulsion have only presented the amorphous phase, leaving many questions unanswered, whilst failing to reveal the underlying cause. Further, traditional methods of quartz synthesis employs hydrothermal conditions, or temperatures >1100 ^{0}C. Microemulsions were adopted to behave as confined mini reactors for the synthesis of α-quartz at room temperature and pressure from a precursor from sodium metasilicate nonahydrate (SMS) which can be used as a precursor of silica, circumnavigating the traditional hydrothermal methodologies. At higher supersaturations, both the metastable amorphous phase and the high temperature polymorph, cristobalite were also observed. Upon the acidification of the microemulsions, the size and morphology of the quartz nanoparticles was found to be dependent upon the pH and the ratio of surfactant:silica units.

Conventional wisdom stipulates that graphite can only be produced using high temperatures, with natural graphite arising via progressive metamorphisms of carbonaceous material subjected to temperatures above ~600 K and pressures >2 kbar. Previous attempts to use carbohydrate precursors have resulted in the formation of luminescent carbon dots or required templation, followed by calcination. In these prior investigations, high temperatures or extremely severe reactants are used to drive the precipitation of graphitic forms.

Analogous experiments were successful in employing the 3D nano-confinement microemulsions as confined mini reactors for the synthesis of nanographite at room temperature and pressure from a sucrose precursor, through a simple process of acidifying sucrose microemulsions.

Crucially, the reaction was conducted in nanometre-sized microemulsion droplets to exert control over the reaction and sheet stacking process, ensuring that only sufficiently pristine graphene nanosheets could stack, thereby producing nanographite in a simple one-step synthesis under ambient conditions. The primary nanographitic particles of size ~3-30 nm stacked to form larger μm-sized nanographitic aggregates. The amount of nanographite produced from the microemulsions is limited as sucrose concentration must be kept very low to slow the reaction kinetics to ensure the mainly graphitic, rather than amorphous, product.

Thesis outline

This thesis contains six Chapters, which are structured as follows:

Chapter 1: States the aim of this project and provides a literature review of the background information for this thesis. The topics included are: Polymorphism, surfactants, confinement and crystallisation.

Chapter 2: Experimental methods and techniques are described. It includes methodologies for microemulsion preparation in addition to describing the theoretical origin and indeed the application of the analytical techniques employed to analyse product.

Chapter 3: Nano-quartz synthesis and crystallisation, from a sodium metasilicate nonahydrate precursor, within the 3D-nanoconfinement of the microemulsion droplets is detailed. The experimental details and results are presented and discussed with respect to the literature. The conditions where thermodynamic control is achieved are assessed.

Chapter 4: The crystallisation of nano-quartz within acidified microemulsions is detailed. The experimental details and results are presented and discussed with respect to the literature. The conditions where thermodynamic control is achieved are assessed, in addition to the conditions required for various morphologies and particle size control.

Chapter 5: Nanographite synthesis and crystallisation, from a sucrose precursor, within the 3D-nanoconfinement of an acidified microemulsion droplets is detailed. The experimental details and results are presented and discussed with respect to the literature. The conditions where thermodynamic control is achieved are assessed.

Chapter 6: To summarise, brief conclusions are presented with possible further areas for development.

List of abbreviations

SMS	Sodium metasilicate nonahydrate
SiO_2	Silicon dioxide
fcc	Face centred cubic
CTAB	Cetyltrimethylammonium bromide
CTAC	Cetyltrimethylammonium chloride
AOT	Dioctyl sulfosuccinate sodium salt
CMC	Critical Micelle Concentration
SOBS	Sodium-4-n-octylbenzene-1-sulfonate
PIT	Phase Inversion Temperature
o/w	Oil in water
w/o	Water in oil
HLB	Hydrophilic-Lipophilic balance
CPG	Controlled pore glasses
rpm	Revolutions per minute
TEOS	Tetraethyl orthosilicate
CNT	Classical Nucleation Theory
Span 80®	Sorbitan Monooleate
Brij 30 ®	Polyethylene Glycol Dodecyl Ether
HCl	Hydrochloric acid
H_2SO_4	Sulfuric acid
ATR-FTIR	Attenuated Total Reflectance Fourier Transform Infrared Spectroscopy
SAXS	Small Angle X-Ray Scattering
WAXS	Wide Angle X-Ray Scattering
TEM	Transmission Electron Microscopy
ESEM	Environmental Scanning Electron Microscopy
AFM	Atomic Force Microscopy
IR	Infrared
GIFT	Generalised Indirect Fourier Transformation
EDX	Energy-dispersive X-ray spectroscopy

HREM	High resolution electron microscopy
FFT	Fast Fourier Transform
DP	Diffraction pattern
NaOH	Sodium hydroxide
NP	Polyoxyethylene nonylphenyl ether surfactant
H^+	Hydrogen ion
OH^-	Hydroxide group
SBC7	Span 80:Brij 30:heptane
TX-114	1,1,3,3-Tetramethylbutyl)phenyl-polyethylene glycol
TX-100 glycol	4-(1,1,3,3-Tetramethylbutyl)phenyl-polyethylene
DPA	Dipicolinic acid
PXRD	Powder X-ray diffraction
wt %.	Weight percentage
BF	Bright field image
PEO	Polyethylene oxide
PEG	Polyethylene glycol
AA	Hexagonal stacking
AB	Bernal stacking
ABC	Rhombohedral stacking
CNTs	Carbon nanotubes
CVD	Chemical vapour deposition
PAH	Polyacyclic hydrocarbon
HMF	Hydroxymethylfurfural

List of symbols

T_k	Krafft temperature
T_c	Cloud point
T	Temperature
T_r	Roughening temperature
Mr	Molecular mass
E	Weight percentage of oxyethylene
P	Weight percentage of polyhydric alcohol
G	Gibbs free energy
h	Planck’s constant
H	Enthalpy
S	Entropy
k	Boltzmann constant
R	Radial distance
r	Microemulsion droplet radius
C_0	Film curvature
A	Interfacial area
γ	Interfacial tension
$\Delta\mu$	Supersaturation
P	Pressure
f	Degrees of freedom
J	Rate of nucleation
W*	Impingement rate of a solute onto a nuclei
n(i*)	Equilibrium concentration of critical nuclei
i	Number of monomers in a cluster
n	Concentration of crystallising nuclei
Δ	Change in a given quantity
μ	Chemical potential
θ	Angle
F	Helmholtz free energy

E	Energy
υ	Frequency
d	Crystal interplanar spacing
λ	Wavelength
β	Beam broadening
t	Thickness of finite crystal
P(q)	Form factor
S(q)	Structure factor
I(q)	Scattering function
p(r)	Pair-distance function
q	Scattering vector
A	Surface area
N_s	Number of surfactant molecules per unit volume
m_e	Mass of electron
v	Velocity
ε	Refractive index
δ	Resolution limit
R_{gyr}	Radius of gyration
R_{core}	Hydrophilic core radius

List of figures

Chapter 1

Figure 1.1: A diagram illustrating the occurrence of polymorphs in rigid and flexible molecules.[11]..3

Figure 1.2: Schematic to illustrate the variation in hydrogen bonding of form 1 and form 2 of Ritonavir (1,3-thiazol-5-ylmethyl N-[(2S,3S,5S)-3-hydroxy-5-[(2S)-3-methyl-2-{[methyl({[2-(propan-2-yl)-1,3-thiazol-4-yl]methyl})carbamoyl] amino}butanamido]-1,6-diphenylhexan-2-yl]carbamate).[12] 4

Figure 1.3: An image depicting the morphology of the two polymorphs of Ritonavir, followed by the molecular structure of Ritonavir.[12-13]....................5

Figure 1.4: A simplified illustration of the 4 differing types of surfactants with respect to the charge on the hydrophilic head group.....................................7

Figure 1.5: Hypothetical solubility curve to illustrate how the Krafft point can be determined from the intersection of the cmc curve and the solubility curve.[24]..8

Figure 1.6: Graphical results indicating the effect of variation of the composition of an anionic/anionic/non-ionic system (Sodium Dodecyl sulphate/Sodium-4-n-octylbenzene-1-sulfonate/nonylphenol polyethoxylate, SOBS).[26]...................9

Figure 1.7: A schematic to illustrate the three quantities on which the packing parameter and consequently the micelle structure are dependent on.[24]..15

Figure 1.8: Schematic of the effect of the surfactant structure on the packing parameter and micelle structure..17

Figure 1.9: Calcium carbonate crystals grown from pore sizes of 10, 3, 0.8 and 0.2 μm respectively from left to right. In each case it is apparent, when compared to the 10 μm pore, that the use of an effective pore confinement has had an effect on the morphology of the crystal. [53].....................................19

Figure 1.10: A phase diagram to illustrate how the composition of the confinement solution can be altered. This system uses a SPAN / TWEEN mixture as the surfactant, decane and water as the oil and aqueous phases respectively.[50]..20

Figure 1.11: Optical microscope images illustrating stirring speed on the emulsion crystallisation of g–glutamic acid hydrochloride. [20] 22

Figure 1.12:Graphical illustration of the variation in droplet size with oil (A-C) and drug (D-F) concentration.[57]...23

Figure 1.13: An illustrative view of the 4 classes of microemulsions, consisting of varying amounts of surfactant, an aqueous and an oil phase. [63].................25

Figure 1.14: A distribution curve of simvastin particles prepared as a result of the dispersion of simvastin flakes in water.[73] 27

Figure 1.15: A hypothetical solubility curve to show the limits above and below the solubility curve.(solid curve) [62]..29

Figure 1.16: A diagram to represent the change in free energy for the two processes involved in nucleation: creation of a new phase and formation of new phase, combined together to give the overall (dashed) curve for nucleation.[77]..30

Figure 1.17: A pictorial description of the interfacial tensions acting as forces..33

Figure 1.18: Schematic representation of the Kossel crystal model, exhibiting each crystal face: F, S and K.[78]...34

Figure 1.19: The effect of the level of supersaturation upon the growth mechanism/growth rate.[78]...35

Figure 1.20 : Free energy profile of a polymorphic melt crystallization, for the thermodynamically stable and a metastable case. [1] 36

Figure 1.21: Free energy profile for a polymorphic system, crystallized within the confinement of a microemulsion for the thermodynamically stable, A and a metastable, B case.[1]...37

Figure 1.22: An illustration depicting the exchange of material upon the formation of transient dimers, when sufficiently energetic collisions occur...38

Chapter 2

Figure 2.1 – Schematic diagram illustrating the formation of a micellar solution upon addition of a dispersed phase..44

Figure 2.2: Direct addition schematic[1]...44

Figure 2.3: Mixed microemulsion addition schematic[1]................................45

Figure 2.4: Crystal dissolution method schematic[1]....................................45

Figure 2.5a: Schematic of a simplified Michelson interferometer...................47

Figure 2.5b: Schematic of an FT-IR spectrometer..48

Figure 2.6 Resultant scattering based on the frequency of light....................50

Figure 2.7: Schematic of a simplified Raman spectrometer...........................51

Figure 2.8 Depiction of determination of Braggs' law.................................52

Figure 2.9: Ewald sphere construction...53

Figure 2.10: Illustration to show the occurrence of rel-rods..........................54

Figure 2.11: Overlay of Ewald sphere for both an X-ray and electron source..55

Figure 2.12: Schematic of beam path within the SAXS setup........................56

Figure 2.13: Typically p(r) for a core-shell model..58

Figure 2.14: Schematic of the WAXS setup..59

Figure 2.15 Schematic of the JEOL 2100 F Schottky field emission gun TEM setup [9]...60
Figure 2.16: Illustration of scattering and X-ray photon emission upon collision of an electron with a sample..62

Figure 2.17a and b: External configuration of a polarised optical microscope. **[16]** A schematic depicting the effect of the combination of a polariser and an analyser on refracted light from a birefringent material. **[17]**.......................64

Figure 2.18: A schematic demonstrating the effect of crossed polarisers on unpolarised light.**[18]** 64

Figure 2.19: A spherulite imaged using a polarised microscope, with and without the compensator plate...66

Chapter 3

Figure 3.1: The thermodynamic phase diagram for the various high pressure and high temperature polymorphs of silicon dioxide.[2]................................69
Figure 3.2 a: Clusters of SiO_4 tetrahedra, b: bonding of Si and O and c: the unit cell of 1: Quartz and 2: Cristobalite. [1]...70
Figure 3.3: Yang *et al.*[17] illustrates the effect of concentration and pH upon the distribution of silicate anions in solution. 74

Figure 3.4: XRD pattern of amorphous silica precipitate[26], b: XRD pattern of precipitate from aqueous sodium metasilicate solution and c: XRD pattern of aqueous sodium silicate structures.[27]..78

Figure 3.5 Results of curve fitting of IR spectra of aqueous silicate solutions at a range of pH levels between 7.5-11.5.[17]..79

Figure 3.6: 79 a: IR spectrum of aqueous sodium metasilicate solution (pH 10.5)[17], b: IR spectrum of solid sodium metasilicate nonahydrate, c: Amorphous silica and d: Precipitate obtained from sodium metasilicate aqueous solutions.79

Figure 3.7 a: Optical microscope image of film precipitate from aqueous solution of sodium metasilicate, b: Bright field TEM, c: High resolution image and d: EDX spectrum of aqueous sodium metasilicate solution.....................................81

Figure 3.8: Molecular structure of the TX-114 surfactant, where n = 7 or 8......82

Figure 3.9: Ternary phase diagram illustrating the dependence of the oil:water:surfactant composition upon the resultant phase for a cyclohexane:water:TX-114 combination..83

Figure 3.10a and b: Molecular structure of the Span 80 and Brij 30 surfactants respectively...83

Figure 3.11: Ternary phase diagram illustrating the dependence of the oil:water:surfactant composition upon the resultant phase for a heptane: water: 1:1 Span80:Brij30 combination……………………………………………………84

Figure 3.12 Graphical display of microemulsion compositions with varying SMS concentration and dispersed volume, and the effect upon the stability……….85

Figure 3.13 a, b and c: HREM, FFT and BF images of a representative quartz nanocrystal from a TX-114/cyclohexane microemulsion with 10 μl/2g 1 wt %. SMS precursor………………………………………………………………………86

Figure 3.14 a, b and c: HREM, FFT and BF images of a representative quartz nanocrystal from a TX-114/cyclohexane microemulsion with 10 μl/2g 4 wt %. SMS precursor………………………………………………………………………87

Figure 3.15 a, b and c: HREM, FFT and BF images of a representative quartz nanocrystal from a TX-114/cyclohexane microemulsion with 10 μl/2g 6 wt %. SMS precursor………………………………………………………………………87

Figure 3.16: Distribution of silicate species as a function of pH and concentration. Upper: 10 mmol L^{-1}, lower: 2 mmol L^{-1} aqueous sodium metasilicate solution.[17]………………………………………………………………89

Figure 3.17: Calculated oxovanadate speciation profile when in an aqueous solution.[35]………………………………………………………………………………92

Figure 3.18: ^{51}V NMR spectra of oxovanadate species in AOT reverse micelles, originally prepared with pH 10.5 stock solution of ammonia metavanadate.[35]…………………………………………………………………………93

Figure 3.19; Graphical display of variation in pH with concentration of pH at various dispersed volumes within 2g of 30 wt %. TX-114/cyclohexane continuum: 10 μl (Δ), 50 μl (□), 100 μl (x) and the comparable aqueous sodium metasilicate solutions……………………………………………………………………………94

Figure 3.20 Change in the solubility of quartz (solid) and amorphous (dashed) with pH.[36]……………………………………………………………………………95

Figure 3.21: Graphical representation to illustrate the dependence of the fraction of free water on the total water content within a microemulsion system. x : free water and ◊: interphasal water. [38]…………………………………………98

Figure 3.22 a, b and c: HREM of representative quartz material produced from a TX-114/cyclohexane microemulsion with 10 μl/2g a:2 wt %, b:4 wt % and c: 6 wt % SMS precursor……………………………………………………………101

Figure 3.23 a-d: a and b: HREM and FFT images of a representative quartz nanocrystal, c and d: HREM and FFT images of representative cristobalite material produced from a TX-114/cyclohexane microemulsion with 10 μl/2g 10 wt %. SMS precursor……………………………………………………………101

Figure 3.24 a-c: a and b: HREM and corresponding FFT images of representative material produced from a TX-114/cyclohexane microemulsion with 10 μl/2g 15 wt % and c: BF image of representative material from a 20 wt %. SMS precursor microemulsion……………………………………………………………………101

Figure 3.25 Rolafenol molecular structure [40-41]…………………………………102

Figure 3.26 a and b: SEM and Laser Doppler electrophoretic light scattering characterisation of silica particles synthesised from Rolafenol/cyclohexane emulsions.[27] ……………………………………………………………………102

Figure 3.27 a and b: HREM and FFT of a representative quartz nanocrystal indexed to be the [201] zone axis of quartz and c: BF image of representative material from a TX-114/cyclohexane microemulsion with 10 µl/2g 4 wt %. SMS precursor……………………………………………………………………104

Figure 3.28 a and b: HREM and FFT of a representative quartz nanocrystal indexed to be the [201] zone axis of quartz and c and d: BF images of representative material from a TX-114/cyclohexane microemulsion with 50 µl/2g 4 wt %. SMS precursor……………………………………………………………104

Figure 3.29 a: SAXS scattering function for dispersed 1% aqueous sodium metasilicate nonahydrate within a 30 wt %. TX-114/cyclohexane system. Blue: 5 µl/g, red: 25 µl/g and black: 50 µl/g……………………………………………108

Figure 3.29b: Pair distance distribution function p(r) for dispersed 1% aqueous sodium metasilicate nonahydrate within a 30 wt %. TX-114/cyclohexane system. Blue: 5 µl/g, red: 25 µl/g and black: 50 µl/g………………………………………108

Figure 3.30 Graphical display of microemulsion compositions with varying SMS concentration and dispersed volume, and the effect upon the stability. Black = microemulsion and red = immediate precipitation of amorphous silicate phase……………………………………………………………………………113

Figure 3.31 a and b: HREM and BF of representative quartz nanocrystals from a Span 80/Brij 30/heptane microemulsion with 10 µl/2g 3 wt %. SMS precursor……………………………………………………………………………115

Figure 3.32 a, b and c: HREM, FFT and BF of representative quartz nanocrystals respectively from a Span 80/Brij 30/heptane microemulsion with 10 µl/2g 5 wt %. SMS precursor………………………………………………………115

Figure 3.33 a and b: HREM and FFT, ([201] zone axis) of a representative quartz nanocrystal from a Span 80/Brij 30/heptane microemulsion with 10 µl/2g 7.5 wt %. SMS precursor……………………………………………………………………115

Figure 3.34 a and b: HREM and FFT, ([201] zone axis of quartz) of a representative quartz nanocrystal from a Span 80/Brij 30/heptane microemulsion with 10 µl/2g 10 wt %. SMS precursor……………………………116

Figure 3.35 a, b and c: BF, HREM and FFT, ([110] zone axis) of representative cristobalite nanomaterial from a Span 80/Brij 30/heptane microemulsion with 10 µl/2g 10 wt %. SMS precursor………………………………………………117

Figure 3.36 a and b: HREM and FFT, ([200] zone axis of nanoparticles of quartz and c: representative dominant metastable amorphous silica material from a Span 80/Brij 30/heptane microemulsion with 10 µl/2g 14 wt %. SMS precursor..117

Figure 3.37: a, b and c: HREM, FFT (indexed to be the zone [0-4-2] zone axis) and BF of representative quartz nanocrystals respectively from a Span 80/Brij 30/heptane microemulsion with 100 µl/2g 1 wt %. SMS precursor..118

Figure 3.38: a and b: HREM and FFT of representative cristobalite nanocrystal from a Span 80/Brij 30/heptane microemulsion with 100 µl/2g 1 wt %. SMS precursor..118

Figure 3.39: a SAXS scattering function and b: Pair distance distribution function p(r) for dispersed 1% aqueous sodium metasilicate nonahydrate within a 40 wt %. Span 80/Brij 30/heptane system. Blue: 5 µl/g, red: 25 µl/g and black: 50 µl/g..120

Figure 3.40 a: BF, b: HREM and c: corresponding FFT indexed to be the [0-4-2] zone axis of representative material for 1:1 Span80/Brij30/heptane microemulsion with 10 µl/2g 7.5 wt % SMS 121

Figure 3.41 a: BF, b: corresponding DP for the representative nanoquartz material obtained from a 1:1 Span80/Brij30/heptane microemulsion with 10 µl/2g 7.5 wt % SMS after 9 days. 121

Figure 3.42: Corresponding EDX spectrum highlighting the elemental composition of the nanoaggregate structures observed in Figure 3.41..........123

Chapter 4

Figure 4.1 Distribution curves for the different protolytic species of DPA in aqueous solution.[4]..128

Figure 4.2: a and b: BF, HREM, DP and FFT images of DPA crystals from a non-ionic surfactant/alcohol co-surfactant system, with 225 µl/g of a supersaturated DPA solution in 2M HCl.[1]..129

Figure 4.3 a: IR spectrum of precipitate obtained upon mixing 25 wt %. (blue), 30 wt %. (red) and 40 wt %. (black) aqueous SMS solutions in a 1:1 vol. ratio with 2.2 M HCl solutions. Figure b: Yang et al [6]....................................132

Figure 4.4: XRD pattern of remaining precipitate when silica gel phase is rinsed with acetone..132

Figure 4.5: IR spectrum of precipitate obtained upon mixing 20 wt %. (blue) and 25 wt %. (red) aqueous SMS solutions in a 1:1 vol. ratio with 1.5 M HCl solutions..133

Figure 4.6: Optical microscopy images of precipitate formed from the addition of 1:1 vol. 2.2 M, 1.5 M and 0.3 M HCl to 20, 25 and 30 % wt. aqueous sodium metasilicate solution respectively..135

Figure 4.7: a and b: Ternary phase diagram illustrating the dependence of the oil:acid:surfactant composition upon the resultant phase for a (a) heptane: water: 1:1 Span80:Brij30 combination and (b) heptane: 2.2 M HCl: 1:1 Span80:Brij30 combination.[1]..136

Figure 4.8: a and b: Ternary phase diagram illustrating the dependence of the oil:acid:surfactant composition upon the resultant phase for a cyclohexane:water:TX-100 and 1-hexanol combination (a) and for a cyclohexane:2.2 M HCl:TX-100-1 hexanol combination (b)[1]......................137

Figure 4.9: Graphical display of microemulsion compositions with varying SMS concentration and dispersed volume, and the effect upon the stability. Black = microemulsion and red = immediate precipitation of amorphous silicate phase and green = stable microemulsion with impurities from Span 80 surfactant present at the bottom of the vial. 139

Figure 4.10: Graphical display of microemulsion compositions with varying SMS concentration and dispersed volume, and the effect upon the stability upon the addition of a 1:1 0.3 M HCl acid via a mixed microemulsion method. Black = microemulsion and red = immediate precipitation of amorphous silicate phase and green = stable microemulsion with impurities from Span 80 surfactant present at the bottom of the vial..140

Figure 4.11: Graphical display of microemulsion compositions with varying SMS concentration and dispersed volume, and the effect upon the stability upon the addition of a 1:1 1.5 M HCl acid via a mixed microemulsion method. Black = microemulsion, red = immediate precipitation of amorphous silicate phase and green = stable microemulsion with impurities from Span 80 surfactant present at the bottom of the vial. 141

Figure 4.12: Graphical display of microemulsion compositions with varying SMS concentration and dispersed volume, and the effect upon the stability upon the addition of a 1:1 2.2 M HCl acid via a mixed microemulsion method. Black = microemulsion, red = immediate precipitation of amorphous silicate phase and green= microemulsion with Span 80 surfactant impurities........................141

Figure 4.13: a BF image of representative material from a 1:1 Span80/Brij30/heptane microemulsion with 10 µl/2g 5 wt % SMS, b and c: HREM of nanoquartz, with EDX spectra illustrating elemental composition of sample from a 1:1 Span80/Brij30/heptane microemulsion with 10 µl/2g 5 wt % SMS + and 10 µl/2g 0.3 M HCl, d and e: HREM and corresponding FFT - [0-4-2] zone axis of nanoquartz from 10 µl/2g 5 wt % SMS + 10 µl/2g 1.5 M HCl sample and f: HREM of nanoquartz from 1:1 Span80/Brij30/heptane microemulsion with 10 µl/2g 5 wt % SMS + 10 µl/2g 2.2 M HCl sample...........................145

Figure 4.14: a, b and c: BF and HREM images of representative material, with corresponding d: FFT of a representative quartz nanocrystal indexed to be the [0-4-2] zone axis of quartz for a 1:1 Span80/Brij30/heptane microemulsion with 100 µl/2g 1 wt % SMS sample with a pH of 6.5...146

Figure 4.15: a and b: BF and HREM image of representative material, with corresponding c: FFT of a representative cristobalite nanocrystal of 1:1 Span80/Brij30/heptane microemulsion with 100 µl/2g 1 wt % SMS + 100 µl/2g 0.3 M HCl sample with a pH of 4.8..147

Figure 4.16: a BF images of sample, b and d: HREM image of representative material, with corresponding c and e respectively: FFT of a representative quartz nanocrystal indexed to be the [-1-10] and [201] zone axis respectively, of 1:1 Span80/Brij30/heptane microemulsion with 100 µl/2g 1 wt % SMS + 100 µl/2g 1.5 M HCl sample with a pH of 1.6. 147

Figure 4.17: a and b: BF images of representative material, with corresponding c: DP of a representative quartz nanocrystal indexed to be the [001] zone axis of 1:1 Span80/Brij30/heptane microemulsion with 100 µl/2g 1 wt % SMS + 100 µl/2g 2.2 M HCl sample with a pH of 0.8. 148

Figure 4.17: a and b: BF images of representative material, with corresponding c: DP of a representative quartz nanocrystal indexed to be the [001] zone axis of 1:1 Span80/Brij30/heptane microemulsion with 100 µl/2g 1 wt % SMS + 100 µl/2g 2.2 M HCl sample with a pH of 0.8. 149

Figure 4.18: a - c, BF images for 0.25 wt %, 1 wt % and 5 wt % SMS respectively of 1:1 Span80/Brij30/heptane microemulsion with 10 µl/2g SMS + 10 µl/2g 0.3 M HCl sample. 156

Figure 4.19:a, and c: BF or b: HREM images of representative material for 0.25 wt %, 3 wt % and 5 wt % SMS respectively of 1:1 Span80/Brij30/heptane microemulsion with 10 µl/2g SMS + 10 µl/2g 1.5 M HCl sample. 156

Figure 4.20: a, c, e and g: BF images of representative material for 0.25 wt %, 1 wt %,3 wt % and 5 wt % SMS respectively and b, d, f and I: HREM images of representative material of 1:1 Span80/Brij30/heptane microemulsion with 10 µl/2g SMS + 10 µl/2g 2.2 M HCl sample..157

Figure 4.21: Graphical display of microemulsion compositions with varying SMS concentration and dispersed volume, and the effect upon the stability. Black = microemulsion, red = immediate precipitation of amorphous silicate phase and blue = unstable..160

Figure 4.22: Graphical display of microemulsion compositions with varying SMS concentration and dispersed volume, and the effect upon the stability upon the direct addition of 2.2 M HCl. Black = microemulsion, red = immediate precipitation of amorphous silicate phase...161

Figure 4.23: Graphical display of microemulsion compositions with varying SMS concentration and dispersed volume, and the effect upon the stability upon the mixed microemulsion addition of 2.2 M HCl. Black = microemulsion, red = immediate precipitation of amorphous silicate phase and blue = unstable......162

Figure 4.24: a HREM image of representative material, and b: corresponding FFT indexed to be the [00-1] zone axis of 55 wt % (2.2) Triton X-100 : (1) 1-

hexanol in cyclohexane microemulsion with 25 µl/2g 5 wt % SMS sample. pH = 9.60……………………………………………………………………………………164

Figure 4.25: a: BF, b: HREM image of representative material, and c: corresponding FFT indexed to be the [1-1-4] zone axis for a 55 wt % (2.2) Triton X-100 : (1) 1-hexanol in cyclohexane microemulsion with 25 µl/2g 5 wt % SMS + 1:1 2.2 M HCl direct addition sample. pH = 1.65……………………………………165

Figure 4.26: a: BF, b: HREM image of representative material, and c: corresponding FFT indexed to be the [001] zone axis of quartz in a 55 wt % (2.2) Triton X-100 : (1) 1-hexanol in cyclohexane microemulsion with 25 µl/2g 5 wt % SMS + 1:1 2.2 M HCl mixed microemulsion addition sample. pH = 0.36………165

Figure 4.27: a: BF, b: HREM image of representative material, and c: corresponding FFT indexed to be the [00-1] zone axis of quartz for 55 wt % (2.2) Triton X-100 : (1) 1-hexanol in cyclohexane microemulsion with 10 µl/2g 5 wt % SMS. pH ~ 9.60……………………………………………………………………………167

Figure 4.28a and b: BF, and c: corresponding DP highlighting the material to be an amorphous silica phase of 55 wt % (2.2) Triton X-100 : (1) 1-hexanol in cyclohexane microemulsion with 10 µl/2g 15 wt % SMS. pH > 11……………….167

Figure 4.29 a: BF, b and c: HREM image of representative material, and d: corresponding DP indexed to be the [1-1-4] zone axis of quartz for 55 wt % (2.2) Triton X-100 : (1) 1-hexanol in cyclohexane microemulsion with 25 µl/2g 2.5 wt % SMS + 1:1 2.2 M HCl direct addition sample. pH = 1.14……………………….168

Figure 4.30 a and d: BF, b and e: HREM image of representative material, and c and f: corresponding FFT and DP indexed to be the [1-1-4] zone axis of quartz for 55 wt % (2.2) Triton X-100 : (1) 1-hexanol in cyclohexane microemulsion with 25 µl/2g 5 wt % SMS + 1:1 2.2 M HCl direct addition sample. pH = 1.65……..169

Figure 4.31 a and c: BF, b: HREM image of representative material, and d: corresponding FFT of the individual nanoparticles indexed to be the [1-1-4] zone axis of quartz for 55 wt % (2.2) Triton X-100 : (1) 1-hexanol in cyclohexane microemulsion with 25 µl/2g 7.5 wt % SMS + 1:1 2.2 M HCl direct addition sample. pH = 1.03…………………………………………………………………………169

Figure 4.32 a and b: BF, c: HREM image of representative material, and d: corresponding FFT indexed to be the [1-1-4] zone axis of quartz for 55 wt % (2.2) Triton X-100 : (1) 1-hexanol in cyclohexane microemulsion with 25 µl/2g 2.5 wt % SMS + 1:1 2.2 M HCl direct addition sample. pH = 1.14……………………171

Figure 4.33 a and b: BF, c: HREM image of representative material, and d: corresponding FFT indexed to be the [1-1-4] zone axis of quartz for 55 wt % (2.2) Triton X-100 : (1) 1-hexanol in cyclohexane microemulsion with 100 µl/2g 2.5 wt % SMS + 1:1 2.2 M HCl direct addition sample. pH = 1.00……………………….172

Figure 4.34 a: BF, b: HREM image of representative material, c: corresponding FFT indexed to be the [1-1-4] zone axis of quartz and d: EDX spectrum highlighting the elemental composition of 55 wt % (2.2) Triton X-100 : (1) 1-

hexanol in cyclohexane microemulsion with 25 µl/2g 2.5 wt % SMS + 1:1 2.2 M HCl direct addition sample. pH = 1.65..173

Figure 4.35 a BF: amorphous silica b: BF, c: HREM image of representative crystalline material, d: corresponding FFT indexed to be the [110] zone axis of quartz and e: EDX spectrum highlighting the elemental composition of 55 wt % (2.2) Triton X-100 : (1) 1-hexanol in cyclohexane microemulsion with 25 µl/2g 2.5 wt % SMS + 1:1 2.2 M HCl direct addition sample. pH = 1.65.................173

Figure 4.36 a BF, b: HREM image of representative material, c: corresponding FFT indexed to be the [201] zone axis of quartz for 55 wt % (2.2) Triton X-100 : (1) 1-hexanol in cyclohexane microemulsion with 25 µl/2g 2.5 wt % SMS + 1:1 2.2 M HCl mixed microemulsion addition sample. pH = 0.12.....................174

Figure 4.37 a BF, b: HREM image of representative material from of 55 wt % (2.2) Triton X-100 : (1) 1-hexanol in cyclohexane microemulsion with 100 µl/2g 2.5 wt % SMS + 1:1 2.2 M HCl mixed microemulsion addition sample. pH = 0.97..175

Chapter 5

Figure 5.1: Hybridized states of carbon[3]..190

Figure 5.2: Allotropes of carbon: a: diamond, b: graphite, c: buckyball, d: carbon nanotubes and e: graphene.[4]...190

Figure 5.3: Simplified ternary "phase" diagram of carbon allotropes. [5]........191

Figure 5.4: The thermodynamic phase diagram for the various high pressure and high temperature polymorphs of carbon.[8]..192

Figure 5.5: Three common orientations of stacking arrangements of graphene layers. [12] 193

Figure 5.6: Representative image of turbostratic graphene sheets.[18]............194

Figure 5.7: Illustration of the potential overview for the dehydration of sugars to humin type structures.[50]..199

Figure 5.8 Schematic diagram depicting the nanographite synthesis mechanism.[51]...200

Figure 5.9: Images of the progression of the 'black carbon snake' experiment using sucrose and concentrated sulfuric acid. 203

Figure 5.10: a and b:a:Infra-red spectrum of the (black) carbonaceous material produced from the reaction of granulated sugar and sulphuric acid in the bulk, b : Infra-red spectrum of the (long dash) concentrated sulphuric acid, (star) water and (short dash) sucrose...204

Figure 5.11: Experimental pXRD of the bulk product of sulphuric acid and sucrose……………………………………………………………………………………2 06
Figure 5.12: Literature pXRD of amorphous carbon[57]…………………………206
Figure 5.13: XRD data from a commercial multi-layer (12 nm flake) graphene sample purchased from Graphene Supermarket…………………………………207
Figure 5.14: Raman spectra of material precipitated from the bulk reaction of sucrose with sulfuric acid (black) and a commercial multi-layer (12 nm flake) graphene sample purchased from Graphene Supermarket (red) …………….207
Figure 5.15: TEM images showing the humins amorphous carbon product that arises from the reaction of sulfuric acid with sucrose in the bulk. (a) Bright field TEM image, (b) HREM image and (c) Energy-dispersive X-ray (EDX) spectra of the region displayed in (b). Note the relatively large oxygen peak in (c) showing that a significant proportion of oxygen remains in the amorphous carbonaceous product……………………………………………………………………………………208
Figure 5.16: TEM data from a commercial multi-layer (12 nm flake) graphene sample purchased from Graphene Supermarket. (c) TEM bright field image, (d) electron diffraction pattern from region (c) and (e) EDX spectrum from region (c). ……………………………………………………………………………………...208
Figure 5.17: Structure of the microemulsion components clockwise from top: Hexadecyltrimethylammonium chloride (CTAC), sucrose, water, sulfuric acid, pentan-1-ol and cyclohexane……………………………………………………...210
Figures 5.18: a and b: Phase diagrams for the CTAC/pentan-1-ol and cyclohexane system with water and sulphuric respectively……………………210

Figure 5.19: Photograph of microemulsions after 7 days under ambient conditions……………………………………………………………………………212

Figure 5.20: a-d: TEM of the primary nanographitic particles synthesised from 0.25 to 1 wt %. aqueous sucrose and sulfuric acid mixed microemulsions. (a) Bright field image of a group of ~3–30 nm particles. (b) High resolution image (HREM) of an 8 nm particle. The FFT (inset) shows the expected graphitic 0.213 nm hexagonal pattern. (c) HREM of a hexagonal ~25 nm particle. (d) A ~15 nm particle folded on the right-hand side, showing 15 layers. The FFT (inset) gives the expected 0.34 nm interlayer graphite spacing. ……………………………...213

Figure 5.21: c-f: TEM Bright field images of the nanographitic aggregates synthesised from 0.25 to 1 wt.% aqueous sucrose and sulfuric acid mixed microemulsions showing ~ 250 nm particles, surrounded by smaller primary particles……………………………………………………………………………...215
Figure 5.22: b-c: TEM of the nanographitic aggregates synthesised from 0.25 to 1 wt.% aqueous sucrose and sulfuric acid mixed microemulsions. (b) Bright field image of a thin and patchy μm-sized particle. Its weak electron diffraction pattern (inset) shows the expected 0.213 nm hexagon and (c) a μm-sized particle. Its electron diffraction pattern (inset) shows the expected 0.213 nm hexagon……………………………………………………………………………...216
Figure 5.23: Raman spectra of material precipitated from the bulk reaction of sucrose with sulfuric acid (black), a commercial multi-layer (12 nm flake) graphene sample purchased from Graphene Supermarket (red) and spectrum

from a 3 μm particle synthesised from a 1 wt.% aqueous sucrose and sulfuric acid mixed microemulsion (green) 217
Figure 5.24: a-c: Representative AFM images and ESEM micrograph of the μm-sized graphitic particles synthesised from 0.25 to 1 wt %. aqueous sucrose and sulfuric acid mixed microemulsions. a and b show AFM phase contrast images from a 3 μm graphitic particle and c, shows an ESEM micrograph highlighting multiple steps on the surface of a 10 μm graphitic particle........................218
Figure 5.25: a-b: TEM of the nanographitic aggregates synthesised from 5 wt.% aqueous sucrose and sulfuric acid mixed microemulsions. (a) Bright field image of a large μm-sized particle and (b) a μm-sized particle. Its electron diffraction pattern (inset) shows the expected 0.213 nm hexagon..............................219
Figure 5.26: a-c : TEM of the nanographitic material synthesised from 30 wt.% aqueous sucrose and sulfuric acid mixed microemulsions. (a) Bright field image of a 150-200 nm sized particle, (b) a HREM imaging revealing a folded edge of graphitic material and (c) a depth profile of the folded material in (b), showing the expected 0.34 nm graphitic interlayer spacing...................................220

Figure 5.27: a-d: TEM images showing carbon nano-onions synthesised from a 30 wt %. sucrose and 95 wt %. sulfuric acid mixed microemulsions..............221

Figure 5.28: Raman spectra of material precipitated from the bulk reaction of sucrose with sulfuric acid (black), a commercial multi-layer (12 nm flake) graphene sample purchased from Graphene Supermarket (red) bought sample, a spectrum from a 3 μm particle synthesised from a 1 wt.% aqueous sucrose and sulfuric acid mixed microemulsion (green) and spectrum from a precipitate synthesised from a microemulsion ≥ 30 wt.% aqueous sucrose and sulfuric acid mixed microemulsion (purple)..222
Figure 5.29: Experimental pXRD of the precipitate synthesised from a microemulsion ≥ 30 wt.% aqueous sucrose and sulfuric acid mixed microemulsion. XRD showing only a broad amorphous peak centred at 2θ ~ 21^0. 222
Figure 5.30: a: Low magnitude and b: Bright field images of μm sized amorphous type material from a 60 μl/g 1 wt % aqueous sucrose and sulfuric acid mixed microemulsions..225

Figure 5.31: a-d: a and b :Scattering curves I(q) vs. q for the mixed microemulsion containing 1 wt.% sucrose, for a: 20 μl/g and b: 60 μl /g. c and d: Pair-distance distribution curves for mixed microemulsion containing 1 wt.% sucrose , for c: 20 μl/g and d: 60 μl /g..227

Figure 5.32: Black precipitate observed from sucrose crystal dissolution methodology for 2 mg/g sucrose crystals in 50 μl/g sulfuric acid microemulsion...230
Figure 5.33: a-b: a: Raman spectra of material precipitated from the sucrose crystal dissolution methodology for 2 mg/g sucrose crystals in 50 μl/g sulfuric acid microemulsion quantities of sucrose addition. b: 2 mg/g sucrose crystals in 45 μl/g sulfuric acid microemulsion quantities of sucrose addition. The bulk reaction of sucrose with sulfuric acid Raman spectrum is included on both for comparison..231

Figure 5.34: Expansion of Figure 5.33 b - Raman spectra of the nanographitic aggregates. Spectrum from a 3 μm particle synthesised from a 1 wt.% aqueous sucrose and sulfuric acid mixed microemulsion (dashed curve). The D peak at ~1350 cm-1 also contains a significant contribution from the silicon wafer 3rd order peak at ~1450 cm-1. The black curve shows the spectrum of the black precipitate from the microemulsion containing 45 μl g^{-1} sulfuric acid with 2 mg g^{-1} added sucrose and has D, G, 2D, D+G and 2G peaks............................231
Figure 5.35: a-b: XRD data from <0.1 mg of graphitic nanoaggregates precipitated in 1 month from a 50 μl g^{-1} sulfuric acid microemulsion with 2 mg/g added sucrose. (a) 2D XRD detector image obtained after two hours showing a the graphite (100)(101)(102) peaks and a very weak amorphous halo and b: Chi integration of the data shown in (a). 232
Figure 5.36: a-b: XRD data from <0.1 mg of graphitic nanoaggregates precipitated in 1 month from a 45 μl g^{-1} sulfuric acid microemulsion with 2 mg/g added sucrose. (a) 2D XRD detector image obtained after two hours showing a the graphite (002) peak and a very weak amorphous halo and b: Chi integration of the data shown in (a)...233
Figure 5.37: a-g: a and b. TEM Bright field images of the nanographitic material comparable to the nanoparticle observed by the mixed microemulsion method, c: corresponding DP to b, with expected 0.213 nm hexagon, d: HREM image of part of the aggregate shown in a, encompassing a folded region, eLFFT of the region around this HREM image, showing the 0.213 nm hexagonal spacing and the 0.34 nm interlayer spacing arising from the folded region, f and g: TEM bright field image showing amorphous carbons that comprised the majority of the precipitate along with a minority of the nanographitic particles...........234
Figure 5.38: Scattering curves I(q) vs. q for the sulfuric acid microemulsion with 20 μl/g (squares), 45 μl /g(triangles) and 50 μl /g (crosses) dispersed phase volume...236
Figure 5.39: Pair-distance distribution curves for the sulfuric acid microemulsions with 20 μl/g (squares), 45 μl /g(triangles) and 50 μl /g (crosses) dispersed phase volume...237

List of tables

Chapter 1

Table 1.1: Dependence of the temperature relative to the PIT temperature on the microemulsion structure.[24]……………………………………………………10

Table 1.2: Listings of HLB ranges and appropriate applications.[32]……………12

Table 1.3: A table to document the effect of co-surfactants on various parameters of constructed phase diagrams. % Microemulsion-Area of microemulsion region, % Liquid crystalline- Area of liquid crystalline region, % Amphiphile – Amount of amphiphile required to stabilise a microemulsion, % Water- Maximum amount of water stabilised.[34]……………………………………………………13

Table 1.4: Table to indicate the effect of the surfactant structure and packing parameter on the resultant micelle structure. [24,41]………………………………16

Table 1.5: Tabulated characteristics for microemulsions, nanoemulsions and emulsions……………………………………………………………………………21

Chapter 3

Table 3.1: Measured solubility of sodium metasilicate nonahydrate in various solvents……………………………………………………………………………76

Table 3.2: pH measurements of bulk sodium metasilicate solutions upon mixing and after precipitation of solid material is observed. ………………………………77

Table 3.3: pH measurements of TX-114/cyclohexane system with variation of both dispersed volume and SMS precursor concentration…………………………92

Table 3.4: Estimation of the nominal mean number of silica molecules residing in the microemulsion droplets (based upon the GIFT-determined estimation)……………………………………………………………………………97

Table 3.5: The electron densities of the components of the microemulsion .A range is given upon the likely density range of the surfactant…………………108

Table 3.6: Prediction of droplet dimensions using geometric and GIFT calculations…………………………………………………………………………110

Table 3.7: Estimation of perturbed water molecules by surfactant from GIFT radii……………………………………………………………………………………112

Table 3.8: Conventional pH probe measurements of 40 wt %. 1:1 Span 80 : Brij 30 /heptane microemulsions with SMS aqueous dispersed phases……………115

Table 3.9: The electron densities of the components of the microemulsion .A range is given based upon the likely density range of the surfactant…………120

Chapter 4

Table 4.1: Measured solubility of sodium metasilicate nonahydrate in various solvents……………………………………………………………………………130

Table 4.2: pH measurement of bulk sodium metasilicate solutions upon mixing with a 1:1 vol. ratio of 2.2 M HCl solution. 131

Table 4.3: pH measurement of bulk sodium metasilicate solutions upon mixing with a 1:1 vol. ratio of 1.5 M HCl solution..133

Table 4.4: pH measurement of bulk sodium metasilicate solutions upon mixing with a 1:1 vol. ratio of 0.3 M HCl solution..134

Table 4.5: pH measurements of 40 wt %. 1:1 Span 80: Brij30/heptane microemulsion system with variation of both dispersed volume and SMS precursor concentration and various concentrations of HCl added by the mixed microemulsion method...142

Table 4.6: The electron densities of the components of the microemulsion......150

Table 4.7: Comparison of the droplet size of 1:1 Span80:Brij30 microemulsion with aqueous, 0.3 M, 1.5 M and 2.2 M HCl dispersed phase at various dispersed volumes...152

Table 4.8: Estimation of perturbed water molecules by surfactant from GIFT radii upon no HCl addition...153

Table 4.9: Estimation of perturbed water molecules by surfactant from GIFT radii upon 0.3 M HCl addition...154

Table 4.10: Estimation of perturbed water molecules by surfactant from GIFT radii upon 2.2 M HCl addition...154

Table 4.11: Estimation of silica molecule number in each droplet................158

Table 4.12: pH measurements of 55 wt % (2.2) Triton X-100 : (1) 1-hexanol in cyclohexane microemulsion system with variation of both dispersed volume and SMS precursor concentration and 2.2 M HCl added by a direct addition and a mixed microemulsion method..163

Table 4.13: The electron densities of the components of the microemulsion. A range is given upon different densities of components being adopted...........176

Table 4.14: Estimation of perturbed water molecules by surfactant from GIFT radii upon no HCl addition...179

Table 4.15: Estimation of perturbed water molecules by surfactant from GIFT radii upon direct addition of HCl..179

Table 4.16: Estimation of perturbed water molecules by surfactant from GIFT radii upon mixed microemulsion addition of HCl....................................179

Table 4.17: Estimation of the nominal mean number of silica units residing in the microemulsion droplets (based upon the GIFT-determined droplet radius)..181

Table 4.18: Estimation of surfactant:silica molecule number in each droplet...183

Table 4.19: Summary of precipitate conditions for the 30 wt % 1:1 Span 80:Brij 30: heptane microemulsion system……………………………………………………186

Table 4.20: Summary of precipitate conditions for the 55 wt % 2.2:1 Triton X-100:1-hexanol:cyclohexane microemulsion system………………………………187

Chapter 5

Table 5.1: Assignment of IR peaks of carbonaceous material[56]………………..205

Table 5.2: Estimation of the average number of sucrose molecules residing in the microemulsion droplets (GIFT estimation)…………………………………..223

Table 5.3: Estimation of the ratio of sulfuric acid to the sucrose molecules in a droplet, assuming a constant dispersed phase of 20 µl/g (gift estimation)……224

Table 5.4: The electron densities of the components of the microemulsion ….226

Table 5.5: Estimation of the average number of sucrose molecules residing in the microemulsion droplets (gift estimation)……………………………………..229

Table 5.6: The electron densities of the components of the microemulsion…..235

Table 5.7: Summary of carbonaceous precipitate synthesised from various microemulsion compositions…………………………………………………………..240

List of graphs

Chapter 4

Graph 4.1: pH measurements of microemulsion as a function of dispersed phase for microemulsions with 1 wt % SMS………………………………………………143

Graph 4.2: Correlation plot between the pH of the bulk HCl and SMS solutions and the pH of HCl and SMS microemulsions with a dispersed phase of 100 µl/2g AND SMS concentration of 1 wt %...143

Graph 4.3a SAXS scattering function for dispersed 1 wt %. aqueous sodium metasilicate nonahydrate within a 40 wt %. Span 80/Brij 30/heptane system. Blue: 5 µl/g, red: 25 µl/g and black: 50 µl/g ……………………………………151

Graph 4.3b: Pair distribution function for dispersed 1% aqueous sodium metasilicate nonahydrate within a 40 wt %. Span 80/Brij 30/heptane system. Blue: 5 µl/g, red: 25 µl/g and black: 50 µl/g………………………………………151

Graph 4.4: a SAXS scattering function and b: Pair distribution function for dispersed 1% aqueous sodium metasilicate nonahydrate within a TX100/Hexanol/cyclohexane system………………………………………………177

Table of contents

Chapter 1 - Introduction

1.1 Aim…………1

1.2 Polymorphism…………2

1.3 Surfactants…………6

1.3.1 Classification of surfactants…………7

1.3.1.1 Krafft Phenomenon…………8

1.3.1.2 Clouding Phenomenon…………9

1.3.1.3 Phase Inversion Temperature (PIT)…………10

1.3.1.4 Hydrophilic-Lipophilic balance (HLB)…………11

1.3.1.5 Surfactant effectiveness and efficiency…………12

1.3.1.6 Interfacial tension…………12

1.3.1.7 Co-surfactant…………13

1.3.1.8 Micellisation…………14

1.3.1.9 Packing parameter…………15

1.3.1.10 Film curvature…………17

1.4 Confinement…………18

1.4.1 Rigid confinement…………18

1.4.2 Droplet confinement…………20

1.4.2.1 Macroemulsions…………21

1.4.2.2 Nanoemulsions…………22

1.4.2.3 Microemulsions…………23

1.4.2.3.1 Microemulsion structure…………25

1.5 Crystallisation…………27

1.5.1 Supersaturation…………28

1.5.2 Classical Nucleation Theory (CNT)…………29

1.5.2.1 Homogeneous nucleation…………31

1.5.2.2 Heterogeneous nucleation…………32

1.5.3 Crystal growth…………33

1.5.3.1 Crystal growth mechanisms…………34

1.5.4 Kinetic vs. thermodynamic control…………36

Chapter 2 – Experimental methods and techniques

2.1 Materials....43

2.2 Experimental methods....43

2.2.1 Microemulsion preparation....43

2.2.1.1 Acid addition....44

2.2.1.1.1 Direct addition....44

2.2.1.1.2 Mixed microemulsion addition....45

2.2.1.1.3 Crystal dissolution method....45

2.3 Experimental techniques....46

2.3.1 Attentuated Total Reflectance Fourier Transform Infrared Spectroscopy (ATR-FTIR/FTIR)....46

2.3.2 Raman Spectroscopy....48

2.3.3 Diffraction Theory....51

2.3.3.1 Small-Angle X-Ray Scattering....55

2.3.3.1.1 Generalised Indirect Fourier Transformation (GIFT) Analysis....56

2.3.3.2 Wide-Angle X-Ray Scattering (WAXS)....58

2.3.4 Transmission Electron Microscopy (TEM)....59

2.3.4.1 Energy-Dispersive X-Ray Scattering(EDX)....61

2.3.4.2 Beam damage....62

2.3.5 pH probe....63

2.3.6 Optical Microscopy....63

Chapter 3 – Quartz crystallisation

3.1 Introduction....69

3.2 Choice of system....71

3.3 Project outline....75

3.4 Experimental....76

3.4.1 Control experiments....76

3.4.2 Solubility tests....76

3.4.3 Unconfined experiments....77

3.4.3.1 pH measurements....77

3.4.3.2 XRD....78

3.4.3.3 IR....79

3.4.3.4 Optical and electron microscopy....................81

3.4.4 Phase diagrams....................81

3.4.4.1 TX-114/cyclohexane system....................82

3.4.4.2 Span80/Brij30/heptane system....................83

3.5 Triton X-114 system....................84

3.5.1 Microemulsion preparation....................84

3.5.2 Microemulsion experiments....................84

3.6 TX-114 / cyclohexane: Results and discussion....................85

3.6.1 30 wt %. TX-114 / 60 wt %. cyclohexane microemulsion system....................85

3.6.1.1 Effect of varying the SMS precursor concentration....................86

3.7 Variables affecting condensation and precipitation of silica....................88

3.7.1 Temperature....................88

3.7.2 pH....................89

3.7.3 Solubility....................94

3.7.4 Confined of restricted growth....................95

3.8 Estimation of silica concentration within the droplet....................96

3.8.1 Effect of increased variation of SMS precursor concentration....................98

3.8.2 Effect of varying the dispersed volume....................103

3.8.3 SAXS analysis and geometric droplet size....................106

3.8.3.1 Water perturbation....................110

3.9 Span80/Brij30/heptane system....................111

3.9.1 Microemulsion preparation....................111

3.9.2 Microemulsion experiments....................112

3.10 Span80/Brij30/heptane: Results and discussion....................113

3.10.1 40 wt %. 1:1 Span 80: Brij30/heptane microemulsion system....................112

3.10.1.1 pH....................113

3.10.1.2 Effect of varying the SMS precursor concentration....................114

3.10.1.3 Effect of varying the dispersed volume....................118

3.10.1.3.1 SAXS analysis of geometric droplet size....................119

3.10.1.4 Aging experiments 2 vs. 9 days....................121

3.10.1.4.1 Two day old samples....................121

3.10.1.4.2 Nine day old samples....................121

3.11 Conclusion..124

Chapter 4 – Acidified quartz crystallisation

4.1 Introduction..128
4.2 Experimental..130
4.2.1 Control experiments..130
4.2.2 Solubility tests..130
4.2.3 Unconfined experiments..131
4.2.3.1 2.2 M HCl and aqueous SMS bulk experiments..131
4.2.3.1.1 pH measurements..131
4.2.3.1.2 IR Spectroscopy..132
4.2.3.1.3 XRD..132
4.2.3.2 1.5 M HCl and aqueous SMS bulk experiments..133
4.2.3.2.1 pH..133
4.2.3.2.2 IR Spectroscopy..133
4.2.3.3 0.3 M HCl and aqueous SMS bulk experiments..134
4.2.3.3.1 pH..134
4.2.3.4 Optical microscopy..135
4.2.4 Phase diagrams..135
4.2.4.1 Span 80/Brij 30/heptane system..136
4.2.4.2 TX-100/hexanol/cyclohexane system..137
4.3 Span80:Brij30 system..138
4.3.1 Microemulsion preparation..138
4.3.2 Microemulsion experiments..138
4.4 Span80/Brij30/heptane: Results and discussion..138
4.4.1 40 wt %. 1:1 Span 80: Brij30/heptane microemulsion system..139
4.4.1.1 Effect of HCl acid upon the phase diagram stability..140
4.4.1.1.1 No HCl addition..140
4.4.1.1.2 0.3 M HCl addition..141
4.4.1.1.3 1.5 M HCl addition..141
4.4.1.1.4 2.2 M HCl addition..142
4.4.1.2 pH..143
4.4.1.3 Effect of varying the pH and the dispersed phase volume..146

4.4.1.3.1 No HCl addition: pH ~ 7....147
4.4.1.3.2 0.3 M HCl addition: pH ~ 5....148
4.4.1.3.3 1.5 M HCl addition: pH ~ 2....148
4.4.1.3.4 2.2 M HCl addition: pH < 1....149
4.4.1.4 SAXS Analysis and geometric droplet sizes....150
4.4.1.4.1 Electron density....150
4.4.1.5 Water perturbation....153
4.4.1.5.1 No HCl addition....154
4.4.1.5.2 0.3 M HCl addition....155
4.4.1.5.3 1.5 and 2.2 M HCl addition....155
4.4.1.6 Effect of varying the SMS precursor concentration....155
4.4.1.6.1 No HCl addition....155
4.4.1.6.2 0.3 M HCl addition....156
4.4.1.6.3 1.5 M HCl addition....156
4.4.1.6.4 2.2 M HCl addition....157
4.4.1.7 Estimated silica concentration within the droplet....158
4.5 Triton X-100 system....159
4.5.1 Microemulsion preparation....159
4.5.2 Microemulsion experiments....159
4.6 TX-100/hexanol/cyclohexane: Results and discussion....159
4.6.1 55 wt % (2.2) Triton X-100 : (1) 1-hexanol in cyclohexane microemulsion system....160
4.6.1.1 Effect of acid addition upon the phase diagram stability....160
4.6.1.1.1 No HCl addition....160
4.6.1.1.2 2.2 M HCl direct addition....161
4.6.1.1.3 2.2 M HCl mixed microemulsion addition....162
4.6.1.2 pH....163
4.6.1.2.1 Effect of varying the pH for a given dispersed phase volume....164
4.6.1.2.1.1 No HCl addition....164
4.6.1.2.1.2 2.2 M HCl – Direct addition....165
4.6.1.2.1.3 2.2 M HCl – Mixed microemulsion addition....165
4.6.1.3 Effect of varying the SMS precursor concentration....166

4.6.1.3.1 No HCl addition......166
4.6.1.3.2 2.2 M HCl – Direct addition......168
4.6.1.3.3 2.2 M HCl – Mixed microemulsion addition......170
4.6.1.4 Effect of varying the dispersed phase volume......170
4.6.1.4.1 2.2 M HCl – Direct addition......171
4.6.1.4.2 2.2 M HCl – Mixed microemulsion addition......174
4.6.1.5 SAXS analysis and geometric droplet size......175
4.6.1.5.1 Electron density......175
4.6.1.6 Water perturbation......179
4.6.1.6.1 No HCl addition......179
4.6.1.6.2 2.2 M HCl – Direct addition......179
4.6.1.6.3 2.2 M HCl – Mixed microemulsion addition......180
4.6.1.7 Estimated silica concentration within the droplet......180
4.6.1.7.1 Effect of varying the silica to surfactant ratio......181
4.6.1.8 Proposed formation mechanism......184
4.7 Conclusion......186

Chapter 5 – Nanographite crystallisation

5.1 Introduction......190
5.2 Project outline......198
5.3 Formation mechanism......198
5.4 Thermodynamic control......200
5.5 Experimental......202
5.5.1 Control experiments......202
5.5.2 Solubility tests......202
5.5.3 Unconfined bulk experiments......202
5.5.3.1 Visual observations......203
5.5.3.2 IR 204
5.5.3.3 XRD......206
5.5.3.4 Raman Spectroscopy......207
5.5.3.5 TEM......208
5.5.4 Phase diagrams......209
5.6 CTAC/Pentanol/cyclohexane system......211

5.6.1 Microemulsion preparation using a mixed microemulsion methodology……211
5.6.2 Microemulsion experiments……138
5.7 Mixed microemulsion method :Results and discussion……211
5.7.1 Effect of varying the sucrose precursor concentration……212
5.7.1.1 TEM……212
5.7.1.2 Raman Spectroscopy……217
5.7.1.3 XRD……218
5.7.1.4 AFM and ESEM……218
5.7.2 Effect of increased variation of sucrose concentration……219
5.7.2.1 TEM……219
5.7.2.2 Raman Spectroscopy……222
5.7.2.3 XRD……222
5.7.3 Estimation of the amount of carbon within the droplet……223
5.7.3.1 Ratio of sulfuric acid: sucrose molecules……224
5.7.4 Effect of varying the dispersed phase volume……225
5.7.4.1 TEM……225
5.7.4.2 SAXS analysis and geometric droplet sizes……226
5.7.4.2.1 Electron density……226
5.7.4.3 Estimated carbon concentration within the droplet……228
5.8 Sucrose crystal dissolution methodology……229
5.8.1 Effect of varying the dispersed phase volume……230
5.8.1.1 Visual observations……230
5.8.1.2 Raman Spectroscopy……231
5.8.1.3 XRD……232
5.8.1.4 TEM……234
5.8.1.5 SAXS analysis and geometric droplet sizes……235
5.8.1.5.1 Electron density……235
5.9 Conclusions……239

Chapter 6: **Conclusions and further work**

6.1 Overview of the work……244
6.2 Further work……250

Chapter 1

1.1 Aim

The principal basis for the following work is to demonstrate the importance of controllable crystallisation and consequential applications. This has recently been demonstrated for organic pharmaceutical compounds,[1] but the aim of the thesis will be to show its significance for inorganic and carbonaceous materials.

Microemulsions have been employed as a vector to explore the possibility of thermodynamically controlling the crystallisation process, utilising the 3D confinement of crystallisable material within nano-scale droplets. This opens a route to circumvent Ostwald's Rule of Stages, for potential applications in the pharmaceutical and agrochemical industries.[1] Water, heptane and Span80:Brij30 microemulsions were adopted to behave as confined mini reactors for the synthesis of α-quartz and graphite at room temperature and pressure from sodium metasilicate nonahydrate (SMS) and sucrose respectively, which can be used as a precursor to silica and graphite respectively.

Previous attempts at silica synthesis from within the microemulsion have only presented the amorphous phase, leaving many questions unanswered/whilst failing to reveal the underlying cause. Further, traditional methods of quartz synthesis employ hydrothermal conditions, or temperatures >1100 ^{0}C.[3]

Traditionally graphite can only be produced using high temperatures, with natural graphite arising via progressive metamorphisms of carbonaceous material subjected to temperatures above ~600 K and pressures >2 kbar. Synthetic pyrolytic graphite requires temperatures >2500 K and even nanographite formation from amorphous carbons requires temperatures >850 K.[4-6] Previous attempts to use carbohydrates in the old school carbon snake experiment have produced luminescent carbon dots by treatment of the deposited particles with nitric acid and 4,7,10-trioxa-1,13-tridecanediamine.[7] The ~5 nm particles had a mean interlayer spacing of

≈3.4 Å, similar to graphite, but lacked 3D crystalline order. Glucose has also been calcined at 873 K in the presence of dicyandiamide to produce graphene via growth on a sacrificial carbon nitride template, which was subsequently removed by heating to 1273 K.[8] In these prior investigations, high temperatures or extremely severe reactants are used to drive the precipitation of graphitic forms.

1.2 Polymorphism

Polymorphism is the ability of a crystalline compound to exhibit different crystal structures, whilst retaining the same molecular composition.[1] The phenomenon was first explored by F. Wöhler and J. von Liebig with the case of benzamide, where it was observed upon cooling that the metastable needle-like form 1 phase transformed into the more thermodynamically stable, rhombic form 1.[2]

In 1897, Friedrich Wilhelm Ostwald introduced Ostwald's Rule of Stages, drawing attention to the kinetic control of crystallisation. In brief, for the crystallisation process, Ostwald states, "A low energy system is produced from one with a greater initial energy, via the smallest possible changes in the free energy."[9] For a polymorphic system, this suggests a metastable form has the tendency to crystallize initially, before transforming to a more thermodynamically stable form.

The work of Wöhler and Liebig is continued by many researchers, both computational and experimental, attempting to understand and utilize polymorphism for a variety of reasons, most notably in the pharmaceutical applications.

For a given system, each polymorph differs in a variety of physical properties including: bioavailability, solubility, dissolution rate, chemical stability, physical stability, melting point, and colouration.[10]

Typically, organic molecules exhibit conformational polymorphism, as exhibited in the schematic below.[11] It can arise from rotation around a single bond, a change in torsion angle, a varied degree of hydrogen bonding as a result of rotation or the introduction of a solvent. As is demonstrated in Figure 1.1a-c, increased flexibility within a molecule allows for a greater degree of rotation, bending and stretching of both fixed and dispersive bonds by varying degrees allowing an array of polymorphs to be formed.

A well-documented, highly publicised and costly case highlighting the desirability of controllable crystallisation of pharmaceuticals is that of Ritonavir: a protease inhibitor prescribed as an anti-HIV drug by Abbot Laboratories in 1992. The primary mechanism of crystal growth and exhibition of conformational polymorphism for Ritonavir is via breaking and making new hydrogen bonds. This is demonstrated in Figures 1.2a-c.[12]

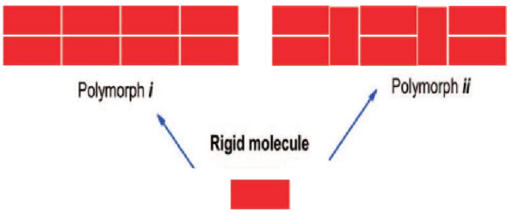

Figure 1.1a: A schematic representing the stacking of rigid molecules, generating two polymorphs, highlighting the limited ability to form different crystalline structures from rigid molecules.[11]

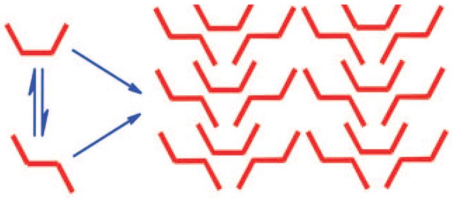

Figure 1.1b: A diagram to represent the varying types of stacking for a flexible molecule, with rotation around a torsional angle. By simply creating two conformers, cis and trans, the molecules can be arranged in a number of ways as demonstrated. [11]

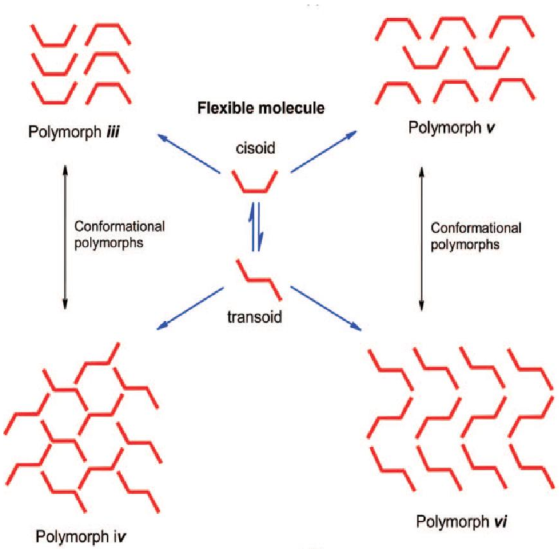

Figure 1.1c: A schematic representing stacking, created by a mixture of both the cis and trans flexible polymorphs.[11]

Reprinted (adapted) with permission from A. Nangia, *'Accounts of Chemical Research'*, 2008, **41(5)**, 595-604. Copyright 2008 American Chemical Society.

Form 1, indicated in Figure 1.2a-b, illustrates the hydrogen bonding network via amide linkages, generating ß-like stacks that pair up via hydrogen bonding between an alcohol of one molecule and a thiazole ring of another. In comparison, for form 2 (Figure 1.2c) the alcohol group acts synergistically, as both a hydrogen donor and acceptor, making both bonds stronger, relative to those in form 1.[12] It is obvious from Figure 1.2c that all strong hydrogen donors and acceptors within form 2 are satisfied, and therefore due to the growth mechanism, form 1 crystallises preferentially.

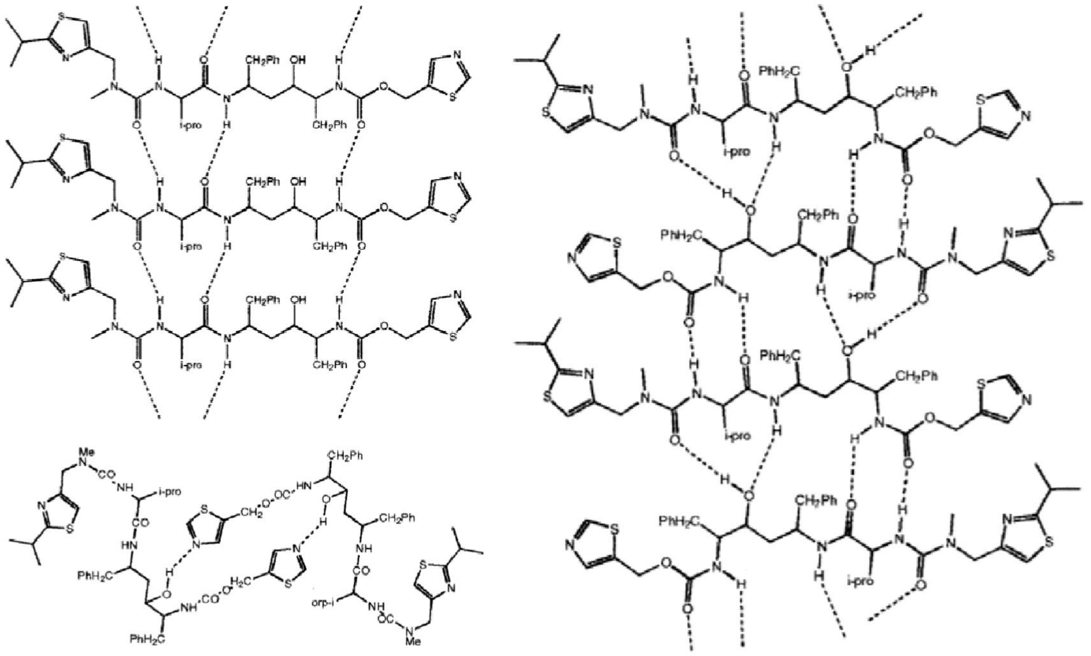

Figure 1.2a-c: Schematic to illustrate the variation in hydrogen bonding of form 1 and form 2 of Ritonavir (1,3-thiazol-5-ylmethyl N-[(2S,3S,5S)-3-hydroxy-5-[(2S)-3-methyl-2-{[methyl({[2-(propan-2-yl)-1,3-thiazol-4-yl]methyl})carbamoyl] amino}butanamido]-1,6-diphenylhexan-2-yl]carbamate).[12] Reprinted (adapted) with permission from J. Bauer, S. Spanton, R. Henry, J. Quick, W. Dziki, W. Porter and J. Morris. *'Pharmaceutical research'* 2001, **18(6),** 859-866. Copyright © 2001, Plenum Publishing Corporation.

Naively, Abbott Laboratories initially marketed the metastable form (Form 1) of the compound. Only upon further testing in 1998 was the more thermodynamically stable conformational polymorph (Form 2) found to exist, with a lower solubility, hence reducing the delivered dose. As a consequence Ritonavir had to be withdrawn and redeveloped. The morphology of the two forms and the molecular structure can be seen in Figure 1.3 below.

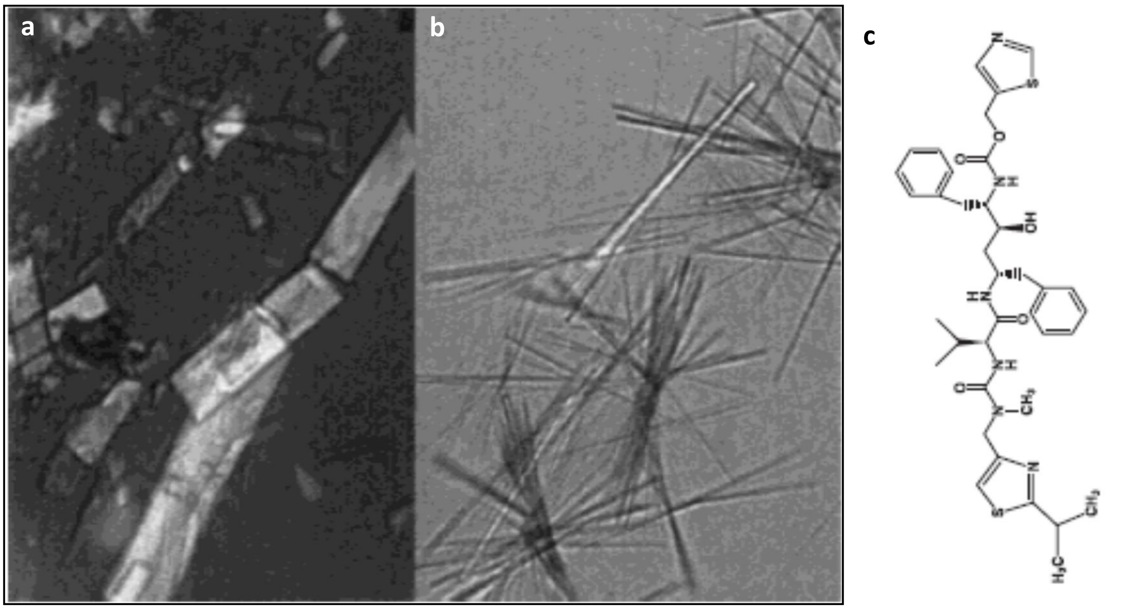

Figure 1.3a - b: An image depicting the morphology of the two polymorphs of Ritonavir, followed by (c) the molecular structure of Ritonavir.[12] Reprinted (adapted) with permission from J. Bauer, S. Spanton, R. Henry, J. Quick, W. Dziki, W. Porter and J. Morris. '*Pharmaceutical research*' 2001, **18(6),** 859-866. Copyright © 2001, Plenum Publishing Corporation.

In contrast, for inorganic materials, such as alumina (Al_2O_3), silica (SiO_2) and titanium dioxide (TiO_2), differentiation between polymorphs is primarily based on the order of packing or stacking within the crystal structure.[14-16] Taking alumina as a primary example, there exists many metastable forms besides the thermodynamically stable corundum (α-Al_2O_3). The various polymorphs are each based on a close packing structure of the oxygen anions, either cubic (γ, η, θ and δ) or hexagonal (α, κ or χ), with differing arrangements of the aluminium cations within the interstitial sites of the oxygen atom sublattices.[17] Hence polymorphism arises from different oxygen-layer stacking sequences, and variations in the distribution of both aluminium cations and vacancies within the two types of sites specified above.[14] Various phase transitions between the polymorphs have been documented. Initially, looking at fcc → fcc transitions: boehmite$\rightarrow\gamma\rightarrow\delta\rightarrow\theta$ by conventional transmission electron microscopy, it was noted that there was a gradual decline of the aluminium cations in the tetrahedral sites and an increase in their appearance in the octahedral sites, in addition to a decrease in cation vacancies.[18]

The γ→δ transition was observed by two groups, individually noting the continuous increase in the ordering of the cations from γ to δ.[17] Furthermore, phase transitions have been modelled and observed from fcc to hcp. Experimentally, the thermodynamically stable form is typically reached indirectly from a given precursor, via the sintering (>1000 °C) of the hydroxide or the oxy-hydroxide, as follows: [19]

$$\text{Precursor} \rightarrow Al(OH)_3 \rightarrow AlOOH + H_2O,\ AlOOH \rightarrow Al_2O_3 + H_2O.$$

For any system the time scale for which a metastable form converts to a more thermodynamically stable form varies greatly, due to dependence on the rate of nucleation. Consequently, the prediction of the resultant polymorph is difficult. Nevertheless, there are many variables which can be utilized to attempt to control and influence the nature of the resultant polymorph. Two general changes can be made, either to the system, i.e. the type of crystallisation method used or external effects.

Previous attempts have been made to alter the system composition and resultant polymorph. These include: taking advantage of the reaction by-products, templating, mechanical grinding, co-crystallisation, supercritical fluids, varying the pH, varying the temperature,[4] the variation of the solvent,[20] and the introduction of additives,[21] such as the choice of a specific surfactant.

1.3 Surfactants

A fundamental property of <u>surf</u>ace <u>act</u>ive <u>ag</u>e<u>nts</u> is the ability to adsorb at surfaces and interfaces, tending to lower the interfacial free energy for a given system.[22]. They play an essential role in a variety of applications, ranging from detergents, adhesives, laxatives and surface coatings.[11] However, upon increasing the concentration, aggregation of surfactant molecules limits such behaviour.

Physical properties particularly relevant to surfactants are: the degree of solubility (relying on the type of interactions), adsorption levels (dependent on the nature of the solvent and the molecular structure)[23] and interactions with the molecules in solution.

1.3.1 Classification of Surfactants

Broadly, all surfactants donning a wide range of structural forms can be catalogued into two bands, with either ionic (though often highly polar) or non-ionic, extremely polar head groups. Furthermore, the structure of both the hydrophilic head and hydrophobic tail can vary by incorporating such moieties as fluorocarbons or aromatic rings.[23]

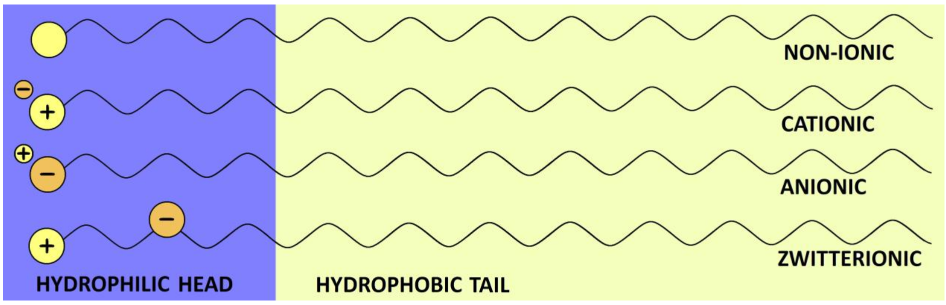

Figure 1.4: A simplified illustration of the 4 differing types of surfactants with respect to the charge on the hydrophilic head group.

Ionic surfactants are further categorized into three sub-groups dependent on their head group type: anionics, cationics, amphoterics, as illustrated in Figure 1.4.

Anionic and cationic surfactants carry a negatively or positively charged head group respectively. Anionic examples include: AOT (Aerosol-OT) typically carboxylates (CO_2^-), sulphonates (SO_3^-) and sulphates (OSO_3^-),[23] with CTAB/C (cetyltrimethylammonium bromide/chloride) being popular examples of cationic surfactants. Anionic surfactants are typically used in detergency, whilst cationics are used in personal care products in addition to substances such as anticorrosion agents.[23]

Non-ionic surfactants, such as polysorbate and sorbitan, contain highly polar groups which interact strongly with water via hydrogen bonding. Such surfactants have the advantage of a variable hydrophobic chain length and structure of the philic moieties allowing the surfactant to be optimised for a specific use, especially for low-temperature applications.[23]

The final class is the amphoteric or the zwitterionics, which consist of a hydrophobic tail and a doubly charged head group as shown in Figure 1.4.

Furthermore, ionic and non-ionic surfactants differ in performance with respect to temperature. Ionic surfactants' behaviour follows the Krafft phenomenon, whilst non-ionics follow the Clouding phenomenon.

1.3.1.1 Krafft Phenomenon

The Krafft phenomenon is observed for ionic surfactants only. Ionic surfactants are insoluble in cold conditions, however there is such a temperature where a sudden increase in solubility occurs, known as the Krafft point or Krafft temperature (**T_k**). The Krafft temperature is defined as the temperature where the solubility of the surfactant is equal to the CMC value at the same temperature.[24] As apparent from Figure 1.5, below **T_k** surfactant monomers exist in equilibrium with the hydrated crystalline phase[25], whilst above **T_k** there is a rapid increase in solubility and aggregation occurs. **T_k** can be determined from the intersection of the solubility and CMC curves as displayed in Figure 1.5.

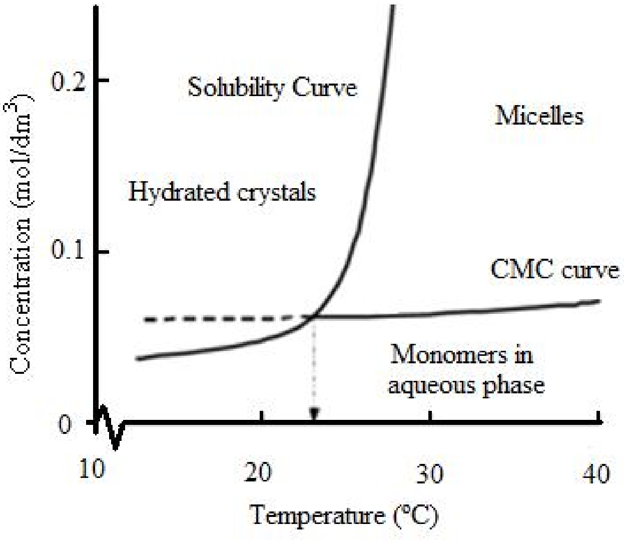

Figure 1.5: Hypothetical solubility curve to illustrate how the Krafft point can be determined from the intersection of the cmc curve and the solubility curve.[86] Reprinted (adapted) with permission from Schramm. L.L, Stasiuk. E.N and Gerrard Marangoni. D, '*Annu. Rep. Prog. Chem., Sect. C: Phys. Chem.*', 2003, **99**, 3-48 Copyright © 2003, Royal Society of Chemistry.

$\mathbf{T_k}$ for ionic surfactants is dependent on variables such as the chain length and chain structure. It is well documented, the introduction of bulkier hydrophilic head groups or chain branching reduces intermolecular interactions, inhibiting crystallisation and reducing the Krafft temperature.[24]

Such an investigation has been carried out by Rodriguez C H and Scamehorn J F, determining the effect of various surfactant compositions on $\mathbf{T_k}$.[26]

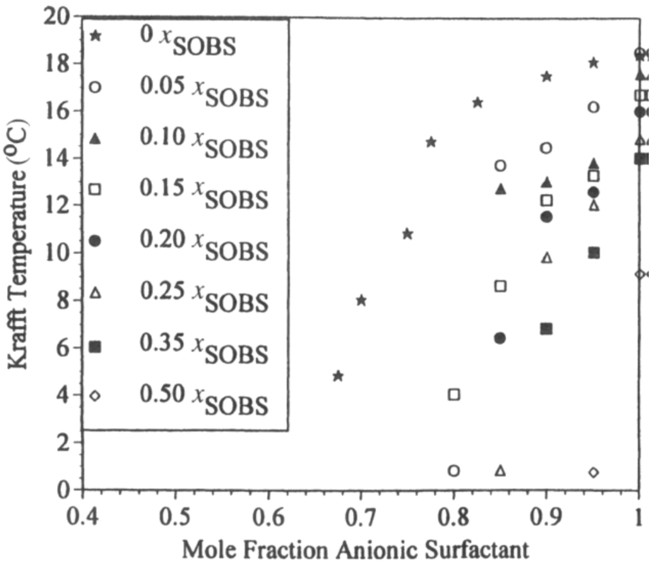

Figure 1.6: Graphical results indicating the effect of variation of the composition of an anionic/anionic/non-ionic system (Sodium Dodecyl sulphate/Sodium-4-n-octylbenzene-1-sulfonate (SOBS) /nonylphenol polyethoxylate). The mole fraction of the anionic surfactant SOBS is varied as follows: ★ -0, ○ -0.05, ▲ -0.10, □ -0.15, ● -0.20, △ -0.25, ■ -0.35 and ◇ -0.50 SOBS.[26] Reprinted (adapted) with permission from C. H. Rodriguez and J. F. Scamehorn, *'Journal of Surfactants and Detergents'*, 1999, **2(1)**, 17-28. Copyright © 1999, AOCS Press

Overall, the results illustrated in graphical form in Figure 1.6 indicate, for an anionic/anionic/non-ionic mixture, as the concentration of the bulkier/more branched anionic surfactant is increased, $\mathbf{T_k}$ decreases. The result coincides with the prediction that bulkier groups result in a lower Krafft temperature.

1.3.1.2 Clouding Phenomenon

For non-ionic surfactants in aqueous solution, there exists a temperature above which phase separation occurs, producing two isotropic phases:[27] a surfactant rich and a water rich phase, resulting in a cloudy appearance due to light scattering from the initial formation of droplets due to the aggregation of micelles.[28] This temperature is referred to as the cloud point (**T_c**).

Many possible causes for this separation have been proposed. Mukherjee (1972), stated as the temperature increases, a decrease in surfactant solubility results from the breaking of hydrogen bonds between the water soluble surfactant and water.[27] Furthermore, Staples and Tiddy (1978) suggested a decrease in hydration-repulsion interactions between the micelles caused the phase separation, in addition to a simultaneous increase in aggregation due to van der Waals forces.[29] Corti and Degiorgio (1980) explained the separation as a result of increased intermicellar interactions.[19] More recent investigations advise the formation of connected micellar networks or orientation of hydrogen-bonds could be responsible for the phase separation at **T_c**.[30]. Similarly to the Krafft temperature, **T_c** can be varied by altering the chemical structure or the addition of additives to the system.[24]

1.3.1.3 Phase Inversion Temperature (PIT)

Additionally, for non-ionic surfactants in emulsion there exists the phase inversion temperature, defined by Shinoda K *et al.* in 1969.[31] At the PIT, the surfactant film curvature inverts resulting in the Winsor type of microemulsion changing from an o/w-w/o or vice versa. The effect of the system temperature relative to the PIT is shown in Table 1.1.

System temperature, T, relative to the PIT	**Type of microemulsion**
T < PIT	Type 1 Winsor: o/w microemulsion.
T = PIT	Type 3 Winsor: middle phase microemulsion, with spontaneous curvature=0, and HLB~10.
T > PIT	Type 2 Winsor: w/o microemulsion.

Table 1.1: Dependence of the temperature relative to the PIT temperature on the microemulsion structure.[24]

1.3.1.4 Hydrophilic-Lipophilic balance (HLB)

Griffin W C (1949)[32] introduced the HLB scale, allowing the selection of a non-ionic surfactant suitable to form a w/o or o/w emulsion.

The HLB scale is a balance between the strength and size of the hydrophilic and lipophilic regions of a surfactant molecule and consequently the interfacial packing and film structure.[32] It is determined from the empirical formula (1.1):

$$HLB = 20.\frac{Mr_h}{Mr} \tag{1.1}$$

where Mr_h is the molecular mass of the hydrophilic moieties of the surfactant and Mr is the molecular mass of the entire surfactant monomer. Consequently, a surfactant which is highly hydrophilic is assigned a high HLB value, typically > 10, whilst a highly lipophilic surfactant is assigned a low HLB value, typically < 10. Griffin characterised a variety of surfactants, deriving an empirical equation (1.2) for non-ionic alkyl polyoxyethylenes, based on the chemical composition.[33]

$$HLB = \frac{E + P}{5} \tag{1.2}$$

Where **E** is the weight percentage of oxyethylene and **P** is the weight percentage of polyhydric alcohol. Much further work was carried out on establishing a rapid method for the determination of HLB values.[34]

In a study about the kinetics of emulsions, J T Davies illustrated the HLB could be directly determined from the chemical formula. Equations (1.3) and (1.4) summarise Davies' findings.[35-36]

$$HLB = \sum(hydrophilic\ group\ numbers) - n(group\ number\ per\ CH_2\ group) + 7 \tag{1.3}$$

where **n** is the number of CH_2 groups.[36]

Equation (1.3) can be simplified to (1.4):

$$HLB = [(nH) - (mL)] + 7 \tag{1.4}$$

where **H** and **L** are constants associated with the hydrophilic and hydrophobic groups respectively, with **n** and **m** being the number of each of these groups per surfactant molecule.

Applications for surfactants which fall in specific ranges of HLB values are documented in Table. 1.2.

HLB range	**Application**
4 – 6	Water-in-oil emulsifiers
7 – 9	Wetting agents
8 – 18	Oil-in-water emulsifiers
13 – 15	Detergents
15 – 18	Solubilizers

Table 1.2: Listings of HLB ranges and appropriate applications.[32]

When calculating the HLB of a surfactant blend an additive approach is used. For example, for a 1:1 blend of Span80 (HLB:4.3) and Tween 80 (HLB:15.0),[37] the resultant HLB value would be equal to $(50\% * 4.3) + (50\% * 15.0) = 9.7$

1.3.1.5 Surfactant effectiveness and efficiency.

The 'ability' of a surfactant can be measured in 2 ways: **effectiveness** and **efficiency** of surface tension reduction. The effectiveness of a surfactant is described as the maximum decrease in interfacial tension that can be achieved for a given surfactant, whilst efficiency is defined as the required concentration of surfactant to produce a given decrease in interfacial tension.[24]

1.3.1.6 Interfacial tension

The surface or interfacial tension is defined as the minimum amount of work required to create a new unit area of surface or interface. Absorption of surfactant molecules at an interface causes a decrease in the surface free energy relative to the bulk solution, resulting in spontaneous aggregation, typically as a monolayer at an interface.[1]

1.3.1.7 Co-surfactant

It is possible for molecules such as medium and long chain alcohols to aid surfactants in lowering the interfacial tension,[38,24] due to their amphiphilic nature, i.e. a short hydrophobic chain and hydroxyl group, which enables them to interfere with surfactant packing, manipulating the curvature and the surface tension.[34]

Recent research carried out by R G Alany *et al.*[34], presents a thorough investigation on the effect of various related short chain alcohols and diols on the phase behaviour of a quaternary system.[34] The data presented in Table 1.3, illustrates the effect of varying the co-surfactant on the phase stability of emulsions consisting of an ethyl oleate oil phase, sorbitan monolaurate and polyoxyethylene 20 sorbitan mono-oleate surfactants and a water aqueous phase.

Co-surfactant	**% Micro-emulsion**	**% Liquid Crystalline**	**% Amphiphile**	**% Water**
Co-surfactant free	19	28	67	15
1-Propanol	15	0	70	60
1-Butanol	43	0	40	62
1-Hexanol	23.5	29.5	60	22
1-Octanol	1.5	22.5	92	5
1,2-Propanediol	11.5	49	78	15
1,2-Pentanediol	30	13	50	52
1,2-Hexanediol	43	0	40	72
1,2-Octanediol	48	12	25	40

Table 1.3: A table to document the effect of co-surfactants on various parameters of constructed phase diagrams. % Microemulsion-Area of microemulsion region, % Liquid crystalline- Area of liquid crystalline region, % Amphiphile – Amount of amphiphile required to stabilise a microemulsion, % Water- Maximum amount of water stabilised.[34]

Reprinted (adapted) with permission from R. G. Alany, T. Rades, S. Agatonivc-Kustrin, N.M. Davies and I.G. Tucker, '*International Journal of Pharmaceutics*', 2000, **196**, 141-145. Copyright © 2000 Elsevier Science B.V

No obvious trends were determined from the findings, however it is apparent that the addition of any given co-surfactant has a significant effect on the phase behaviour of the original system.[34] Further research by Mendonça *et al.* investigated the role of two isomeric co-surfactants, (1-pentanol and 3-methyl-1-butanol) using a w/o microemulsions, with soybean oil and sodium dodecyl sulfate.[39] The two co-surfactants, differing in structure: unbranched, short chain hydrocarbon with a hydroxyl group and a shorter chain, with a branched methyl group respectively, were determined to govern the physicochemical properties as a result of dissimilar steric effects.[39]

1.3.1.8 Micellisation

Micellisation is an entropically driven process which occurs when the concentration of the surfactant is increased above the CMC causing the aggregation of surfactant molecules. Micellisation results partly from the tendency of hydrophobic tail groups to minimise contact with water, allowing maximisation of interaction between such tail groups, whilst the hydrophilic head groups remain in contact with the water.

The Gibbs-Helmholtz equation provides an insight into the thermodynamics of micelle formation, equation (1.5):

$$\Delta G_m = \Delta H_m - T\Delta S_m \tag{1.5}$$

where $\boldsymbol{\Delta G_m}$ is the free energy change of micellisation, $\boldsymbol{\Delta H_m}$ is the enthalpy change of micellization, $\mathbf{T}$ is the temperature of the system and $\boldsymbol{\Delta S_m}$ is the entropy change of micellisation.

Unexpectedly, micelle formation results in a small positive increase in the enthalpy and a large positive entropy, suggesting the process is entropy driven. However, aggregation of monomers may be expected to result in negative entropy, due to a decrease in the configurational entropy of the surfactant molecules, which can no longer explore the system volume individually. In addition, the typically water insoluble hydrocarbon, hydrophobic tail of the surfactant, suggests a negative enthalpy value is expected.[24] The fact this does not occur can be reasoned by understanding the hydrophobic tailgroup and water-structure effect. The individual alkyl chains of the monomer act to force structure upon the surrounding H_2O molecules because the water molecules can only hydrogen bond effectively with themselves and not the neighbouring hydrocarbon chain. Consequently, the water molecules can only adopt a limited number of configurations whilst still maintaining their hydrogen-bonding, resulting in a cage-like structure around the hydrocarbon chain and a reduced configurational entropy for these molecules. Upon micellisation, this order is broken, resulting in the overall increase in the entropy and a negative standard free energy.

1.3.1.9 Packing parameter

Micelles can take four main structural forms: spherical micelle, inverted micelles, cylindrical micelles and bilayers. Consider a spherical micelle, as pictured in Figure 1.7.

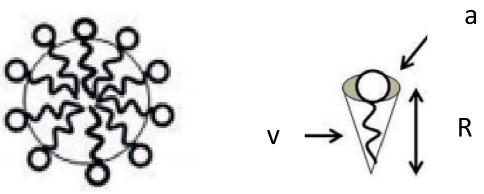

Figure 1.7: A schematic to illustrate the three quantities on which the packing parameter and consequently the micelle structure are dependent on.[87]

Reprinted (adapted) with permission from Salim. M, Minamaikawa. H, Sugimura. A and Hashim. R, *'Med. Chem. Commun.'*, 2014, **5**, 1602-1618. Copyright © 2014, Royal Society of Chemistry.

The components can be related by equation (1.6) as a consequence of equations (1.7) and (1.8)

$$R = \frac{3\nu}{a} \tag{1.6}$$

where **R** is the radius, **v** is the hydrophobic core volume and **a** is the surface area of the surfactant molecule at the interface.

The volume of a sphere and the surface area of a sphere are, respectively:

$$\frac{4\pi R^3}{3} \quad and \quad 4\pi R^2 \qquad (1.7 \text{ and } 1.8)$$

Furthermore, assuming **R** for a spherical micelle cannot exceed a critical length, $\mathbf{l_c}$, and that a zeroth-order theory applies: one where intermolecular interactions are ignored [40], $\mathbf{a} \cong \mathbf{a_0}$, (i.e the mean area of the surfactant molecule is considered to be close to the optimum area),[41] then geometric arguments alone allow the determination of micellar packing. In particular, it is apparent that the critical condition for the formation of spherical micelles is:[42]

$$\frac{v l_c}{a_o} = \frac{1}{3} \qquad (1.9)$$

In general the adopted structure is assumed to be determined by the following critical packing parameter, equation (1.10):

$$P_c = \frac{v}{a_0 l_c} \qquad (1.10)$$

where **v** is the volume of the hydrophobic chain, $\mathbf{a_0}$ is the optimised interfacial area of the hydrophilic head group and $\mathbf{l_c}$ is the critical extended length of the chain in the micelle. [41]

The condition for the resultant structure is given in the Table 1.4 below.[24,41]

Packing Parameter	**Micelle Structure**	**Typical Surfactant structure**
$\frac{v}{a_0 l_c} < 1/3$	Spherical	Single alkyl hydrophobic chain, large hydrophilic head group.
$1/3 < \frac{v}{a_0 l_c} < 1/2$	Cylindrical/ Hexagonal	Single alkyl hydrophobic chain, small hydrophilic head group.
$1/2 < \frac{v}{a_0 l_c} < 1$	Bilayers	Double flexible alkyl hydrophobic chain, large hydrophilic head group.
$\frac{v}{a_0 l_c} > 1$	Inverted	Double bulky alkyl hydrophobic chain, small hydrophilic head group.

Table 1.4: Table to indicate the effect of the surfactant structure and packing parameter on the resultant micelle structure.

Reproduced with permission from D. J. Mitchell and B. Ninham, *'J. Chem Soc. Faraday Trans 2'*, 1981, **77**, 601-629. Copyright © 1969, Royal Society of Chemistry

The resultant packing parameter and micelle structure indicates the type of emulsion possible or vice versa.

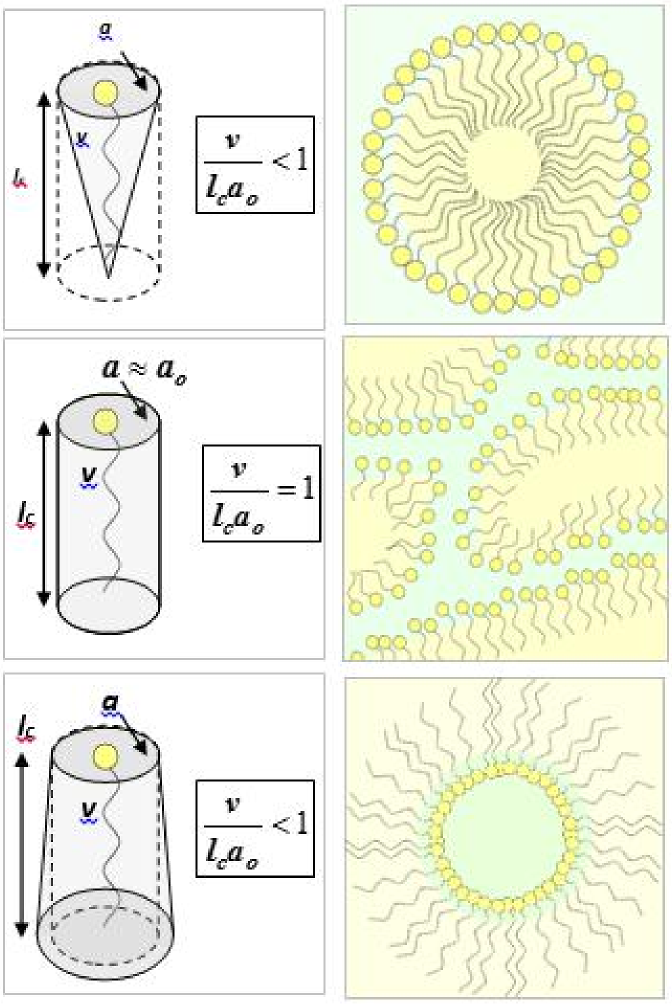

Figure 1.8: Schematic of the effect of the surfactant structure on the packing parameter and micelle structure.

1.3.1.10 Film Curvature

The packing parameter is related to the spontaneous film curvature, **C_0**: the curvature of the surfactant film when there are equal amounts of oil and aqueous phase.[41] If one of the phases dominates, or a modification to the surfactant is made, a deviation is made from **C_0**. For $C_0 < 0$, negative curvature, occurs and this suggests the surfactant film bends towards the aqueous phase, forming a w/o emulsion. This arises from competition between packing areas of the hydrophilic head groups and the hydrophobic tails.

Specifically, this occurs when interactions between head groups favour a decrease in packing area[43] or if the oil phase has the ability to significantly penetrate the hydrophobic tails of the surfactant molecules, as is the case with shorter hydrophobic tails.[38] This corresponds to a packing parameter > 1 and inverted micelle geometry. Conversely, positive curvature ($C_0 > 0$), suggests the film bends towards the oil phase producing o/w emulsions, corresponding to $P_c < 1$. Zero curvature indicates the film has no preference, such that $P_c \sim 1$ and bicontinuous emulsions are preferred. Evidently, the preferential aggregate structure is not dependent on any one variable, but a combination of factors including: the packing parameter, film curvature and the HLB (Hydrophilic-Lipophilic Balance).

1.4 Confinement

There are a vast number of confinements available to the research community with varying size, porosity and dimensionality. These include: track-etch membranes, controlled pore glasses,[44 - 46] mesoporous solids, gold-islands,[47] nanoporous alumina,[44,48] macroemulsions,[49] nanoemulsions[50] and microemulsions.[1,51] Each of the named confinements have been recently applied by various research teams to attempt to understand the effect on nucleation and crystallisation.

1.4.1 Rigid confinement

Contolled pore glasses (CPGs) have been utilised to attempt to control nucleation, crystallisation and crystal growth, particularly polymorphism. Originally developed for their use in chromatography, CPGs are efficient at providing regulated pore sizes, varying average pore sizes as a confinement for a crystallisable substrate.[45] Various groups, including Ha J-H and Beiner M individually exploited CPGs to investigate the stabilisation of polymorphs within nanoscopic confinement. Ha J-H, has crystallised multiple examples in CPGs: pimelic acid, glutaric acid, suberic acid, coumarin and anthranilic acid,[52] where results either caused polymorph stability crossover or presentation of undiscovered polymorphs.

The Beiner M group crystallised acetaminophen within the nanoconfinement, claiming to gain a certain degree of polymorph control by variation of the crystallisation conditions. Innovatively, the elusive form III was able to be stabilised within this confinement.[46]

Understanding of what causes the crystallisation of unstable forms is rather weak. It has been suggested it is due to critical size constraints, whilst others contest the effect is due to changes in crystallisation kinetics and thermodynamic equilibrium due to interfacial effects.[46]

Meldrum *et al.* explored the possibility of imitating natural crystallisation within track-etch membranes,[44] to produce intricate single crystals such as those exhibited by sea urchins. The 'body' of a sea urchin comprises of a single crystal of calcium carbonate, created in a unique environment with little control over synthetic variables such as temperature and pressure. Instead, there is evidence to suggest that the morphology and control over the crystallisation is determined by the adsorption of macromolecules and confinement.[44] It was found that the result of crystallizing amorphous $CaCO_3$ in the bulk solution was dependent on the experimental conditions.

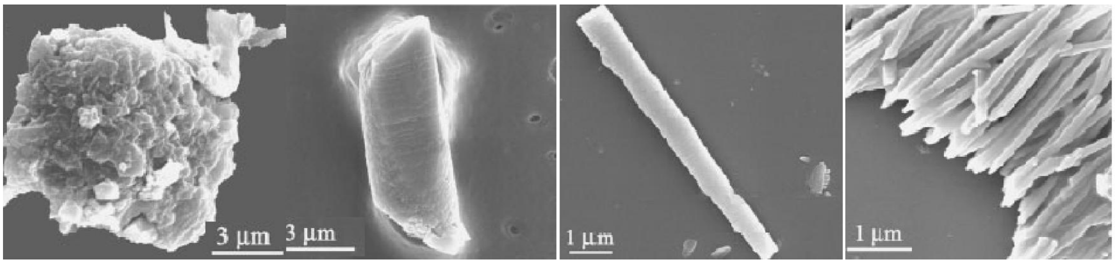

Figure 1.9: Calcium carbonate crystals grown from pore sizes of 10, 3, 0.8 and 0.2 µm respectively from left to right. In each case it is apparent, when compared to the 10 µm pore, that the use of an effective pore confinement has had an effect on the morphology of the crystal. [53]

Reprinted with permission from E. Loste, R. J. Park, J. Warren and F. C. Meldrum, *'Advanced Functional Materials',* 2004, **14(12)**, 1211-1220. Copyright © 2004 WILEY-VCH Verlag GmbH & Co. KGaA, Weinheim

However, as seen in Figure 1.9, the confinement of track-etch membranes, although dependent on pore size, rod shaped crystals were preferred, suggesting confinement does influence resultant morphology.[53]

Further research into confinement, includes that conducted by Myerson A S *et al.* using metallic hydrophilic gold islands to both nucleate and grow crystals confined by hydrophobic regions, hence the crystallisation process is controlled solely by the domain size of the island.[47] Myerson utilises the size control to investigate the possibility of nano-sized crystal in addition to polymorph screening due to the efficiency in the evaporation of the bulk solution providing varied supersaturation levels.

However these forms of rigid confinement are limited in application to systems such as in vivo crystallisation. Subsequently, particular interest has been paid to understanding the use of confinement by emulsion droplets to control nucleation and crystallisation.

1.4.2 Droplet confinement-Emulsions

Essentially, emulsions are created by stabilising for sufficient time two immiscible phases with a surfactant. By varying the concentration of the three fundamental components, it is possible to produce macroemulsions, nanoemulsions and microemulsions, as illustrated in the ternary phase diagram. (Figure 1.10)

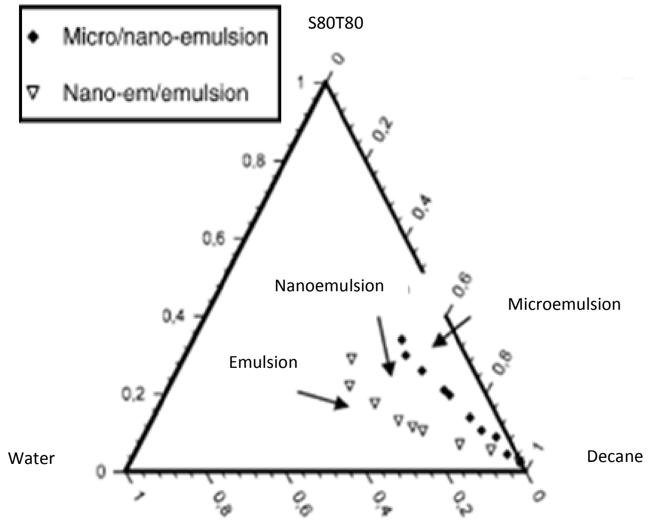

Figure 1.10: A phase diagram to illustrate how the composition of the confinement solution can be altered. This system uses a SPAN / TWEEN mixture as the surfactant, decane and water as the oil and aqueous phases respectively.[50]

Reprinted with permission from M. Porras, C. Solans, C. González, A. Martínez, A. Guinart and J. M. Gutiérrez, *'Colloids and Surfaces A: Physicochem. Eng. Aspects',* 2004, **249**, 115-118. Copyright © 2004 Elsevier B.V.

	Macroemulsion (White emulsion)	Nanoemulsion (Blue emulsion)	Microemulsion
Visible	Creamy white	Blue-semi opaque	Transparent
Droplet size (nm)	>400	20-500	<50
Thermodynamic stability	Unstable	Metastable	Stable
Picture			

Table 1.5: Tabulated characteristics for microemulsions, nanoemulsions and emulsions.

The three confinements differ in a numerous ways, such as droplet size, colour and stability. A brief summary is given in Table 1.5.

1.4.2.1 Macroemulsions

White emulsions or macroemulsions have the largest droplet size, ranging from 400 nm to µm range. Upon agitation, a thermodynamically unstable, but often metastable mixture of immiscible liquids with a white cloudy appearance can be formed, however with time phase separation will occur, producing the lowest energy state.[54]

Davey *et al.* investigated the use of macroemulsions to control particle properties, with particular interest in creating spherical particles, providing advantageous properties for the production of pharmaceutically active compounds.[20,55] Glycine and glutamic acid hydrochloride were crystallised from water-in-oil emulsions, highlighting both the effect of stirring, choice of surfactant and additive upon crystallisation from an emulsion.

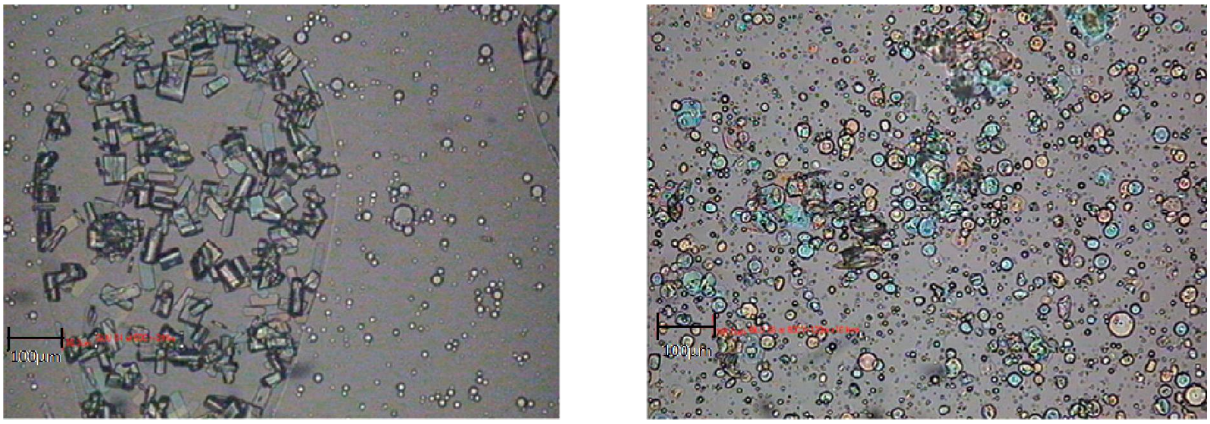

300 rpm

700 rpm

1400 rpm

Figure 1.11: Optical microscope images illustrating stirring speed on the emulsion crystallisation of g–glutamic acid hydrochloride. [20] Scale bar = 100 µm. Reprinted with permission from K. Chadwick, R. J. Davey and R. Mughal, *'Organic Process Research Development'*, 2009, **13**, 1284-1290. Copyright © 2009, American Chemical Society

The results show how a change in stirring speed affects the location of the crystallisation: 300rpm – oil phase, 700rpm – oil phase/droplets and 1400rpm - droplets.

1.4.2.2 Nanoemulsions

Blue emulsions or nanoemulsions are a metastable system with a dispersed phase between 20-500 nm, in-between emulsions and micromeulsions.[50] Similarly to an emulsion, nanoemulsion formation can be dependent not only on the thermodynamic state, but also the order of mixing.[50] A nanoemulsion appears blue in colour due to the droplets of the dispersed phase preferentially scattering blue light as it passes through the solution.

As nanoemulsion preparation remains problematic, interest in utilising them in e.g. drug delivery[49] i.e. in the case of eye drops, is still limited. In fact, much research is still being done to understand their structure, stability and how variables such as the surfactant type and concentration can affect these properties.[56] It is evident a major defining factor of emulsions is their droplet size, especially between micro and nanoemulsions. Sakeena. M H F *et al.* recently researched the effect of both oil and drug concentration on the droplet size of nanoemulsions.[57]

Both an increase in oil and drug (ketoprofen) concentrations were found to increase both the size and distribution of the droplets, as demonstrated in Figure 1.12.

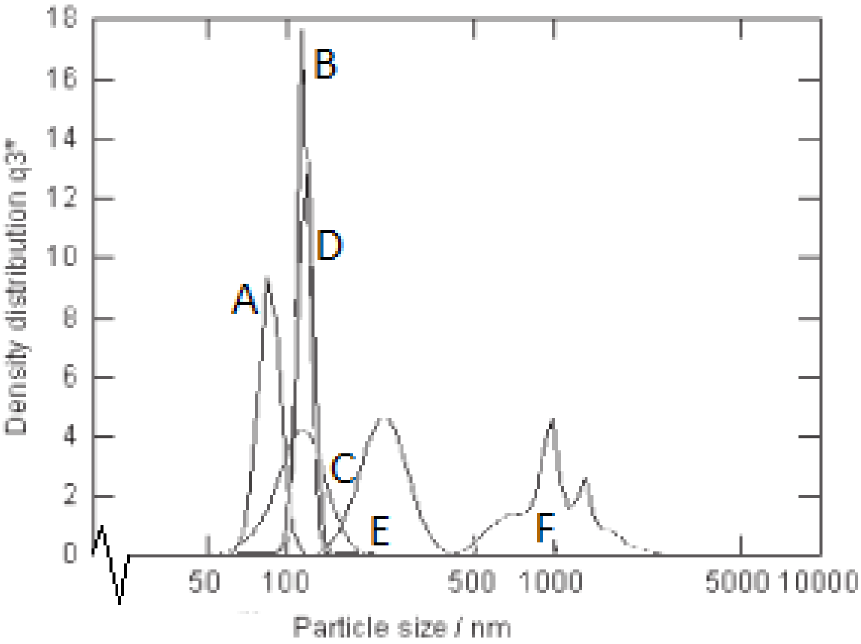

Figure 1.12: Graphical illustration of the variation in droplet size with oil (A-C) and drug (D-F) concentration. Weight percentages of each phase for each composition is as follows: A: 37:38:25, B: 30:30:40, C: 23:24:53 (Water:Surfactant:Oil), D: 1.25:24.69:37.52:36.54, E: 2.5:24.35:37.05:36.1, F: 5:23.75:36.1:35.15 (Drug:Oil:Surfactant:Water).[57]

Reprinted with requested permission from M. H. F. Sakeena, *'J. Oleo Sco',* 2011, **60(4),** 155-158. Copyright © 2011 by Japan Oil Chemists' Societyz

Such findings for the prior case were attributed to increase in oil in the lipophilic core of the surfactant, with aggregation of drug molecule on the surface of the oil droplets. In addition it is possible that the amphiphilic behaviour of the drug molecule helped support larger droplet sizes.[57]

1.4.2.3 Microemulsions

Hoar and Schulman (1943) first documented the existence of microemulsions, despite their common usage as detergents in most homes from the 1920s.[58]

However, it wasn't until the 1970s, when it was realised they could be used to improve oil recovery,[59] that extensive research began, such as that carried out by E W Kaler *et al.* in the early 1980s to gain an understanding of the microstructure of microemulsions[60-61] and the differences between micellar, inverted micellar and bicontinuous structures with variation of the composition.

Microemulsions are thermodynamically stable homogeneous/micro-heterogeneous mixtures, with droplet sizes typically < 50 nm. In addition, microemulsions appear optically transparent, due to the wavelength of visible light being greater than the droplets, allowing this section of the electromagnetic spectrum to pass through unscattered.

For microemulsions, their thermodynamic stability arises from the amphiphilic behaviour of the surfactants, working to lower the interfacial tension between the immiscible phases to $\sim 10^{-3}$ mN m^{-1}. Microemulsion formation generates a huge surface area as a result of the small droplet size. Consequently, without the influence of surfactants, miroemulsification would not spontaneously occur. Such behaviour can be reasoned by rationalising the free energy of formation stated in equation (1.11).[62]

$$\Delta G_{form} = \Delta A\gamma - T\Delta S_{conf} \qquad (1.11)$$

where $\mathbf{\Delta A}$ is the change in the interfacial area, $\boldsymbol{\gamma}$ is the interfacial tension, **T** is temperature and $\mathbf{\Delta S_{conf}}$ is the change in configurational entropy, which is larger and positive as it results from the increased entropy of the dispersed phase which can now access the entire system volume rather than being confined to a thin layer above (for an oil-in-water microemulsion) the aqueous phase. Minimisation of $\boldsymbol{\gamma}$ through the use of appropriate surfactants returns a negligible area term, thus resulting in a negative free energy of formation so that the microemulsion can form.[23]

1.4.2.3.1 Microemulsion structure

P.A. Winsor (1947), introduced a classification system for emulsions and proposed a theory underlining their formation.[63] Each class may be created by varying the concentration of each of the three essential components; oil phase, aqueous phase (or two immiscible phases) and surfactant, as illustrated in Figure 1.13.

- Type 1 consists of an oil-rich phase, with a second co-existing surfactant and aqueous phase: an oil-in-water microemulsion.
- Type 2 consists mostly of an aqueous phase, with a second co-existing surfactant and oil phase: a water-in-oil microemulsion.
- Type 3 consists of three phases. A oil-rich and aqueous phase in equilibrium with an additional surfactant rich middle phase: a middle phase microemulsion.
- Type 4 consists of a single mixed phase of oil, water and surfactant: a microemulsion that can be of type oil-in-water, water-in-oil or bicontinuous.[24,63]

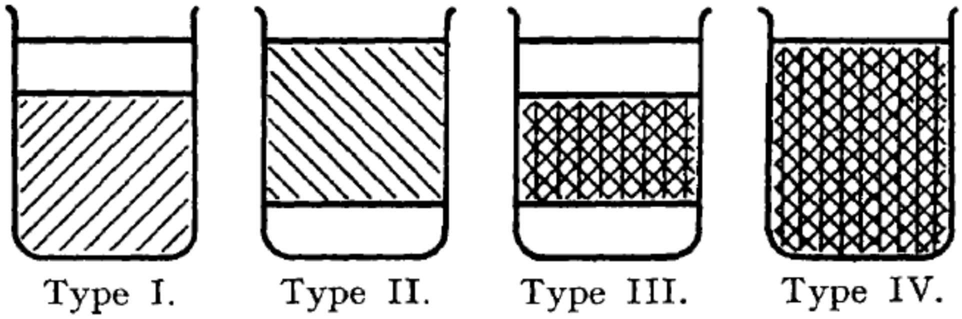

Figure 1.13: An illustrative view of the 4 classes of microemulsions, consisting of varying amounts of surfactant, an aqueous and an oil phase. [63]

Reprinted with permission from P. A. Winsor, '*Transactions of the Faraday Society*',1948, **44(6)**, 376-398. Copyright © 1969, Royal Society of Chemistry.

The structure which is adopted depends on the packing parameter, or more explicitly the dimensions of the surfactant monomer. By varying the surfactant dimensions; the packing parameter, film curvature and HLB values, this alters the micellar structure and the incidence of the macroscopic phases. Furthermore, for crystallisation processes within emulsions, surfactants are required in order to maintain a low surface tension. Note that for crystallisation in microemulsions, Ostwald ripening is often reduced because the rate of smaller crystals dissolving can be limited due to surfactant adsorption onto the small crystals. In addition, the smaller crystals often reside in separate droplets to the larger ones, so that the different-sized crystals are not bathed in the same solution. [62]

Various attempts have been made to take advantage of microemulsions' droplet confinement because microemulsions are thermodynamically stable. Quantum dots and nanoparticles have both been synthesised via utilising the nanoscopic confinement, whilst such confinement has been exploited further in attempts to gain control over polymorphism and morphology of various systems.

Numerous publications have documented the synthesis of quantum dots and nanoparticles since 1896. Until 1969, such behaviour was inexplicable, when the 'quantum size effect' was introduced via studies of the absorption spectra of CdS.[64] Further work was left until the mid-1980s, when groups such as Y Wang[64] led investigations into the synthesis, characterisation and properties of nanoscale semi-conductors.

Typically, nanoparticulate semiconductors' preparation is dependent on confining the excitons (a state where an excited electron and positive valence hole exist) in three dimensions, i.e. by lithography,[65] colloidal synthesis[66] or epitaxy[67] (patterned/self-organised growth). Further research has focused on the use of microemulsion droplets/surfactant micelles as a source of confinement for the synthesis of quantum dots and nanoparticles. CdS/CdSe quantum dots have been readily produced from the microemulsions via a number of different processing techniques: refluxing with methanol/toluene,[65] ultrasonic waves,[68] variation in temperature,[68] variation in surfactant chain length[69] and the use of the mixed microemulsion method.[70]. The body of work on quantum dot synthesis was extended by S Y Chang[71] (1994) *et al.* preparing CdS quantum dots confined by silica spheres within w/o microemulsions, where silica spheres are formed via the Stöber process: the hydrolysis and condensation of TEOS. Combining this method with the precipitation of CdS within the dispersed phase, monodisperse CdS quantum dots within monodisperse colloidal silica spheres are yielded.[72]

K. Margulis-Goshen demonstrated the effect of the microemulsion confinement on the preparation of organic/pharmaceutical nanoparticles. Simvastin, a poorly water-soluble drug,[73] has previously been synthesised within the confinement of an oil-in-water (o/w) microemulsion. The system of choice is: a butyl-acteate, ethanol and soybean oil phase with tween 80 surfactant and a water/simvastin flakes aqueous layer.

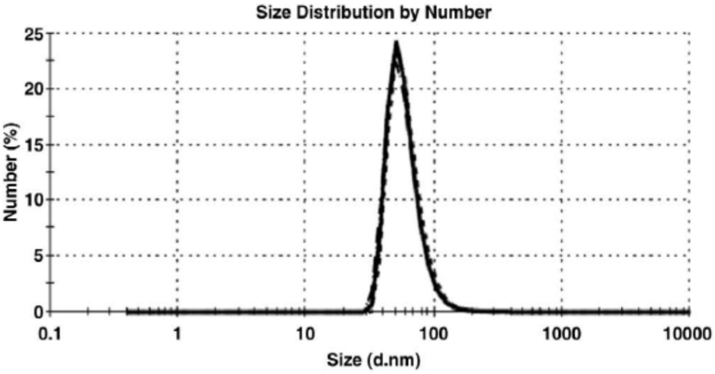

Figure 1.14: A distribution curve of simvastin particles prepared as a result of the dispersion of simvastin flakes in water.[73]
Reprinted with permission from K. Margulis-Goshen and S. Magdassi, *'Nanomedicine',* 2009, **5**, 274-281.Copyright © 2009 Elsevier Inc.

Apparent from Figure. 1.14, numerous repeats at various time intervals produced the same narrow range of simvastin particle sizes when prepared within the microemulsion.

1.5 Crystallisation

At the simplest level the process of crystallisation is the formation of solid crystalline phase precipitated from a solution (purely homogeneous mixture of more than one species) or a melt (a pure molten solid, or a molten solution which is typically solid at room temperature).[72] For a crystallisable material dissolved in a solution, the supersaturation limit is reached either by cooling, adding an antisolvent or solvent evaporation,[62] allowing precipitation to occur via nucleation and crystal growth processes, before the composition of the solution returns to equilibrium, saturation value.

1.5.1 Supersaturation

For spontaneous crystal growth to occur, a supersaturated solution is a known requirement.[74]

Supersaturation, **$\Delta\upsilon$**, formally defined as the difference between the chemical potentials of a supersaturated state, **μ_{ss}** (the surrounding solution) and the equilibrium state, **μ_{eq}** (the bulk crystal structure). This can mathematically be expressed as shown in equation (1.12).

$$\sigma = \frac{\mu_{ss} - \mu_{eq}}{k\mathrm{T}} \tag{1.12}$$

where **k** is the Boltzmann constant and **T** is the temperature. Assuming an ideal solution, (one where the activity coefficient is equal to 1) the supersaturation can be rewritten in terms of mole fractions and in turn, concentration, equation (1.13).

$$\sigma = ln(\frac{c_{ss}}{c_{eq}}) \tag{1.13}$$

where $\frac{c_{ss}}{c_{eq}}$ is the concentration ratio, otherwise denoted as the supersaturation ratio. Substituting and rearranging, gives equations (1.14) and (1.15).

$$\Delta\mu = kT_s ln\left(\frac{c_{ss}}{c_{eq}}\right)\ or\ \frac{\Delta_{sol}H\Delta T}{T_{sat}} \tag{1.14/1.15}$$

where, **Δ_{sol}H** is the enthalpy of the solution and **T_{sat}** is the temperature of saturation.

The importance of the degree of supersaturation is illustrated in Figure 1.15. As previously stated, for a supersaturated solution (above the dashed curve) spontaneously nucleation is viable, whereas for an undersaturated solution, (below the solid curve) neither nucleation or growth can occur.[75] However, for the metastable region (between the dashed and solid curves), the width of the region is dependent on the ability and ease with which new crystals can be produced.

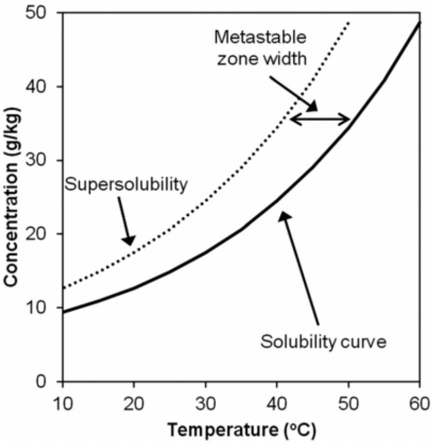

Figure 1.15: A hypothetical solubility curve to show the limits above and below the solubility curve.(solid curve) [88]
Reprinted with permission from Brown. C. J and Ni. X-W, *'Cryst Eng Comm',* 2012, **14,** 2944-2949. Copyright © 2012, Royal Society of Chemistry

Supersaturation promotes the formation of nuclei, however the work required in creating the new phase makes the nuclei unstable with respect to the bulk solution, due to their large surface area to volume ratio.[54]

1.5.2 Classical Nucleation Theory (CNT)

Classical nucleation theory was originally developed to explain the condensation of a vapour to a liquid from a supersaturated vapour; however adaptations allow the explanation of crystallisation from a supersaturated melt or solution. The nucleation process, whether homogeneous or heterogeneous can be described by CNT. Homogeneous nucleation refers to the formation of nuclei within a supersaturated solution, whilst heterogeneous nucleation refers to the formation of nuclei on a foreign species.

Generally, for daughter nuclei to aggregate from the parent phase, an interface must form between the aggregate and surrounding solution, invoking an energy barrier which must be overcome. The height of such a barrier is dependent on both the work required to create the interface per unit area and interfacial tension. As a result of their large surface area to volume ratio, this causes initial aggregates to be unstable with respect to their parent phase.[76] The effect of size of the clusters on the equilibrium conditions is accounted for in the case of the liquid droplet formation from the vapour by the Laplace equation and the Gibbs-Thomson equations, (1.17/1.18)

$$\Delta P = \frac{2\gamma}{r} \, and \, \Delta\mu = \frac{2\gamma v_d}{r} \qquad (1.17/1.18)$$

where $\Delta \boldsymbol{P}$, is the difference in pressure between the interior of the droplet and the bulk vapour, **γ** is the interfacial tension, **r** is the radius of the new droplet, $\Delta\boldsymbol{\mu}$ is the difference in chemical potential between the daughter and parent phase and $\mathbf{v_d}$ is the molecular volume of the droplet. As a consequence of the inverse relationship of the radial size to **ΔP** and **Δμ**, small droplets cause a large pressure or chemical potential difference with an associated large energy barrier of formation.[54]

Thus, to allow the daughter phase to form, the energy barrier is overcome via thermal fluctuations within the system which are larger than the energy barrier. The new phase is able to grow via aggregation of material to form larger clusters, until the critical radius, $\mathbf{r_{critical}}$ is reached, indicated on Figure 1.16. Similar arguments apply for the crystallisation from the solution. Consequently, if the radius of the cluster is greater than $\mathbf{r_{critical}}$, the nucleus becomes 'viable' and crystallisation is able to occur via a decrease in free energy. For a cluster, where the radius is smaller than $\mathbf{r_{critical}}$, the nucleus is likely to dissolve back into the solution as crystal growth is energetically unfavourable.[89]

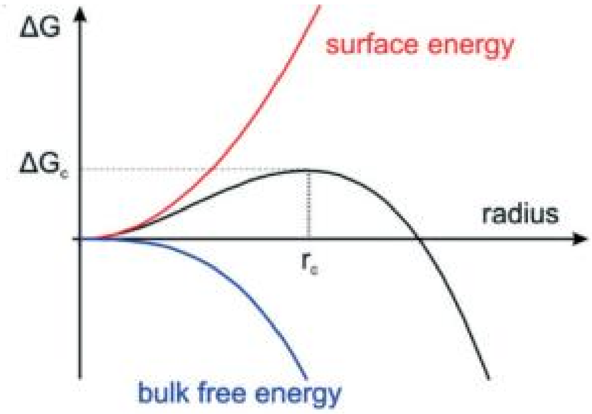

Figure 1.16: A diagram to represent the change in free energy for the two processes involved in nucleation: creation of a new phase and formation of new phase, combined together to give the overall (dashed) curve for nucleation.[89]

Reproduced with permission from Polte. J, *'Cryst Eng Comm',* 2015, **17,** 6809-6830. Published by The Royal Society of Chemistry.

It is apparent that a decrease in **$\Delta G_{critical}$** and **$r_{critical}$** is favourable in terms of crystallisation. For a crystal to nucleate and consequently grow, a sufficient level of supersaturation is required, although this is able to take place in the metastable region.[75] If the supersaturation falls within the metastable region, see Figure 1.15, the nucleation rate is low.[75] If the supersaturation is great enough, **$\Delta G_{critical}$** and **$r_{critical}$** become small enough to cause to spontaneous nucleation and the supersaturation level resides in the unstable region in Figure 1.15.[62] Hence the rate of nucleation is dependent on the supersaturation of the system.

1.5.2.1 Homogeneous nucleation

The rate of nucleation is dependent on the concentration of critical nuclei and the rate at which aggregation occurs.[54] Consequently, the rate of nucleation, **J,** can be expressed as follows:

$$J = W^{*}.n(i^{*}) \tag{1.19}$$

where **W^*** is the rate of aggregation of crystallisable species upon the nuclei, whilst **$n(i^*)$** is the near equilibrium concentration of critical nuclei, denoted as

$$n(i^{*}) = nexp^{\frac{-\Delta G_{critical}}{kT}} \tag{1.20}$$

where **$\Delta G_{critical}$** is the Gibbs free energy of formation for the critical nuclei, **k** is the Boltzmann constant and **T** is the temperature of the system.
Thus there is a general consensus, the equation to describe the rate of nucleation is:

$$J = Aexp^{\frac{-\Delta G_{critical}}{kT}} \tag{1.21}$$

where **A** is the pre-exponential factor,[77] which is dependent on the frequency of collisions between molecules, surface energy and the energy barrier of diffusion.[75]

The work of formation (**$\Delta G_{critical}$**) for liquid condensation from the vapour is determined as follows:[78]

$$\Delta G_n = G_n - n\mu_v \tag{1.22}$$

where **G_n** is the clusters' thermodynamic potential, when containing **n** molecules and **μ_v** is the chemical potential of the vapour, assuming constant temperature and pressure.[79] To determine **G_n,** the chemical potential of the liquid phase (**μ_l**) and the surface energy of the droplet (**γ**) are required.

$$\Delta G_n = n\mu_l - n\mu_v + 4\pi r^2 \tag{1.23}$$

Furthermore, assuming spherical droplets, **n** becomes[78]:

$$n = \frac{4\pi r^3}{3v_l} \tag{1.24}$$

subsequently,

$$\Delta G_n = \frac{4\pi r^3}{3v_c}\Delta\mu + 4\pi r^2\gamma \tag{1.25}$$

$\Delta \boldsymbol{G_{critical}}$ is set to a maximum, thus by differentiating $\Delta \boldsymbol{G_n}$ and re-substituting **$r_{critical}$**[54]:

$$\Delta G_{critical} = \frac{16\pi\gamma^3 v^2}{3\Delta\mu^2} \tag{1.26}$$

1.5.2.2 Heterogeneous nucleation

Heterogeneous nucleation results from nucleation upon foreign bodies such as the walls of the container, an impurity or a crystalline structure. Hence, faster laws of kinetics are followed as a result of the wetting effects.[78] Assuming a similar approach to that for homogeneous nucleation, heterogeneous nucleation can be determined to behave as follows:

$$\Delta Gcrit = \frac{16\pi\gamma^3 v^2}{3\Delta\mu^2}.f(\theta) \tag{1.27}$$

where **f(θ)** is the wetting function, dependent on the contact angle, illustrated in Figure 1.17.

The contact angle can be determined by assuming the surface tensions act as forces. By geometrically equating the forces in the horizontal plane, Young's equation is derived:

$$cos\theta = \frac{\gamma_{sv} - \gamma_{sl}}{\gamma_{lv}} \tag{1.28}$$

The value of $\boldsymbol{\theta}$ determines the degree of wetting and as a result the kinetics of nucleation, indicating the type of nucleation occurring.

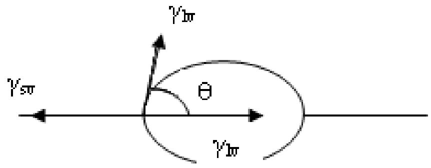

Figure 1.17: A pictorial description of the interfacial tensions acting as forces.

Intuitively, for θ = 0°, f(θ)=0, implying $\Delta G_{critical}$=0, i.e. there is no energy barrier to be overcome during nucleation, as complete wetting occurs. This situation is analogous to layer by layer crystal growth on flat faces (see Section 1.5.3.1), and in fact an energy barrier still exists but this is significantly lower than that required for nucleation. Whilst for θ=180°, f(θ)=1, suggesting heterogeneous nucleation no longer occurs, and homogeneous nucleation dominates.[54]

As the general rate equation mentioned for homogeneous nucleation is appropriate for heterogeneous nucleation, the rate at which nucleation proceeds depends on the degree of wetting. For example, the larger **f(θ)** is, the greater the amount of work required to overcome the energy barrier, thus slowing the rate of nucleation.

1.5.3 Crystal growth

A burst of interest in developing an understanding of the mechanisms behind crystal growth began in 1949, with a host of papers released attempting to describe crystal growth theory, the effect of the crystal surface and dislocations.[74,80-85]

The mechanism of crystal growth is explicitly determined by the structure of the crystal face. Burton and Cabrera (1949)[81], classified the crystal surfaces with respect to their potential to grow into close packed and non-close packed (stepped) surfaces. Close-packed surfaces occur “when it is as flat as possible, all the surface molecules are at the same distance from a plane parallel to it”, whilst non-close-packed surfaces consist of steps and kinks.[80-81] Further deviation between the surfaces has been made:

F (flat) faces: parallel to at least two most dense rows of atoms.

S (stepped) faces: parallel to one most dense row of atoms.

K (kinked) faces: not parallel to any most dense rows of atoms.

Each group is illustrated in Figure 1.18 below.[78]

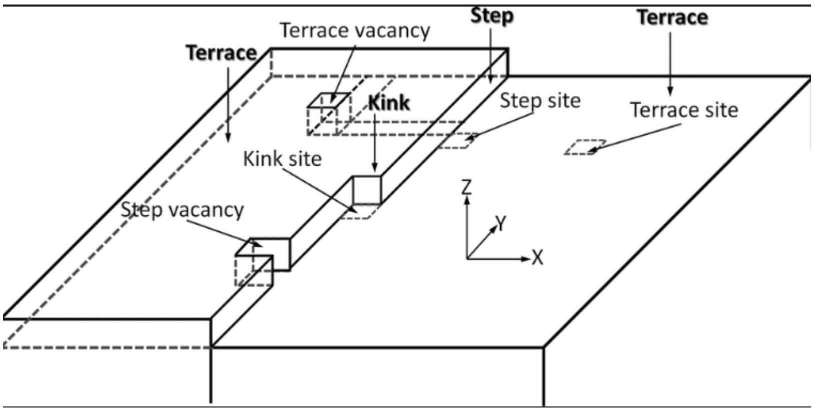

Figure 1.18: Schematic representation of the Kossel crystal model, exhibiting each crystal face: F, S and K. [90] Reproduced with permission from Bahrig. L, Hickey. S.G and Eychmuller. A, *'Cryst Eng Comm',* 2014, **16,** 9408-9424. Copyright © 2014, Royal Society of Chemistry

1.5.3.1 Crystal growth mechanisms

Major work was carried out by F.C. Frank, W.C. Burton and N. Cabrera in the late 1940's into understanding the mechanisms of crystal growth. It was suggested the mechanism by which crystal growth occurs is dependent not only on the structure of the crystal face as seen above, but also temperature, impurities adsorbed and the imperfections in the crystal planes.[80-81]

Typically the mechanism of growth at atomically rough sites (S or K) differs to that at the F site. For a solution at a sufficient supersaturation, atomically rough faces follow a continual growth mechanism due to the high density of kink sites. Thus the rate is simply dependent on the flux of atoms from the parent phase. Hence;

$$R = \lambda \Delta\mu \tag{1.29}$$

where **λ** is a kinetic coefficient, and the growth rate, **R** is linearly dependent on the supersaturation. F sites above a given temperature, the roughening temperature, $\mathbf{T_r}$, undergo a surface roughening transition to S or K. For a F site below $\mathbf{T_r}$, this mechanism is blocked by the inherent energy barrier accompanying the attachment of a single adatom upon a flat face. As this barrier is dependent on a summation of the number of broken and formed interactions between the solid and fluid,[62] hence the rate of growth is now dependent on the ability/frequency of the formation of 2D critical nuclei. Hence either 2D nucleation and lateral spreading or screw dislocation (at low supersaturations) growth mechanisms are followed. At higher supersaturations multiple 2D nucleation growth mechanisms may be observed due to the formation of more nucleation sites. As such processes occur, the density of 2D critical nuclei increases such that arriving adatoms can be added at almost any site. This leads to kinetic roughening, where the surface becomes atomically rough, allowing continual growth mechanisms to proceed. In summary, the ability of a crystal face to grow is dependent on two main points: the number of interactions and the strength of those interactions.[62]

The effect of the supersaturation on the growth rate for each mechanism mentioned above is illustrated in Figure 1.19.

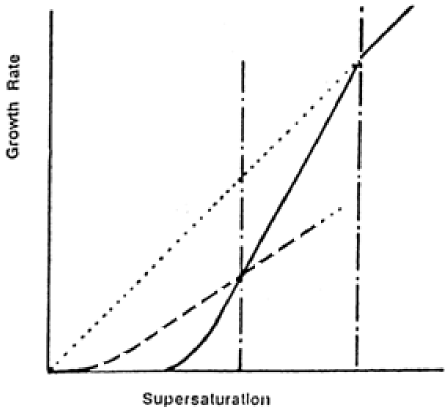

Figure 1.19: The effect of the level of supersaturation upon the growth mechanism/growth rate.[91] Reproduced with permission from Nguyen. T.T.H, Hammond. R.B, Roberts. K.J, Marziano. I and Nichols. G, '*Cryst Eng Comm',* 2014, **16,** 4568-4568. Copyright © 2014, Royal Society of Chemistry

The dotted linear line represents continual growth on atomically roughened surfaces. The dashed line indicates the relationship for a screw dislocation growth mechanism, whilst the solid line illustrates the effect for a 2D nucleation mechanism. It is evident that a screw dislocation growth mechanism is favoured for flat faces at low supersaturations, with respect to 2D nucleation. However in both cases, as the supersaturation increases it is apparent kinetic roughening is exhibited and a linear relationship is observed.

1.5.4 Kinetic vs. thermodynamic control

Previously, Ostwald's rule of stages was introduced to explain the kinetic control of crystallisation, and the preferential crystallisation of the metastable form from a polymorphic system. Recent work, by S J Cooper *et al.*[1] has been carried out, leading to both a theoretical and experimental understanding of how Ostwald's Rule of Stages can be overcome. [1]

The method suggests the use of supersaturated solutions, stabilized and confined by the 3D nano-confinement of droplets within a microemulsion, which forces the process of crystallisation to be brought under thermodynamic control. Hence, the crystallisation of the most thermodynamically stable polymorph for a given system is selectively permitted.

As discussed previously, the crystallisation process involves two stages: nucleation and crystal growth. Nucleation, the formation of a daughter phase from the parent phase, requires surmounting the nucleation free energy barrier. Nuclei corresponding to this energy maximum are denoted critical nuclei, which are able to grow until the supersaturation is diminished. An illustration of the free energy profile for a polymorphic system, consisting of a stable and metastable form is given in Figure 1.20.

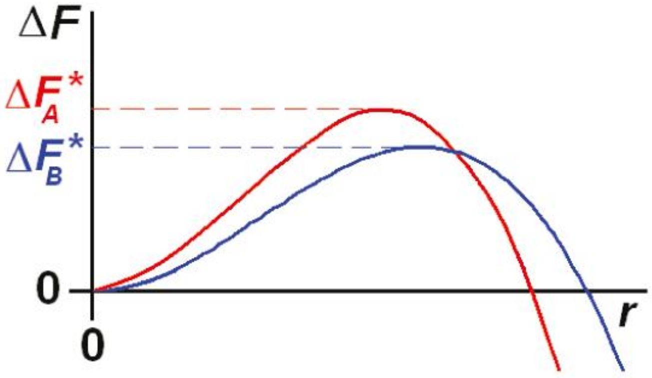

Figure 1.20: Free energy profile of a polymorphic melt crystallisation, for the thermodynamically stable (red) and a metastable case (blue). [1] Reprinted with permission from C. E. Nicholson, C. Chen, B. Mendis and S.J. Cooper, 'Crystal Growth and Design', 2011, 11(2), 363-366. Copyright © 2011, American Chemical Society

In accordance with Ostwald's rule of stages, the metastable form exhibits a smaller nucleation barrier, ΔF^*_B, than the thermodynamically stable form, ΔF^*_A. It is evident from Figure 1.20, polymorph, 'B' will tend to crystallise first due to the lower energy barrier. Conversely, if the energy barrier of the more stable form is surmountable, this form has the ability to crystallise out simultaneously, hence limited control over the selectivity of the crystallized polymorph occurs.

To achieve the most stable polymorph selectively, crystallisation can be carried out in the nanoconfinement of microemulsions so that the crystallisation is limited by the requirement to form a long-lived near stable nucleus, rather than a critical nucleus. This is illustrated in Figure 1.21, where a minimum appears in the plot of free energy versus nucleus size, corresponding to the case in which a nucleus is surrounded by saturated solution and so it is not favourable to grow any further. In crystallisation from the bulk, this minimum would occur at large crystal sizes but in a nanoconfined system, the supply of crystallisable molecules is so limited, the minima occurs in the nm-size range. The free energy change at the minimum is denoted ΔF^*_{min}. As the more stable polymorph is less soluble, the surrounding solution has a greater supersaturation for the stable form that the metastable form. Consequently, the stable form can grow to larger sizes that the metastable one before the supersaturation is relieved: $r^*_{min,A} > r^*_{min,B}$ and consequently, $\Delta F^*_{min,A} < \Delta F^*_{min,B}$.

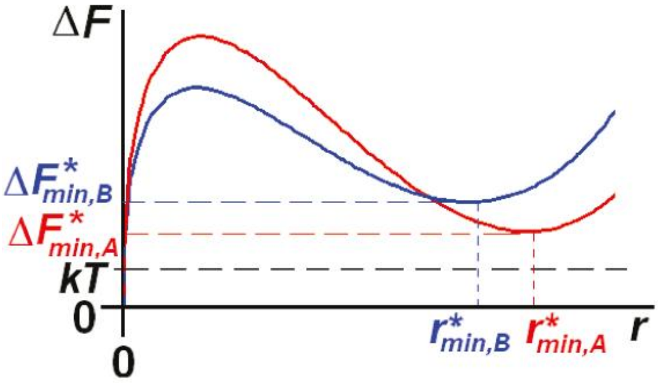

Figure 1.21: Free energy profile for a polymorphic system, crystallized within the confinement of a microemulsion for the thermodynamically stable, A (red) and a metastable, B (blue) case.[1]

Assuming the population of nuclei, sized $\mathbf{r^*_{min}}$ is dependent on the Boltzmann factor, i.e quasi-equilibrium conditions exist, then:

$$exp^{\frac{-\Delta F^*_{min}}{kT}} \tag{1.30}$$

and a significant population exists for $\Delta F^*_{min} \leq kT$, thus thermodynamic control is obtained in 3D nanoconfinement only upon satisfying the conditions $\Delta F^*_{min,A} \leq kT$, whilst $\Delta F^*_{min,B} \geq kT$. If this is the case, only polymorph A will have a significant population of near stable nuclei, assuming $\mathbf{\Delta F^*_A}$ is surmountable, which requires a high initial supersaturation since the supersaturation rapidly depletes as the nucleus grows.

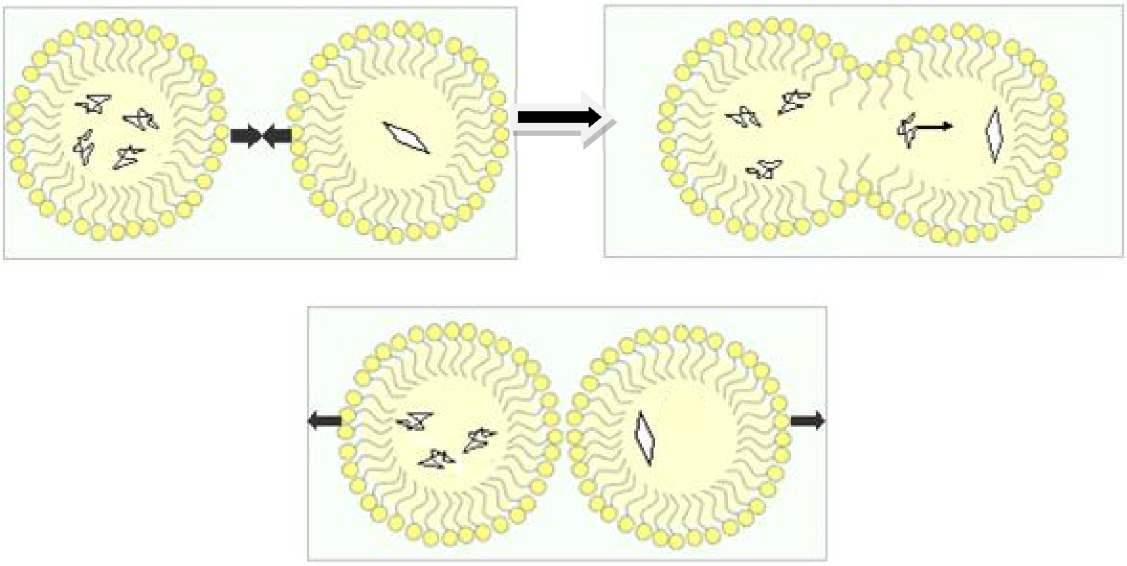

Figure 1.22: An illustration depicting the exchange of material upon the formation of transient dimers, when sufficiently energetic collisions occur. The squiggly line denotes a solute molecule that may crystallise.

For the near stable nuclei to grow to larger dimensions exchange of material between microemulsion droplets must take place. This occurs, via rare energetic collisions driven by Brownian motion, allowing the formation of transient droplet dimers and the exchange of crystallisable material from the interior of the droplets as illustrated above in Figure 1.22. By such a process, the nuclei are able to grow and fill out the encapsulating droplet, before expanding out of the droplet confinement. Subsequent growth proceeds via collisions between such crystals and surrounding droplets containing crystallisable material.

Ensuring that $\Delta F^*min,_A \leq kT$, whilst $\Delta F^*min,_B \geq kT$. may be achieved by finding the minimum initial supersaturation required in order to induce crystallisation in the microemulsion. Practically this is achieved by starting with a set of microemulsions with different initial supersaturations, such that the highest supersaturation systems crystallise whilst the lowest supersaturations do not crystallise in any reasonable timeframe because they are stabilised due to the nanoconfinement; although they have a relatively high supersaturation, this supersaturation is depleted before a near stable nucleus can be grown. The lowest supersaturation at which crystallisation proceeds in a reasonable timeframe corresponds to the case where the crystals will be of predominantly the stable form. At higher supersaturations, the crystals will contain a higher proportion of the metastable form, but the exact proportion will depend upon the difference between $\Delta F^*min,_A$ and $\Delta F^*min,_B$ and so will be highly system dependant.

Examples of microemulsions being used as a source of confinement were described previously. However, the potential for thermodynamic control under these specific conditions has only recently been realised, and so previously any particular polymorphic outcome was ascribed to the surfactant templating etc, rather than the 3D nano-confinement[20,21 ,62,47, 72-73,64] In particular, all previous attempts used specific additives or surfactants, rather than exploiting the inherent thermodynamic control of crystallisation that can arise in nanoconfinement.

References

1. C. E. Nicholson, C. Chen, B. Mendis and S.J. Cooper, 'Crystal Growth and Design', 2011, 11(2), 363-366.
2. J. Thun, L. Seyfarth, C. Butterhof, J. Senker, R. E. Dinnebier and J. Breu, *Cryst. Growth. Des,* 2009, **9(5)**, 2435-2441.
3. V. Bansal, A. Ahmad and M. Sastry, *'J. Am. Chem. Soc',* 2006, **128**, 14059-14066
4. Kwiecinska. B.; Petersen, H. I. *Int. J. Coal Geology* **2004**, *57*, 99-116.

5. Fitzer, E.; Köchling, K. H.; Boehm, H. P.; Marsh H. *Pure & Appl. Chem*. **1995**, *67*, 473-506
6. Takai, K.; Oga, M.; Sato, H.; Enoki, T.; Ohki, Y.; Taomoto, A.; Suenaga K.; Iijima, S. *Phys. Rev. B*: *Condens. Matter Mater. Phys*. **2003**, *67*, 21420
7. Peng, H.; Travas-Sejdic, J. *Chem. Mater*. **2009**, *21*, 5563–5565.
8. Li, X.-H.; Kurasch, S.; Kaiser, U.; Antonietti, M. *Angew. Chem. Int. Ed.* **2012**, *51*, 9689 –9692
9. J. C. Burley, M. J. Duer, R. S. Stein and R. M. Vrcelj, *'European Journal of Pharmaceutical Sciences',* 2007, **31**, 271-276.
10. A. Llinàs and J.M. Goodman, *Drug Discovery Today,* 2008, **13(5/6)**, 198-210.
11. A. Nangia, *'Accounts of Chemical Research'*, 2008, **41(5)**, 595-604
12. J. Bauer, S. Spanton, R. Henry, J. Quick, W. Dziki, W. Porter and J. Morris. '*Pharmaceutical research'* 2001, **18(6),** 859-866.
13. Patient advice leaflet, Ritonavir, Abbott laboratories, North Chicago, IL 60064, U.S.A. Ref: 03-A358-R28-Rev. April, 2010, 036-377646
14. H.A. Wriedt, *'Bulletin of Alloy Phase Diagrams',*1985, **6(6),** 548-553.
15. G. Behnke, H. Bilz and H. Büttner, *'Physical Review Letters'* 1986, **56**(12), 1276-1279.
16. A. A. Levchenko *et al, 'Chem. Mater,'* 2006, *18,* 6324-6332.
17. I. Levin, '*J. Am. Ceram. Soc',* 1998, **81(8)**, 1995-2012
18. S.J. Wilson, *' Proc. Br. Ceram. Soc*', 1979, **28**, 281–94.
19. J. Chandradass and D-S. Bae, *'Materials and Manufacturing Processes',* 2008, **23**, 494-498.
20. K. Chadwick, R. J. Davey and R. Mughal, *'Organic Process Research Development',* 2009, **13**, 1284-1290.
21. R. J. Davey, N. Blagden, G. D. Potts and R. Docherty, *'J. Am. Chem. Soc',* 1997, **119**, 1767-1772.
22. K. Holmberg, B. Jönsson, B. Kronberg and B. Lindman, *'Surfactants and Polymers in Aqueous Solution',* 2nd edition, John Wiley & Sons Ltd, 2003
23. J. Eastoe, *'Surfactant Chemistry',* Chapter 1: Surfactant chemistry and General Phase Behaviour. Unpublished work. (http://www.chm.bris.ac.uk/pt/eastoe/
24. J. Eastoe, '*Surfactant Chemistry',* Chapter 2: Aggregation and adsorption at interfaces. Unpublished work. http://www.chm.bris.ac.uk/pt/eastoe/Surf_Chem
25. T. Tadros. *'Applied Surfactants: Principles and Application',* 2005, Wilet-VCH Verlag GmbH & Co. KGaA, Weinheim
26. C. H. Rodriguez and J. F. Scamehorn, *'Journal of Surfactants and Detergents',* 1999, **2(1)**, 17-28.
27. P. Mukherjee *et al, 'Advances in Colloid and Interdace Science',* 2011, **162**, 59-79
28. C. Manohar, *'Bull. Matter. Sci',* 1994, **17(7)**, 1299-1306.
29. E. J. Staples and G. J. T. Tiddy, *'Journal of Chemical Society-Faraday Transactions 1',* 1978, **10**, 2530-2541

30. A. Bernheim-Groswasser, *'Langmuir',* 1999, **15**, 5448-5453
31. Shinoda, K.; Saito, H. J. Colloid Interface Sci. **1969**, 34, 238.
32. W. C. Griffin, '*Classification of surface-active agents by HLB'*, 1949, **1**, 311-326.
33. W. C. Griffin, *'J. Soc. Cosmet. Chem',* 1949, **1**, 311-326
34. R. G. Alany*,* T. Rades, S. Agatonivc-Kustrin, N.M. Davies and I.G. Tucker, '*International Journal of Pharmaceutics',* 2000, **196**, 141-145.
35. R. C. Pasquali, N. Sacco and C. Bregni, *'Lat. Am. J. Pharm',* 2009, **28(2)**, 313-317.
36. J. T. Davies, *'Perf. Essential Oil Record',* 1952, **43**, 338.
37. ICI Americas, *'The HLB system: A Time-Saving Guide to Emulsifier Selection',* 1992, Wilmington, DE.
38. J.Eastoe, '*Surfactant Chemistry',* Chapter 3: Microemulsions. Unpublished work. (http://www.chm.bris.ac.uk/pt/eastoe/Surf_Chem/3%20Microemulsions. pdf)
39. C. R. B. Mendonça, Y. P .Silva, W. J. Böckel, E. F. Simó-Alfonso, G. Ramis-Ramos, C. M. S. Piatnicki and C. I. D. Bica, '*Journal of Colloid and Interface Science'*, 2009, **337**, 579-585.
40. R. M. Pashley, '*J. Phys. Chem',* 1994, **98**, 11512-11518.
41. D. J. Mitchell and B. Ninham, *'J. Chem Soc. Faraday Trans 2'*, 1981, **77**, 601-629
42. R. Nagarajan and E. Ruckenstein, *'Langmuir'*, 1991, **7**, 2934-2969.
43. B. Duke and E. W. Plummer, *'Frontiers in surface and the interface science,'* North Holland, 2002
44. F. C. Meldrum and H. Cölfen, *'Chem. Rev',* 2008, **108**, 4332-4432.
45. L. D. Gelb, Research Group Washington University, St. Louis http://www.chemistry. wustl.edu/~gelb/cpg.html, accessed 11/04/2010.
46. Beiner *et al, 'Nano Lett',* 2007, **7(5)**
47. A. S. Myerson *et al*, *'J. Am. Chem. Soc',* 2005, **127**, 14982-14983
48. K. Shin, E. Woo, Y. G. Jeong, C. Kim, J. Huh, and K. W. Kim, '*Macromolecules',* 2007**, 40***,* 6617-6623.
49. D. K. Sarker, *'Current Drug Delivery',* 2005, **2(4),** 297-310.
50. M. Porras, C. Solans, C. González, A. Martínez, A. Guinart and J. M. Gutiérrez, *'Colloids and Surfaces A: Physicochem. Eng. Aspects',* 2004, **249**, 115-118
51. C. Chen, O. Cook, C. E. Nicholson and S. J. Cooper, *'Crystal Growth and Design',* 2011, **11(6)**, 2228-2237.
52. J-H. Ha, *'J. Am. Chem. Soc',* 2004, **126**, 3382-3383
53. E. Loste, R. J. Park, J. Warren and F. C. Meldrum, *'Advanced Functional Materials',* 2004, **14(12)**, 1211-1220
54. S.J. Cooper, *'Crystallisation Kinetics',* Lecture course notes, 2008
55. K. Allen, R. J. Davey, E. Ferrari, C. Towler and G. J. Tiddy, *'Cryst. Growth. Des',* 2002, **2(6)**, 523-527.
56. A. Amani, P. York, H. Chrystyn and B. J. Clark, *'Pharmaceutical Research',* 2009, **27(1)**, 37-45.
57. M. H. F. Sakeena, *'J. Oleo Soc',* 2011, **60(4),** 155-158
58. J. Sjöblom, R. Lindberg, S. E. Friberg, *'Adv. Colloid Interface Sci'*, 1996, **125**, 95.
59. D. O. Shah, *'Surface Phenomena in Enhanced Recovery',* Plenum Press, 1981.
60. E. W. Kaler, K. E. Bennett, H. T. Davis and L. E. Scriven, *'J. Chem. Phys',* 1983, **79(11)**, 5673-5684.
61. E. W. Kaler, H. T. Davis and L. E. Scriven, *'J. Chem. Phys',* 1983, **79(11)**, 5685-5692.

62. R.J. Davey and J. Garside, *'From molecules to crystallizers: An Introduction to Crystallisation',* Oxford University Press, 2001.
63. P. A. Winsor, '*Transactions of the Faraday Society'*,1948, **44(6)**, 376-398
64. Y. Wang and N. Herron, *'Research of Chemical Intermediates',* 1991, **15**, 17-29
65. E. Hao, H. Sun and Z. Zhou, *'Chem Mater',* **11(11),** 1999, 825
66. H. J. Watzke, and J. H. Fendler, *'J. Phys. Chem,'* 1987, **91**, 854-861.
67. L. Jacak, P. Hawrylak and A. Wojs, *'Quantum Dots',* 1998, Springer Verlag.
68. N. Ghows and M.H. Entezari, '*Ultrasonics Sonochemistry'* 2011, **18**, 269-275
69. R. Khurana, S. Vaidya, M. Manolata Devi and A.K. Ganguli, *'Journal of Colloid and Interface Science',* 2010, **352**, 470-475
70. A. Agostiano, M. Catalano, M.L. Curri, M. Della Monica, L. Manna and L. Vasanelli, *'Micron',* 2000, **31**, 253-258.
71. S-Y. Chang, Liu. L and Asher. S, '*J. Am. Chem. Soc',* 1994, **116,** 6739-6744
72. A. S. Myerson, *'Handbook on industrial crystallisation',* Second edition, 2002, Elsevier Inc
73. K. Margulis-Goshen and S. Magdassi, '*Nanomedicine',* 2009, **5**, 274-281.
74. W. E. Garner, *'Discuss. Faraday Soc',* 1949, **5**, 7-10
75. H. M. Schoen, *'Crystallisation Equipment',* 1961, **53(8)**, 607-611
76. L. Yu, G. A. Stephenson, C. A. Mitchell, C. A. Bunnell, S. V. Snorek, J. J .Bowyer, T. B. Borchardt, J. G. Stowell and S. R. Byrn, *'J. Am. Chem. Soc',* 2000, **122**, 585-591.
77. S. Teychené and B. Biscans, '*Cryst. Growth. Des',* 2008, **8(4),** 1133-1139
78. I. V. Markov, '*Crystal Growth for Beginners: Fundamentals of Nucleation, Crystal Growth and Epitaxy'*, Edition 2, World Scientific Publishing Co. Ptc. Ltd, 2003.
79. D. M. Blow, N. E. Chayen, L. F. Lloyd and E.Saridakis, *'Protein* Science', 1994, **3**, 1638-1643.
80. N. F. Mott, *'Nature'*, 1950, **165**, 295-297
81. W. K. Burton and N. Cabrera, *'Discuss. Faraday Soc',* 1949, **5**, 33-39
82. F. C. Frank, *'Discuss. Faraday Soc',* 1949, **5**, 48-54
83. P. H. Egli and S. Zerfoss, '*Discuss. Faraday Soc'*, 1949, **5**, 61-66
84. A. Kogan, I. Popov, V. Uvarov, S. Cohen, A. Aserin and N. Garti, *'Langmuir',* 2008, **24**, 722-733
85. W. K. Burton, N. Cabrera, F. C. Frank, *'Philosophical Transactions of the Royal Society of London. Series A, Mathematical and Physical Sciences',* 1951, **243(866)**, 299-358
86. Schramm. L.L, Stasiuk. E.N and Gerrard Marangoni. D, '*Annu. Rep. Prog. Chem., Sect. C: Phys. Chem.*'**,** 2003, **99**, 3-48
87. Salim. M, Minamaikawa. H, Sugimura. A and Hashim. R, *'Med. Chem. Commun.***'**, 2014, **5**, 1602-1618.

88. Brown. C. J and Ni. X-W, *'Cryst Eng Comm',* 2012, **14,** 2944-2949
89. Polte. J, *'Cryst Eng Comm',* 2015, **17,** 6809-6830
90. Bahrig. L, Hickey. S.G and Eychmuller. A, *'Cryst Eng Comm',* 2014, **16,** 9408-9424
91. Nguyen. T.T.H, Hammond. R.B, Roberts. K.J, Marziano. I and Nichols. G, '*Cryst Eng Comm',* 2014, **16,** 4568-4568

Chapter 2 – Experimental methods and techniques

2.1 Materials

The materials used were as follows: Sodium metasilicate nonahydrate (≥98%, Aldrich), UHQ water (Purelab UHQ water filtration unit), heptane (≥99%, Aldrich), Span®80 (Aldrich), Brij® 30 (Acros Organics), AOT (98%, Aldrich), Hydrochloric acid (HCl) (5M, Fisher Scientific), Silver Spoon® granulated sugar, pentan-1-ol (ACS reagent ≥99%, Aldrich), hexadecyltrimethylammonium chloride (CTAC) (99%, Acros Organics), cyclohexane (99% GLC Specified, Fisher Scientific) and sulphuric acid (>95%, Fisher Scientific).

2.2 Experimental methods

2.2.1 Microemulsion preparation

Upon establishing the solubility of the precursor material in various solvents, the type of micelles required is apparent, thus a suitable combination of surfactants, continuous and dispersed phases can be selected.

Microemulsions were prepared for all of the subsequent experiments via the method described below.

The surfactant blend is dissolved in the continuous phase, before being divided into smaller aliquots. The dispersed phase, containing the precursor material, is added to the surfactant solution, using a Gilson-type pipette in the required quantities. Thorough mixing of the phases follows, either by vigorous hand-shaking, ultrasound sonication or vortexing to achieve a single transparent, homogeneous phase. For mixed microemulsions, two corresponding microemulsions are prepared, before being combined. The preparation methods are illustrated in Figure 2.1.

The characterisation of the microemulsions is achieved using a Small-Angle X-Ray Scattering technique. This is detailed in Section 2.3.3.1.

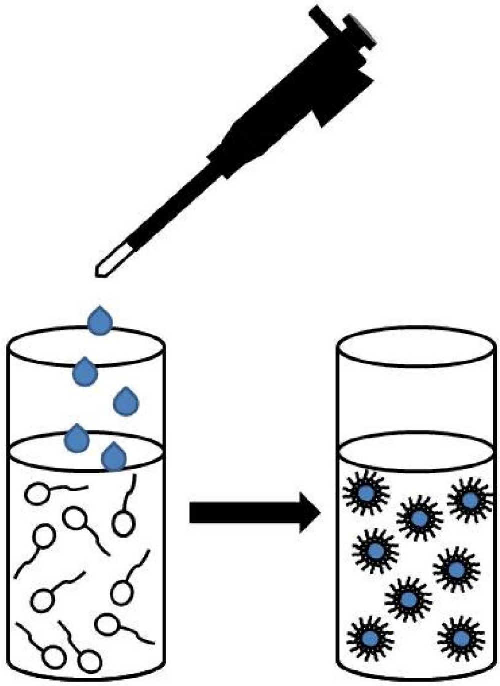

Figure 2.1 – Schematic diagram illustrating the formation of a micellar solution upon addition of a dispersed phase.

2.2.1.1 Acid addition

Acid was added to both catalyse the synthesis and alter the pH of the emulsion media. There are three methods by which this was achieved.

2.2.1.1.1 Direct addition

For direct addition, acid is pipetted in to the pre-prepared aqueous microemulsion. (Figure 2.2)

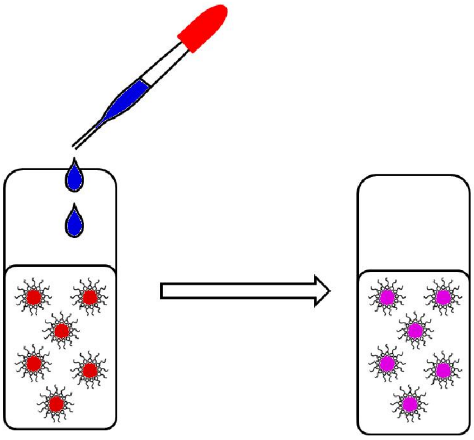

Figure 2.2: Direct addition schematic (Reproduced with permission from reference 1)

2.2.1.1.2 Mixed microemulsion addition

For mixed microemulsion addition, the acid is encapsulated in a microemulsion prior to being added to the aqueous microemulsion to form a single phase microemulsion. (Figure 2.3)

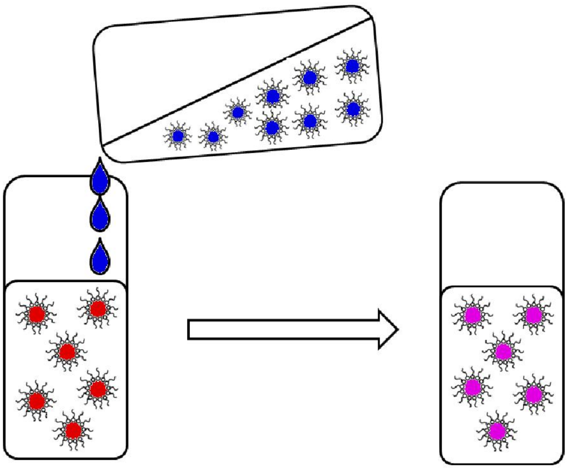

Figure 2.3: Mixed microemulsion addition schematic (Reproduced with permission from reference 1)

2.2.1.1.3 Crystal dissolution method

For crystal dissolution method, the acid is encapsulated in a microemulsion prior to being added to crystals of precursor. The precursor was able to dissolve in to the microemulsion droplets through the continuous phase. (Figure 2.4)

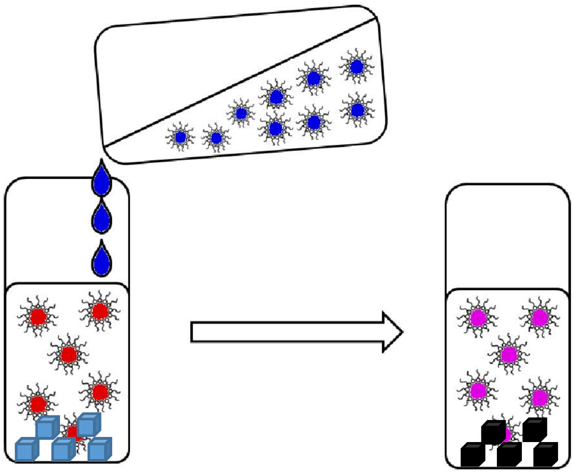

Figure 2.4: Crystal dissolution method schematic. (Adapted with permission from reference 1)

2.3 Experimental techniques

The following analytic techniques were utilised as appropriate; Attenuated Total Reflectance Fourier Transform Infrared Spectroscopy (ATR-FTIR spectroscopy), Raman spectroscopy, Small-Angle X-Ray scattering (SAXS), Wide-Angle X-Ray scattering (WAXS), Transmission electron microscopy (TEM), Environmental scanning electron microscopy (ESEM), Atomic force microscopy (AFM), and centrifugation.

2.3.1 Attenuated Total Reflectance Fourier Transform Infrared Spectroscopy (ATR-FTIR/FTIR)

On a basic level, a FT-IR spectrometer, passes an infrared beam through a sample, measures the transmitted light and interprets the results as an absorbance or transmission spectra as illustrated by the schematic layout in Figure 2.5b.

Further simplification of most interferometers and consequently spectrometers begins with a Michelson interferometer, as seen in Figure 2.5a.

From Figure 2.5a and b, it is can be followed that the beam is split upon entering the interferometer, with one beam reflected from a fixed mirror and the other from a 'moveable' mirror. The adjustment of the latter leads to different wavelength configurations passing, whilst others remain blocked; hence the resultant wave form is no longer in phase due to both constructive and destructive interference. This forwarded interferogram signal interacts with the energy levels of the material where matching frequencies of the stretching and bending vibrations of bonds are absorbed, causing a quantised increase in the vibrational energy level of specific bonds. Hence the conjugation of different functional groups present characteristic absorption peaks, enabling trivial identification. A Fourier transform is performed on the resultant interferogram to provide a legible spectrum. Providing the Selection Rules are observed and the material is deemed IR active, one can identify unknown compounds, determine the quality of a sample or determine the individual components of a material. Simply, the selection rules indicate that the dipole moment of the molecule must change during the vibration, hence homonuclear diatomics are considered infrared inactive as the dipole moment of the molecule remains negligibly close to zero, however a heteronuclear diatomic may be infrared active as the distance between the positive and negative regions may change, dependent on the stretch or bend, thus changing the dipole moment. The intensity of the observed absorption band thus depends on the degree to which the dipole moment changes during the vibration.

FTIR analysis was carried out using a Nicolet Nexus Spectrometer complete with a $N_2(l)$ cooled HgCdTe crystal detector and germanium or diamond crystal platform. Experiments were carried out to confirm product identity. Samples were prepared by filtration from the microemulsion, dried, placed on the stage and clamped under the detector. 128 scans at 4 cm^{-1} were collected for each of the spectra from 500 to 4000 cm^{-1}. A background spectrum, taken immediately prior to the sample spectra were collected and ratioed against the sample spectra.

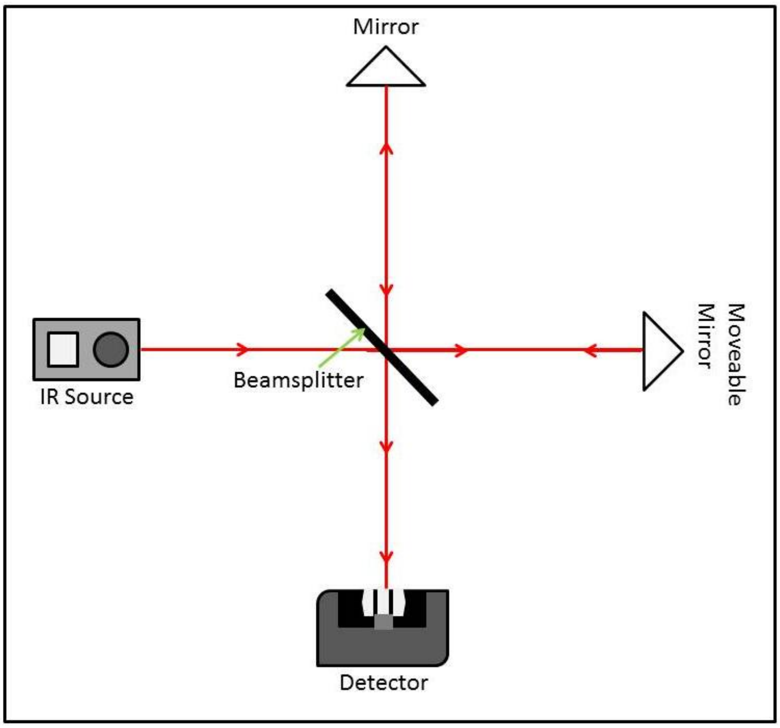

Figure 2.5 a: Schematic of a simplified Michelson interferometer.

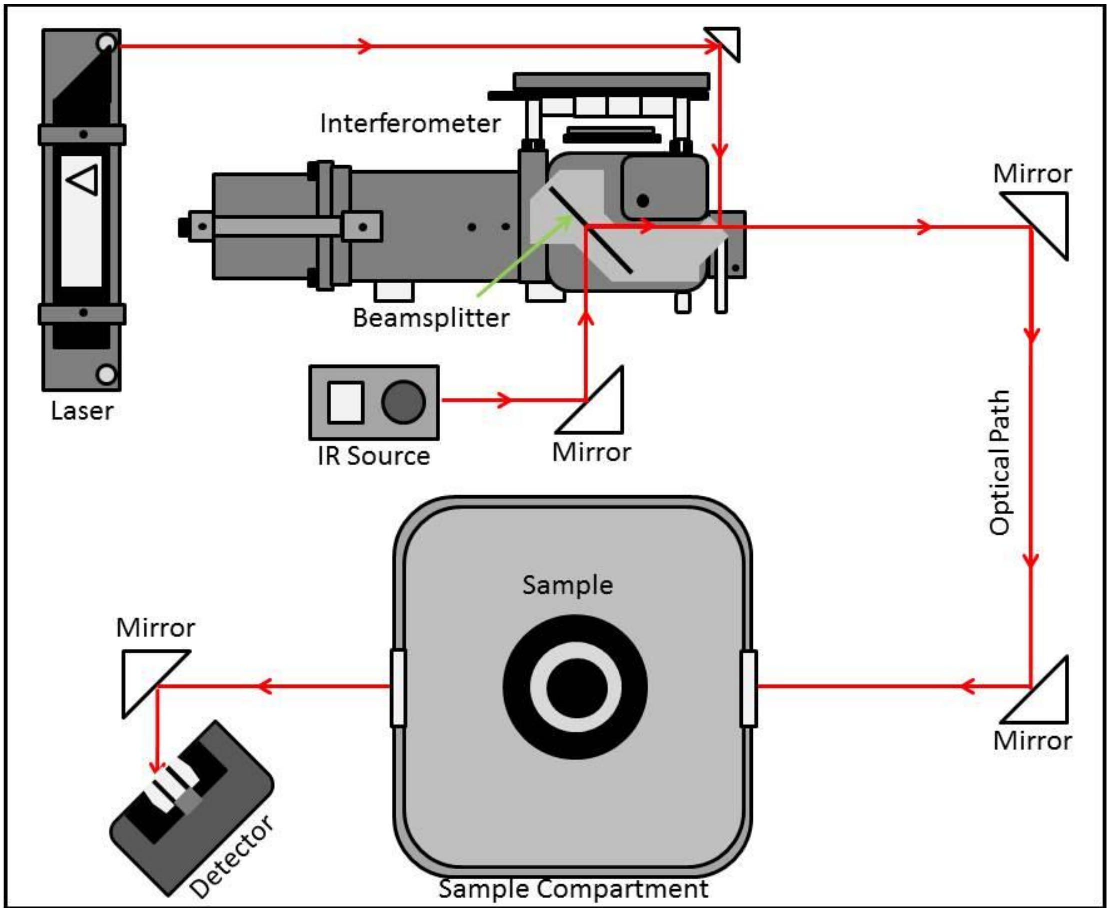

Figure 2.5b: Schematic of an FT-IR spectrometer.

2.3.2 Raman spectroscopy

A complementary technique to infrared spectroscopy is Raman spectroscopy, as some allowed transitions in Raman may be forbidden in IR or vice-versa. For a material to be deemed Raman active, the Selection Rules insist that the polarizability of the molecule changes during the vibration, i.e. the ease with which the electron cloud of the molecule can become distorted. Analogous to infrared spectroscopy, the intensity of the observed absorption band thus depends on the degree to which the polarizability changes during the vibration.

Upon irradiating a sample with a monochromatic light, the photons can typically be reflected, absorbed or scattered by the molecules. Conversely to IR spectroscopy, Raman spectroscopy relies on the scattering of light from a sample, rather than the transmission. Upon interaction with light, the photons produce an oscillating polarisation within the molecule, exciting them to a virtual state. The emission of light occurs by the following three frequencies, as depicted in Figure 2.6. The major component of incident photons will be elastically Rayleigh scattered. This occurs when the polarisation of the molecule does not couple to a Raman active vibrational or electronic mode; hence the emitted light is of the same frequency as the incident light. i.e. $v_0 = v_0$. However, this signal is not useful for molecular characterisation. A minute proportion of the photons undergo one of two inelastic scattering processes, where the emitted photons have a range of frequencies determined by the energies of light absorbed by the sample: $\Delta E = h| v_0 - v_i|$. The process which produces light of v_i, is known as Raman Scattering. For a Raman-active molecule in its ground vibrational state; upon adsorbing a photon of frequency v_0, a fraction of the photons energy is transferred to the molecule; reducing the emitted frequency to $v_0 - v_i$. This is known as Stokes radiation. For a small number of pre-excited Raman-active molecules, upon adsorbing a photon of frequency v_0, the molecule returns to the ground state by the emission of a higher energy photon with frequency, $v_0 + v_i$. This process is the much weaker anti-Stokes radiation.[2] Raman scattering is a relatively weak process in comparison to Rayleigh scattering, thus corrections, such as: interference filters and apertures must be factored into the instrument setup. [3] The change in the frequency between the incident and emitted photons is characteristic of a molecular vibration. By drawing on data tables of Raman band positions, an accurate chemical identification can be deduced.

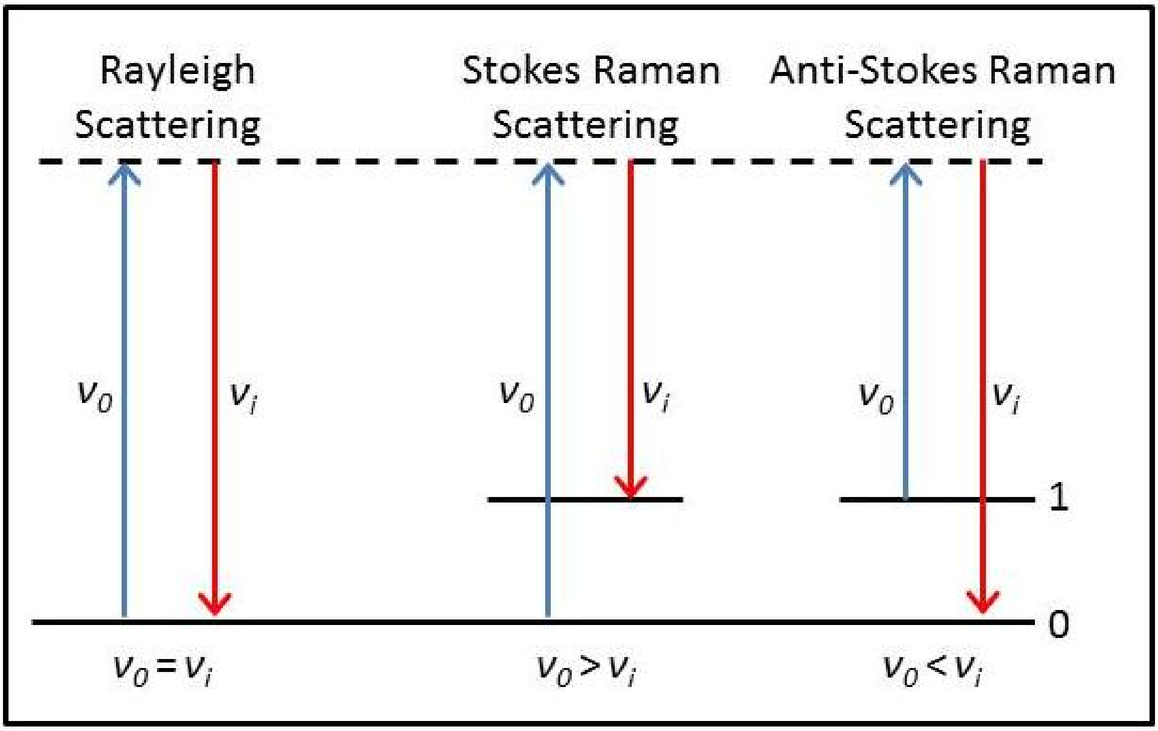

Figure 2.6 Resultant scattering based on the frequency of light

Raman analysis was carried out using a Jobin Yvon LabRAM (Horiba Scientific) spectrometer in a back-scattered confocal configuration, complete with a frequency doubled Nd:YAG (532nm, 2.33 eV) and a HeNe laser (633nm, 1.96eV). The unit consists of an Olympus optical light microscope, motorised translational stage and a Peltier-cooled silicon CCD camera. The samples were deposited on Boron-doped P-type silicon wafer, with a 285 nm oxide layer to provide optimal visibility of carbonaceous material. (Graphene Supermarket) For each sample the spectra was collected over a range of 500 to 3500 cm^{-1}. Data was processed and analysed using LabSpec V5.63. A simplified layout is depicted in Figure 2.7.

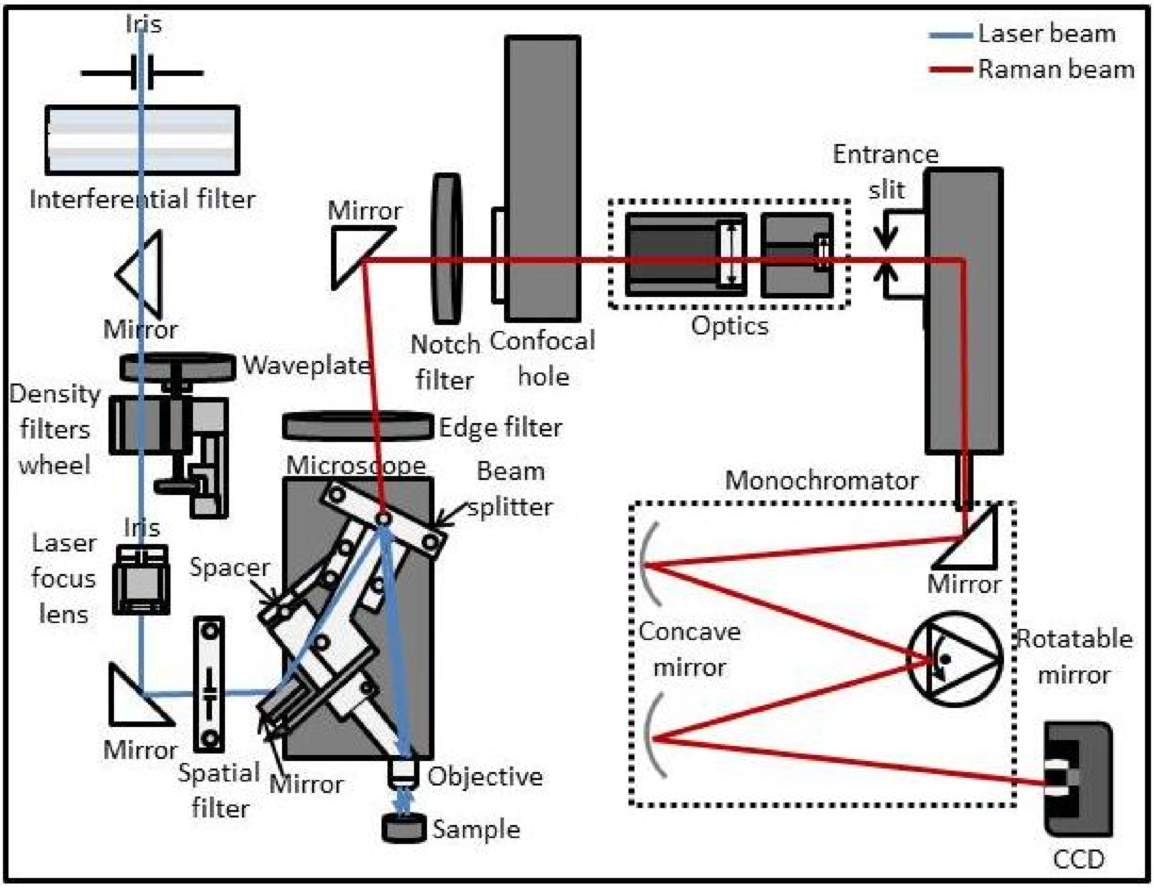

Figure 2.7: Schematic of a simplified Raman spectrometer.

2.3.3 Diffraction Theory

Diffraction techniques are used to determine structural information of crystalline materials. When X-rays are scattered from a crystalline material, for Bragg peaks to be observed Bragg's condition must be satisfied; the reflections from the various planes of atoms, separated by the interplanar distance, d_{hkl}, must constructively interfere, remaining in phase as a consequence of the wave path length being equal to an integer multiple, n of the wavelength, λ. This leads to Bragg's law where the path difference between two waves is $2d_{hkl}sin\theta$.

$$n\lambda = 2d_{hkl}sin\theta$$

where; n is an integer value, λ is the wavelength of the X-rays, d_{hkl} is the interplanar spacing and θ is the angle between the crystal planes and incident X-rays, see Figure 2.8.

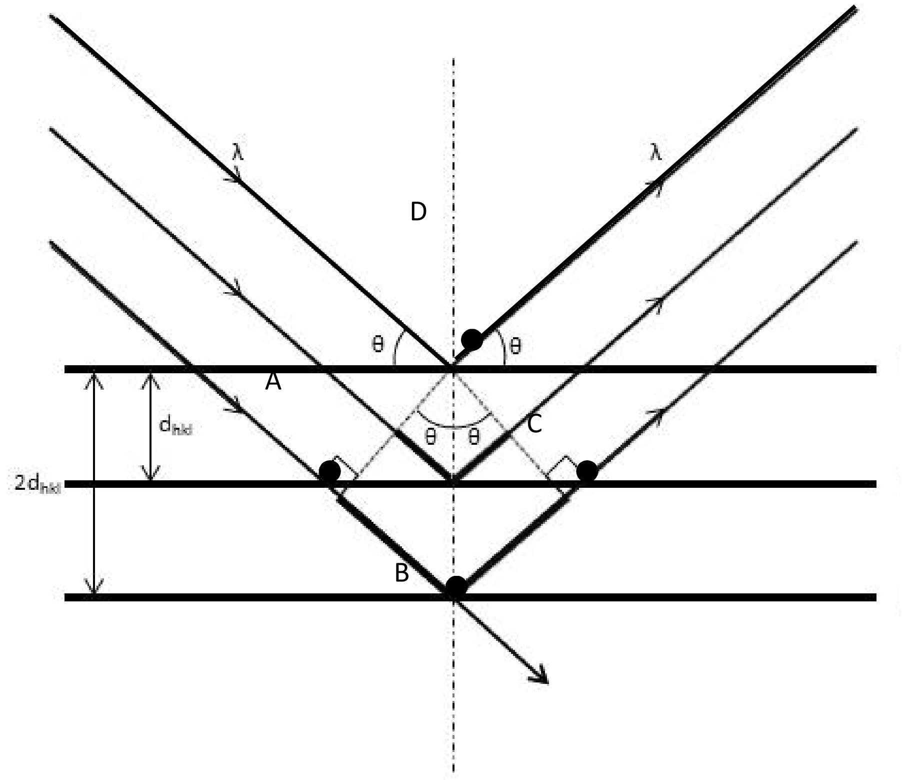

Figure 2.8 Depiction of determination of Braggs' law

One must note the oversight of the simplified derivation of Braggs' law presented above, where it is assumed that the X-rays are scattered by planes, when it is the electrons bound to the atoms that cause the scattering. From this it will be apparent that the scattering will be stronger when there are large electron density differences in the crystal structure.

By deriving the Bragg equation in reciprocal space, it can be simply demonstrated that Bragg diffraction occurs when a reciprocal lattice vector, $d^*{}_{hkl}$ intersects the Ewald sphere of radius 1/λ, as seen in Figure 2.9. By changing the orientation of the crystal, and thus the reciprocal lattice orientation, different lattice points may intersect the Ewald sphere and hence Bragg diffraction is observed.

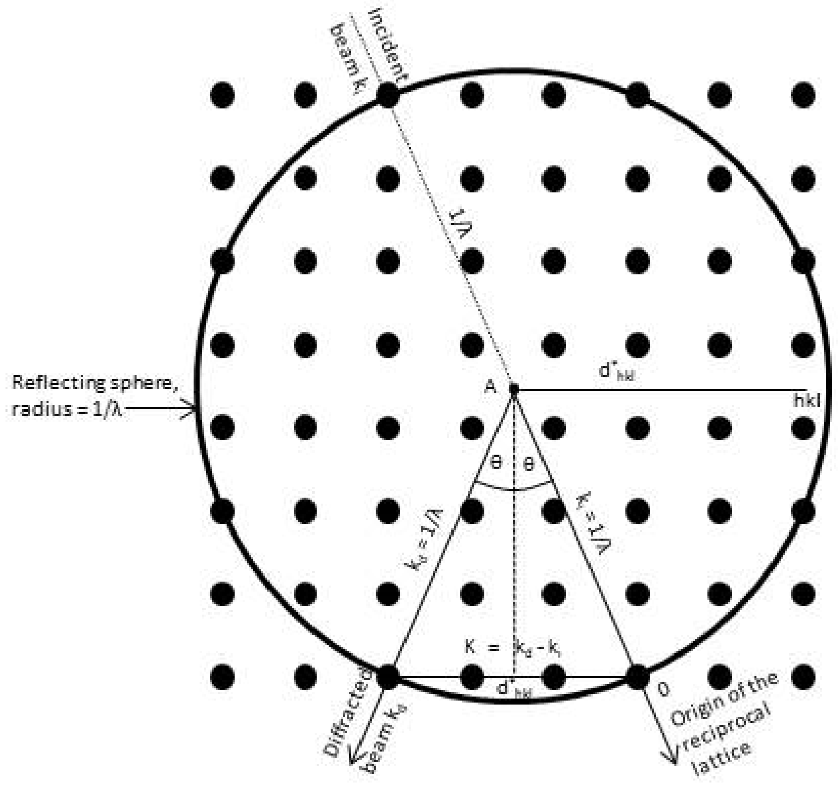

Figure 2.9: Ewald sphere construction.

One can determine which reflections are experimentally accessible and hence situate the sample and/or the detector to the required position. However, for an ideal powder sample, the individual crystallites are deemed to present each possible orientation with equal probability, thus Bragg reflections are observed in all directions, generating a two-dimensional smeared 'ring-shaped' diffraction projection.[4] Further, the above description assumes that the lattice points are geometrical points, when indeed they do have finite size and shape, which are inversely related to the dimensions of the crystal. This effect is exaggerated in the case of thin-films or thin plate-like crystals. The following principle applies to both the X-ray and electron diffraction case, for a crystal of finite size and hence a limited number of reflection planes. This finite nodal size, or broadening of the reflected beams can be simply mathematically derived and summarised by the Scherrer equation: $\beta = \frac{\lambda}{t\cos\theta} = \frac{2\tan\theta}{m}$, where β is effectively the broadening of a beam or the FWHM of the beam, λ is the wavelength, t is the thickness of the finite crystal in the direction perpendicular to the planes, θ is the Bragg angle and m is the number of reflecting planes within the crystal. This broadening can be illustrated, see Figure 2.10 by the lengthening of the reciprocal lattice nodes intersecting the Ewald sphere, replacing them with reciprocal lattice rods, commonly named rel-rods.[5]

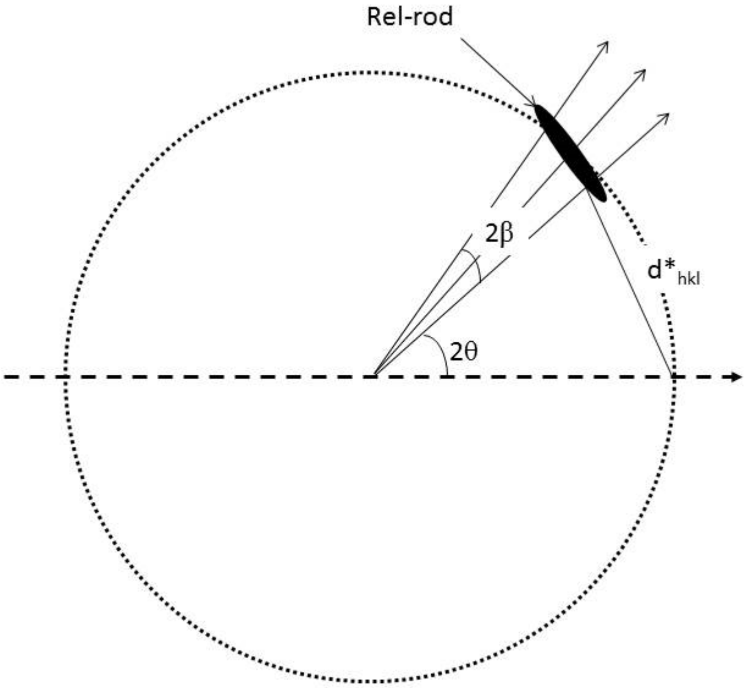

Figure 2.10: Illustration to show the occurrence of rel-rods.

It must be noted that this is a simplified use of the Scherrer equation. The complete Scherrer equation is typically applied to the broadening observed when analysing polycrystalline powder samples, incorporating a correction factor to allow for particle shape.[5]

Furthermore, the analytical wavelength used strongly affects the effective curvature of the Ewald sphere and thus the ability to intersect the reciprocal lattice nodes. This can be illustrated by making a comparison of a typical X-ray source with an electron source. Taking a 1.54 Å, Cu Kα x-ray source, the Ewald sphere has a diameter of ~1.3x10^{10} m, whilst the electrons from an electron source operating at accelerating voltages of 80 and 200 kV, will have wavelengths of 4.0 pm ($1/\lambda = 250$ nm^{-1}) and 2.5 pm ($1/\lambda = 400$ nm^{-1}), respectively and corresponding sphere diameters of 5x10^{11} m and 800x10^{11} m, respectively. The Ewald sphere for the two sources are overlaid in Figure 2.11 [6]

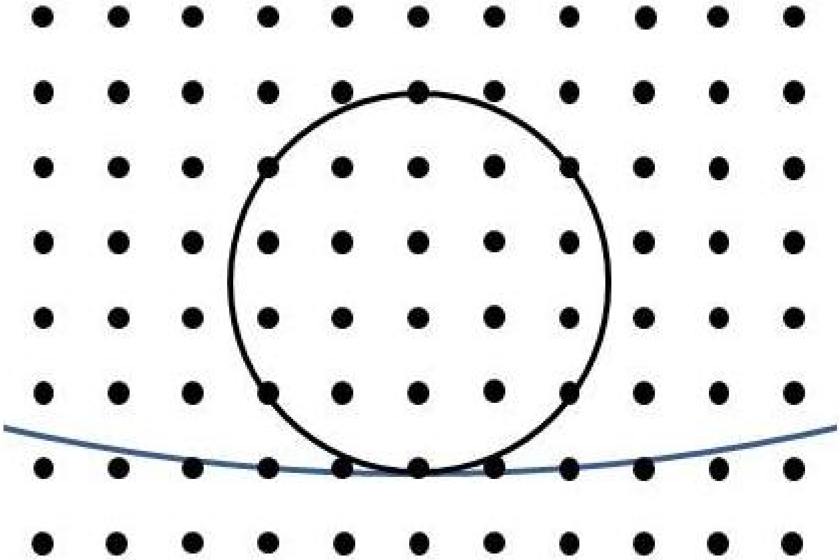

Figure 2.11: Overlay of Ewald sphere for both an X-ray and electron source.

It is clear that the reflecting sphere for the electron source appears much flatter, and thus the sphere intersects a greater number of reciprocal lattice points and 'Bragg' peaks are observed. This is further unravelled if we assume that a typical crystal lattice parameter, d_{hkl}, is ~ 0.3 nm, then $1/d_{hkl}$ = K is ~ 3 nm^{-1}, whilst that for an x-ray source is ~6.5 nm^{-1}, compared to 250-400 nm^{-1} for an electron source.[6]

2.3.3.1 Small-Angle X-Ray Scattering (SAXS)

Small-angle X-Ray scattering measurements, to determine the droplet size of the microemulsion, were carried out using a Bruker Nanostar SAXS machine with cross-coupled Gδbel mirrors and pin-hole collimation for point focus geometry, see Figure 2.12 for a schematic of the set-up. A sealed tube X-ray source operated at 40 kV and 35 mA to produce Cu Kα radiation of wavelength 1.54 Å is used in combination with a SAXS camera fitted with a Hi-star 2D detector, with an effective pixel size of 100 µm. Samples were contained in a 2 mm glass capillary. To minimise air scatter, the optics and sample chamber are kept under vacuum. Analysis of the droplet size was determined from use of the

GIFT package with comparisons drawn to the geometric predictions. Background scattering files were subtracted using a solvent-filled capillary. The scattering pattern of the sample is then integrated to give the one-dimensional scattering function I(q), where q is the length of the scattering vector, defined by $q = \left({}^{4\pi}/_{\lambda}\right) \sin {}^{\theta}/_{2}$. λ is the wavelength and 2θ is the scattering angle. The sample-to-detector distance was 650 mm, providing a q range of 0.2 to 3.2 nm^{-1}. The collection time was consistently 8 hours due to poor electron density contrast of the microemulsion components.

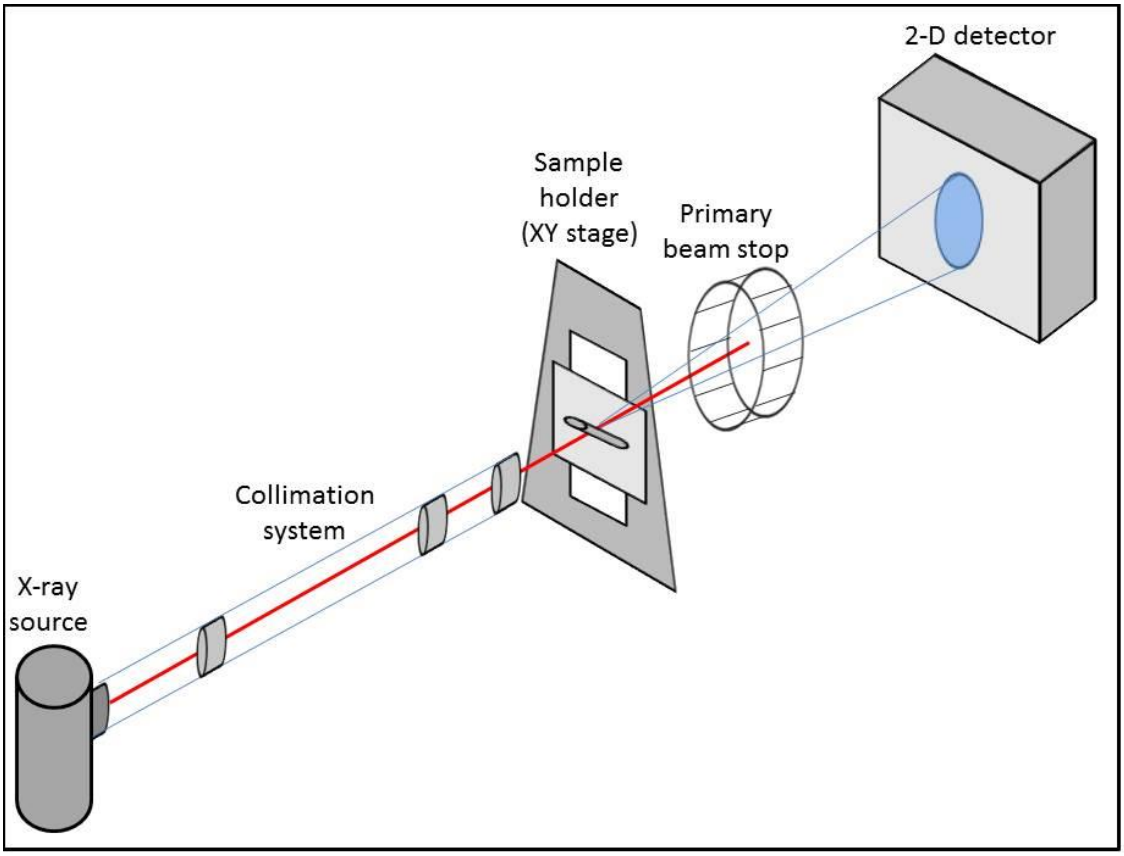

Figure 2.12: Schematic of beam path within the SAXS setup.

2.3.3.1.1 Generalised Indirect Fourier Transformation (GIFT) Analysis

The GIFT analysis package was used to manipulate the scattering data to generate a pair distance distribution function, p(r), from which the average droplet size can be determined. To remove the background , a Porod extrapolation is applied to the scattering function I(q). The subtraction ensures that the resultant p(r) function has a value ≈ 0, at r = 0, but this has little effect on the determined droplet sizes. I(q) is comprised of two components; a form factor: P(q) and a structure factor: S(q).

P(q) represents the intraparticle scattering. I(q) is dominated by the intraparticle scattering for dilute solutions where the dimensions of the droplet are much smaller than distance between neighbouring particles. However as the particle concentration is increased, both intramolecular and intermolecular scattering from neighbouring particles are observed requiring the introduction of a structure factor, S(q) to account for the interparticle scattering effects. I(q) α P(q).S(q), whilst p(r) is determined from the intensity by applying a Fourier transform. $p(r) = (\frac{1}{2\pi^2}) \int I(q).qr.sin(qr).dq$, which gives the frequency of occurrence of vectors of length r, weighted by the electron density at either end of the vector. The function contains essential information about both the size and the shape of the scattering particles.[7] The p(r) function was determined from I(q) using a structure factor representing the hard sphere interactions. The resultant curves for user inputted maximum particle sizes and software generated Lagrange multipliers are analysed until the most suitable fit is determined. The average size of the aqueous core of the w/o microemulsion droplets is determined from the point of inflexion separating the minimum and last maximum of the p(r) function, see Figure 2.13. This value is then compared to the geometric predictions. To calculate the geometric prediction, the assumption is made that the droplets are spherical and the small concentration of surfactant monomers is neglected. This allows the aqueous core size for a given composition to be determined by the basic relationship: $R_{core} = \frac{3\theta}{A_o N_s}$, where θ is the volume fraction of the confined phase, comprised of both the volume fraction of the immiscible aqueous phase and the volume fraction of the surfactant hydrophilic portion in contact with the immiscible phase. N_s is the number of surfactant molecules per unit volume and A_o is the surface area of the surfactant molecules taken from the literature.

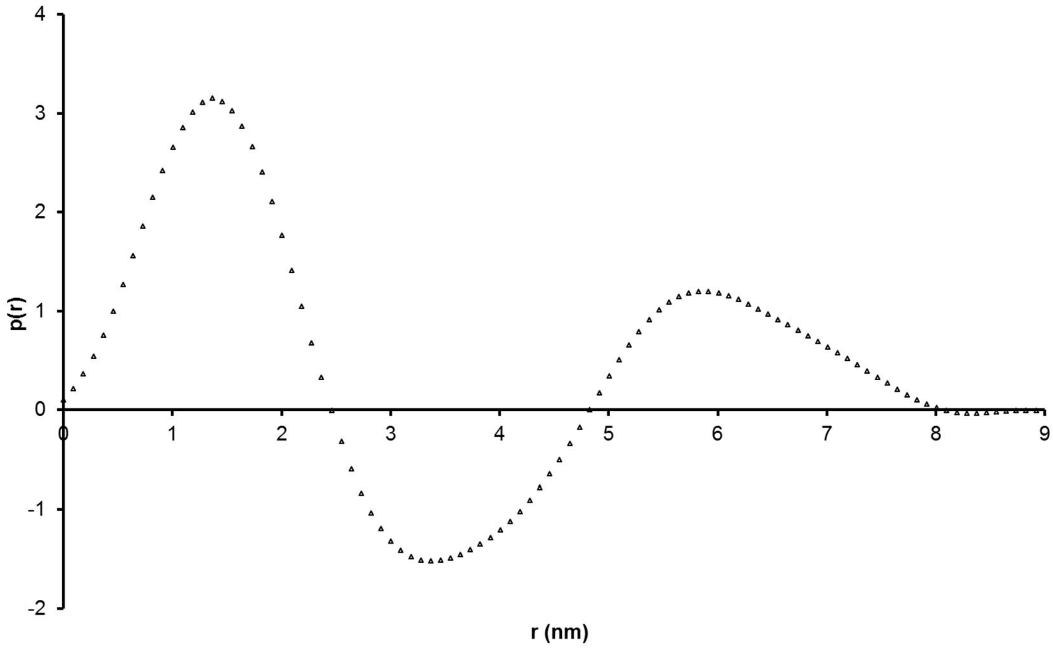

Figure 2.13: Typically p(r) for a core-shell model.

2.3.3.2 Wide-Angle X-Ray Scattering (WAXS)

Wide-angle X-Ray scattering (WAXS) measurements were carried out using a Bruker D8 diffractometer system (see Figure 2.14 for a schematic of the set up) with a sealed tube X-ray source operated at 30 kV and 10 mA to produce Cu Kα radiation of wavelength 1.54 Å. This is used in combination with a horizontal sample stage and a 2D multi-wire detector. Samples were ground to a fine powder and placed on a silicon wafer (100 face) to minimise background scattering. Analysis of the diffraction pattern was performed using GADDS and EVA software. By varying the angles of incidence and the angle of reflection, 2θ values in the range of 5-50° were covered. The collection time was varied between 1 hour and 18 hours.

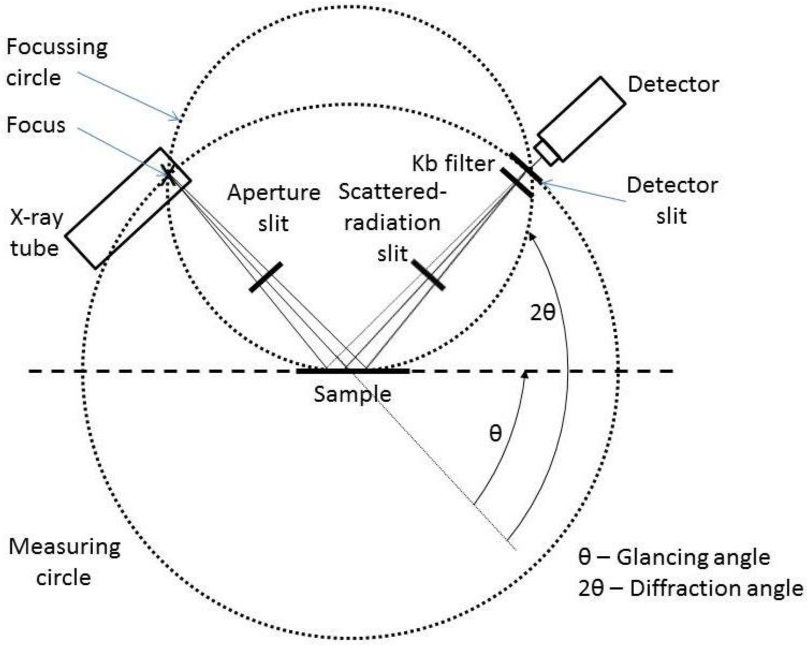

Figure 2.14: Schematic of the WAXS setup.

2.3.4 Transmission Electron Microscopy (TEM)

TEM is employed to allow both the structural and chemical analysis of nano-sized material. Samples were prepared by directly pipetting onto a holey carbon film on 200 mesh copper grid, before washing with a compatible solvent to remove excess surfactant. Examination of the sample was performed in a JEOL 2100F field emission gun TEM (FEG TEM) operating at 80/200 kV ZrO/W (100) Schottky Field Emission analytical emission microscope, in combination with an Oxford INCAx-Sight Si(Li) detector for Energy-dispersive X-ray spectroscopy and a Gatan Orius CCD camera to image the nanometre sized crystals, see Figure 2.15 for a schematic of the setup. A magnification range of x50- 1.5M was possible.

Phase contrast high resolution electron microscopy (HREM) was used to image nano-sized crystals. The structure of an individual nanocrystal was determined by indexing the fast Fourier transform and selected area diffraction patterns.[8] Digital Micrograph ® software was employed to capture the images and perform all further analysis.

The high resolution is achieved from the small de Broglie wavelength of the electrons defined by:

$$\lambda = \frac{h}{m_e v}$$

Where λ is the wavelength, h is Planck's constant, m_e is the mass of an electron and v is the velocity of the beam.

The wavelength typically used for TEM is ~ 0.02 Å. The resolution limit can be theoretically determined from the above equation, whereby the net resolution is affected by the diffraction limit and spherical aberration. Thus the resolution limit is ~ 0.1-0.2 Å. Thus assuming a wavelength of 0.02 Å and a semi-convergence angle of ~ 0.1 radians, the resolution limit can be determined to be:

$$\delta = \frac{0.61\lambda}{\varepsilon sin\varphi}$$

based on the diffraction spot size where ε is the refractive index between object and lens = 1 for air, and φ is the semi- convergence angle, with sinφ ~ φ for small angles.

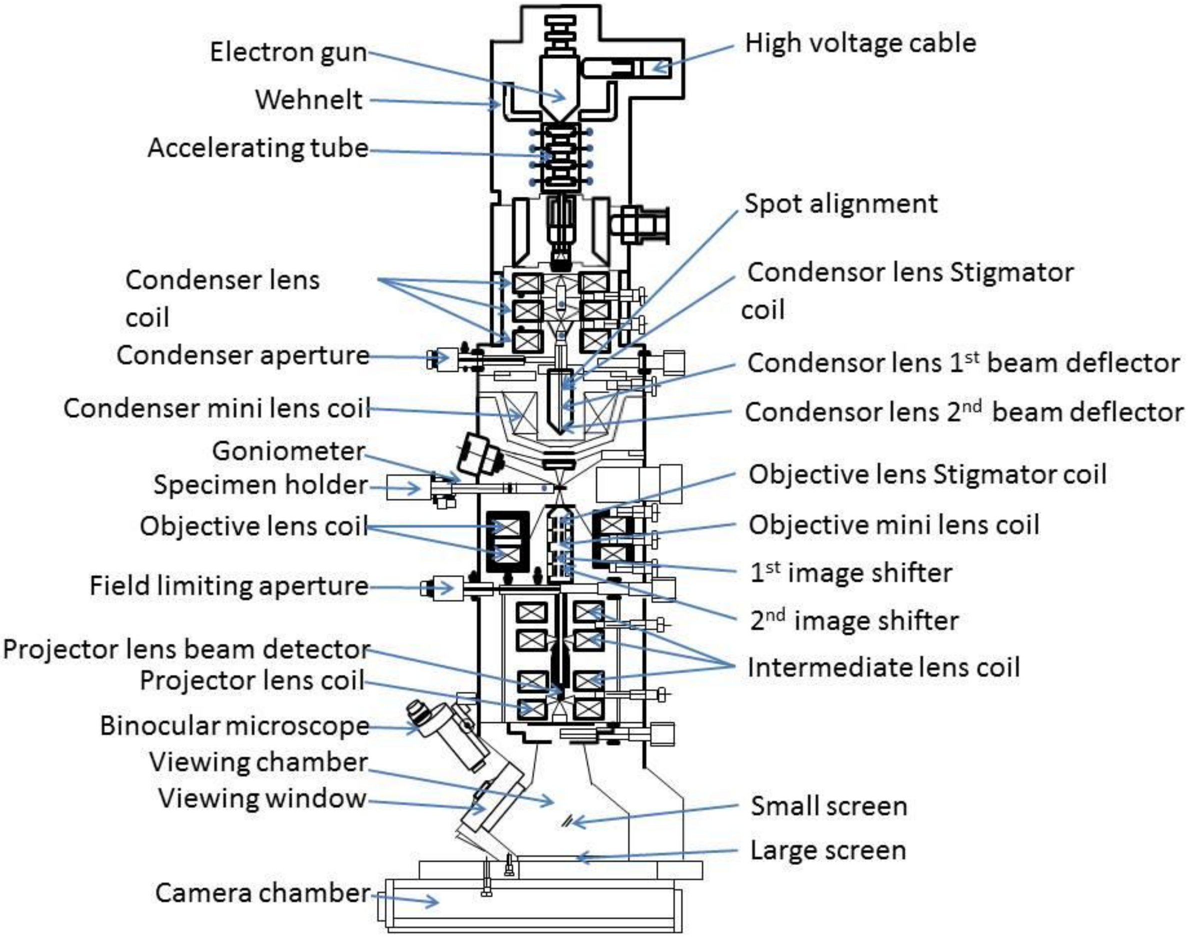

Figure 2.15 Schematic of the JEOL 2100 F Schottky field emission gun TEM setup [9]

2.3.4.1 Energy-Dispersive X-Ray Spectroscopy (EDX)

The high-energy incident electron beam may interact with the sample in a number of ways. However these can all be categorised as elastic or inelastic.[10] Elastic scattering, as described in Section 2.3.2 may result in a change in direction of the incident radiation, but there is no associated energy change. In the case of electron microscopy, elastic scattering occurs as a result of coulombic interactions with the nucleus of an atom and associated electrons. The elastically scattered electrons play an important contribution to the deflection of electrons and building of diffraction patterns. [11]

Conversely, inelastic scattering refers to any interaction where the incident electron loses a detectable proportion of energy. There are four major inelastic mechanisms: phonon scattering, plasmon scattering, single valence electron excitation and inner shell excitation. Phonon scattering typically results in heating of the sample due to atomic vibrations. Plasmon scattering is initiated by incident electrons instigating resonant oscillations of the bonding/valence electrons of a solid. Alternatively, single-electron excitations are a minor feature where incident electrons excite a single valence electron. Comparatively, inner shell excitations result from an energy transfer to a tightly bound atomic electron, causing ionisation of the atom. A significant proportion of energy is required, thus this characteristic energy loss can be utilised in electron energy-loss spectroscopy. Further, secondary emissions of X-ray photons or Auger electrons can be used for analytical techniques such as energy dispersive x-ray spectroscopy (EDX). In brief, the incident electron 'knocks-out' a localised electron, an outer electron falls into the vacancy, emitting an X-ray photon of energy equivalent to the difference between the two excited states, see Figure 2.16 These energies are characteristic of a given atomic species.

The semi-conducting SiLi detector is orientated to absorb the maximum number of emitted X-rays from the sample. On contact, the X-ray excites the electrons within the conduction band of SiLi leaving a number of positively charged holes. The energy required to generate the electron-hole pairs is relatively small, and so the number of these pairs is proportional to the energy of the detected X-ray.[11]

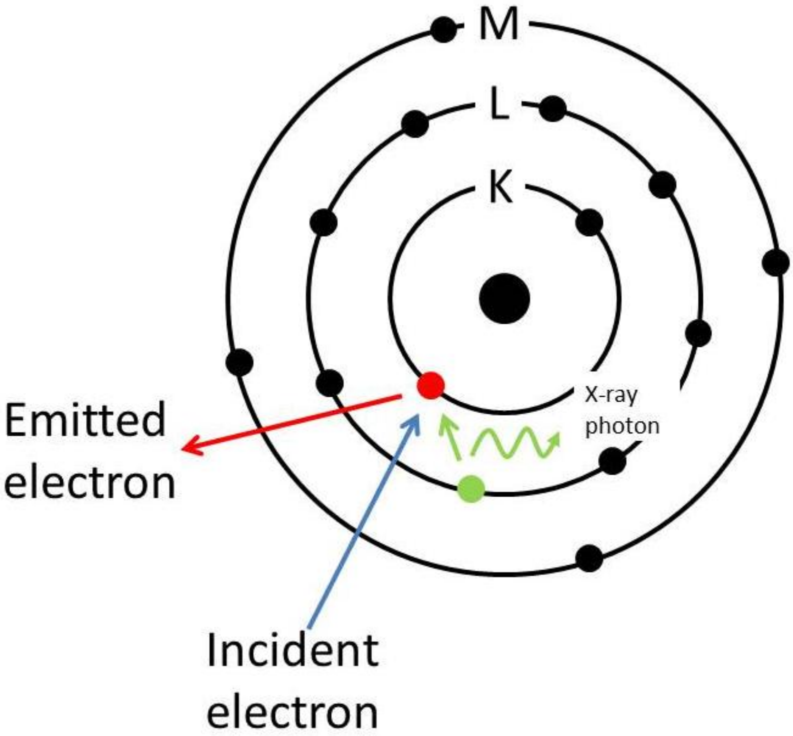

Figure 2.16: Illustration of scattering and X-ray photon emission upon collision of an electron with a sample.

2.3.4.2 Beam damage

Beam damage (radiation damage) can occur via two possible mechanisms: knock-on damage or radiolysis (ionisation damage). The former is a consequence of the displacement or deflection of incident electrons by the electrostatic field of atomic nuclei. For low energy transfers this may result in sputtering of atoms, or for higher energy cases, the displacement of atoms from a crystal lattice, creating point defects. The latter is a result of inelastic scattering, where the excess energy is transferred to a single atomic electron causing an electronic transitions and chemical bonds to break.[12-13]

For carbon nanostructures, beam damage occurs primarily via the knock-on mechanism.[14] Knock-on damage is directly related to the beam energy, thus a reduction in the incident beam energy is sufficient to cause less damage. As suggested by Egerton R.J[12], if the incident electron energy is reduced to below twice the threshold energy then less beam damage will result. The threshold energy can be simply defined as, ‘the minimum energy acquired by an atom through the impact of an energetic particle that enables it to leave its position in the atomic network.'[15] For the case of sp^2 carbon, the threshold energy has been determined to be in the range of 15-60 eV[12,14-15], comparable to an incident beam energy of 100-300 keV. This is dependent on the direction of elimination, i.e. whether parallel to the hexagonal axis or the basal plane respectively. Thus by reducing the acceleration voltage to 80 kV, one can assume limited damage to the graphitic material.

2.3.5 pH probe

A pH meter is utilised to measure the pH of a liquid. The probe itself is made of a H^+ sensitive doped glass membrane, measuring the activity of the H^+ as an indication of the pH. Typically pH meters and probes are designed for use in aqueous phases, however they can be employed in non-aqueous phases such as an emulsion system. The pH meter/probe was a Hanna HI 221 meter attached to a HI 1131P glass body and a HI 7669/2W steel probe, which is suitable to measure the pH in the range of (-2 – 16) ± 0.01 within a temperature range of (-20 – 120) ±0.01 ^{0}C. Calibration reference fluids at pH 4 and 10 were used prior to measurement of pH.

2.3.6 Optical Microscopy

Optical microscope experiments were carried out using a combination of an Olympus Optical Microsope, complete with a 10x, 50x and 100x lens, Olympus Camedia 2.1megapixel digital camera and Linkam Linksys software. Samples were uploaded on glass slides and analysed to determine the state of the system, i.e. microemulsion, nanoemulsion, emulsion or liquid crystalline, to capture images of the precipitate from bulk phases and micellar solutions.

Polarised light microscopy primarily provides the ability to detect image contrast of samples with inherently optically anisotropic behaviour, i.e. birefringent materials. It is a popular technique within the geology and chemistry disciplines, easily incorporated within a standard optical microscope.

To achieve this, the combination of a polariser and an analyser is required in addition to the conventional optical microscope components (stage, strain free objective, revolving nosepiece, condenser, eyepieces, lens) as depicted in Figure 2.17 a and b.

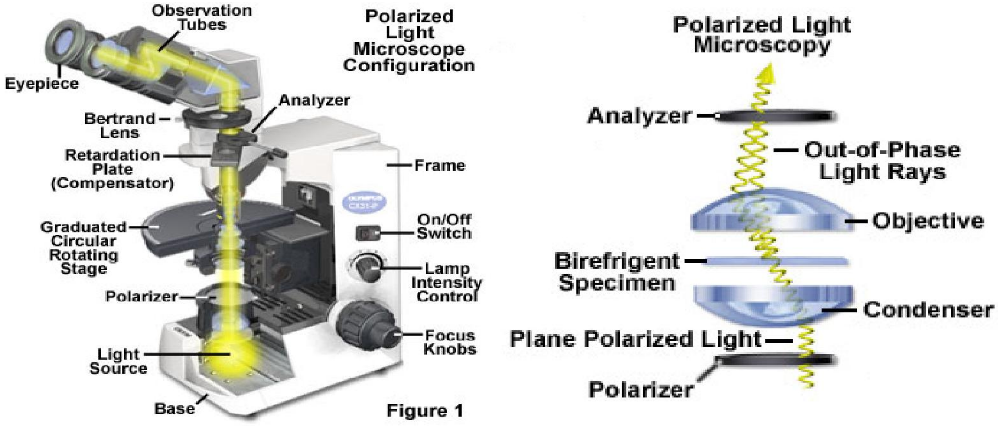

Figure 2.17a and b: External configuration of a polarised optical microscope. [16] A schematic depicting the effect of the combination of a polariser and an analyser on refracted light from a birefringent material. [17]

Images reprinted from http://www.olympusmicro.com/primer/techniques/polarized/polmicroali gnment.html and http://zeiss-campus.magnet.fsu.edu/articles/livecellimaging/ techniques.html respectively.

From Figure 2.17a it can be seen the polariser is fixed before the sample, whilst typically the analyser is placed between the objective(s) and the eyepieces. To understand the need for such an arrangement, a brief on both polarised light and birefringence is essential.

Light is composed of electric field vectors travelling perpendicularly to the direction of propagation, though oscillating in all perpendicular directions. When net unpolarised light passes through a polariser, the vibrations are restricted to a given plane- such resultant light is termed polarised.

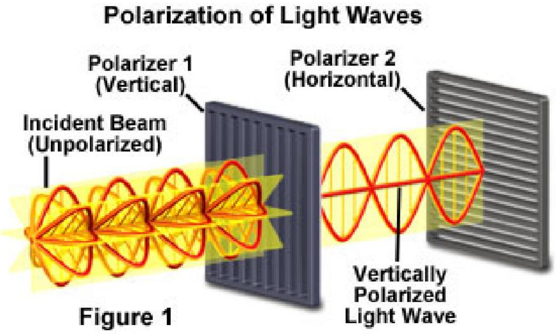

Figure 2.18: A schematic demonstrating the effect of crossed polarisers on unpolarised light.[18] Image reprinted from http://www.microscopyu.com/articles/polarized/polarizedlight intro.html.

The combination of a crossed polariser and an analyser, i.e. two polarisers oriented at right angles with respect to each other, allows the ‘full’ absorption of the initially unpolarised light. How this is achieved is illustrated in Figure 2.18, from which it is evident that only light oscillating parallel to that of the polariser direction has the ability to pass through polariser 1, whilst the subsequent light is absorbed by the analyser.

Crystals may be isotropic or anisotropic. Isotropic materials, such as simple cubic structures have equivalent axes which refract light at a constant angle in addition to maintaining a single light velocity given by the refractive index value. Conversely, anisotropic crystals with distinct crystallographic axes refract light differently depending on the incident angle because the refractive index value varies with crystal orientation: such crystals are termed birefringent. Subsequently, light entering a non-equivalent axis is refracted into 2 rays, denoted the ordinary ray and the extraordinary ray, which are oscillating perpendicular and propagating at different velocities. Thus when the two waves emerge from a birefringent material, interference of such waves is not possible hence image production of such crystals is hindered in techniques such as: darkfield, brightfield illumination, differential interference and phase contrast and fluorescence microscopy. To enhance such images, the application of crossed polarisers forces the out of phase waves to oscillate in the same plane, making interference possible. This technique is illustrated in Figure 2.17b. To further enhance the image, a compensator/retardation plate may be inserted between the crossed polarisers in an attempt to optimise the optical path differences within the sample.

Polarised optical microscopy is advantageous over conventional optical microscopy for observing a number of materials leading to medical applications (primarily the identification of gout crystals), identification of asbestos fibres, geological minerals (history and identification) and observation of natural and synthetic materials such as the crystallisation of polymer melts to form spherulites. The latter is shown in Figure 2.19.

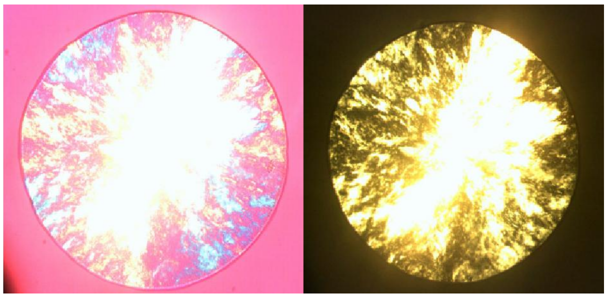

Figure 2.19: A spherulite imaged using a polarised microscope, with and without the compensator plate

References

1. Chen, ‘Crystallisation of glycine and dipicolinic acid (DPA) from microemulsions’, 2012, Durham PhD thesis.
2. D.C. Harris and M.D. Bertolucci, ‘Symmetry and Spectroscopy: Introduction to Vibrational and Electronic Spectroscopy’, 1990, Courier Corporation, 1978
3. http://www.horiba.com/uk/scientific/products/raman-spectroscopy/raman-academy/raman-tutorial/the-theory-of-raman-spectroscopy/ accessed 27/03/2016
4. R. E. Dinnebier and S.J.L Billinge, ‘Principles of powder diffraction’, 2008, Royal Society of Chemistry,
5. C. Hammond, ‘Basics of crystallography and diffraction: Third Edition’, 2009, Oxford University Press
6. D.B Williams and C.B Carter, Transmission Electron Microscopy: A textbook for Materials Science. Diffraction II, Springer Science and Business Media, 1996
7. Glatter, O, ‘J. Appl. Cryst’. 1979, 12, 166-175.
8. C. Chen, O. Cook, C.E. Nicholson and S.J. Cooper, ‘Cryst. Growth Des’, 2011, 11(6), 2228-2237
9. TEM –Manual- Jeol – 2100, Copyright 2004 JEOL Ltd.
10. J. Hutchinson and A. Kirkland, ‘Nanocharacterisation’, Royal Society of Chemistry, 2007, Chapter 4.
11. P.J. Goodhew, J. Humphreys and R. Beanland, ‘Electron Microscopy and Analysis’, Taylor and Francis, 2001
12. R.F Egerton, Ultramicroscopy, Electron microscopy in materials science’, 2013, 127, 100-108
13. D.B Williams and C.B Carter, Transmission Electron Microscopy: A textbook for Materials Science. Basics I, Springer Science and Business Media, 1996
14. F. Banhart, ‘Reports on progress in physics’ 1999, 62 (8) 1181
15. A.V. Krasheninnikov and F. Banhart, ‘Nature Materials’, 2007, 6, 723-733

16. http://www.olympusmicro.com/primer/techniques/polarized/polmicroalignment.html (15/12/11)
17. http://zeiss-campus.magnet.fsu.edu/articles/livecellimaging/techniques.html (15/12/11)
18. http://www.microscopyu.com/articles/polarized/polarizedlightintro.html (15/12/11)

Chapter 3 – Quartz crystallisation

3.1 Introduction

Silicon dioxide, the oxide of silicon (SiO_2) exhibits three stable phases at standard pressure: quartz, cristobalite and tridymite, each of which undergoes inversions at higher temperatures, in addition to high pressure polymorphs including coesite and stishovite.[1] The FTIR spectra and diffraction spacings for the three low pressure polymorphs is given in Appendix 1. The thermodynamic relationship of the most common forms can be seen in Figure 3.1.

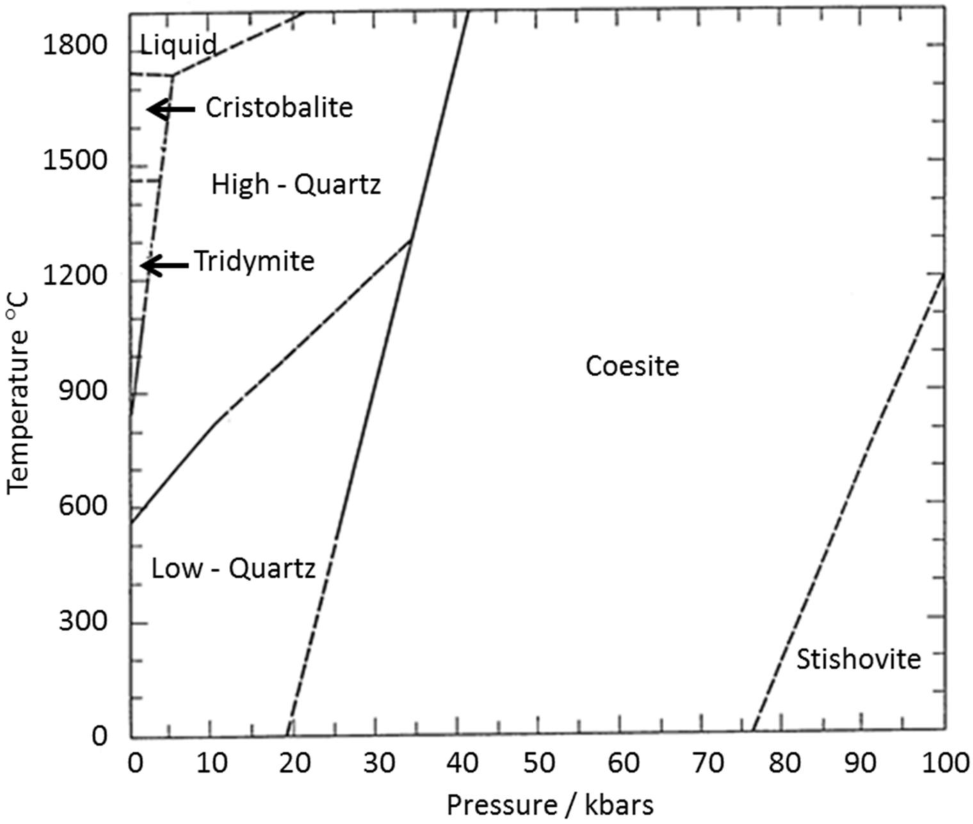

Figure 3.1: The thermodynamic phase diagram for the various high pressure and high temperature polymorphs of silicon dioxide.[48]

Reproduced with permission from Yoo. C-S, *'Phys. Chem. Chem. Phys',* 2013, **15**, 7949-7966. Copyright © 2013, Royal Society of Chemistry

Silicon dioxide is derived from the basic SiO_4 tetrahedral unit. The tetrahedra are interlinked at the corners, with each oxygen atom shared by two tetrahedra. Polymorphism is exhibited via variation in the connection and arrangement of SiO_4 tetrahedra into 6, 8 and even 12 membered rings. The changes in these linkages lead to different crystal structures. [1]

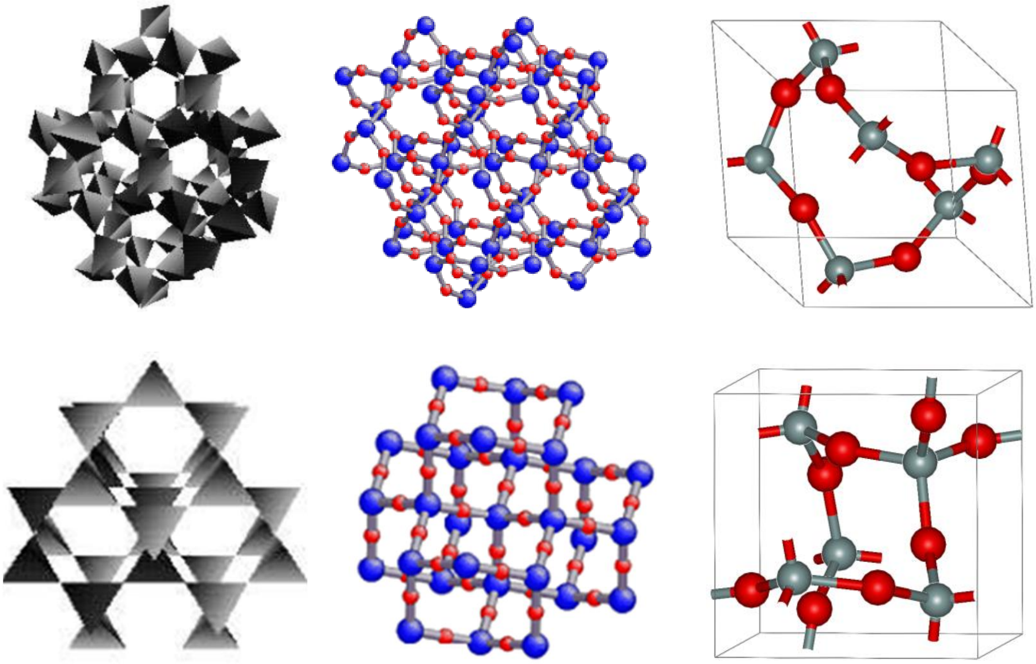

Figure 3.2 a: Clusters of SiO_4 tetrahedra, b: bonding of Si and O and c: the unit cell of 1: Quartz and 2: Cristobalite. [1] Reproduced with permission from Hobbs. L.W and Yaun. X, *'Science and Technology'*, 2000, 37-71. Copyright © 2000, Springer Science+Business Media Dordrecht

In general, synthetic quartz is crystallised via hydrothermal methods employing high temperatures and pressure. Various publications document methods attempting to reduce the typically harsh conditions (hydrothermal methods with temperatures >1100 ^{0}C) required to precipitate the most thermodynamically stable α-quartz form, including the use of biological processes.[3] In general, synthetic quartz is crystallised via hydrothermal methods, i.e. high temperature and pressure. Such an example is exhibited by Bertone J.F. *et al*, starting with the dissolution of amorphous silica in NaOH, before placement into a mini-reactor capable of withstanding high pressures, with a temperature increase of 6 °C/min, up to 200-300 °C.[4] The chosen precursors, i.e. silica glass provide high surface areas,[5-6] which result in a rapid increase in silica solubility levels and basic conditions, favouring rapid quartz nucleation rates. In addition it was found that a pH of 8 was most suitable to maximise the quartz yield, as an increase in basicity results in the dissolution of solid silica, whilst acidic conditions promote the aggregation of amorphous silica powders. In summary, quartz crystallisation occurred after reaction times >5 hours, at temperatures > 250 °C, with a pH ~8.[4]

In addition, to produce quartz nanocrystals with a narrow size distribution for industrial application, further processing to achieve size separation from the polydisperse powders was required via pH controlled dialysis, filtration, and centrifugation.[4]

Further investigations by W L Huang support the requirement of a combination of temperatures between 50 to 450 °C with pressures ranging between 50 MPa to 3 GPa.[7]

Deviations from the above accepted method have been suggested by groups such as V Bansal *et al.* utilising the fungus, *Fusarium oxysporum*, which rapidly bio-transforms the amorphous hydrated silica within rice husks, to protein capped crystalline silica, at ambient temperature.[3] Early efforts by F.T. Mackenzie *et al.* describe the crystallisation of quartz from seawater over a period of three years.[8]

The motivation for such lengthy efforts is endorsed by the numerous applications of both quartz and nano-quartz, including roles in ceramic materials, fillers for plastics/rubbers, thermal insulators and an additive to paint.[9] However quartz is most noted for its piezoelectric properties. Hence questions have been raised as to the possibility of nanoquartz exhibiting nanoscale piezoelectric behaviour, thus providing benefits in helping to achieve small scale motors.[4]

3.2 Choice of system

Previous work has been carried out to investigate the synthesis of amorphous silicon dioxide within microemulsions using sodium meta/orthosilicate or most favourably alkoxysilanes such as TEOS (Tetraethyl orthosilicate). TEOS is available as a colourless liquid which is known to act as an efficient precursor for the production of silicon dioxide. The Stöber process involves the hydrolysis of TEOS is followed by condensation and oligomerisation of silicic acid to form silica.

Hydrolysis: $Si(OC_2H_5)_4 + 4H_2O \rightleftharpoons Si(OH)_4 + 4C_2H_5OH$

Condensation: $Si(OH)_4 \rightleftharpoons SiO_2 + H_2O$

Overall reaction: $Si(OC_2H_5)_4 + 2H_2O \rightleftharpoons SiO_2 + 4C_2H_5OH$

However, the drawback is that TEOS is immiscible with water. Consequently, either a homogenising medium of an alcohol such as ethanol or a w/o microemulsion consisting of a TEOS continuous phase is necessary. For the former case, ethanol is at least partly miscible with most common oil phases, whilst for the latter the reaction is dependent on the penetration of the surfactant interface layer by the TEOS into the aqueous pool of the droplets.[10-11] Conversely, the required nanoconfinement to invoke thermodynamic control over the reaction is jeopardised by the precursors miscibility with the surfactant interface and the continuous phase.

Sodium silicates are inexpensive precursors for the synthesis of silicon dioxide, which are readily soluble in water, with limited solubility in alcohols and acids.[12] Silicates have previously been used to synthesise nano-sized silica powders by L M Gan *et al.* (1996),[13-14] in w/o quaternary microemulsions consisting of a cyclohexane oil phase and a mixture of two non-ionic surfactants: NP-5 and NP-9. Experimental results indicate that the increased concentration of the precursor contributed to an increase in the size of precipitate. In addition, low pH levels promoted larger particles, with basic pH's inhibiting such growth, and also producing non-aggregated spherical particles. The explanation given for this finding relies on the ability of silica particles to absorb hydroxyl ions, thus enforcing segregation of particles via electrostatic repulsion in basic conditions. Conversely in acidic conditions, silicate ions convert to a monomeric silicic acid species, which readily polymerises or condenses to form silica, though only particles < 20 nm are produced.[13-14] In both acidic and basic conditions, there will be an excess of either H^+ or OH^-, hence as suggested by Rimer *et al.* the formation of an effective electrical double layer at the surface of the nanoparticles may be a contributing factor to the confined size and stunted growth.[15]

A simplified reaction mechanism for the above synthesis is postulated below:

Hydrolysis: $Na_2SiO_3 + 3H_2O \rightleftharpoons Si(OH)_4 + 2NaOH$

Condensation: $Si(OH)_4 \rightleftharpoons SiO_2 + 2H_2O$

Overall: $Na_2SiO_3 + H_2O \rightleftharpoons SiO_2 + 2NaOH$

Exploring the process of silica formation from an aqueous silicate solution in more detail, it is known to occur broadly via a three step process: oligomerisation, nucleation and growth. The formation of silica is known to be affected by factors including: the ratio of alkali: silica (Na_2O:SiO_2), the pH of the system and the temperature. [4, 6, 16-19] Various additional factors can modify the formation of silica, such as the presence of a surfactant or acid inducing templation or acid etching of the surface, resulting in modifications to the morphology of the precipitate.[20-22] The effect of HCl addition[20] to the system will be discussed in detail in the following chapter. The effect of temperature and the ratio of alkali:silica are negated, as all experiments are conducted at a constant ambient room temperature, with sodium metasilicate nonahydrate as the sole precursor.

The variable parameters: temperature, surfactant type and pH, mentioned above are known to have a specific effect on each of the stages of silica formation. Moreover, upon the dissolution into a bulk aqueous phase, the alkali silicate species present varies with the concentration of precursor,[17-18] pH and the temperature of the system.[23]

It can be assumed that upon immediate dissolution, monomeric silicic acid in the forms of $Si(OH)_4$, $SiO(OH)^{3-}$ or $SiO_2(OH)_2^{2-}$ will dominate.[17-18,24] However oligomerisation and condensation can then occur and these can be broken down into three processes: polymerisation of monomer, nucleation and particle growth.[18] The primary stage can further be described by a number of chemical reactions to promote the formation of dimers, trimers and larger oligomers. The latter condensation proceeds via the aggregation of monosilicic acid to form dimers, trimers and tetramers. This process is thought to be activated by the formation of anionic monomeric species with uncharged silicic acid. The presence of anionic species is heavily dependent upon both the concentration of aqueous sodium metasilicate and pH as depicted by Yang *et al.* in Figure 3.3.[17]

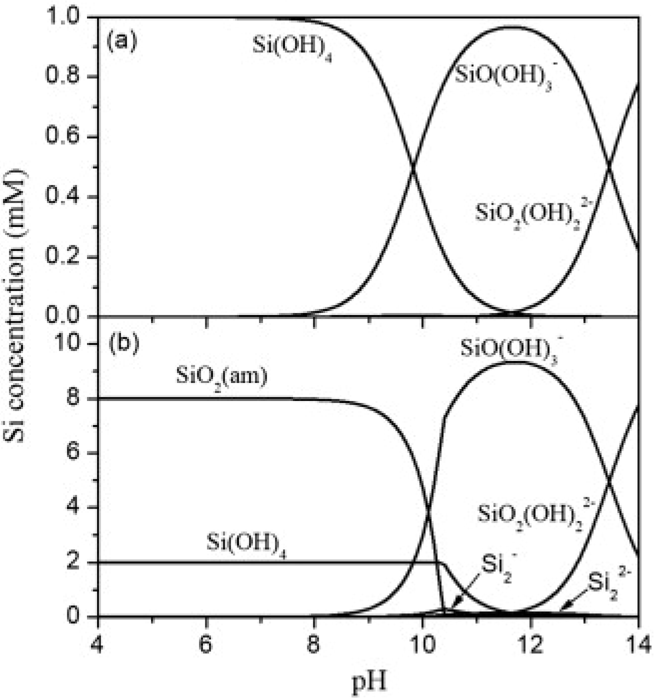

Figure 3.3: Yang *et al.*[17] illustrates the effect of concentration and pH upon the distribution of silicate anions in solution. a: 1 mmol L^{-1} and b: 10 mmol L^{-1} aqueous sodium metasilicate solution. Reproduced (adapted) with permission from X. Yang, P. Roonasi and A. Holmgren, '*J. Colloid Interface Sci'*, 2008, 382(1), 41-47. Copyright © 2008 Published by Elsevier Inc.

Beyond the formation of small oligomers, condensation continues so as to minimise the uncondensed Si(OH) bonds in favour of the more condensed Si-O-Si bonds, particularly the adoption of ring structures over chain-like configurations, when the oligomer size exceeds a trimer. The expansion to larger cyclic ring structures is promoted from the addition of smaller monomer and dimers over the formation of new smaller oligomers, as required for the more stable phases of silica.[19]

With regards to the formation of larger open rings structures, Kinrade and Pole[25] documented the role of small metal positive ions in the stabilisation of these structures. The presence of small metal cations, from Na to Cs are known to contribute to a varying degree to the process of silica precipitation from aqueous silicate solutions in one of three ways: electro-restrictive water structuring increases the degree of polymerisation of silica; silicate-metal cation pairings promote encounters of the silicate anions via the reduction and potential circumnavigation of the electrostatic repulsion; and ion-paired cations promote the stabilisation of open ring oligomer structures over more rigid counterparts.[25] As outlined previously the more stable polymorphs, and indeed quartz are the product of a significant degree of polymerisation with the formation of large open ring structures. Hence, it may be hypothesised that upon dissolution, free sodium cations from the SMS precursor may act to promote quartz formation.

Beyond this initial condensation or oligomerisation, the process continues to aid the formation of stable nuclei beyond a critical size, followed by growth of material. The reaction of silica precipitation can be summarised as in equation below:

$$SiO_{2\,(mono)} \rightarrow SiO_{2\,(critical\ nucleus)} \rightarrow SiO_{2\,(nano)} \rightarrow SiO_{2\,(ppt)}$$

As monomeric silica achieves the critical nucleus size, the relative supersaturation declines and thus is accompanied by an increase in the critical nucleus size and a reduction in the drive for nucleation and growth.

3.3 Project outline

The dynamic medium of nanoconfinement within microemulsion droplets is to be utilised in the exploration to crystallise quartz, the stable phase of silicon dioxide under standard conditions via thermodynamic control (Chapter 1), from a generic precursor; sodium metasilicate nonahydrate. This is investigated as a route to potentially overcome the typically severe conditions required for the production of crystalline silicon dioxide.

The choice of microemulsion system is dependent on the chemical properties and solubility of the reaction precursors and products: sodium metasilicate nonahydrate, (SMS) water, hydrochloric acid, and silica phases.

3.4 Experimental

3.4.1 Control experiments

Unconfined experiments, i.e. experiments conducted in bulk solution, were performed to investigate the solubility of SMS in relevant solvents, in addition to determining the potential for hydrolysis and condensation of SMS to allow comparisons with the synthetic microemulsion route.

3.4.2 Solubility tests

The solubility of SMS was determined in a number of solvents under ambient conditions. Incremental quantities of SMS were added sequentially over a period of ~5-6 weeks to 1g of solvent or liquid surfactant in a stable temperature oven at 25 ± 1 °C, until no further material could be dissolved. Solubility studies were completed in solvents required for the synthesis within a water – in – oil emulsion system: UHQ water, heptane, cyclohexane, and 1-hexanol.

Note the solubility of SMS in the Span80:Brij30.heptane (SBC7) w/o microemulsion < 1 mg/2g.

Solvent	**SMS (mg/ml)**
UHQ Water	390
Heptane	< 0.1
0.2 M HCl	> 350
1.5 M HCl	< 15
2.2 M HCl	< 10
Cyclohexane	< 1
TX-114	< 1
Span 80	< 1
Brij 30	< 1

Table 3.1: Measured solubility of sodium metasilicate nonahydrate in various solvents. Each is measured to

Table 3.1 indicates heptane and cyclohexane are suitable liquids to fulfil the role of a continuous phase in an emulsion due to the low solubility of SMS within these liquids. Further, findings support the dramatic reduction in SMS solubility with increasing HCl concentration highlighted in the literature.[12]

3.4.3 Unconfined experiments

Comparable concentrations of SMS in bulk UHQ water to those adopted in the inner phase of the microemulsions were prepared and left to precipitate. Aqueous compositions of 1 – 40 wt %. SMS were created. Concentrations ≥ 3 wt %. SMS gave precipitate and were analysed by FTIR spectroscopy and PXRD. Additionally the pH of the solutions was measured to enable comparison to the pH changes made in the microemulsion system.

3.4.3.1 pH measurements

Aqueous SMS compositions – no HCl. pH					
SMS (% wt.)	**pH (0 h)**	**pH (upon precipitation)**	**SMS (% wt.)**	**pH (0 h)**	**pH (upon precipitation)**
1	12.39 ± 0.04	No precipitate			
2.5	12.06 ± 0.04	No precipitate	20	12.88 ± 0.06	Too viscous
5	12.84 ± 0.02	12.69 ± 0.04	25	12.95 ± 0.07	12.84 ± 0.06
7.5	13.04 ± 0.05	12.73 ± 0.06	30	13.18 ± 0.08	12.80 ± 0.07
10	13.07 ± 0.07	12.05 ± 0.02	40	13.15 ± 0.06	Too viscous

Table 3.2 – pH measurements of bulk sodium metasilicate solutions upon mixing and after precipitation of solid material is observed.

3.4.3.2 XRD

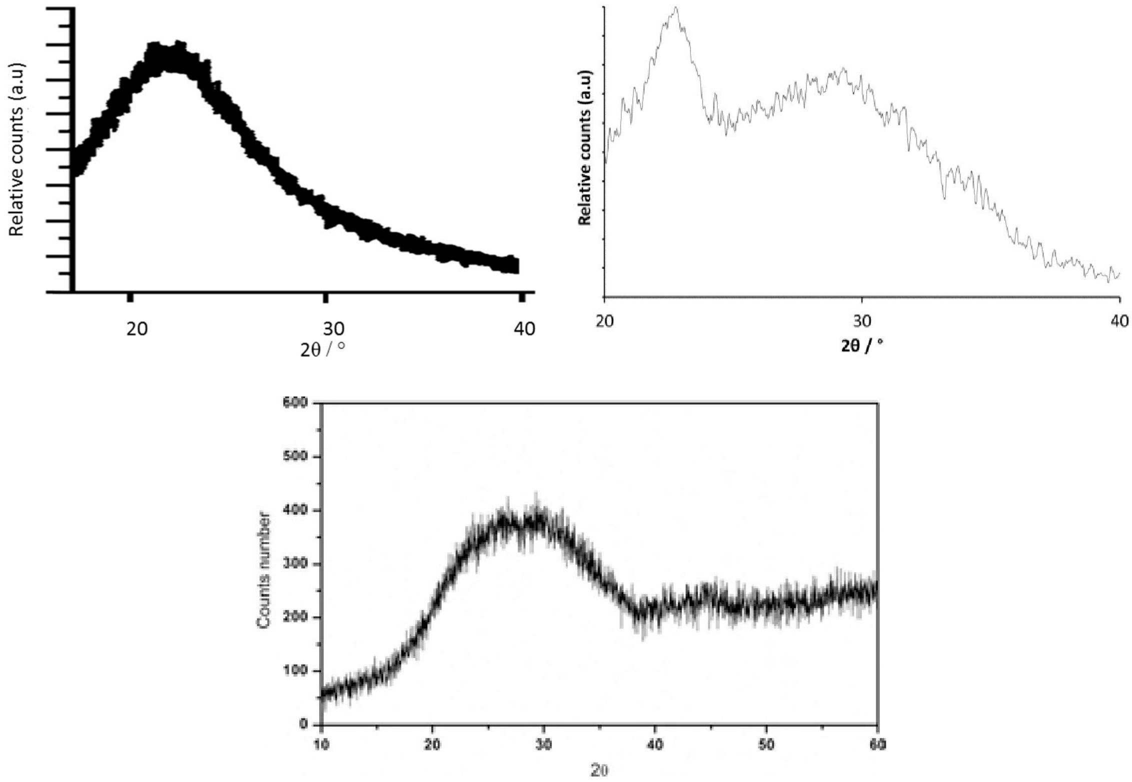

Figure 3.4: XRD pattern of amorphous silica precipitate[26], b: XRD pattern of precipitate from aqueous sodium metasilicate solution and c: XRD pattern of aqueous sodium silicate structures.[27]

Comparison of the experimental XRD pattern with accepted literature data (Figure 3.4a), confirms amorphous silica is deposited from unconfined aqueous sodium metasilicate solutions. Amorphous silica presents a broad amorphous peak centre around $2\theta = 21.8^0$. In addition a broad amorphous peak is present between $2\theta = 20$ and 40 ^{0}, which is indicative of sodium silicates of the type ($Na_2SiO_3 \cdot nH_2O$).[27]

3.4.3.3 IR

The bulk solutions of aqueous sodium metasilicate have a pH in the order of 12-13, with a slight reduction with time and upon precipitation, see Figure 3.5.

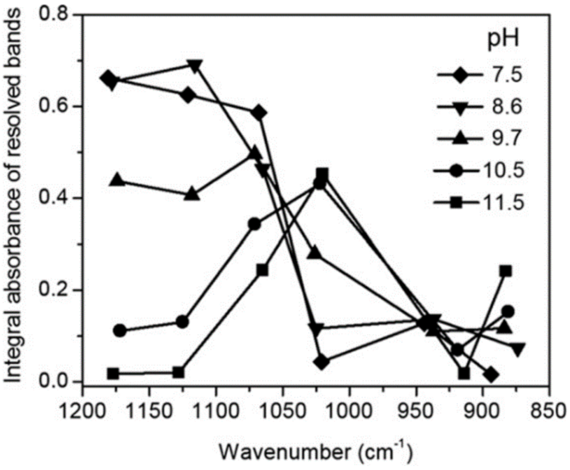

Wavenumber (cm^{-1})	Species	Peak assignment
~ 1020	$SiO(OH)^{-}_{3}$	Si – O
~ 890	$SiO(OH)^{-}_{3}$	Si – O
~ 1000	$SiO_2(OH)^{2-}_{2}$	Caused by undissociated Na-silicate species
~ 930	$SiO_2(OH)^{2-}_{2}$	
~ 945	$Si(OH)_4$	Si – OH
~ 1070	-	Si – O – Si
~1050 – 1200	-	Si – O – Si

Figure 3.5: Results of curve fitting of IR spectra of aqueous 10 mmol L^{-1} silicate solutions at a range of pH levels between 7.5-11.5. Accompanying table highlights species present and vibration resulting in peak.[17] Reproduced (adapted) with permission from X. Yang, P. Roonasi and A. Holmgren, '*J. Colloid Interface Sci*', 2008, 382(1), 41-47. Copyright © 2008 Published by Elsevier Inc.

Regarding literature findings, at such pH levels, one would expect the IR spectra to be dominated by a peak at ~ 1000 cm^{-1}, with smaller contributions at ~1050 cm^{-1}, 950 cm^{-1} and 880 cm^{-1}, in addition to minimal features at 1120 cm^{-1}, 1170 cm^{-1} and 920 cm^{-1}.

Referring to Figure 3.6d it is clear that the major features presented are as expected. The dominant peak at ~1000 cm^{-1}, in addition to an expected weak contribution ~930 cm^{-1}, is assigned to un-dissociated sodium silicate species as per the work performed by Yang *et al.*[17] and Bass and Turner.[16] No distinct peak is observed at 1020 cm^{-1}, however the 880 cm^{-1} component can be distinguished. One can further add that the absorbance in the region ~950 cm^{-1} is likely to originate from Si-OH stretching, in the form of $Si(OH)_4$ monomers.

The broad shoulder, sloping feature between 1070-1125 cm^{-1} can be assigned to the Si-O-Si stretch within silica phases. At such high initial pH levels within the bulk solution one can see from Figure 3.5 that this should be a minimal contribution. Moreover, one can rationalise that sodium metasilicate dissociates in aqueous solution to form $SiO_2(OH)_2^{2-}$ or $SiO_2(OH)_3^-$, or $Si(OH)_4$ depending on the pH and concentration of silicate.[17] However, even a negligible amount of silicic acid will initiate the polymerisation reaction for the formation of silica, thus lowering the pH at least locally, inducing a supersaturation and promoting the formation of silica over sufficient time.[17,19]

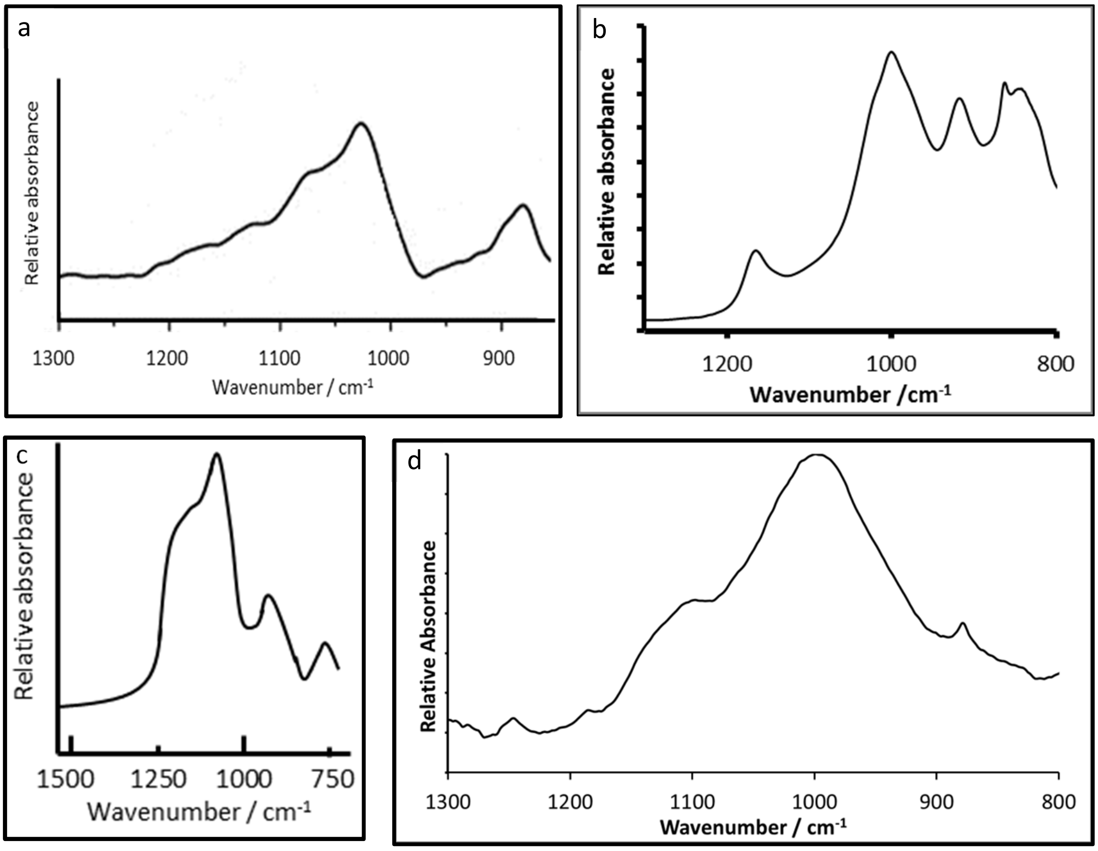

Figure 3.6 a: IR spectrum of aqueous sodium metasilicate solution (pH 10.5)[17] Reproduced (adapted) with permission from X. Yang, P. Roonasi and A. Holmgren, *'J. Colloid Interface Sci'*, 2008, 382(1), 41-47. Copyright © 2008 Published by Elsevier Inc. b: IR spectrum of solid sodium metasilicate nonahydrate, c: Amorphous silica and d: Precipitate obtained from sodium metasilicate aqueous solutions

More broadly the detailed region, 1050 – 1200 cm^{-1} indicates the presence of condensed Si-O-Si entities. However identification of specific structurally forms is not possible due to this IR feature being dominated by the vibrations from the short range order of the Si-O chemical bond, found in all SiO_2 forms.[17,28] In the region below 825 cm^{-1} the various forms of silica are readily discernible. The full IR spectra of the relevant forms of silica can be found in Appendix 1 or Figure 3.5; however in brief the forms exhibit the following: quartz: a doublet ~800 cm^{-1} and a singlet ~700 cm^{-1}, cristobalite: a singlet ~790 cm^{-1} and 620 cm^{-1} and amorphous silica: a minor singlet ~795 cm^{-1}. The higher frequency indicates the symmetric Si-O vibration, whilst the lower frequency highlights the presence of ring structures.[29]

It can be concluded that from an unconfined aqueous sodium metasilicate nonahydrate solution, either a silicate or amorphous phase silica precipitates upon leaving to equilibriate.

3.4.3.4 Optical and electron microscopy

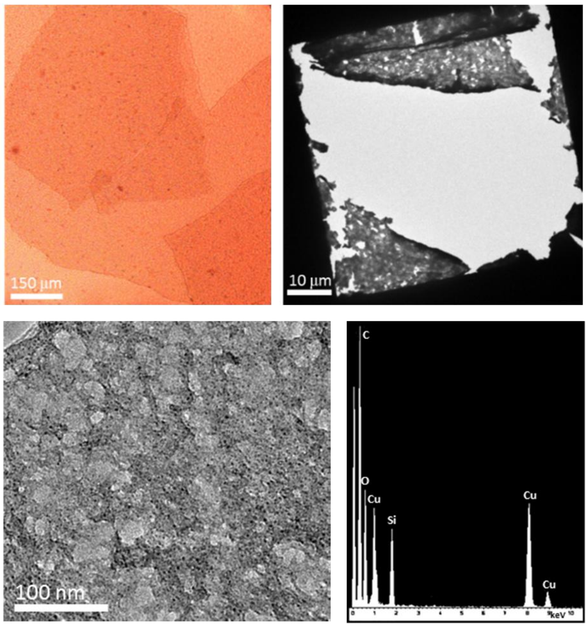

Figure 3.7a: Optical microscope image of film precipitate from aqueous solution of sodium metasilicate, b: Bright field TEM, c: High resolution image and d: EDX spectrum of aqueous sodium metasilicate solution.

To look at the morphology of the precipitate from unconfined SMS solutions, an optical microscope was utilised. The images presented in Figure 3.7a and b reveal thin amorphous films, which from the IR and XRD studies can be confirmed to be silicate and silica based. When no precipitate is observed for lower SMS concentrations, TEM, in combination with EDX spectroscopy allowed comparable images of precipitate to be produced. The EDX spectroscopy confirmed the presence of silicon and oxygen only.

3.4.4 Phase diagrams

A phase diagram is an essential pre-requisite to identify a suitable composition to form a microemulsion within a ternary or quaternary system comprised of an aqueous, organic (oil) and surfactant or co-surfactant components. The phase diagram allows the homogeneous Winsor IV single phase microemulsion region to be recognized effectively.

The choice of microemulsion system is dependent on the chemical properties and the solubility of the precursors, in addition to the possible products. The SMS solubility data in cyclohexane and heptane presented in Table 3.1, combined with known immiscibility with both water and HCl, highlight these liquids as potential microemulsion continuous phases. The behaviour of microemulsions containing these liquids and three non-ionic surfactants have been documented with respect to the investigation presented in this chapter and Chapter 4.

3.4.4.1 TX-114/cyclohexane system

Triton X-114 is a non-ionic surfactant with an HLB of 12.3, cmc = 0.21 mM and a cloud point = 23 °C. This suggests an o/w system is favoured, however a w/o system may still be supported. The distinct hydrophilic polyethylene oxide head group and the hydrophobic aromatic hydrocarbon tail portions of the surfactant are apparent from the molecular structure presented in Figure 3.8.

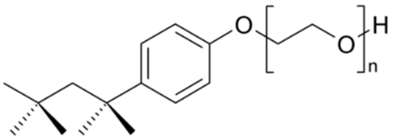

Figure 3.8: Molecular structure of the TX-114 surfactant, where n = 7 or 8.

From analysis of the phase diagram, a single phase microemulsion region can be identified in Figure 3.9 (labelled 1Φ) where a 30 wt %. Triton X-114 surfactant in a cyclohexane continuous phase was employed. The volume of aqueous dispersed phase stabilised by the surfactant/oil continuum was varied between 5 - 50 µl/g. A narrow range was adopted due to the SMS precursor destabilising the microemulsion system and hence reducing the single phase region relative to the water case.[30] The concentrations of aqueous SMS were varied between 0.25 – 20 wt %.

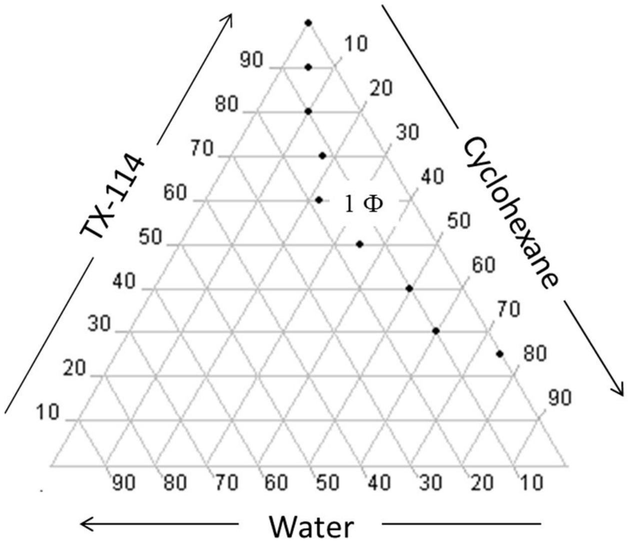

Figure 3.9: Ternary phase diagram illustrating the dependence of the oil:water:surfactant composition upon the resultant phase for a cyclohexane:water:TX-114 combination.

3.4.4.2 Span 80/Brij 30/heptane system

A 1:1 wt. combination of two non-ionic surfactants: sorbitane monooleate (Span 80) and polyoxyethylene (23) lauryl ether (Brij 30), used by Chen *et al.* for a comparable procedure was used.[30] Span 80 has a HLB value of 4.3 and a cmc = 2 mM[31], whilst Brij 30 has an HLB value of 9, with a cmc = 0.3 mM[32]. A 1:1 combination of the surfactant results in an overall HLB of 6.6, hence a w/o emulsion system is readily promoted and stabilised.

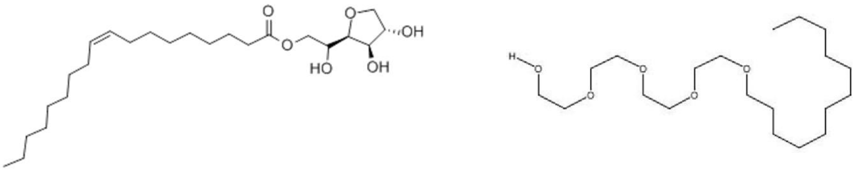

Figure 3.10a and b: Molecular structure of the Span 80 and Brij 30 surfactants respectively.

The molecular structure of the above surfactants is shown in Figure 3.10 above. It is clear that Span 80 consists essentially of a sorbitan hydrophilic head group and an oleic acid hydrophobic portion, whereas Brij 30 or L4 has a much shorter dodecane alkane tail group with an ethylene oxide based head group, similar to TX-114.

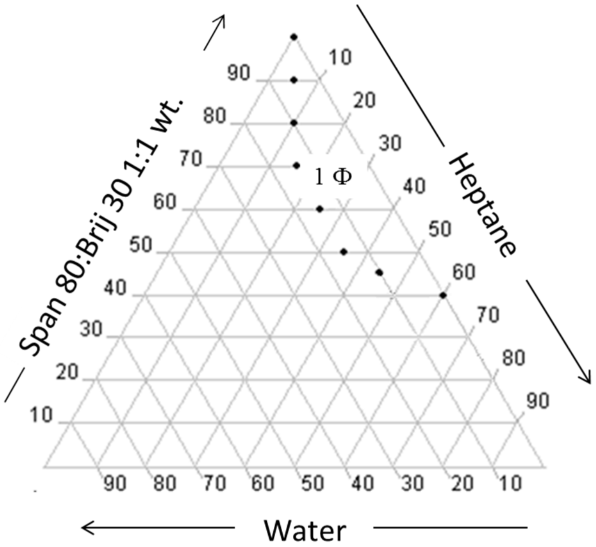

Figure 3.11: Ternary phase diagram illustrating the dependence of the oil:water:surfactant composition upon the resultant phase for a heptane: water: 1:1 Span80:Brij30 combination.

The single phase w/o microemulsion region (1Φ) was identified. A 1:1 40 wt %. surfactant: 60 wt %. heptane composition was deemed to provide the greatest degree of flexibility with variation of the aqueous phase volume. The volume of aqueous dispersed phase added to the surfactant continuum was varied between 5 - 50 μl/g, again due to destabilisation effects of the SMS precursor. The concentration of aqueous SMS was varied between 0.25 – 15 wt %.

3.5 Triton X-114 system

3.5.1 Microemulsion preparation

Aqueous sodium metasilicate nonahydrate (SMS) was dissolved in UHQ water at 0.25 and 20 wt %. 2 g aliquots of the various stock surfactant solutions in oil were prepared and sonicated until homogeneous, to which the aqueous SMS was added and dispersed. Microemulsions were left for varying degrees of time (1 hour – 3 years) before analysis was performed.

3.5.2 Microemulsion experiments

Using the 3D nanoconfinement of microemulsion droplets, the following variables are to be investigated: the effect of the concentration of precursor and the droplet size upon nucleation, precipitation and crystal growth and/or aggregation will be discussed below in Chapter 3, whilst the effect of the addition of HCl upon the process will be discussed in Chapter 4 via TEM analysis of selected samples.

3.6 TX-114/cyclohexane: Results and discussion

To determine the range over which 3D confinement within the microemulsion is maintained, a series of systematic experiments, varying the concentration of aqueous SMS alongside the droplet size of the dispersed phase were completed. The range of concentrations and volumes stabilised are illustrated in Figure 3.12.

Despite SMS being readily soluble in water, from initial studies, supersaturated solutions often initiated immediate destabilisation of the microemulsion. This may be due to a number of factors including: perturbation of water molecules by the surfactant or altered pH levels within the dispersed phase.

3.6.1 30 wt %. TX-114 / 60 wt %. cyclohexane microemulsion system.

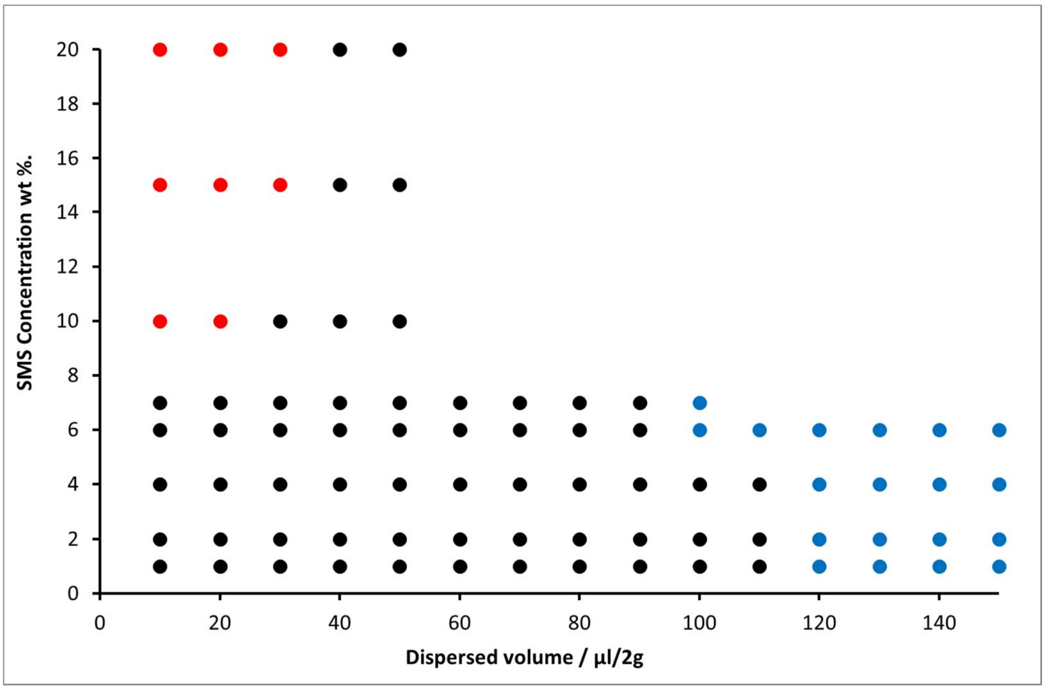

Figure 3.12 Graphical display of microemulsion compositions with varying SMS concentration and dispersed volume, and the effect upon the stability. Black = microemulsion, red = immediate precipitation of amorphous silicate phase and blue = unstable.

As one would expect the material synthesised from the microemulsion is dependent upon a combination of both the SMS precursor concentration and the dispersed volume.

3.6.1.1 Effect of varying the SMS precursor concentration.

As observed from Figure 3.12, SMS concentrations between 1 and 20 wt %. were employed in the microemulsion system. No macroscopic precipitate was observed for any concentration of SMS, thus TEM was utilised to image any nanoscopic material which is documented below. From Figures 3.13-3.15 for a constant dispersed phase of 10 µl/2g surfactant solution, it is apparent that for SMS precursor concentrations < 10 wt %. SMS, quartz particles in the order of 2-5 nm dominate. For 1, 4 and 6 wt %. SMS, a bright field, high resolution and the corresponding fast Fourier transform (FFT) are presented in Figures 3.13-3.15a,b and c.

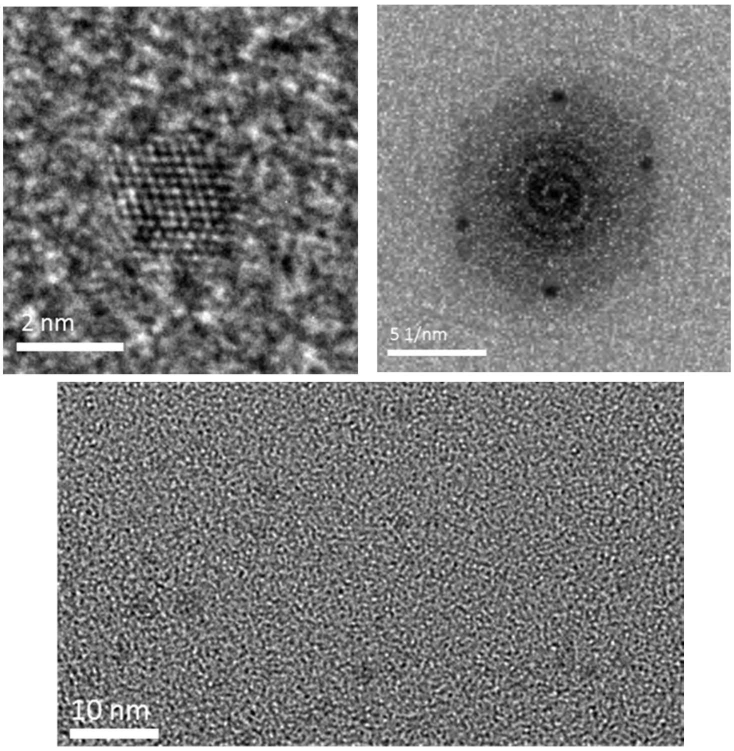

Figure 3.13 a, b and c: HREM, FFT and BF images of a representative quartz nanocrystal from a TX-114/cyclohexane microemulsion with 10 µl/2g 1 wt %. SMS precursor. ([212] zone axis of quartz)

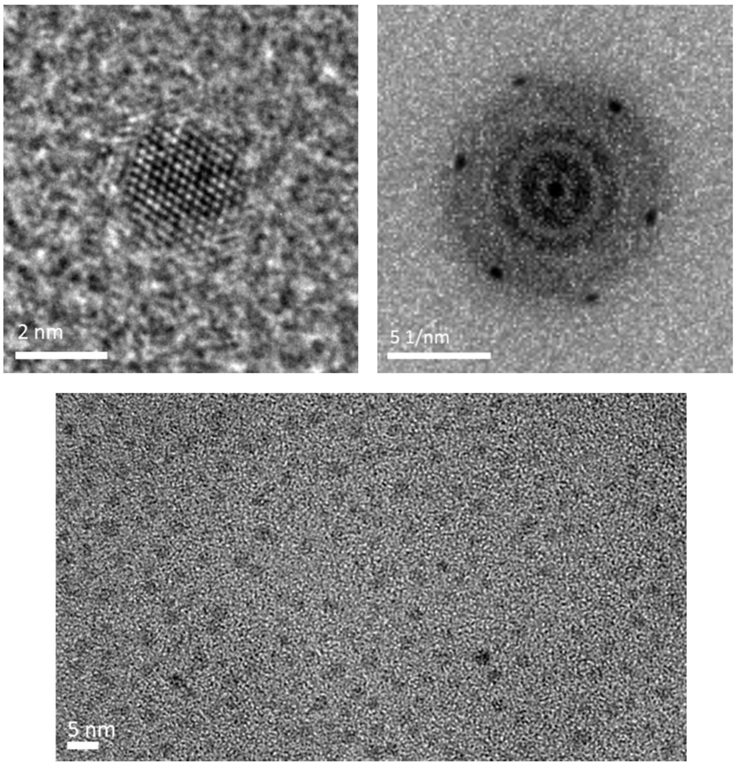

Figure 3.14 a, b and c: HREM, FFT and BF images of a representative quartz nanocrystal from a TX-114/cyclohexane microemulsion with 10 µl/2g 4 wt %. SMS precursor. ([212] zone axis of quartz)

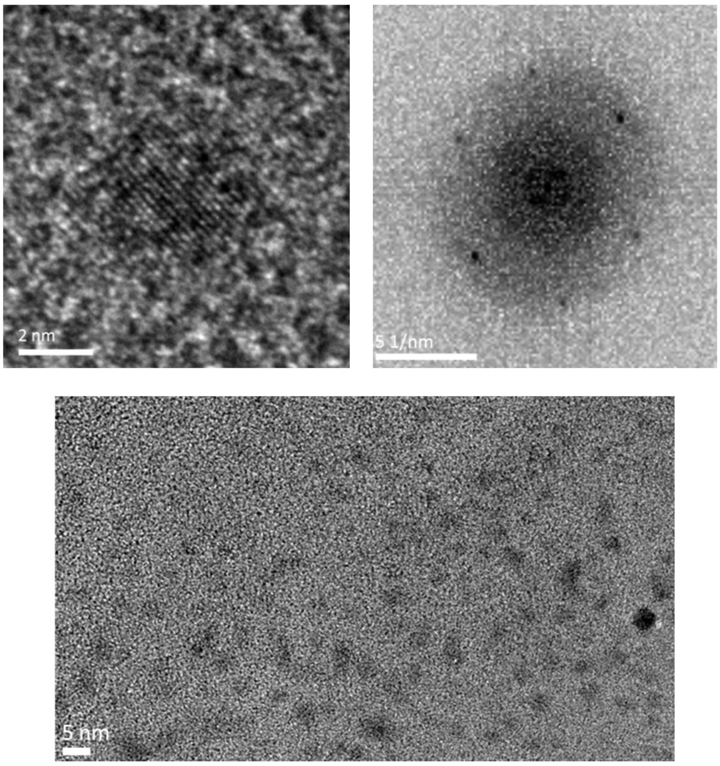

Figure 3.15 a, b and c: HREM, FFT and BF images of a representative quartz nanocrystal from a TX-114/cyclohexane microemulsion with 10 µl/2g 6 wt %. SMS precursor. ([212] zone axis of quartz)

Comparisons of the bright field (BF) images of the three samples show an associated increase in the quantity of nanoparticles precipitated with increasing precursor concentration; however no change in the morphology or size of the aforementioned particles is observed. Each of the representative nanoparticles presented in Figures 3.13-3.15 are seen to be around 2-5 nm and from the corresponding Fast Fourier Transforms they can each be indexed to the [212] zone axis of quartz.

It is apparent the thermodynamically stable quartz silica phase obtained from within the 3D-nanoconfinement is distinctly different to the amorphous phase precipitated from the unconfined aqueous silicate solutions. With regards to the theorem presented in Chapter 2, this is as one would expect, providing the conditions for silica formation are satisfied within the confinement. Primarily, one must note the impressive feat of overcoming the usual hydrothermal synthesis route.

The following will try to address how quartz formation is possible within the confinement of the 3D-nanodroplets of a microemulsion under ambient conditions, and the factors affecting the overall process of silica formation. As detailed previously, silica formation proceeds via a hydrothermal synthesis requiring high temperature and/or pressure through a process involving oligomerisation, nucleation, growth and precipitation.

3.7 Variables affecting condensation and precipitation of silica

3.7.1 Temperature

Utilising the 3D nano-confinement, the common hydrothermal synthesis methodology involving either high temperatures and/or pressures are able to be negated, with the energy barrier to formation/nucleation deemed surmountable by fluctuations in thermal energy within the system. As previously stated, the effect of varying temperature has not been studied in this investigation, however the work of Belton *et al.*[33] regarding the solution study of silica condensation must be noted. Belton suggests that although the formation of silicic acid monomer is essentially irreversible, the case of addition and removal of said monomers from larger oligomers may well be reversible. If the reaction is completed below 20 °C, the activation energy of small oligomer formation and addition to larger oligomers is measured to be in the range 13 – 85 kJ mol^{-1}, with dependence upon pH and temperature of the system.[33] However, if the temperature of reaction occurs between 20 – 30 °C, the activation energy is measured to reduce to 6.1 and 7.3 kJ mol^{-1} for the forward and reverse reaction respectively, noting that an excess of water is expected to reduce the required energy by a factor of 1/3, compared to the anhydrous case.[33] As described in Chapter 1, for the process of precipitation or crystallisation to be under thermodynamic control, a degree of reversibility in the process must exist. Further, for a process to be deemed reversible, one would expect that the energy associated is comparable to k_BT or RT per mole, where R is the gas constant, as illustrated in Figures 1.20-1.21 in Chapter 1. As all experiments are undertaken within the temperature range of 20 – 30 ºC, comparing RT at 25 ºC (2.5 kJ mol^{-1}), one can see that the activation energy is of the same order of magnitude for small oligomer formation and dissolution.

3.7.2 pH

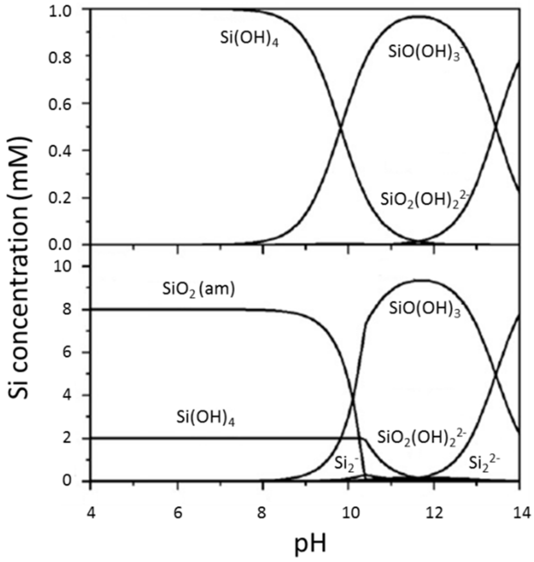

Figure 3.16: Distribution of silicate species as a function of pH and concentration. Upper: 10 mmol L^{-1}, lower: 2 mmol L^{-1} aqueous sodium metasilicate solution.[17] Reproduced (adapted) with permission from X. Yang, P. Roonasi and A. Holmgren, *'J. Colloid Interface Sci'*, 2008, 382(1), 41-47. Copyright © 2008 Published by Elsevier Inc.

Combining the results presented in Section 3.4.3.1 with the literature Figure 3.16 one can demonstrate and expect that from an unconfined solution of basic aqueous sodium metasilicate, the precipitate is a combination of silicate and amorphous silica. Focussing on Figure 3.16, one can see that a reduction in the pH of the system to ~9 and below is desirable to promote a majority of silica (SiO_2).

The idea of pH in confined partitions of a microemulsion is difficult to comprehend as pH is a macroscopic property where pH – neutral is defined as the dissociation of one water molecule in the presence of 10^7 undissociated water molecules. Hence considering a typical reverse micelle contains between 10 and 1000 water molecules, the conventional definition of pH does not hold. However, an indication of the local pH reveals important details about the structure of reverse micelles and where certain species reside. The measurement of pH within a micelle has obvious difficulties as typical pH probes are extremely large compared to the droplets in question, and thus result in a catastrophic perturbation to the system.[34]

The use of UV-vis, fluorescence and ^{51}V NMR spectroscopic techniques have been employed to monitor the state and movement of pH sensitive molecular probes, without causing disruption to the micellar structure. An example is the work of Crans *et al.*[34-35] which provides an insight into the possibility of recording an indicative pH within the aqueous phase of reverse micelles, via the interpretation of the oxidation state of the oxovanadates. Crans concludes that for the dispersion of initially acidic solutions, the predominant decavanadate species loses two or three protons indicating a shift towards a pH neutral environment, via the diffusion of protons towards the interface where the H_3O^+ ion is preferentially stabilised via both enthalpic and entropic contributions. The enthalpic effects arise from the partial positive charge on the oxygen acting to destabilise the O-H interactions between neighbouring water molecules. The entropic stabilisation is a result of the greater randomisation presented at the interface with respect to the interior of the droplet.[35]

The case for an initial alkaline solution is a little more complex due to speciation and oligomerisation reactions of the pH probe molecule being complex within this pH range. However, the speciation of simple oxovanadates under alkaline conditions behaves sufficiently well to probe, indicating a similar shift towards pH neutral. From the studies of Baruah and Crans, systems with a large w_o, where w_o = [water]/[surfactant], a reduction in the pH is observed, however for smaller droplets strong interactions between the oxovanadate species introduces complications. Nevertheless, one can infer that regardless of the initial pH of the dispersed phase, a move towards neutrality occurs once in the confinement of the reverse micelles.[34-35]

Despite the highlighted issues, conventional pH probe methods were used to estimate the pH of the system, to give an indication of the pH levels within the microemulsions. The values are documented in Table 3.3 below. As a note, the pH of the comparable system with a UHQ water dispersed phase is ~5.6, for the range of dispersed phase employed, whereas the pH of the unconfined bulk aqueous metasilicate solutions ranges between 12-13.

30 wt %. TX-114 in cyclohexane					
SMS (wt %.)	**Dispersed volume (μl/2g)**	**pH**	**SMS (wt %.)**	**Dispersed volume (μl/2g)**	**pH**
1	10	9.9 ± 0.1	6	10	10.0 ± 0.1
	50	9.5 ± 0.2		50	9.9 ± 0.1
	100	10.0 ± 0.1		100	11.7 ± 0.2
2	10	10.6 ± 0.1	10	10	10.2 ± 0.1
	50	9.9 ± 0.1		50	10.3 ± 0.1
	100	11.0 ± 0.2	15	10	10.4 ± 0.1
4	10	11.0 ± 0.1		50	10.5 ± 0.1
	50	10.5 ± 0.1	20	10	10.6 ± 0.1
	100	11.4 ± 0.1		50	10.6 ± 0.1

Table 3.3: pH measurements of TX-114/cyclohexane system with variation of both dispersed volume and SMS precursor concentration.

Considering the data from Table 3.3, one can infer that for all dispersed phases a move towards neutrality is observed with respect to the unconfined aqueous silicate solutions. The pH measurement for the addition of a UHQ water dispersed phase to the TX-114/cyclohexane composition is ~7.4. For smaller dispersed volumes, i.e. 10 and 50 µl/2g the pH readings show a greater shift towards neutrality, whilst the pH of higher dispersed phases remains close to that of sodium silicate solutions, i.e. in the order of 12-13 as might be expected for larger droplet systems. This observation is supported by the work of Baruah *et al*,[35] which utilised a simple oxovanadium compound as a probe of the intramicellar pH via monitoring with ^{51}V NMR spectroscopy. Vanadium was chosen due to the associated speciation chemistry, where a series of highly pH dependent oxovanadates are formed in solution. For alkaline pH values, the monomer and dimer (V_1 and V_2) species dominate, whereas higher oligomers such as linear trimers and tetramers (V_3 and V_4) appear for a lower pH range, as predicted in Baruah's simulation below in Figure 3.17

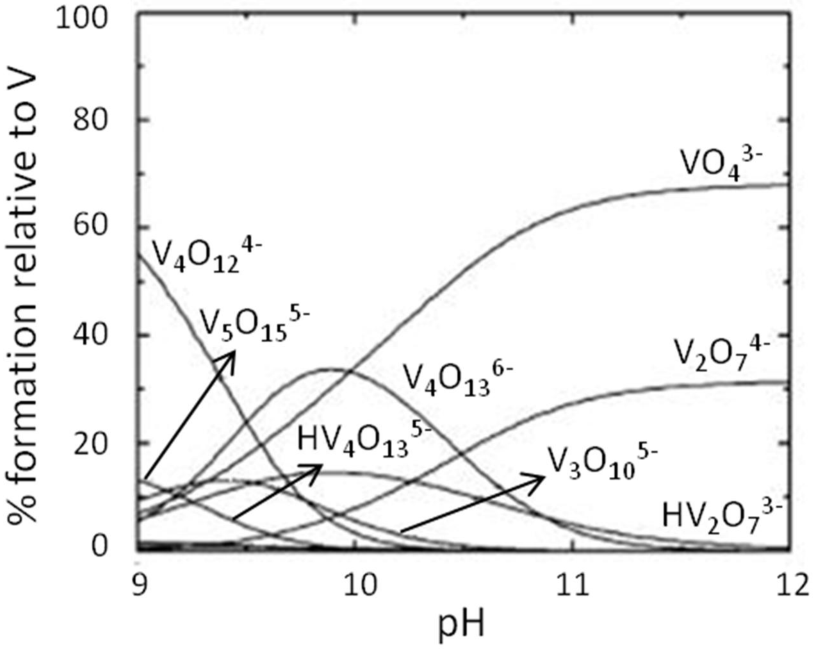

Figure 3.17: Calculated oxovanadate speciation profile when in an aqueous solution.[35] Reproduced with permission from Baruah. B, Crans. D.C and Levinger. N, *'Langmuir'*, 2007, 23(12), 6510-8. Copyright © 2007, American Chemical Society

Typically in bulk solution, only V_1 and V_2 are observed. However when Baruah dispersed the solution into reverse micelles, a majority of V_3 and V_4 were observed. The study highlighted that smaller aqueous fractions, and hence smaller reverse micelles have an increased proportion of higher vanadate oligomers, indicating a greater degree in the pH shift towards neutrality, compared to larger micelles. The corresponding ^{51}V NMR are presented in Figure 3.18. The increase in the trimer and tetramer signal, in addition to broadening of the monomer and dimer signals is obvious, as the aqueous fraction is reduced. The effect was considered to be due to a decrease in mobility and microfluidity, or increased viscosity thus enabling the formation of larger species.[35]

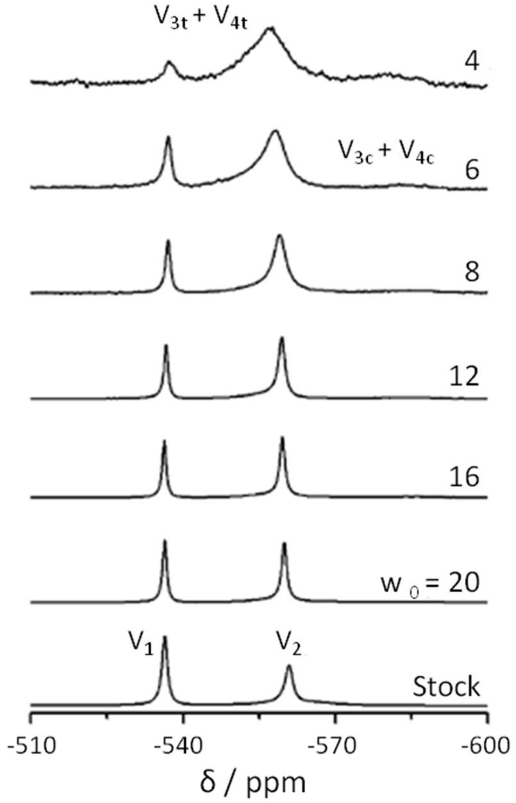

Figure 3.18: ^{51}V NMR spectra of oxovanadate species in AOT reverse micelles, originally prepared with pH 10.5 stock solution of ammonia metavanadate.[35]
Reproduced with permission from Baruah. B, Crans. D.C and Levinger. N, *'Langmuir',* 2007, 23(12), 6510-8. Copyright © 2007, American Chemical Society

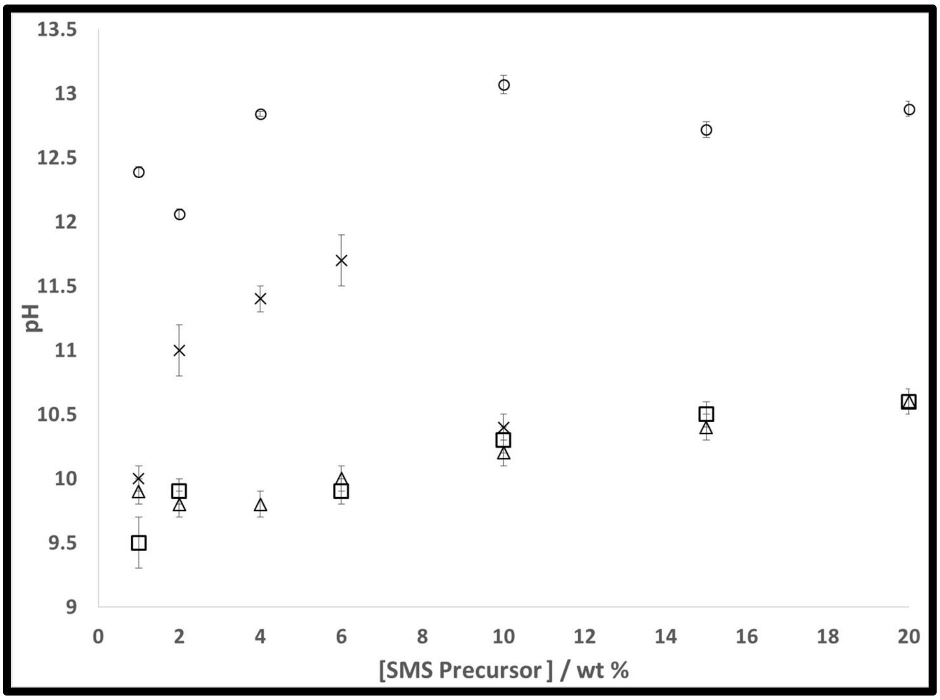

Figure 3.19: Graphical display of variation in pH with concentration of pH at various dispersed volumes within 2g of 30 wt %. TX-114/cyclohexane continuum: 10 µl (∆), 50 µl (□), 100 µl (x) and the comparable aqueous sodium metasilicate solutions (o).

With respect to variation of silicate concentration for a constant micellar size, a general increase in pH is observed as one would expect due to an increase in the fraction of silicate precursor. One must note that these measurements are merely a relative indication, however the results suggest that a lowering in the pH with respect to the aqueous silicate solution is observed. If the pH of the microemulsions are compared (Figure 3.16) one can see that providing the silicate concentration is above the solubility limit, in the pH range 9-10 SiO_2 formation is possible. To understand the effect of the precursor concentration upon the equilibrium pH, Baruah *et al.*[35] maintained the number of probe molecules per micelle, in addition to the overall concentration, as the micellar size was varied. ^{51}V NMR highlighted the presence of a significant number of higher order oligomers (V_3 and V_4), indicating that the concentration of vanadate has a negligible effect on the equilibrium pH obtained.[35]

3.7.3 Solubility

The above observations regarding variation in speciation with pH are supported by the change in solubility of all silica phases with variation in pH. In particularly at pH > 10, a rapid increase in solubility of all silica phases is observed. (See Figure 3.20 below) This dramatic increase is associated with the formation of silicate monomers ($SiO_2(OH)_2^{2-}$, $SiO(OH)_3^-$ and $Si(OH)_4$ as described previously.[2] With limited initial concentrations of silicate precursor, one must note the greater significance of the observed reduction of the pH within the microemulsion, with respect to the aqueous solutions, since it is this that raises the supersaturation and enables crystallisation to occur.

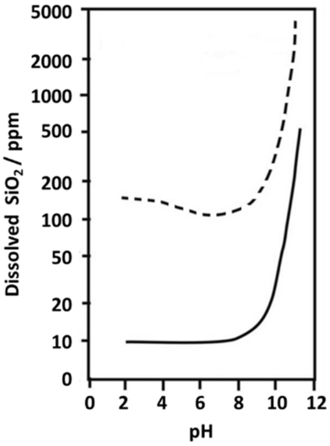

Figure 3.20 Change in the solubility of quartz (solid) and amorphous (dashed) with pH.[36,]

3.7.4 Confined or restricted growth

Visual comparison of the bright field (BF) images presented in Figures 3.13-3.15 above, suggests that upon increasing the concentration of precursor, no further growth beyond the ~2 nm dimension is observed for any SMS precursor concentrations. This directs ones thinking towards the idea that upon the addition of further precursor material, nucleation dominates over crystal growth. Moreover, it is worth noting that the size of the nanoparticles are comparable to, and hence appear to be restricted by the size of the microemulsion droplets.

Drawing on the research by Fedeyko *et al.* and Rimer, [37,15] one can attempt to rationalise this observation. Fedeyko *et al.* summarised the formation of silica nanoparticles as conforming to general characteristics of self-aggregating systems such as surfactants: spontaneous formation and a start-stop aggregation where the addition of further precursor will promote nucleation of further nanoparticles with similar properties over growth of the existing particles.[37] They further added that silica based precursors have a critical aggregation concentration similar to a critical micellar concentration whereby below such a value silica is observed as simple monomers and oligomers and above which silica forms nanoparticles of uniform size in solution, further showing that the formation of silica cannot solely be reliant on condensation chemistry.[37] Rimer *et al.*[15] expanded upon this, presenting a study on the phase stability of nanoparticles in the 3-10 nm range, with a minimum in free energy of formation associated with the condensation of nanoparticles of uniform size (< 5 nm). Rimer suggests the formation of an electric double layer surrounding the nanoparticle at the interface between the solid and liquid phases is associated with contributions to the free energy of formation, which is second in magnitude only to the formation of the Si-O-Si bonds, and it is this that limits further growth. For our microemulsions, the confining surfactant layer, though relatively fluid, will also certainly restrict further growth.

3.8 Estimation of silica concentration within the droplet

SAXs measurements were performed to determine an approximate droplet size via GIFT analysis. This procedure will be discussed further in Section 3.8.3. However, assuming the droplet size remains independent of the SMS precursor concentration, one can estimate the average number of silica molecules per droplet to be expected for a completely mono-disperse system, see Table 3.4.

SMS precursor concentration (wt %.)	**Mean number of silica units per droplet – 10 µl/2g**
1	0.02 ± 0.01
4	0.07 ± 0.01
6	0.11 ± 0.01
10	0.19 ± 0.01
15	0.28 ± 0.01
20	0.37 ± 0.01

Table 3.4: Estimation of the nominal mean number of silica molecules residing in the microemulsion droplets (based upon the GIFT-determined estimation).

This approximation indicates that most droplets contain no silica molecules so there appears to be insufficient precursor present to allow the precipitation of silica within any one droplet based on the solubility of silica phases. One can rationalise the observation of crystalline nanomaterial being observed by TEM, primarily by a degree of polydispersity among the droplets within the microemulsion, with further suspected contributing factors. Larger droplets are expected to contain a larger number of silica molecules so that the largest may support quartz nucleation. Secondly, the exchange of material to promote further growth beyond the nucleation stage is supported by the occurrence of transient dimer formation between energetic colliding droplets as detailed in Chapter 1. Moreover, a relative increase in the SMS concentration and hence supersaturation within the microemulsion, with respect to the SMS aqueous solutions is expected due to the ability of the hydrophilic portion of the surfactant to structurally bind and perturb a number of water molecules from the free aqueous pool. Previous publications suggest that an estimated 1-3 water molecules can bind to a given ethylene oxide group, whilst Schott and Royce[2] suggest that for small spherical non-ionic micelles, between 0.4 and 6.5 water molecules may be perturbed by an ether linkages, however the exact number depends on the weight fraction of water.[38]

Work completed by Garti *et al.*[38] illustrates this dependence using DSC measurements, evaluating the behaviour of inter-phasal and free water within a ethoxylated fatty alcohol non-ionic microemulsion system. One can see from Figure 3.21, below ~30 wt %. total water content, no water exists in the free aqueous pool, it is all bound to the surfactant and hence is interphasal water. An increase in the total water content is associated with a linear increase in the interphasal water proportion up to 30 wt %. Beyond this weight fraction of water, a reduction in interphasal water is observed, with a linear increase in the free water proportion.

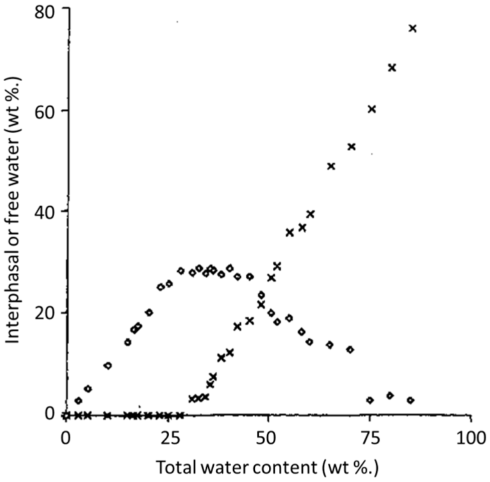

Figure 3.21: Graphical representation to illustrate the dependence of the fraction of free water on the total water content within a microemulsion system. x : free water and ◊: interphasal water. [38] Reproduced with permission from Yaghmur. A, Aserin. A, Tiunova. I and Garti. N, *'Journal of Thermal Analysis and Calorimetry',* 2002, 69, 163-177. Copyright © 2002, Kluwer Academic Publishers/Akadémiai Kiadó

Garti's findings may be applied to the system in question as TX-114 (t-Oct-C_6H_4-$(EO)_{7\text{-}8}OH$) has a comparable number of ethylene oxide groups, i.e. 7-8 to the $C_{12}(EO)_8$ used in Garti's investigation.

For the TX-114 system utilised for this investigation, the total water content is varied between 0.5 – 5 wt %. It can be inferred that all water molecules are structurally perturbed by the surfactant, leaving no free aqueous pool. As such an increase in the relative supersaturation invokes a more defined concentration gradient, and hence a more efficient transfer of material may occur during transient dimer formation. This theorem supports the observation of precipitation of small nano-particulate materials from initially undersaturated bulk systems.

3.8.1 Effect of increased variation of SMS precursor concentration

As the concentration of SMS precursor is increased to and beyond 10 wt %. within the dispersed phase, two metastable silica phases, cristobalite and amorphous silica are observed in addition to the nanoparticles of the thermodynamically stable quartz form. As theoretically predicted in Chapter 1, the concentration of the precursor has a significant effect on the polymorph or allotrope obtained. Precipitation of the most stable form is favoured when crystallisation is just deemed possible, i.e. when there is only just sufficient material present to form near stable nuclei of the thermodynamically most stable form. Increasing the supersaturation beyond this point allows metastable forms to also produce near stable nuclei, and a greater rate. Thus despite the nanoconfinement, the surplus material helps promotes kinetic control, hence thermodynamic control is lost, allowing the formation of metastable nanocrystals.

Cristobalite is a metastable crystalline polymorph which is stable at higher temperatures within the range of 1743 – 2001 K. A local cluster of cristobalite consists solely of 12 less densely packed 'oval' distorted 6-membered SiO_4 tetrahedra rings stacked in a ABCA order, as illustrated in Figure 3.2.[1,39] Cristobalite is one of the least densely packed forms due to the rigidity of the almost planar 6-membered rings, with a density of 2.33 g/cm^3 at 20 °C, whereas amorphous silica is a metastable non-crystalline polymorph of silica which lacks topological order beyond the dimensions of ~ 20 Å.[39]

Comparing these two metastable forms to quartz, the most stable polymorph under ambient conditions, a quartz local cluster consists of both 6 6-membered and 40 8-membered rings. The 8-membered rings are highly convoluted, folding back upon themselves and thus are packed more densely (2.65 g/cm^3 at 25 °C) than is possible for the 6-membered rings. Further, the presence of the higher ordered ring structures gives rise to an increased number of tetrahedra for a given cluster, 63 for the case of quartz. This is presented in Figure 3.2 a.[1] Essentially the size of the cluster, alongside the orientation and size of the composing rings, distinguish the silica forms.

Moving back to Figure 3.22-24a – c below, it may be noted that the metastable forms are observed to typically grow to much larger sizes (> 5 nm – 1 μm) compared to the 2 – 5 nm quartz nanoparticles consistently observed at lower concentrations of SMS precursor. This may be a result of the metastable forms initially growing from droplets in the larger size of the polydisperse microemulsion distribution.

Regardless of the polymorph of silica present, Zhang *et al.*[14] who demonstrated a comparable microemulsion silica synthesis route, documented that upon increasing the concentration of silicate precursor, 'the particle size increased significantly.'[14] Furthermore, Zhang *et al.*[14]contributed the size of the silica particles was 'also dependent upon the pH of the microemulsion system,' whereby those 'formed at pH 11 were more uniform and dense than those prepared at pH 2.'[14]

At high SMS precursor concentrations and larger aqueous volume fractions, the pH of the system is comparable to the unconfined highly alkaline SMS solution. Thus one could imply for larger concentrations of SMS precursor and droplet sizes one would expect large spherical structures, resulting from the occurrence of the ionic species $Si(OH)_5^-$ due to the adsorption of hydroxyl ions onto $Si(OH)_4$ which then induces repulsion of similarly charged species. Figure 3.24c illustrates that for high SMS precursor concentrations of 20 wt %. large spherical silica species are obtained. Conversely, for low pH systems there is an increase in monomeric $Si(OH)_4$, which bears no charge thus potentially allowing aggregation, particularly at higher concentrations of SMS in accordance with Zhang *et al.*[14]. Such could be implied to cases of lower SMS precursor concentrations and small aqueous volume fractions, where basic pH studies indicated that a greater shift towards neutrality was observed.

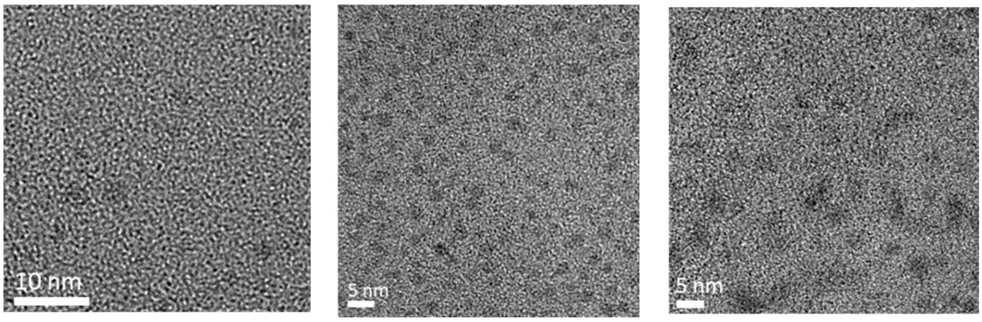

Figure 3.22 a, b and c: HREM of representative quartz material produced from a TX-114/cyclohexane microemulsion with 10 µl/2g a:2 wt %, b:4 wt % and c: 6 wt % SMS precursor.

Such can be depicted in the images above, whereby the volume fraction of aqueous phase remains constant whilst the concentration of precursor increases progressively from 2 – 6 wt % of SMS. The degree of increasing aggregation of particles is apparent from left to right of Figure 3.22 concurring with Zhang *et al.*'s[14] findings, although it is also possible that the aggregation occurred as the microemulsion aliquots placed on the holey carbon TEM grids dried.

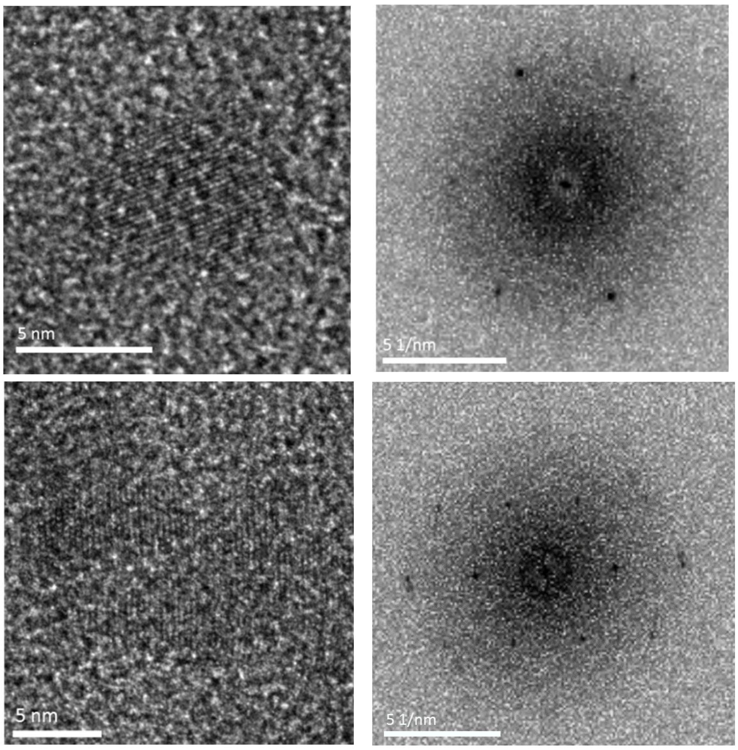

Figure 3.23 a-d: a and b: HREM and FFT images of a representative quartz nanocrystal, c and d: HREM and FFT images of representative cristobalite material produced from a TX-114/cyclohexane microemulsion with 10 µl/2g 10 wt %. SMS precursor.

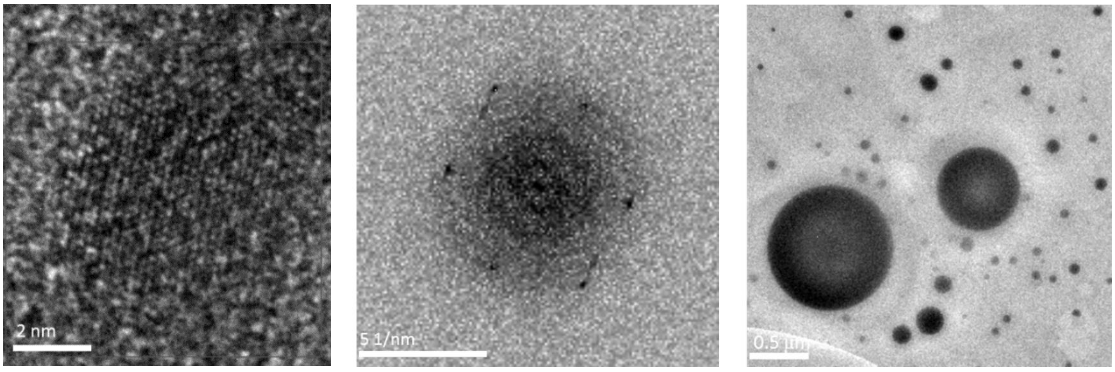

Figure 3.24 a-c: a and b: HREM and corresponding FFT images of representative material produced from a TX-114/cyclohexane microemulsion with 10 µl/2g 15 wt % and c: BF image of representative material from a 20 wt %. SMS precursor microemulsion.

The literature regarding the synthesis of silica from a silicate precursor upon the addition of an acid is heavily dominated by Jesionowski[40-41] whom typically adopts a w/o emulsion system consisting of non-ionic surfactants: Rokafenol N-5, N-6 and N-9 (nonylphenyl polyoxyethylene glycol ethers), where Rokafenol is of the form:

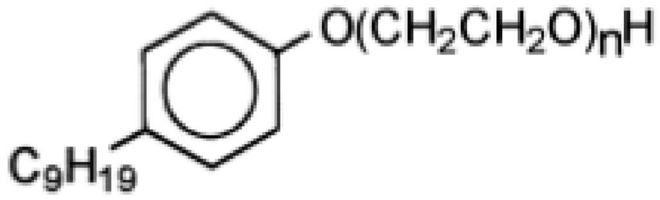

where mean $n = 5$, 6 or 9.

Figure 3.25 Rolafenol molecular structure [40-41] Reproduced with permission from Jesionowski. T, '*Colloids and Surfaces A: Physicochem. Eng Aspects'* 2001, 190(1-2), 153-165 Copyright © 2001 Elsevier Science B.V.

Such a non-ionic surfactant can be deemed comparable to that of TX-114 utilised in this investigation. Moreover, an identical oil phase of cyclohexane was employed. An analogous procedure was followed whereby two separate emulsions were obtained; an SMS emulsion and either a sulphuric acid emulsion or a hydrochloric acid emulsion[40-41], prior to mixing. Note, however that continuous stirring was employed. In all cases amorphous silica was obtained, with a spherical morphology, see Figure 3.26.

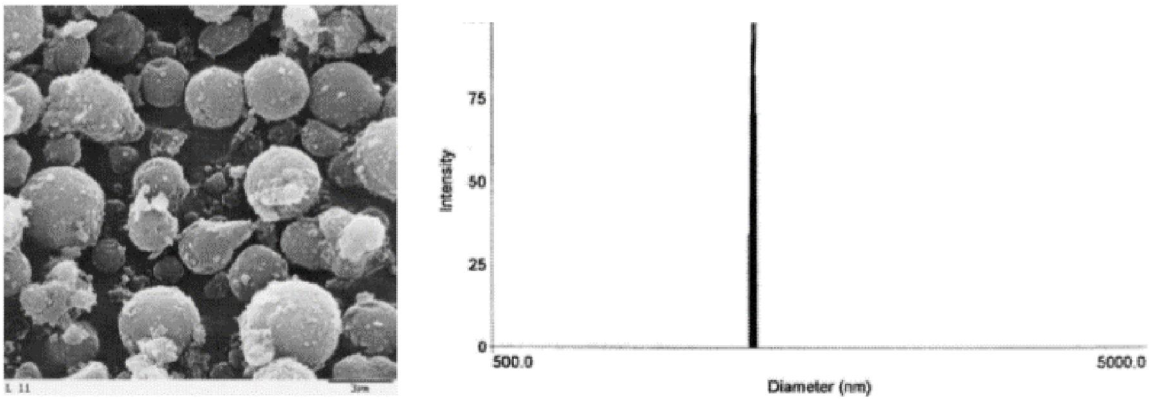

Figure 3.26 a and b: SEM and Laser Doppler electrophoretic light scattering characterisation of silica particles synthesised from Rolafenol/cyclohexane emulsions.[41] Reproduced with permission from Jesionowski. T, '*Colloids and Surfaces A: Physicochem. Eng Aspects'* 2001, 190(1-2), 153-165 Copyright © 2001 Elsevier Science B.V.

One can summarise that precipitation of amorphous silica has two contributing factors: the use of a metastable macroemulsion vector and high precursor concentrations. Primarily the macroemulsion is incapable of providing the necessary thermodynamic control required to ensure the precipitation of the most stable quartz form.

K. Zhang *et al.*[14] moved closer to the 'ideal' of a microemulsion system, utilising a non-ionic NP-5/NP-9 surfactant in petroleum ether or cyclohexane, with a SMS aqueous phase and hydrochloric acid precipitator in reverse bicontinuous microemulsions. Such experimentation yielded amorphous nano-sized silica particles typically in the order of 1-15 nm of varying morphologies as discussed previously. Zhang *et al'*s[14] study limited the SMS precursor concentration, however the use of a bicontinuous microemulsion failed to ensure the 3D nano-confinement encapsulation of the precursors that is essential to ensure the attainment of thermodynamic control over the process.

In a comparable study, Wang *et al.*[42] presented similar findings whilst studying the formation of amorphous silica nanoparticles from a sodium silicate precursor, within a comparable w/o Triton/cyclohexane emulsion. Further to understanding the optimum conditions for the preparation of SiO_2 particles, Wang explores the effect of temperature, alcohol co-surfactant chain length and the Na_2SiO_3 precursor concentration, particularly focussing on the effect upon emulsion stability.

3.8.2 Effect of varying the dispersed volume

Figure 3.12 presents a graphical view of the effect of varying the aqueous fraction upon the phase stability of the TX-114/cyclohexane system. It can be interpreted that for an increasing concentration of SMS precursor, only smaller volumes of dispersed aqueous phase are able to be stabilised by the surfactant. Figures 3.27 and 3.28 reveal TEM data obtained from microemulsion samples of 4 wt % SMS precursor, with differing volumes of dispersed phases: 10 μl and 50 μl/2g.

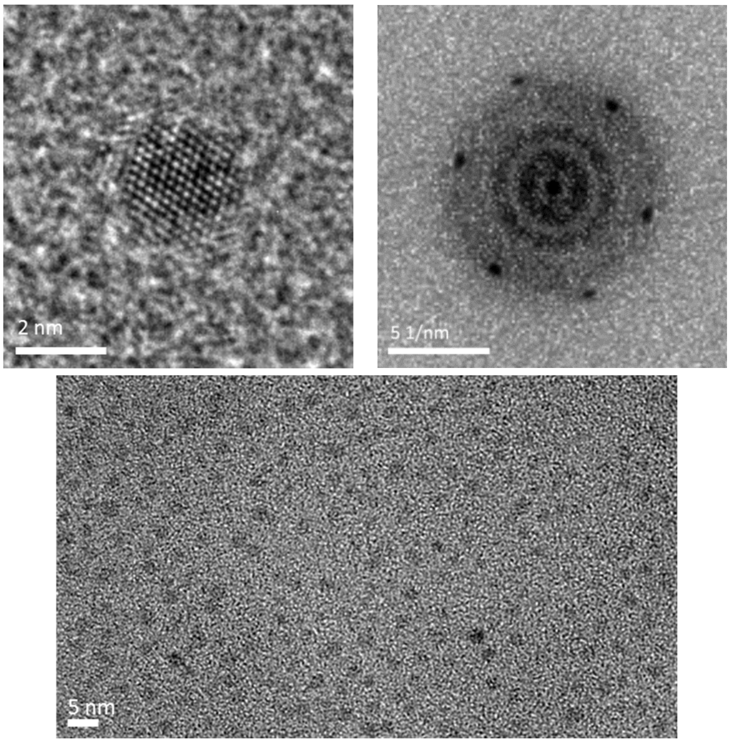

Figure 3.27: a and b: HREM and FFT of a representative quartz nanocrystal indexed to be the [212] zone axis of quartz and c: BF image of representative material from a TX-114/cyclohexane microemulsion with 10 µl/2g 4 wt %. SMS precursor.

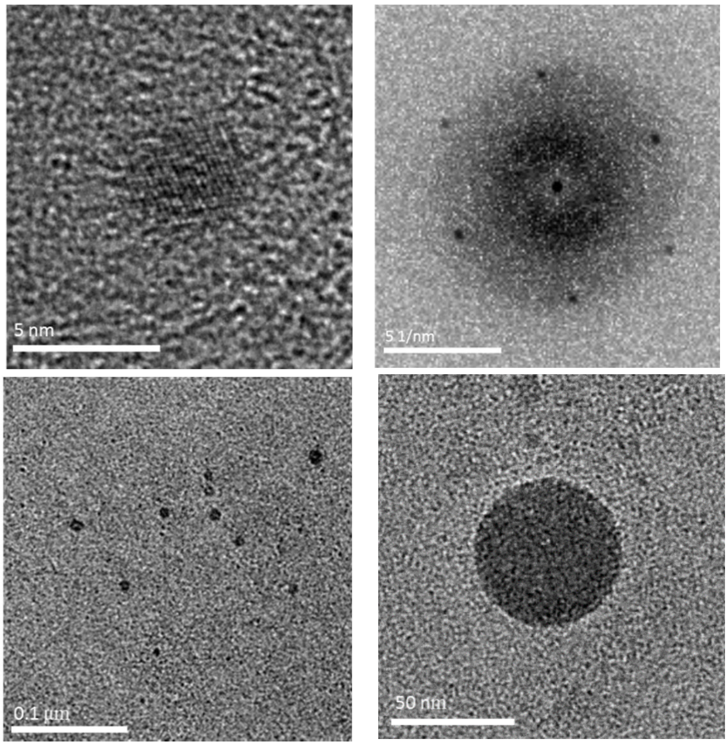

Figure 3.28: a and b: HREM and FFT of a representative quartz nanocrystal indexed to be the [212] zone axis of quartz and c and d: BF images of representative material from a TX-114/cyclohexane microemulsion with 50 µl/2g 4 wt %. SMS precursor.

Comparisons of the data for the two samples shows a change in the majority polymorph produced from the microemulsion, from the stable quartz to a metastable amorphous phase, with an increase in dispersed volume from 10 to 50 µl/2g. Upon the addition of 10 µl of dispersed phase, 2-5 nm quartz nanoparticles are the sole precipitate, whilst for the 50 µl case the metastable amorphous silica phase dominates in the form of much larger spheres, together with a minority of quartz nanoparticles with a size comparable to the corresponding confinement. This observation supports the hypothesis that the interface of the microemulsion droplets may act as a layer to retard the growth of the nanoparticles beyond the confinement. Furthermore comparing Figures 3.27 and 3.28 indicates that larger droplets tend to generate fewer sites of precipitation, with the metastable forms being of larger dimensions. One can rationalise this finding by contemplating the competition of Brownian motion controlled collisions of the microemulsion droplets with the probability of them momentarily forming a transient dimer to allow material exchange.

Typically the motion of the microemulsion droplets is controlled by Brownian motion, which can be defined as the random movement of a species within a gas or liquid which is guided by collisions with molecules in the surrounding medium. Hence, as both systems are held at the same temperature, recalling kinetic theory where the energy can be approximated to ${}^{3}\!/_{2}\, k_b T = {}^{1}\!/_{2}\, m v^2$, where m is the mass and v is the velocity of the particle in question, it is apparent that smaller microemulsion droplets will move with a larger velocity due to their inherent lower mass, and thus will typically collide more frequently in comparison to a system composed of larger species. Furthermore, as established from the droplet size approximation, one can see that there are around 3 times as many droplets per gram of microemulsion for the case of the smaller dispersed phase.

However countering the frequency of the collisions is the theory of film rigidity, which is based on the interfacial free energy or the change in the free energy associated with a change in film curvature, such as during transient dimer formation. Gradzielski[44] followed by Eastoe[43] mathematically summarised the relationship for spherical droplets as:

$$\frac{F}{A} = 2K(\frac{1}{R} - \frac{1}{R_0})^2 + \frac{\underline{K}}{R^2} + \left[\frac{k_B T}{4\pi R^2} f(\varphi)\right]$$

Where F is the total free energy, A is the interfacial area ($n4\pi R^2$), K and $\underline{K}$ are both bending moduli or elastic constants, R is the radius of curvature and R_0 is the spontaneous radius and $f(\varphi)$ is a function which accounts for the entropy of mixing of the droplets, approximated to $[\ln(\varphi) - 1]$ for dilute solutions, where φ is the core volume fraction.[43-44]

Hence for the formation of a transient dimer structure, a change in the curvature and thus radius of curvature, R occurs, for which there will be an associated change in the free energy. As R is a measure of the droplet size, it is clear that a larger free energy barrier is to be surmounted for a greater relative change to the curvature, or smaller R values. Therefore the collision of smaller droplets is less likely to result in the formation of transient dimers. So although larger droplets will collide less frequently, transient droplet dimer formation is more probable and thus material exchange and crystal growth is promoted.

Hence, it is apparent that smaller dispersed volumes will promote a significantly greater number of small precipitation sites, relative to a system composed of larger droplets where transient dimer formation and hence material exchange is more favoured.

3.8.3 SAXS analysis and geometric droplet size

The particular droplet structure for a given aqueous/surfactant/oil system can be deconvoluted and evaluated using the program DECON[50-51] to produce a radial electron density profile provided the droplets are sufficiently spherical and monodisperse. However simply calculating and comparing the electron density of the neighbouring components of the micelle allows the shape and internal structure to be predicted. The electron densities of each of the components or phases are displayed in Table 3.5.

Component	**Electron density / Å^{-3}**	**Electron density relative to the cyclohexane continuous phase / Å^{-3}**
Water	0.33	0.06
SMS	0.30	0.03
TX-114 head groups $(C_2H_4O)_{7.5}OH$	0.35 – 0.37	0.08 – 0.10
TX-114 tail groups	0.27 – 0.29	0.00 – 0.02
Cyclohexane	0.27	0

Table 3.5: The electron densities of the components of the microemulsion .A range is given based upon the likely density range of the surfactant.

The electron density of the dispersed phase may be determined entirely by the relative concentrations of its components. For the SMS concentrations considered in this study, there is only a minor change to the electron density of the aqueous phase.

If the baseline electron density is taken to be that of the cyclohexane continuum, one can see that taking the centre of the micellar core as an arbitrary point and moving radially outwards towards the continuum, no change in sign of the relative electron density is observed. Thus the pair-distance distribution function, p(r), will show a single maximum. Also, there is very little electron density contrast in the system so that analysing the SAXS data using the GIFT software is prone to larger errors. To gain a more detailed perspective, the geometric prediction and GIFT prediction from the experimental SAXS data were computed to estimate the droplet size within the system upon the addition of 10, 50 and 100 µl/2g of surfactant and oil continuum. The scattering and pair-radial distribution functions obtained from the raw data and GIFT analysis, respectively, from SAXS experiments are presented in Figure 3.29.

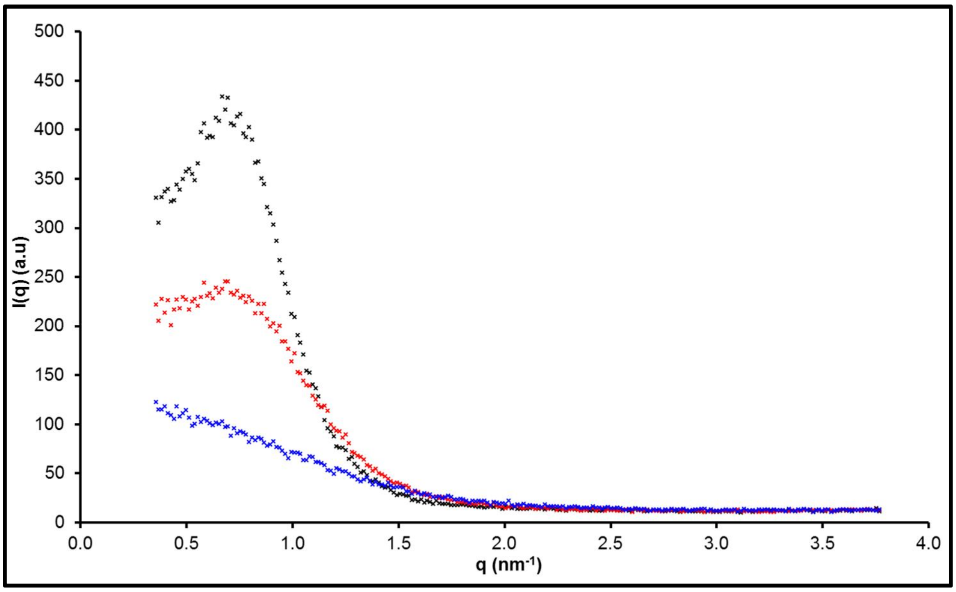

Figure 3.29 a: SAXS scattering function for dispersed 1% aqueous sodium metasilicate nonahydrate within a 30 wt %. TX-114/cyclohexane system. Blue: 5 µl/g, red: 25 µl/g and black: 50 µl/g.

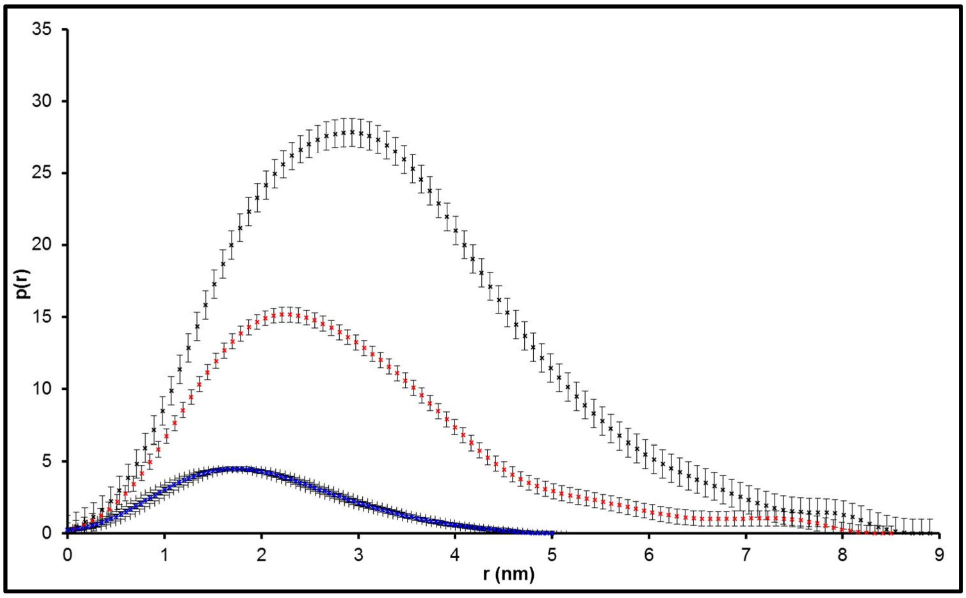

Figure 3.29b: Pair distance distribution function p(r) for dispersed 1% aqueous sodium metasilicate nonahydrate within a 30 wt %. TX-114/cyclohexane system. Blue: 5 µl/g, red: 25 µl/g and black: 50 µl/g.

The pair distance distribution p(r) curves generated from the scattering data in Figure 3.29a are obtained after the incorporation of a hard sphere structure factor in the GIFT analysis. This is included in order to account for the interdroplet interactions This p(r) distribution function can be interpreted as a measure of the probability of the distances inside the droplet, summing over all sizes, and hence provides further information regarding the size, shape and inner structure.[45] However note that the surfactant tails have essentially the same electron density as the cyclohexane continuous phase, and hence only the size of this hydrophilic core can be reliable determined. The surfactant tails may be contributing to the elongation of the p(r) curves at higher r values, since a spherical hydrophilic core would produce a more symmetrical p(r) curve. From Figure 3.29b, there is an apparent increase in droplet size is seen to accompany an increase in the volume of dispersed phase.

Utilising the GIFT software package, the radius of gyration, R_{gyr} can be determined, and used to compute the hydrophilic core radial, $R_{core.}$ The two dimensions are related as follows: $R_{gyr}^2 = \frac{3}{5}R_{core}^2$, for the case of a simple sphere model. The approximate diameter of the hydrophilic core can be determined from the point where the p(r) function returns to zero though this is subject to a large error as there may be small contributions from the surfactant tails.

From Figure 3.29a and b, an apparent increase in droplet size is seen to accompany an increase in the volume of dispersed phase.

Dispersed volume / µl/2g	**10**	**50**	**100**
$R_{geometric - core}$ / nm (± 0.005 nm)	3.075	3.435	3.880
$R_{gift - core}$ / nm (± 0.3 nm)	2.0	3.0	3.4
% Difference geometric : gift	35	13	12
Average surfactant tail length (nm)	1.5		
Volume of aqueous phase / nm^3 (± 0.5 nm^3)	1.0	15	38
Number of droplets per gram of microemulsion (x 10^{18})	10	3.4	2.6
Number of water molecules per droplet	33	492	1269
Number of surfactant molecules per droplet	33	97	121
Mass of silica per droplet / g (1% SMS)	1.9 x 10^{-24}	2.9 x 10^{-23}	7.6 x 10^{-23}
Average number of silica molecules per droplet (1% SMS)	0.02	0.30	0.80

Table 3.6: Prediction of droplet dimensions using geometric and GIFT calculations

Discrepancies between the two predictive GIFT and geometric approximations for Rcore are seen for all dispersed volumes. This difference between the two predicted values is believed to arise from inherent errors from a variety of origins associated with the two approximation models. Primarily the geometric approximation is solely a mathematical model which assumes all of the specified components reside in their expected phases. The accuracy of the GIFT analysis is limited by the poor electron density contrast.

3.8.3.1 Water perturbation

It has been previously highlighted that the outcome of the crystallisation can depend on the droplet size, particularly the water pool size. For small or negligible free water pools, crystallisation may be forced to occur close to the surfactant interface and thus templating by surfactant may dominate. Furthermore at high surfactant:water ratios a high supersaturation may lead to rapid nucleation and less-organised nanocrystals. Thus one must calculate the quantity of water within the aqueous phase that is structurally perturbed by the surfactant interface. Numerous values have been reported regarding the number of water molecules perturbed due to ethylene oxide groups in PEO structures such as TX-114. However, Qi and Ma[46] observed in the degree of hydration of PEO chains, beyond W = 5.3 a free water pool is observed, suggesting a TX-100 molecule can bind to 5.3 water molecules.[46] The calculation of the depth of the hydration layer is based on Qi and Ma's value due to the similarities in the TX-100 and TX-114 surfactant structure. Due to the reduced number of PEO groups for TX-114, one TX-114 molecule is expected to bind to 4.2 water molecules. Table 3.7 shows how the amount of free water varies with a change in radial size of the micelles.

Dispersed volume / µl/2g	**10**	**50**	**100**
$R_{GIFT-core}$ / nm (± 0.3 nm)	2.0	3.0	3.4
Number of droplets per gram of microemulsion (x 10^{18})	10	3.4	2.6
Number of water molecules per droplet	33	492	1269
Number of surfactant molecules per droplet	33	97	121
Water taken by TX114 per droplet	≥33	408	508
Fraction of water bound to TX114	1.00	0.83	0.4

Table 3.7: Estimation of perturbed water molecules by surfactant from GIFT radii.

As shown in the table, when the dispersed phase is increased from 10-100 µl/2g and r from 2.0 to 3.4 nm, the percentage of water molecules perturbed by the surfactant layer decreases from ~100 % to ~ 40 %. This reveals, as expected, an increase in the free-water pool size with dispersed volume.

3.9 Span80/Brij30/heptane system

Following the detailed investigation into the crystallisation of silica from within the TX-114/cyclohexane system, a further surfactant/oil system will be considered briefly as a comparison in Section 3.5, to ensure that the observed phenomena cannot be attributed to an effect such as surfactant templating.

3.9.1 Microemulsion preparation

Aqueous sodium metasilicate nonahydrate (SMS) was dissolved in UHQ water at 0.25 and 20 wt %. 2 g aliquots of the 30 wt % 1:1 Span 80: Brij 30 surfactant solutions in heptane were prepared and sonicated until homogeneous, to which the aqueous SMS was added and dispersed. The microemulsions had a decreased viscosity compared to the surfactant components, however were more viscous than the aqueous phase. Microemulsions were left for varying degrees of time (1 hour – 3 years) before analysis was performed.

3.9.2 Microemulsion experiments

Using the 3D nanoconfinement of microemulsion droplets, the following variables were investigated and are discussed in this chapter: the effect of the concentration of precursor and the droplet size upon nucleation, precipitation and crystal growth and/or aggregation will be discussed below in Chapter 3, with the effect of the addition of HCl upon the process will be discussed in Chapter 4 via TEM analysis of selected samples.

3.10 Span80/Brij30/heptane: Results and discussion

To determine the range over which 3D confinement within the microemulsion is maintained, a series of systematic experiments, varying the concentration of aqueous SMS alongside the droplet size of the dispersed phase were completed. The range of concentrations and volumes stabilised are illustrated in Figure 3.30. It can be seen that for an increasing concentration of SMS precursor, smaller volumes of dispersed aqueous phase are only able to be stabilised by the surfactant. Indeed, despite SMS being readily soluble in water, from initial studies, supersaturated solutions often initiated immediate destabilisation of the microemulsion. This may be due to a number of factors including: perturbation of water molecules by the surfactant or altered pH levels within the dispersed phase.

3.10.1 40 wt %. 1:1 Span 80: Brij30/heptane microemulsion system

In addition to the phase diagrams presented in Section 3.4.4, the macroscopic observations of this heptane: water: 1:1 Span80:Brij30microemulsion system are documented, to show both the dependency on the concentration of the SMS precursor, the concentration of HCl and the volumes of dispersed phase. The effects will be discussed further.

As one would expect the material synthesised from the microemulsion is dependent upon a combination of both the SMS precursor concentration, the dispersed volume and the concentration of HCl added. SMS concentrations between 1 and 14 wt %. SMS were employed in the microemulsion system, however beyond 6 wt % SMS only 10 µl/2g could be stabilised by the specified surfactant combination. Similarly, no macroscopic precipitate was observed for any precursor concentration, hence TEM was utilised to image any nanoscopic material.

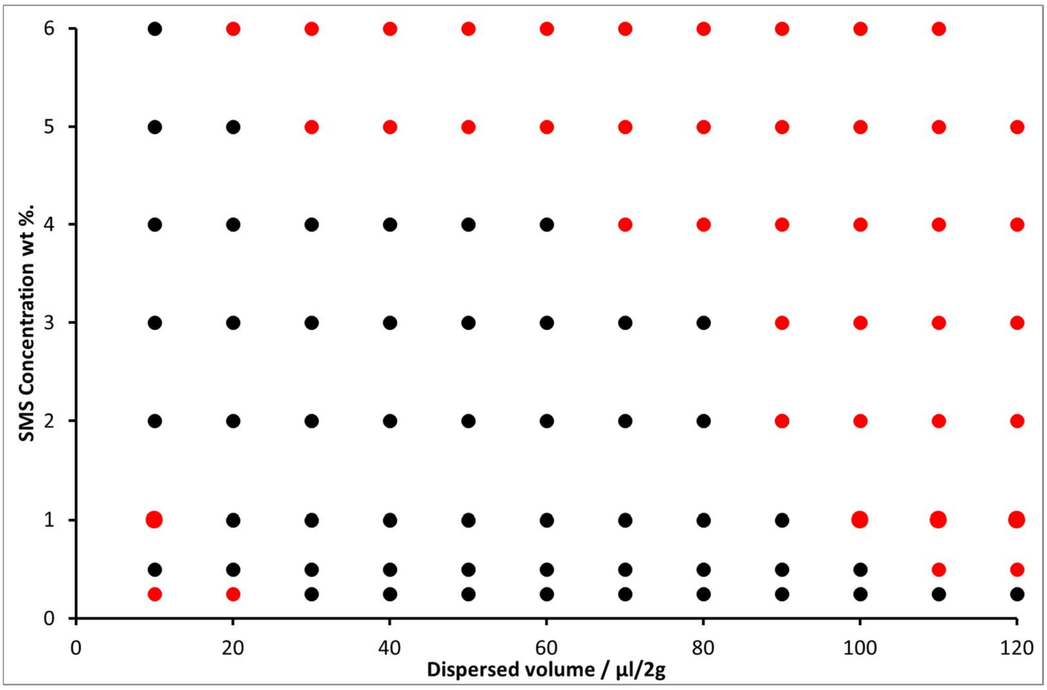

Figure 3.30 Graphical display of microemulsion compositions with varying SMS concentration and dispersed volume, and the effect upon the stability. Black = microemulsion and red = immediate precipitation of amorphous silicate phase.

3.10.1.1 pH

The effect of the pH of the Span 80/ Brij 30/ heptane system will be discussed in much greater detail in Chapter 4, where the effect of the addition of hydrochloric acid will be investigated upon both the precipitation outcome and the overall pH shift effect of the microemulsion.

However a brief summary of the pH measurements of the 40 wt %. 1:1 Span 80: Brij 30/heptane microemulsions are documented in Table 3.8.

40 wt %. 1:1 Span 80:Brij in heptane					
SMS (wt %.)	**Dispersed volume (μl/2g)**	**pH**	**SMS (wt %.)**	**Dispersed volume (μl/2g)**	**pH**
1	10	6.1 ± 0.1	5	10	6.3 ± 0.1
	50	6.0 ± 0.2		50	6.7 ± 0.1
	100	6.5 ± 0.1		100	6.9 ± 0.1

Table 3.8: Conventional pH probe measurements of 40 wt %. 1:1 Span 80 : Brij 30 /heptane microemulsions with SMS aqueous dispersed phases.

From Table 3.8 one can infer that for all dispersed phases, a move towards neutrality is observed with respect to the unconfined aqueous silicate solutions which have a pH in the range of 12-13. The pH measurement for the addition of a UHQ water dispersed phase to the Span 80/Brij 30/heptane composition is ~5.6. For all dispersed volumes, the pH readings show a significant shift towards the water only microemulsion (pH ~ 5.6) is observed. For higher SMS concentrations, and the largest droplet phase volumes, there is a minor reduction in the shift towards the water only microemulsion, due to the higher initial alkalinity of these droplets. Note a greater shift towards neutrality is observed for the Span 80/Brij 30/heptane compositions compared to the TX-114/cyclohexane compositions, one can rationalise this by a comparison of the two systems pH with the dispersion of water only. For Span 80/Brij 30/heptane the pH is ~5.6, whereas for TX-114/cyclohexane the pH is much higher at ~7.4.

3.10.1.2 Effect of varying the SMS precursor concentration.

SMS concentrations between 1 and 14 wt %. SMS were employed in the microemulsion system, however beyond 6 wt % SMS only 10 μl/2g could be stabilised by the specified surfactant combination. Similarly, no macroscopic precipitate was observed for any precursor concentration, hence TEM was utilised to image any nanoscopic material which is documented below.

Upon initial investigations, strong agreement with the observations presented for the TX-114/cyclohexane system can be concluded. From Figure 3.31-3.33 for a consistent dispersed volume, it is apparent that for precursor concentrations < 10 wt %. quartz particles of the order of 2-5 nm dominate. For 3, 5 and 7.5 wt %. SMS the bright field, high resolution and any corresponding fast Fourier transform (FFT) images are presented in Figures 3.31-3.33.

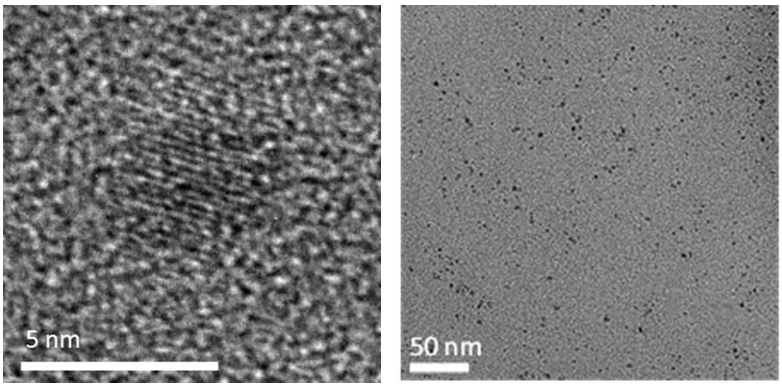

Figure 3.31 a and b: HREM and BF of representative quartz nanocrystals from a Span 80/Brij 30/heptane microemulsion with 10 µl/2g 3 wt %. SMS precursor.

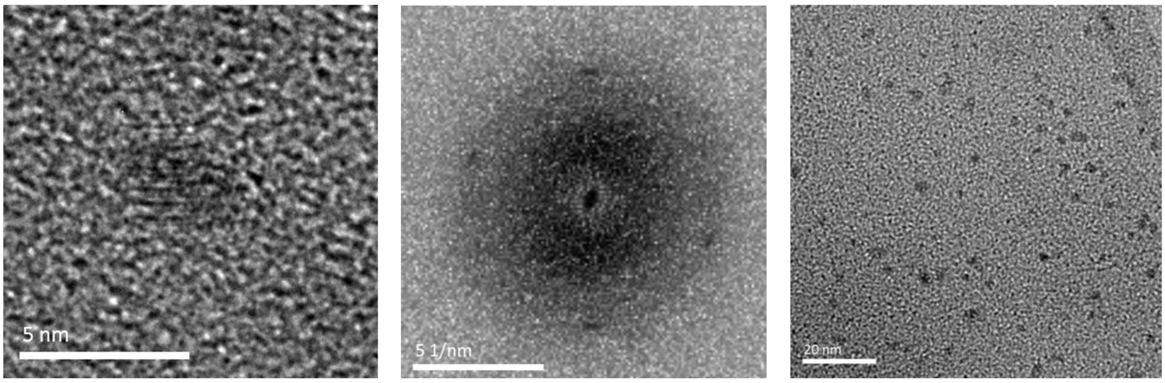

Figure 3.32 a, b and c: HREM, FFT and BF of representative quartz nanocrystals respectively from a Span 80/Brij 30/heptane microemulsion with 10 µl/2g 5 wt %. SMS precursor

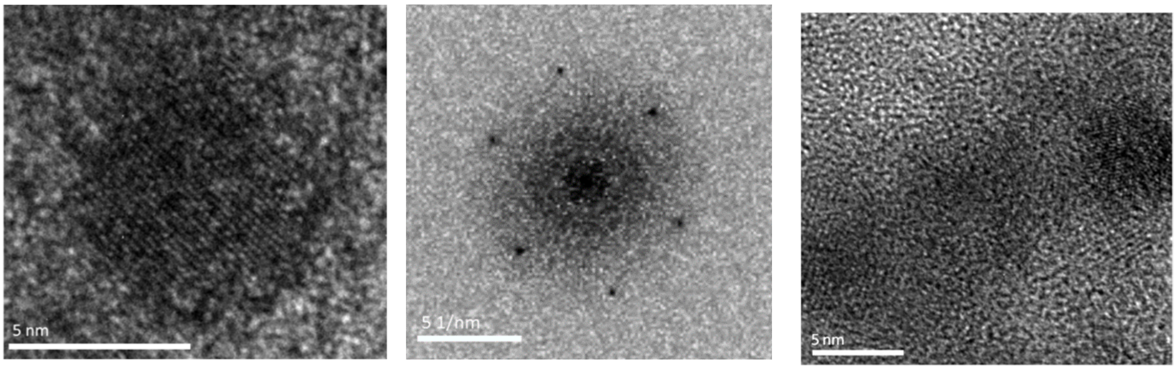

Figure 3.33 a and b: HREM and FFT, ([212] zone axis) of a representative quartz nanocrystal from a Span 80/Brij 30/heptane microemulsion with 10 µl/2g 7.5 wt %. SMS precursor.

Comparisons of the bright field and high-resolution (BF and HREM) images of the three samples show an associated increase in the quantity or density of nanoparticles precipitated with increasing precursor concentration; however no major change in the morphology or size of the aforementioned particles is observed. Each of the representative nanoparticles presented are seen to be around 2-5 nm which is a comparable size to that of the microemulsion droplet size. For the former two SMS precursor concentrations, only one or two sets of diffraction spots are observable and thus a zone axis may not be assigned. However for the case of 7.5 wt % the nanocrystals can clearly be identified as quartz nanoparticles exhibiting the [212] zone axis, as per the case of the TX114/cyclohexane system. Moreover, one can conclude that for the small dispersed volumes, the concentration of SMS precursor has little effect upon the precipitate morphology or size.

Again, it is apparent the thermodynamically quartz silica phase obtained from within the 3D-nanoconfinement is distinctly different to the amorphous phase precipitated from the unconfined aqueous silicate solutions.

For an increase in SMS precursor concentration to ≥ 10 wt %. SMS. The metastable phases, cristobalite and amorphous silica arise alongside the stable quartz nanoparticles. This is observed in Figures 3.34-3.36.

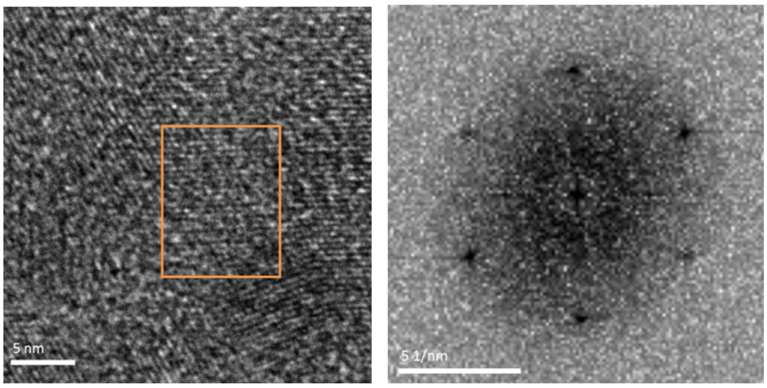

Figure 3.34 a and b: HREM and FFT, ([212] zone axis of quartz) of a representative quartz nanocrystal from a Span 80/Brij 30/heptane microemulsion with 10 μl/2g 10 wt %. SMS precursor.

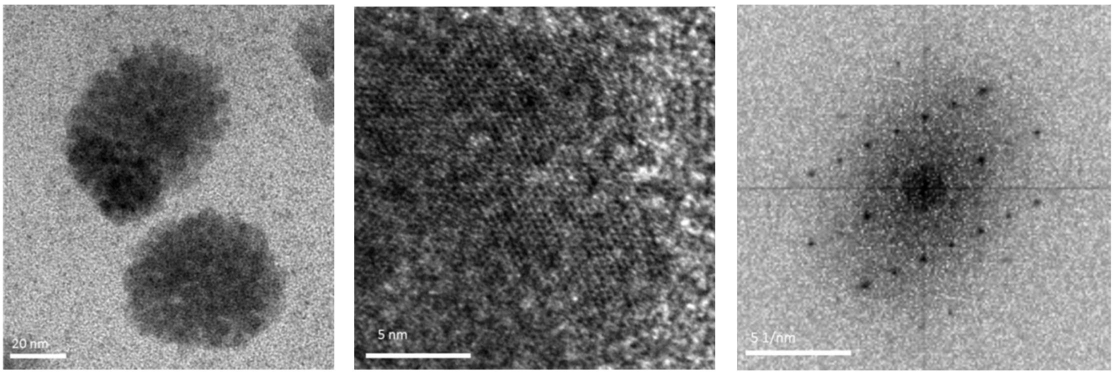

Figure 3.35 a, b and c: BF, HREM and FFT, ([110] zone axis) of representative cristobalite nanomaterial from a Span 80/Brij 30/heptane microemulsion with 10 µl/2g 10 wt %. SMS precursor.

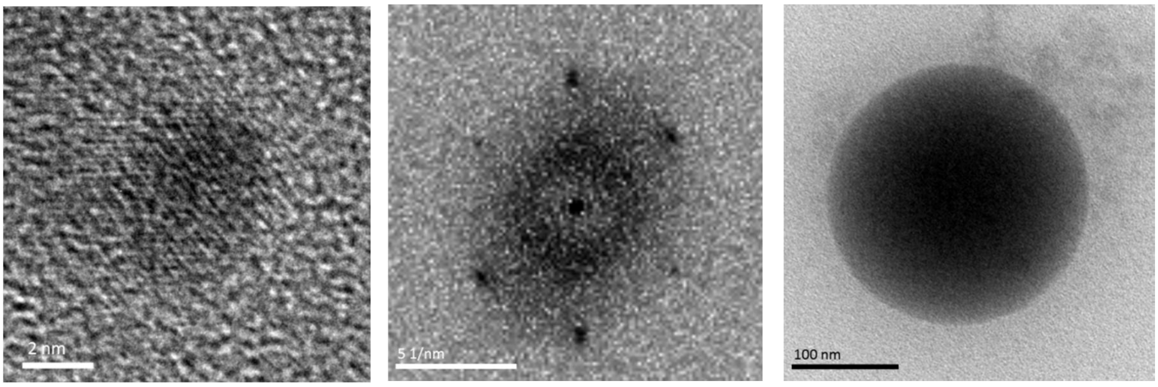

Figure 3.36 a and b: HREM and FFT, ([100] zone axis of nanoparticles of quartz and c: representative dominant metastable amorphous silica material from a Span 80/Brij 30/heptane microemulsion with 10 µl/2g 14 wt %. SMS precursor.

As per the previous case, one can rationalise this observation by noting an increase in the relative supersaturation level of SMS precursor within the droplets. Relating back to the free energy diagrams in Chapter 2, one can see that increasing the supersaturation beyond this point allows metastable forms to also produce near-stable nuclei, and at a greater rate. Thus despite the nanoconfinement, the surplus material helps promote kinetic control, hence thermodynamic control is lost, allowing the formation of metastable nanocrystals. Once again, the metastable material appears much larger than the stable quartz nanoparticles. The same rationale as the previous case can be applied, i.e. within a polydisperse system: the smaller droplets initially promote the formation of the stable form, whilst the larger droplets allow the formation of metastable forms.

3.10.1.3 Effect of varying the dispersed volume

Figures 3.37 and 3.38 reveal TEM data obtained from microemulsion samples of 1 wt % SMS precursor, with dispersed phases of 100 µl/2g which can be compared to samples displayed in the previous section in Figures 3.31 to 3.36 where the dispersed phase volume was only 10 µl/2g, but the SMS concentration was higher at 3 to 14 wt %.

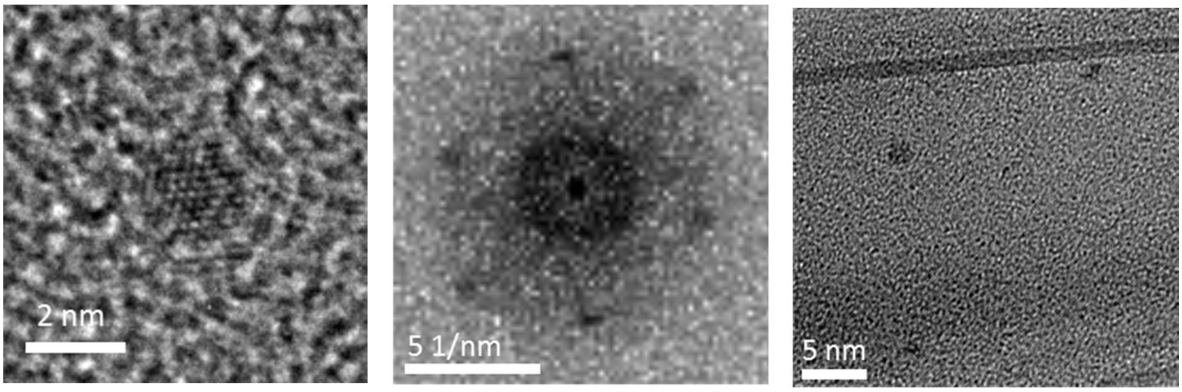

Figure 3.37: a, b and c: HREM, FFT (indexed to be the zone [201] zone axis) and BF of representative quartz nanocrystals respectively from a Span 80/Brij 30/heptane microemulsion with 100 µl/2g 1 wt %. SMS precursor.

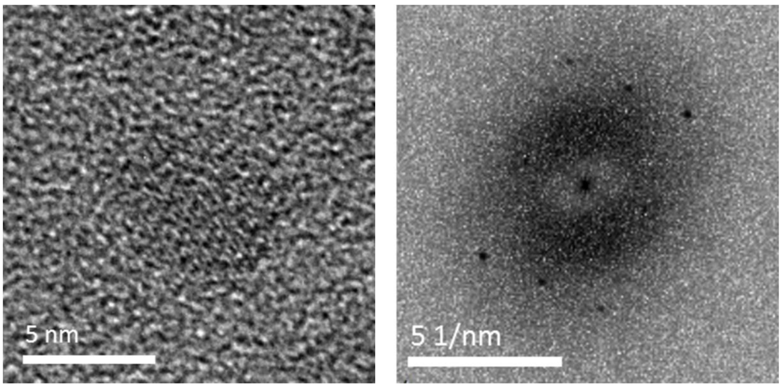

Figure 3.38: a and b: HREM and FFT of representative cristobalite nanocrystal from a Span 80/Brij 30/heptane microemulsion with 100 µl/2g 1 wt %. SMS precursor.

When the dispersed phase volume was only 10 µl/2g, nanoquartz was the majority phase for SMS concentrations up to 7.5 wt %, whereas at a dispersed phase volume of 100 µl/2g, cristobalite was produced along with nanoquartz even at SMS concentrations of 1%. This demonstrates again that larger droplets contain sufficient material to produce near-stable nuclei of metastable forms.

3.10.1.3.1 SAXS analysis and geometric droplet size

The electron densities of each of the microemulsion components or phases are displayed in Table 3.9.

Component	Electron density / Å^{-3}	Electron density relative to the heptane continuous phase / Å^{-3}
Water	0.33	0.09
SMS	0.30	0.06
Span 80 head groups	0.32 – 0.35	0.08 – 0.11
Span 80 tail groups	0.24 – 0.27	0.00 – 0.03
Brij 30 head groups $(OCH_2CH_2)_4OH$	0.32 – 0.37	0.08 – 0.13
Brij 30 tail groups ($C_{12}H_{25}$)	0.24 – 0.27	0.00 – 0.03
Average head groups	0.31 – 0.36	0.07 – 0.12
Average tail groups	0.23 – 0.27	0.01 – 0.03
Heptane	0.24	0

Table 3.9: The electron densities of the components of the microemulsion .A range is given based upon the likely density range of the surfactant.

If the baseline electron density is taken to be that of the heptane continuum, one can see that taking the centre of the micellar core as an arbitrary point and moving radially outwards towards the continuum, there is only a relatively minor change to the electron density and no change in the sign of the electron density contrast relative to heptane. Thus the pair-distance distribution function, p(r), obtained from GIFT analysis of the SAXS data should only show a single maximum. To gain a more detailed perspective, the geometric prediction and GIFT prediction from the experimental SAXS data were computed to estimate the droplet size within the system upon the addition of 10, 50 and 100 µl/2g of surfactant and heptane continuum. The scattering and pair-distance distribution functions obtained from the raw data and GIFT analysis, respectively, from SAXS experiments are presented in Figure 3.39

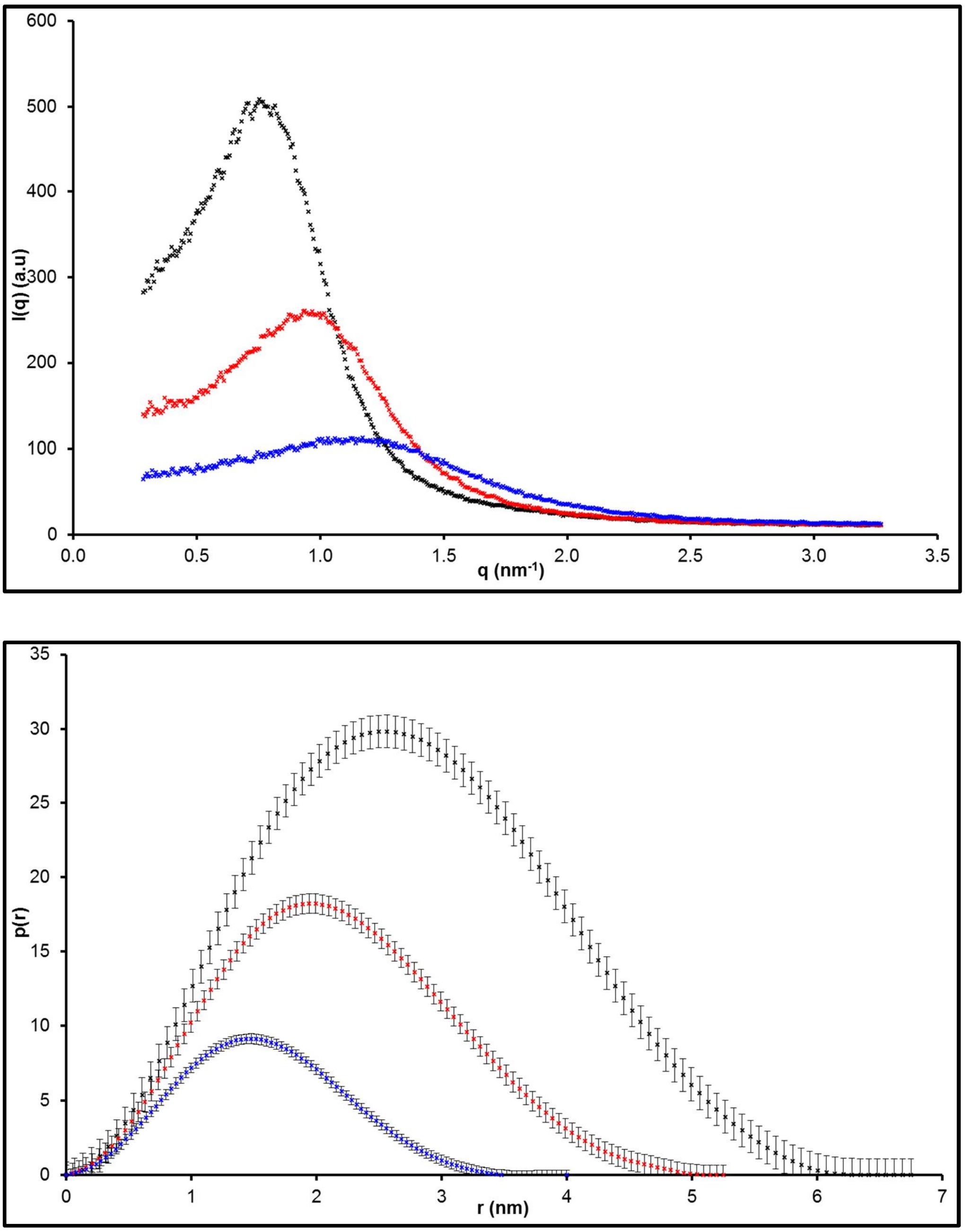

Figure 3.39: a SAXS scattering function and b: Pair distance distribution function p(r) for dispersed 1% aqueous sodium metasilicate nonahydrate within a 40 wt %. Span 80/Brij 30/heptane system. Blue: 5 µl/g, red: 25 µl/g and black: 50 µl/g.

The pair distance distribution p(r) curves generated from the scattering data in Figure 3.39a, are obtained after the incorporation of a hard sphere structure factor in the GIFT analysis to account for the interdroplet interactions. All the p(r) curves show a single maximum as expected since the p(r) curves show a single maximum as expected. Since the surfactant tails have essentially the same electron density as the cyclohexane continuous phase, only the size of the hydrophilic core can be reliably determined.

From Figure 3.39a and b, there is an apparent increase in droplet size as the volume of the dispersed phase increases, as would be expected at constant surfactant concentration.

3.10.1.4 Aging experiments 2 vs. 9 days.

A series of experiments were completed to determine the growth of material over the period of 7 days for the 1:1 Span80: Brij 30 in heptane microemulsions. As per previous experiments no macroscopic material was observed, thus TEM was employed.

3.10.4.1 2 day old samples

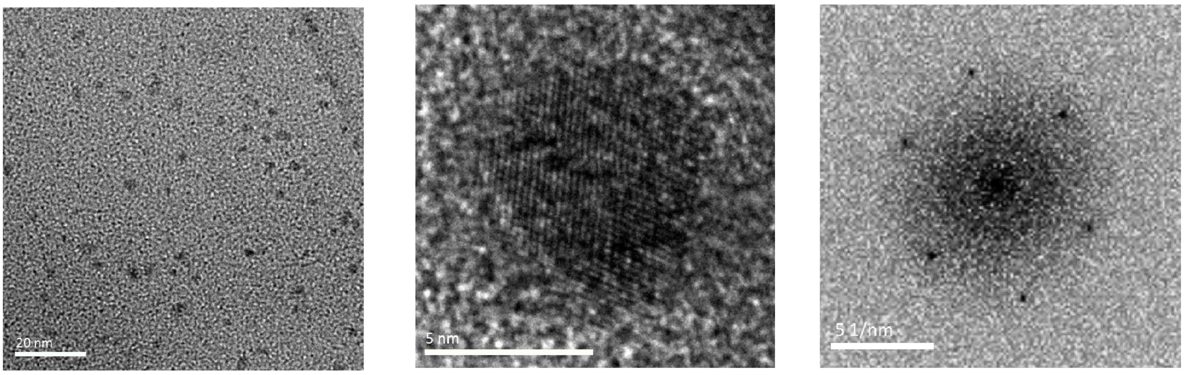

Figure 3.40 a: BF, b: HREM and c: corresponding FFT indexed to be the [0-4-2] zone axis of representative material for 1:1 Span80/Brij30/heptane microemulsion with 10 µl/2g 7.5 wt % SMS

3.10.4.2 9 day old samples

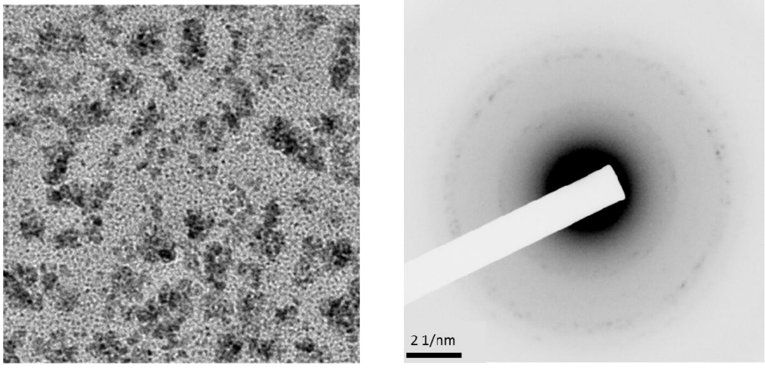

Figure 3.41 a: BF, b: corresponding DP for the representative nanoquartz material obtained from a 1:1 Span80/Brij30/heptane microemulsion with 10 µl/2g 7.5 wt % SMS after 9 days.

Comparing Figure 3.40a and 3.41a one can see that upon aging of the sample, the nanoparticles (~2-5 nm) present on day 2 of synthesis appear to have agglomerated together without any significant ordering to the structures, thereby generating polycrystalline quartz of the order of 50-100 nm.

Figure 3.41b presents the DP corresponding to the nanoaggregate structures, consisting of the following d-spacings: 3.13, 2.47, 2.12, 1.98, 1.80 and 1.36 Å. In addition to the FFT presented for the original nanoparticles in Figure 3.42c, which can be indexed to be the [0-4-2] zone axis for quartz, one can suggest that the 2.47, 2.12, 1.98, 1.80 Å spacing's may be attributed to quartz nanoparticles as these correspond to the diffraction from the corresponding quartz planes :110, 200, 021 or 201, 003. (See Table 1 – Appendix 1) The 3.13 and 1.36 Å do not correspond to a quartz structure. However the d-spacing's observed at 3.13 and 1.36Å may be attributed to the strongly diffracting 111 and 400 diffracting planes of atomic silicon crystal structure. (See Table 1- Appendix 1) Previous work carried out by J.R. Pitts and A.W. Czanderna,[47] presents findings on the electron beam damaging of quartz (SiO_2) to silicon, via a stimulated desorption process of the oxygen.[47] This past work showed beam damage occurring with the beam set as low as 2 kV, hence the use of a beam set to 200 kV for imaging through the surfactant is extremely likely to cause beam damage to the quartz. Two explanations are offered for such damage: firstly that Si-O bonds break, forming molecular oxygen; secondly, that additionally adsorbed components such as CO and molecular hydrogen add to the reduction process by providing stable desorbing groups.[47]

Additional support can be added to the identity of the nanoaggregates through EDX analysis, whereby the elemental analysis of the nano-particles, presented below consists solely of silicon and oxygen.

Figure 3.42: Corresponding EDX spectrum highlighting the elemental composition of the nanoaggregate structures observed in Figure 3.41

From Figure 3.42, the ratio of oxygen : silicon is rather larger than expected, however one would expect residual surfactant of Span80 and Brij30 to remain on the sample/grid despite thorough washings with methanol in attempts to dilute. Hence, a larger ratio of oxygen : silicon is apparent, and the presence of carbon can be expected from EDX analysis due to the holey carbon film. As is discussed further in Chapter 4, the residual surfactant may contribute to the partial agglomeration of the quartz nanoparticles, through the PEO groups interacting with the hydroxyl groups upon the silica phase. Hydrophobic interactions between the surfactant tails can support agglomeration of nanoparticles. No further degree of aggregation was observed over longer time scales.

3.11 Conclusions

Thermodynamic control was exerted over the precipitation of silica from an aqueous SMS solution, via the 3D-nanoconfinement of microemulsion droplets, through careful control of the precursor concentration and volume of aqueous dispersed phase, utilising a sodium metasilicate precursor (SMS) confined in both a TX-114 / 60 wt %. cyclohexane microemulsion system and a 40 wt %. 1:1 Span 80: Brij30/heptane microemulsion system. The most stable crystalline quartz form of silica was solely precipitated for low SMS concentrations; < 6 wt %. SMS for the TX-114 / 60 wt %. Cyclohexane system and < 7.5 wt %. SMS for the 40 wt %. 1:1 Span 80: Brij30/heptane system. Above these SMS concentrations the majority polymorph shifts to the metastable forms: cristobalite and amorphous silica spheres, as the increase in supersaturation allows metastable forms to precipitate. In addition the variation of the volume of the dispersed phase of aqueous SMS precursor in addition to the pH of the microemulsions were noted to have an affect over the silica polymorph precipitates. In summary, low dispersed volumes with low pH precipitated a majority of quartz, whilst higher dispersed volumes and inherently higher pH levels promoted, particularly the amorphous silica phase. Aging of experiments showed significant changes to the morphology of the precipitate, particularly the ability to aggregate, from individual 2-5 nm quartz nanoparticles, however no aggregation above 50-100 nm was observed.

References

1. Hobbs. L.W and Yaun. X, Springer, *'Science and Technology',* 2000, 37-71
2. H. Schott and A.E Royce, 'Journal of Pharmaceutical Sciences' 1984, **73 (6),** 793 June 1984
3. V. Bansal, A. Ahmad and M. Sastry, *'J. Am. Chem. Soc',* 2006, **128**, 14059-14066
4. J. F. Bertone *et al*, '*Nano Lett',* 2003, **3(5),** 655
5. Corwin. J.F, Herzog. A.H, Owen. G.E, Yalman. R.G and Swinnerton. A.C, *'J. Am. Chem. Soc',* 1953, **75(16**), 3933-3934
6. Hemmkamp. M.M and Davis. M.E, *'Annual Review of Material Science',* 1995, **25**, 161-192
7. W-L. Huang, *'Eur. J. Mineral',* 2003, **15**, 843-85
8. F. T. Mackenzie and R. Gees, *'Science*', 1971, **173(3996),** 533-535
9. L-J. Li *et al, 'Journal of the Chinese Chemical Society',* 2003, **50**, 395-398
10. F. Asaro *et al, 'Langmuir',* 2010, **26(15),** 12917-12925
11. J. Esquena, *et al, 'Langmuir',* 1997, **13**, 6400-6406.
12. MSDSheet for Sodium metasilicate, *'ScienceLab.com',* 09/06/2011
13. L. M. Gan, K. Zhang and C. H. Chew, *'Colloids Surfaces A: Physiochem. Eng. Aspects',* 1996, 110, 199-206.
14. K. Zhang, L.M. Gan, C. H. Chew and L. H. Gan, '*Materials Chemistry and Physics',* 1997, 47, 164-170.
15. Rimer J.D, Lobo. R.F and D.G Vlachos, *'Langmuir',* 2005, 21 (19), 8960-71
16. Bass. J.L and Turner. G.L, *'J. Phys. Chem. B'* 1997, 101, 10638-10644
17. X. Yang, P. Roonasi and A. Holmgren, *'J. Colloid Interface Sci',* 2008, 382(1), 41-47
18. Dent Glasser. L.S and Lachowski. E.E, *'J. Chem. Soc., Dalton Trans',* 1980, 393-398
19. Icopini. G.A, Brantley. S.L and Heaney. P.J, *' Geochimica et Cosmochimica Acta'*, 2005, 69(2), 293–303
20. Jesionowski. T, *'Powder Technology',* 2002, 127(1), 56-65
21. Martinez-Rodriguez. R.A, Vidal-Iglesias. F.J, Solla-Gullon.J, Cabrera. C.R and Feliu. J.M, *'J. Am. Chem. Soc',* 2014, 136(4), 1280-1283
22. Liu. M, Zheng. Y, Zhang. L, Guo. L and Xia. Y, *'J. Am. Chem. Soc',* 2013, 135(32), 11752-11755
23. Zhang. X-Q, Trinh. T.T, Santen. R.A and Jansen. A.P.J, *'J. Am. Chem. Soc',* 2011, 133(17), 6613-6625
24. Knight. C.T, Balec. R.J and Kinrade. S.D, *'Angew Chem Int Ed Engl',* 2007, 46(43), 8148-52
25. Kinrade. S. D and D.L Pole, *'Inorg. Chem',* 1992, 31(22), 4558-4563

26. Music.S, Filipovic-Vincekovic. N and Sekovanic. L, *'Braz. J. Chem. Eng',* 2011, 28(1), 89-94
27. Torres-Carrasco. M, Palomo. J.G and Puertas. T, *'Mater. Construcc,'* 2013*,* **64** (314), e014
28. I.W. Boyd, *'Appl. Phys. Lett',* 1987, 51, 418
29. Sitarz. M, Handke. M, and Mozgawa. W, '*Spectrochimica Acta A: Molecular and Biomolecular Spectroscopy',* 2000, 56(9), 1819-1823
30. C. Chen, '*Crystallisation of glycine and dipicolinic acid (DPA) from microemulsions',* 2012, Durham PhD thesis.
31. Peltonen. L, Hirvonen. J and Ylirussi. J, *'J. Colloid Interface Sci',* 2001, 240(1), 272-276
32. Zhu. H and Aitken. M.D, *'Environ. Sci. Technol',* 2010, 44(19), 7260-7265
33. Belton. D.J, Deschuame. O, Patwardhan. S.V and Perry. C.C, *'J. Phys. Chem. B',* 2010, 114(31), 9947-9955
34. Crans. D.C and Levinger. D.C, *'Acc. Chem. Res',* 2012, 45(10), 1637-1645
35. Baruah. B, Crans. D.C and Levinger. N, *'Langmuir',* 2007, 23(12), 6510-8
36. J. R. V. Romani, J. S. Sánchez, M. V. Rodriguez and D. F. Mosquera, '*Géo morphologie'*, 2010, 4, 337-346
37. Fedeyko. J.M, Rimer. J.D, Lobo. R.F and D.G Vlachos, *'J.Phys. Chem.* B', 2004, 108, 12271-12275
38. Yaghmur. A, Aserin. A, Tiunova. I and Garti. N, *'Journal of Thermal Analysis and Calorimetry',* 2002, 69, 163-177
39. Gorlich. E, *'Ceramics International',* 1985, 8(1), 3-16
40. Jesionowski. T, *'Colloids and Surfaces A: Physicochem. Eng Aspects',* 2001, 182, 65-81
41. Jesionowski. T, '*Colloids and Surfaces A: Physicochem. Eng Aspects'* 2001, 190(1-2), 153-165
42. W. Wang et al, '*Colloid Surfaces A: Physicochem. Eng. Aspects'*, 1993, 81, 177-180
43. Eastoe. J, '*3. Microemulsions'* http://www.chm.bris.ac.uk/eastoe/Surf_Chem/3%20Microemulsions.pdf, unpublished work.
44. Gradzielski, M.; Langevin, D.; Farago, B. *'Phys. Rev. E'* 1996, 53, 3900
45. Weyerich. B, Brunner-Popela. J and Glatter. O, *'J. Appl. Cryst',* 1999, 32, 197-209
46. L.Qi and J. Ma, *J. Colloid Interface Sci'* 1998, 197, 36-42
47. J. R. Pitts and A. W. Czanderna, *'Nuclear Instruments and Methods in Physics Research',* 1986, B13, 245-249.
48. Yoo. C-S, *'Phys. Chem. Chem. Phys',* 2013, **15**, 7949-7966
49. Krauskoph. K.B, *'Geochimica of silica at low temperatures',* 1956, **10(1-2),** 1-26
50. Pusey. P.N and Tough. R. J. A, *'Dynamic Light Scattering Applications of Photon Correlation Spectroscopy',* New York. Plenum. 1985

51. Langowsky. J and Brain. R, *‘Neutron, X-Ray and Light Scattering’.* Amsterdam: North Holland. 1991

Chapter 4 – Acidified quartz crystallisation

4.1 Introduction

Recent work completed by Chen. C *et al.*[1] highlighted the effect of the addition of hydrochloric acid to a microemulsion upon the resultant precipitate, the pH and the viscosity. Chen performed extensive studies using dipicolinic acid as a model compound to understand the exertion of thermodynamic control of the crystallisation process within the 3D-nanoconfinement of microemulsion droplets for compounds with the ability to form salts, solvates and hydrates. During such studies, the participation of metal salts persisted unless sufficient HCl was added, which, based on prior work by Peral *et al.*[2-3] and Crans *et al.*[2-3] was postulated to be a result of the metal binding ability of DPA, in combination with the microemulsion-based pH shift towards neutrality and the pH dependent self-assembly behaviour.[1] The pH dependent self-assembly behaviour is illustrated by the distribution curves for the protolytic species of DPA in aqueous solutions in Figure 4.1.[4-5]

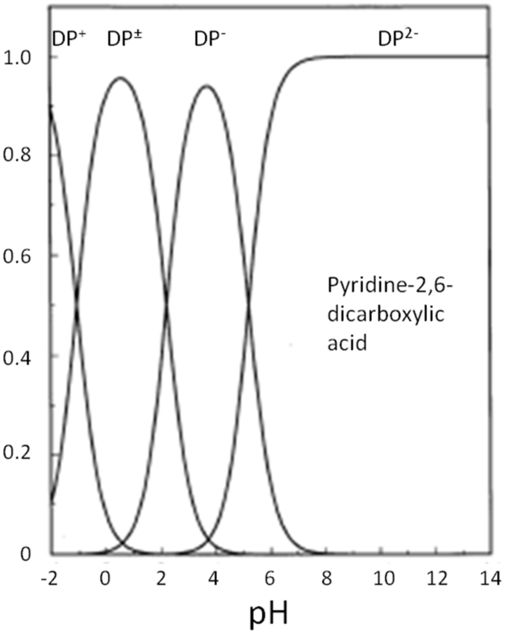

Figure 4.1 Distribution curves for the different protolytic species of DPA in aqueous solution.[5] Reprinted (adapted) with permission from F. Peral and E. Gallego, *'Spectrochim. Acta A,'* 2001, 56, 2149-2155. Copyright © 2000 Elsevier Science B.V

In an attempt to solely precipitate the acidic form of DPA, Chen *et al.* studied the crystallisation of DPA within HCl acidified microemulsions (pH ≤ 1). From two independent microemulsion compositions, ordered nanoaggregates of the DPA monohydrate formed via orientated attachment of primary 2-10 nm nanoparticles to structures which may be considered as iso-orientated crystals or mesocrystals, as presented in Figure 4.2 below. These monohydrate DPA structures crystallised preferentially to the thermodynamically metastable anhydrous form, which typically crystallised in bulk solutions under these conditions.

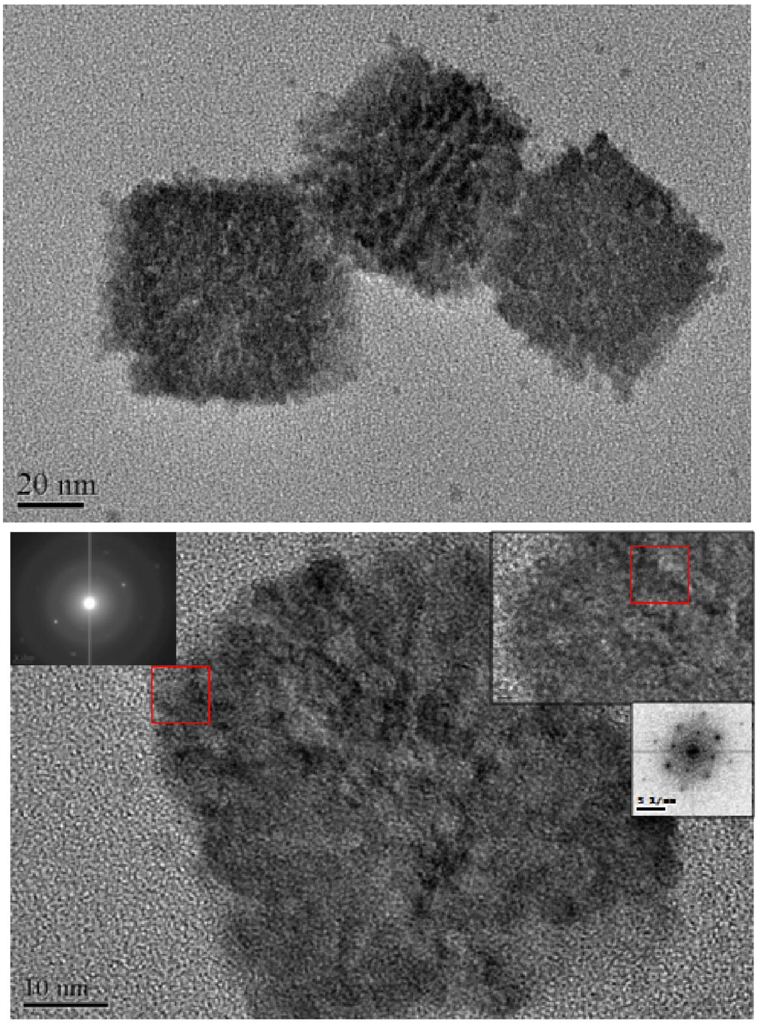

Figure 4.2a and b: BF, HREM, DP and FFT images of DPA crystals from a non-ionic surfactant/alcohol co-surfactant system, with 225 µl/g of a supersaturated DPA solution in 2M HCl.[1]

The similarities between the speciation curves of DPA in Figure 4.1 and that of the distribution of silicate species and their pH dependence are apparent. Thus, as comparable non-ionic surfactant systems were utilised both in the study presented in Chapter 3 and the work of Chen *et al.* it seemed appropriate to extend the work regarding the precipitation of silica phases from an acidified microemulsion.

4.2 Experimental

4.2.1 Control experiments

To investigate the effect of the addition of HCl upon the silica precipitation process, control experiments were conducted via the addition of 0.3, 1.5 and 2.2 M HCl to various concentrations (1 – 40 %wt.) of bulk aqueous SMS solutions at a 1:1 volume ratio. Precipitate formation was both SMS and HCl concentration dependent. Precipitate was analysed by FTIR spectroscopy and PXRD.

4.2.2 Solubility tests

The solubility of SMS was determined in a number of further solvents under ambient conditions. Incremental quantities of SMS were added sequentially over a period of ~ 5-6 weeks to 1 g of solvent or liquid surfactant in a stable temperature oven at 25 ± 1 °C, until no further material could be dissolved. Solubility studies were completed in 0.3 – 2.2 M hydrochloric acid.

Note the solubility of SMS in the Span 80: Brij 30: heptane and the TX100:cyclohexane w/o microemulsion is < 1 mg/2g.

Solvent	SMS (mg/ml)
0.2 M HCl	> 350
1.5 M HCl	< 15
2.2 M HCl	< 10
1-Hexanol	< 1
TX-100	< 1

Table 4.1: Measured solubility of sodium metasilicate nonahydrate in various solvents.

4.2.3 Unconfined experiments

Comparable concentrations of SMS in bulk UHQ water to those adopted in the inner phase of the microemulsions were prepared and added to a HCl solution, and left to precipitate. Aqueous compositions of 1 – 40 wt %. SMS were created. Concentrations ≥ 25 wt %. gave precipitate and were analysed by FTIR spectroscopy and PXRD. Additionally the pH of the solutions was measured to enable comparison to the pH changes made in the microemulsion systems.

4.2.3.1 2.2 M HCl and aqueous SMS bulk experiments

4.2.3.1.1 pH measurements

Aqueous SMS compositions – 1:1 (vol) 2.2 M HCl. pH and observations.				
SMS (% wt.)	**pH**	**SMS (% wt.)**	**pH**	**Observations**
1	0.28 ± 0.07			No precipitate
2.5	0.28 ± 0.05	20	0.70 ± 0.06	No precipitate
5	0.29 ± 0.08	25	2.12 ± 0.07	Film precipitate
7.5	0.35 ± 0.06	30	10.09 ± 0.05	Gel formation - film and white crystalline precipitate
10	0.61 ± 0.07	40	11.15 ± 0.07	Precipitate formed before re-dissolution

Table 4.2 pH measurement of bulk sodium metasilicate solutions upon mixing with a 1:1 vol. ratio of 2.2 M HCl solution. The pH of 2.2 M HCl is ~ -0.3.

Upon the addition of 2.2 M HCl to an alkaline aqueous SMS solution, a decrease in the pH of the system is expected and observed, as the neutralisation reaction proceeds. Approaching neutrality, gelling of the solution is accompanied by the precipitation of both a thin film material, see Figure 4.6 and a white crystalline powder. This precipitate was analysed by optical microscopy, FTIR spectroscopy and PXRD and the findings are discussed in Section 4.2.3.

4.2.3.1.2 IR spectroscopy

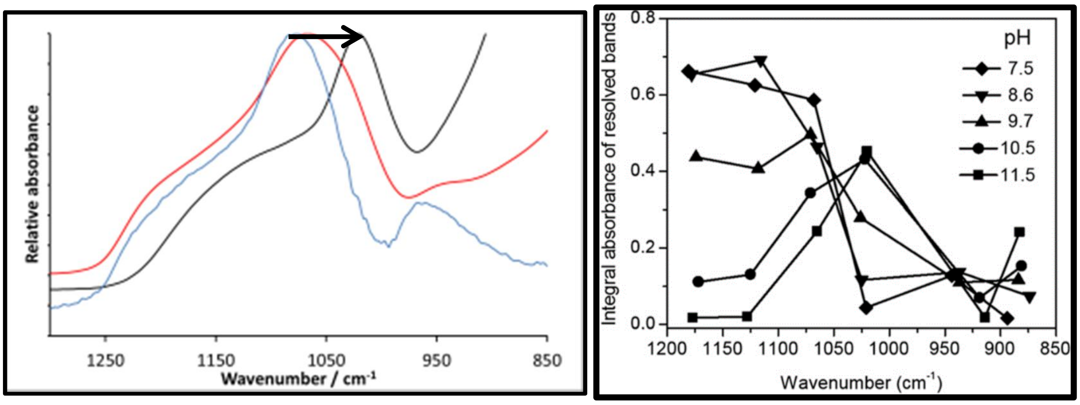

Figure 4.3 a: IR spectrum of precipitate obtained upon mixing 25 wt %. (blue), 30 wt %. (red) and 40 wt %. (black) aqueous SMS solutions in a 1:1 vol. ratio with 2.2 M HCl solutions. Figure b: Yang *et al.* [6] Reproduced (adapted) with permission from X. Yang, P. Roonasi and A. Holmgren, *'J. Colloid Interface Sci',* 2008, 382(1), 41-47. Copyright © 2008 Published by Elsevier Inc.

Compiling IR spectra, analysis suggests the identity of the thin films and gel substance is a silicate based material, with composition dependent upon the sodium metasilicate concentration, and thus pH. Figure 4.3a illustrates the red shift in the Si-O stretching mode with increasing concentration and pH, indicating the move from a silica phase to an undissociated sodium silicate as one would expect when considering the findings of Yang *et al.*[6]

4.2.3.1.3 XRD

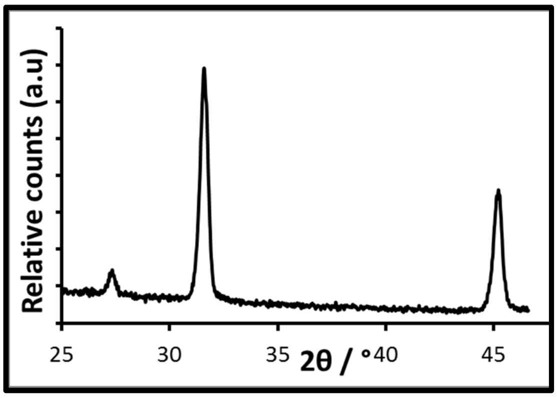

Figure 4.4: XRD pattern of remaining precipitate when silica gel phase is rinsed with acetone.

Upon removal of the gel phase, the white crystalline solid can be identified as sodium chloride via XRD analysis, with characteristic peaks found at: 27.4, 31.7 and 45.4 °. This can be explained by noting the modified neutralisation reaction and dissociation of sodium metasilicate in the presence of hydrochloric acid.

$$Na_2SiO_2 + 2HCl \rightarrow H_2SiO_2 + 2NaCl \tag{1}$$

$$H_2SiO_2 \rightarrow SiO_2 + H_2O \tag{2}$$

4.2.3.2 1.5 M HCl and aqueous SMS bulk experiments

4.2.3.2.1 pH

Aqueous SMS compositions – 1:1 (vol) 1.5 M HCl. pH and observations.				
SMS (% wt.)	**pH**	**SMS (% wt.)**	**pH**	**Observations**
1	1.08 ± 0.06	15	1.69 ± 0.07	No precipitate
2.5	1.19 ± 0.05	20	10.35 ± 0.06	Gel formation
5	1.20 ± 0.08	25	11.18 ± 0.05	Film precipitation
7.5	1.25 ± 0.07	30	11.79 ± 0.06	No precipitate
10	1.30 ± 0.06	40	12.66 ± 0.07	No precipitate

Table 4.3 pH measurement of bulk sodium metasilicate solutions upon mixing with a 1:1 vol. ratio of 1.5 M HCl solution. The pH of 1.5 M HCl is ~ -0.2.

4.2.3.2.2 IR spectroscopy

FTIR analysis of both the 20 and 25 % wt. SMS solutions revealed an analogous trend to that displayed in Chapter 3 previously.

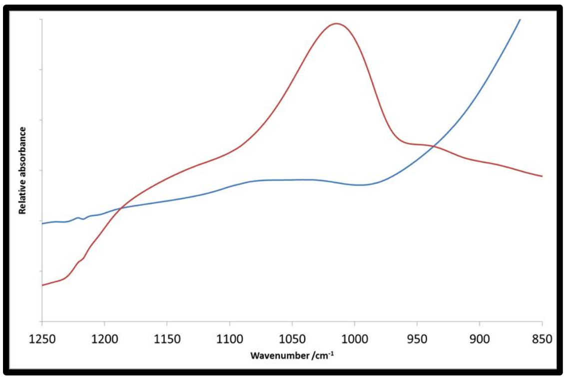

Figure 4.5: IR spectrum of precipitate obtained upon mixing 20 wt %. (blue) and 25 wt %. (red) aqueous SMS solutions in a 1:1 vol. ratio with 1.5 M HCl solutions.

In accordance with Yang *et al.*[6], for a pH between 10.5 and 11.5, one would expect a maximum absorbance at a wavenumber between 1000 cm^{-1} and 1025 cm^{-1}, with a shoulder at ~ 930 cm^{-1} assigned by Yang *et al.*[6] to the un-dissociated sodium silicate species as expected at such high pH levels. In Figure 4.5 one can observe the maxima within the relevant wavenumber window to decrease from between 1100 cm^{-1} – 1000 cm^{-1} to between 1000 cm^{-1} and 1025 cm^{-1} as the concentration of SMS moves from 20 wt % to 25 wt %. This is expected for an increase in pH from ~10.3 to 11.2, as depicted in Figure 4.3b. In addition to the shift in maxima, a further broad shoulder between 1070-1125 cm^{-1} is observed for the material from an increased pH. This can be assigned to an increase in the Si-O-Si stretch within the silica phase.

4.2.3.3 0.3 M HCl and aqueous SMS bulk experiments

4.2.3.3.1 pH

Aqueous SMS compositions – 1:1 (vol) 0.3 M HCl pH and observations.			
SMS (% wt.)	**pH**	**SMS (% wt.)**	**pH**
1	8.86 ± 0.05	10	12.25 ± 0.06
2.5	8.90 ± 0.06	15	12.60 ± 0.05
3	9.21 ± 0.07	20	12.87 ± 0.07
4	9.48 ± 0.06	25	13.02 ± 0.08
5	10.4 ± 0.08	30	13.28 ± 0.06
7.5	11.61 ± 0.04	40	13.23 ± 0.07

Table 4.4: pH measurement of bulk sodium metasilicate solutions upon mixing with a 1:1 vol. ratio of 0.3 M HCl solution. The pH of 0.3 M HCl is ~ -0.5

No macroscopic precipitation was observed upon the addition of 0.3 M HCl acid to aqueous sodium metasilicate solutions. This can be rationalised due to the relative increased water to HCl concentration, based on determination of the solubility of SMS in HCl.

A summary of the above observations are presented below for convenience:

- 1:1 vol. 0.3 M HCl : 1 - 40 % wt. aqueous SMS solutions. No macroscopic precipitation was observed.
- 1:1, 1.5 M HCl : 1 - 40 % wt. aqueous SMS solutions. For 15-25 % wt. gelation of the solution occurred upon mixing, with precipitate in the 25 % wt. case.
- 1:1, 2.2 M HCl : 1 – 40 % wt. aqueous SMS solutions. For 1 – 15 % wt. SMS no immediate visible change was observed. For 20, 25 and 40 % wt. a white precipitate temporarily precipitated upon mixing before re-dissolving within an hour of mixing. A solid gel phase formed in the case of 30 % wt.

4.2.3.4 Optical microscopy

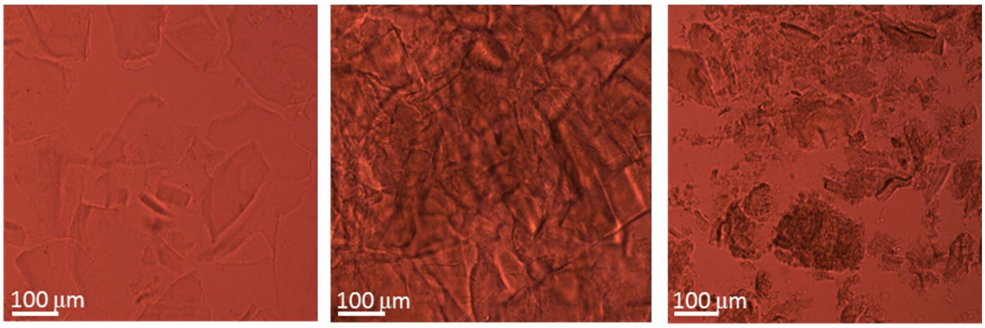

Figure 4.6: Optical microscopy images of precipitate formed from the addition of 1:1 vol. 2.2 M, 1.5 M and 0.3 M HCl to 20, 25 and 30 % wt. aqueous sodium metasilicate solution respectively.

To look at the structure of the precipitate from unconfined SMS solutions with HCl addition, optical microscope was utilised. Optical microscopy revealed the gel phase contained similar thin amorphous silicate/silica based films as those precipitated from the aqueous SMS solutions, see Figure 4.6. Alongside IR analytical techniques, the identity of the films can be confirmed to be silicate and silica based.

4.2.4 Phase diagrams

Further to the surfactant systems and corresponding phase diagrams presented in Chapter 3, an additional non-ionic surfactant system is utilised Moreover, upon the replacement of the aqueous SMS with a HCl solution, the change in the position, shape and size of the Winsor IV single phase microemulsion may be identified for both cases.

4.2.4.1 Span 80/Brij 30/heptane microemulsion

The details of the Span 80/Brij 30/heptane/water microemulsion and the associated phase diagram are presented in Chapter 3. The phase diagram for Span 80: Brij 30/heptane/2.2 M HCl is presented in Figure 4.7.

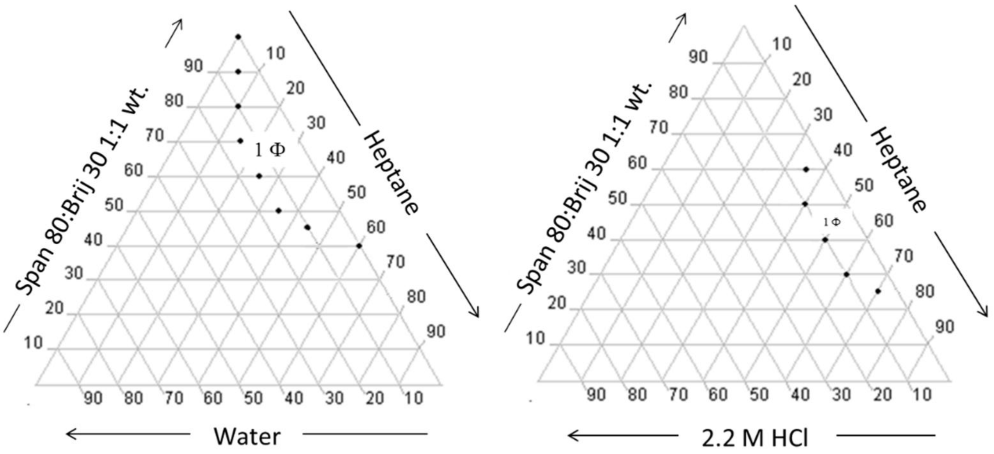

Figure 4.7a and b : Ternary phase diagram illustrating the dependence of the oil:acid:surfactant composition upon the resultant phase for a (a) heptane: water: 1:1 Span80:Brij30 combination and (b) heptane: 2.2 M HCl: 1:1 Span80:Brij30 combination.[1]

It can be noted from a comparison of Figure 4.7b with Figure 4.7a that upon replacing water with 2.2 M HCl, the w/o microemulsion region decreased significantly and translated towards a lower aqueous component and higher heptane component. Various literature sources have documented the varied effect of pH upon microemulsion formation, with a general consensus indicating the impact of the addition of an acid phase is largely dependent upon the type of surfactant.[7-9] The phase diagram for some zwitterionic surfactants were found to be unaffected by a shift in the pH of the dispersed phase, whilst for others, as seen in this study there can be a significant change to the phase diagram. Based on the work of Crans *et al.* [2-4] and Garti[10], one can postulate that this dependence may be a result of the close proximity of the HCl ion components to the surfactant molecules, thus affecting the 'natural' packing of surfactant molecules and hence the phase diagram.[7-9]

Microemulsions containing 0.3, 1.5 and 2.2 M HCl were added in a 1:1 vol. with respect to the volume of SMS aqueous dispersed phase in the microemulsion via a mixed microemulsion methodology.

4.2.4.2 TX100/hexanol/cyclohexane microemulsion

Drawing comparisons between the phase diagrams above in Figure 4.8a and b with published literature based procedures[1], a 2.2 Triton X-100 : 1 1-hexanol wt. ratio of surfactant to co-surfactant was employed at 55 wt%. in a cyclohexane continuous phase. The ternary emulsion system of Triton X-100, 1-hexanol and cyclohexane is well documented. The TX-100 molecular structure differs to that of TX-114 by an increase in n to 9 or 10. This change is accompanied with an increase in HLB to 13.5, cmc ~0.23 mM and a cloud point of 65 °C. The addition of the hexanol co-surfactant acts to increase the hydrophobicity and thus the negative spontaneous curvature of the surfactant bends towards the water phase to stabilise a w/o microemulsion system.

The volume of aqueous dispersed phase added to the surfactant continuum was varied between 5 - 100 µl/g,. The concentrations of aqueous SMS was varied between 0.25 – 10 wt %.

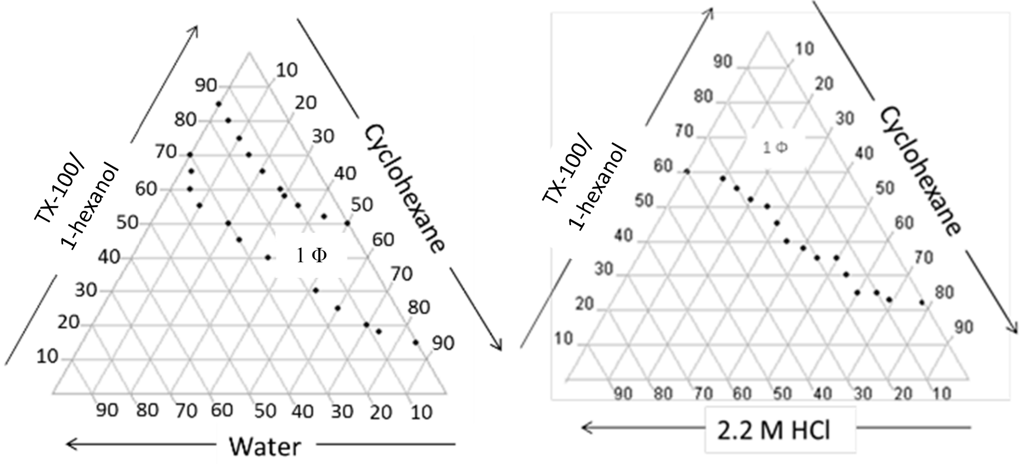

Figure 4.8a and b : Ternary phase diagram illustrating the dependence of the oil:acid:surfactant composition upon the resultant phase for a cyclohexane:water:TX-100 and 1-hexanol combination (a) and for a cyclohexane:2.2 M HCl:TX-100-1 hexanol combination (b)[1]

It can be noted from a comparison of Figure 4.8a and b that upon replacing water with 2.2 M HCl, the w/o microemulsion region increased significantly and particularly for high surfactant concentrations, whereby nanoemulsions were produced. This is the opposing trend compared to the Span 80/Brij 30/heptane microemulsions. As noted previously the addition of an acid is known to have a varied effect upon microemulsion formation which is largely dependent on the surfactant utilised.[3-4] Moreover, the viscosity of the microemulsions was noted to increase with a larger volume of dispersed phase, in comparison to the familial surfactant of TX-114 utilised in chapter 3. Chen. C[1] related the increase in viscosity to the introduction of a co-surfactant, upon comparison of microemulsions both with and without the co-surfactant.

4.3 Span80:Brij30 system

4.3.1 Microemulsion preparation

The same method as described in Chapter 3 was adopted to prepare the microemulsions. The 2.2 M, 1.5 M or 0.5 M HCl was added in a 1:1 vol. with respect to the SMS aqueous dispersed phase via a mixed microemulsion methodology as described in Chapter 2, Section 2.2.1. Microemulsions were left for varying degrees of time (1 hour – 3 years) before analysis was performed.

4.3.2 Microemulsion experiments

Using the 3D nanoconfinement of microemulsion droplets, the following variables were investigated: the effect of the addition of HCl upon the process of nucleation, precipitation and crystal growth or aggregation.

4.4 Span80/Brij30/heptane: Results and discussion

To determine the range over which 3D confinement within the microemulsion is maintained, a series of systematic experiments, varying the concentration of aqueous SMS alongside the droplet size of the dispersed phase were completed. The range of concentrations and volumes stabilised are illustrated in Section 4.4.1.

Despite SMS being readily soluble in water, from initial studies, supersaturated solutions often initiated immediate destabilisation of the microemulsion. This may be due to a number of factors including: perturbation of water molecules by the surfactant or reduced pH levels within the dispersed phase.

4.4.1 40 wt %. 1:1 Span 80: Brij30/heptane microemulsion system

In addition to the phase diagrams presented in Section 4.2.4, the macroscopic observations of the heptane: water: 1:1 Span80:Brij30 and heptane: HCl: 1:1 Span80:Brij30 microemulsion systems are documented, to show the dependency on the concentration of the SMS precursor, the concentration of HCl and the volumes of dispersed phase. The effects will be discussed further throughout Section 4.4.

4.4.1.1 Effect of HCl acid addition upon the phase diagram stability

4.4.1.1.1 No HCl addition

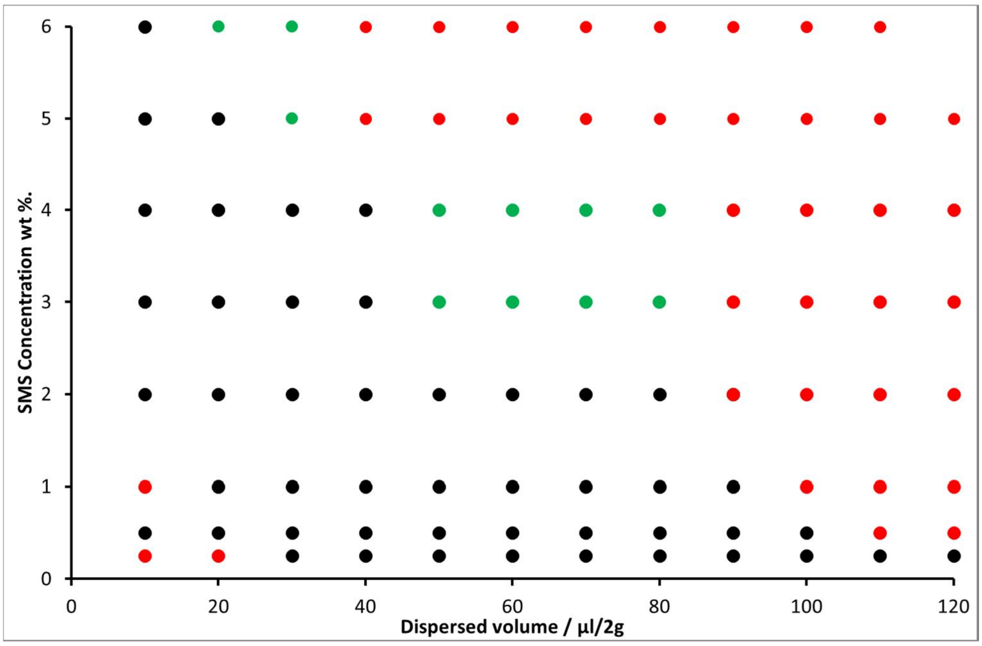

Figure 4.9 Graphical display of microemulsion compositions with varying SMS concentration and dispersed volume, and the effect upon the stability. Black = microemulsion and red = immediate precipitation of amorphous silicate phase and green = stable microemulsion with impurities from Span 80 surfactant present at the bottom of the vial.

As one would expect the material synthesised from the microemulsion is dependent upon a combination of both the SMS precursor concentration, the dispersed volume and the concentration of HCl added. SMS concentrations between 1 and 14 wt %. SMS were employed in the microemulsion system, however beyond 6 wt %. SMS, only 10 µl/2g could be stabilised by the specified surfactant combination. Similarly, to the findings of Chapter 3 little macroscopic precipitate was observed for any precursor concentration, hence TEM was utilised to image any nanoscopic material.

4.4.1.1.2 0.3 M HCl addition

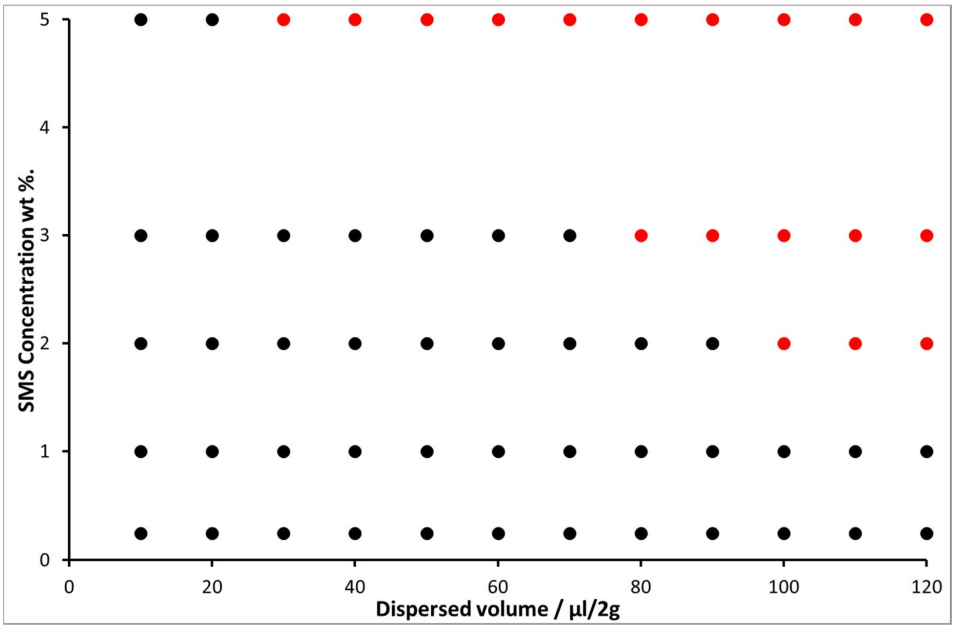

Figure 4.10 Graphical display of microemulsion compositions with varying SMS concentration and dispersed volume, and the effect upon the stability upon the addition of a 1:1 0.3 M HCl acid via a mixed microemulsion method. Black = microemulsion and red = immediate precipitation of amorphous silicate phase and green = stable microemulsion with impurities from Span 80 surfactant present at the bottom of the vial.

4.4.1.1.3 1.5 M HCl addition

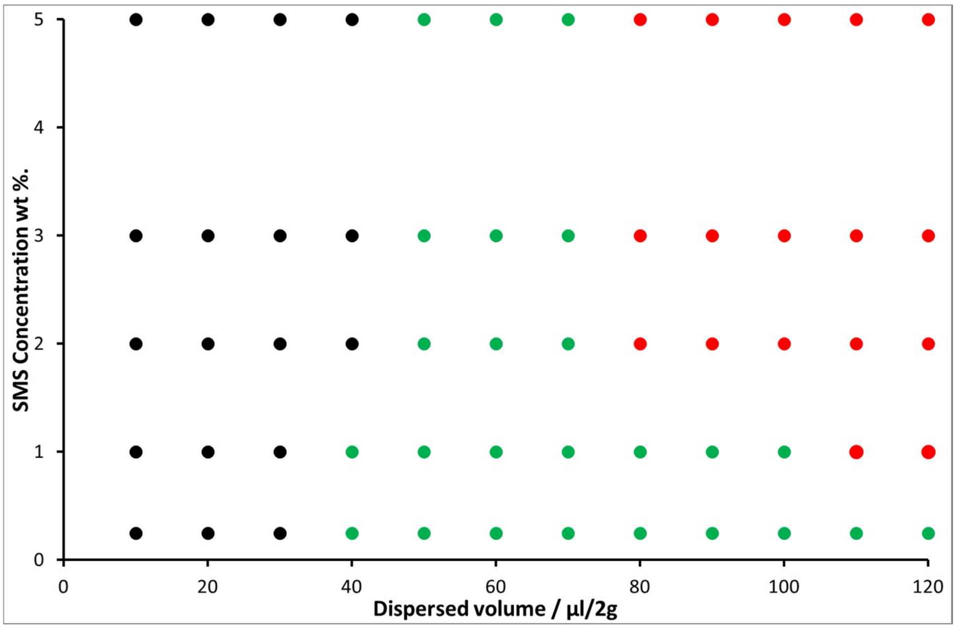

Figure 4.11 Graphical display of microemulsion compositions with varying SMS concentration and dispersed volume, and the effect upon the stability upon the addition of a 1:1 1.5 M HCl acid via a mixed microemulsion method. Black = microemulsion, red = immediate precipitation of amorphous silicate phase and green = stable microemulsion with impurities from Span 80 surfactant present at the bottom of the vial.

4.4.1.1.4 2.2 M HCl addition

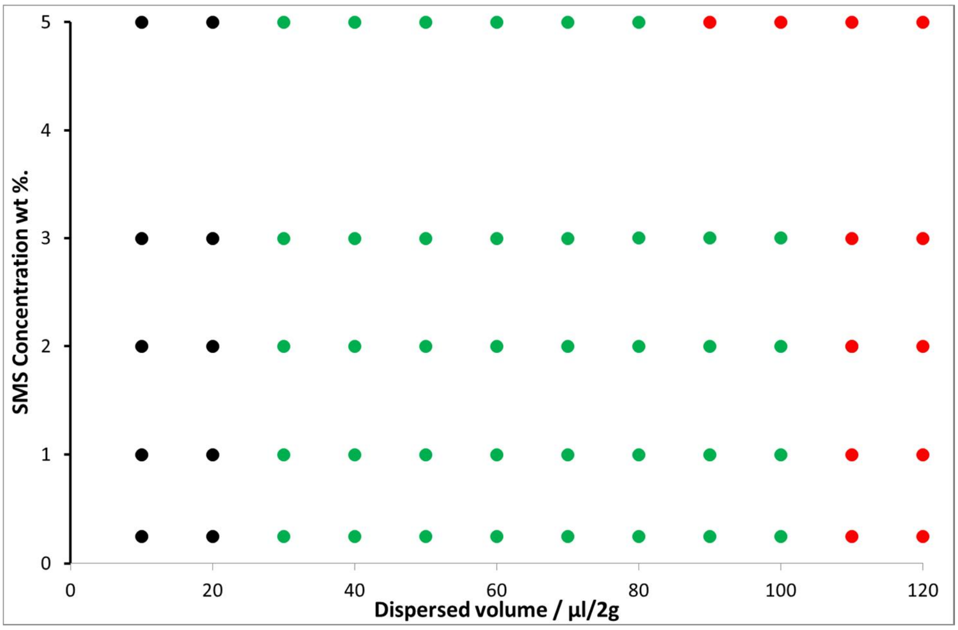

Figure 4.12 Graphical display of microemulsion compositions with varying SMS concentration and dispersed volume, and the effect upon the stability upon the addition of a 1:1 2.2 M HCl acid via a mixed microemulsion method. Black = microemulsion, red = immediate precipitation of amorphous silicate phase and green= microemulsion with Span 80 surfactant impurity precipitate.

As one moves from a microemulsion containing no HCl, through 0.3 M, 1.5 M and 2.2 M HCl as illustrated in Figure 4.9-4.12 there is a reduction in the volume of dispersed phase that can be stabilised within the microemulsion. Moreover, for the incorporation of 0.3 M HCl acid in to the microemulsion a small reduction in the dispersed volume capable of being stabilised is observed, whereas for 1.5 M and 2.2 M HCl, one can imply from Figures 4.11 and 4.12 that there is a shift from the dominating factor upon microemulsion stability being the concentration of SMS precursor to the aqueous dispersed volume. To understand the origin of this shift in the phase diagram one must consider the pH of the microemulsions upon the incorporation of different acid concentrations.

4.4.1.2 pH

SMS (% wt.)	Dispersed volume (μl/2g)	HCl (M)	pH	SMS (% wt.)	Dispersed volume (μl/2g)	HCl (M)	pH
1	10	0	6.1 ± 0.1	5	10	0	6.3 ± 0.1
		0.3	5.8 ± 0.1			0.3	5.6 ± 0.1
		1.5	5.7 ± 0.2			1.5	5.1 ± 0.1
		2.2	5.4 ± 0.1			2.2	5.2 ± 0.2
	50	0	6.0 ± 0.1		50	0	6.7 ± 0.1
		0.3	5.3 ± 0.2			0.3	5.6 ± 0.1
		1.5	2.1 ± 0.1			1.5	2.5 ± 0.1
		2.2	0.8 ± 0.1			2.2	1.0 ± 0.1
	100	0	6.5 ± 0.1		100	0	6.9 ± 0.2
		0.3	4.8 ± 0.1			0.3	5.4 ± 0.1
		1.5	1.6 ± 0.1			1.5	1.0 ± 0.1
		2.2	0.8 ± 0.1			2.2	1.1 ± 0.1

Table 4.5: pH measurements of 40 wt %. 1:1 Span 80: Brij30/heptane microemulsion system with variation of both dispersed volume and SMS precursor concentration and various concentrations of HCl added by the mixed microemulsion method. pH in bulk: 0.3 for 2.2 M, 1 for 1.5 M, 2 for 0.3 M for bulk mixtures

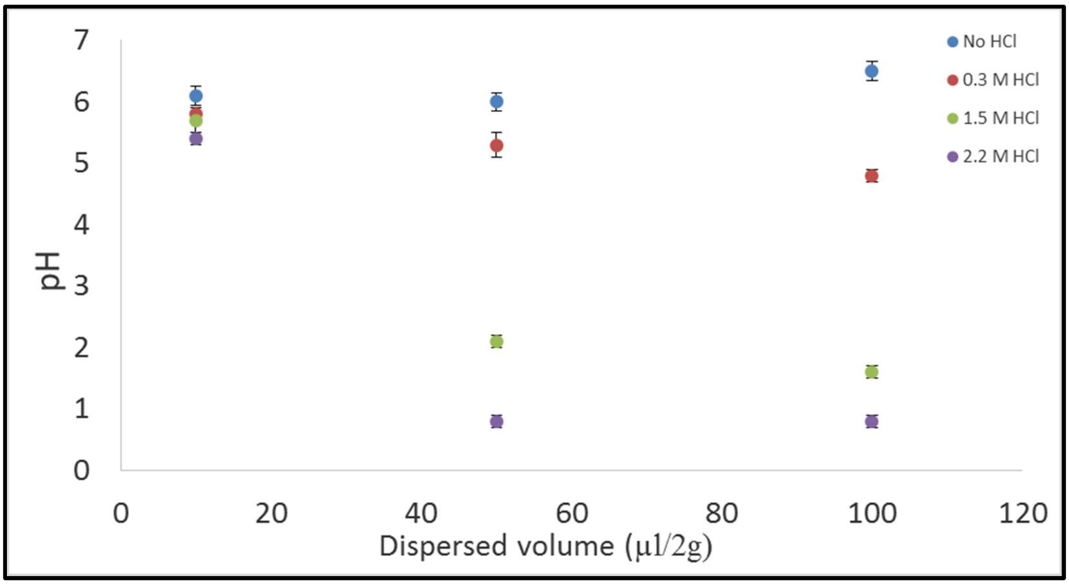

Graph 4.1 : pH measurements of microemulsion as a function of dispersed phase for microemulsions with 1 wt % SMS.

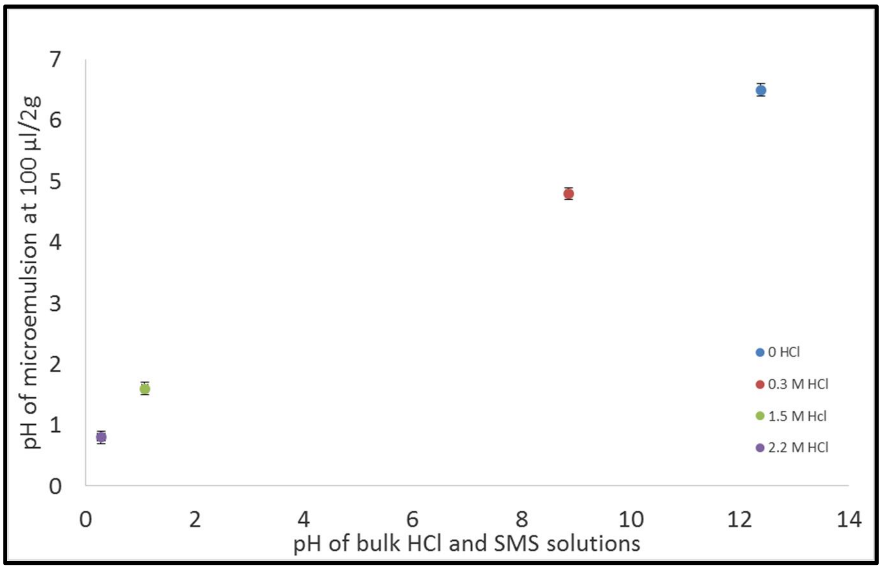

Graph 4.2 Correlation plot between the pH of the bulk HCl and SMS solutions and the pH of HCl and SMS microemulsions with a dispersed phase of 100 µl/2g AND SMS concentration of 1 wt %.

Graph 4.1 illustrates the correlation between the dispersed volume and the pH of the microemulsion. Additionally Graph 4.2 shows a clear linear trend between the pH of the unconfined systems and the 100 µl/2g cases, whereby the microemulsion pH in all cases is closer to neutrality than the bulk system.

For 2.2 M at small droplet sizes, i.e. 10 µl/2g there is the greatest shift towards neutrality, whereas for larger droplet sizes i.e. 50 and 100 µl/2g the pH of the microemulsions remain very acidic and close to the unconfined equivalent solution of pH ~ 0.3.

For 1.5 M again for the smallest droplet size, e.g. 10 µl/2g there is the greatest shift towards neutrality. However, for intermediate dispersed volumes there is a small degree of shift in the pH towards neutrality that diminishes as the dispersed phase increases to 100 µl/2g, where the pH is comparable to the bulk pH of ~ 1.

For high acid concentrations in large dispersed volumes it is apparent that the microemulsions remain very acidic. This can be rationalised by the varying degree to which the pH may be shifted within the microemulsion at different dispersed volumes. For larger dispersed volumes, a smaller influence over the pH is observed relative to the small dispersed phases.

For 0.3 M, a significant shift towards neutrality is observed for all volumes of dispersed phase, i.e. 10, 50 and 100 µl/2g compared to the unconfined equivalent solution of pH ~ 2.0, thus the phase diagram is analogous to that of the heptane: water: 1:1 Span80:Brij30 phase diagram, thus the addition of HCl has a minimal effect upon the phase diagram.

Statistically, one can conclude that the more acidic the microemulsion, i.e. for pH ~ 1 the microemulsions are unstable. For a microemulsion of pH between 1 and 5 a stable microemulsion is yielded however a white precipitate is developed. This can be identified as an impurity from the Span 80 surfactant purchased from Sigma Aldrich. Impurities are known to originate from the synthesis or the oxidative degradation[11]; to include polyunsaturated fatty acid impurities and small ions contained in water contamination and excess ionic reactant.[11,24] Attempts to remove the impurity included pre-preparation of the stock surfactant (1:1 Span 80 : Brij 30) solution, allowing time to settle, thus allowing the upper surfactant solution to be employed. Further, stock solutions of the (1:1 Span 80 : Brij 30) surfactant were centrifuged for 1 hour to separate solid impurities.

For higher pH levels where the microemulsion has pH shifted closer to neutrality, the microemulsions are deemed stable with little macroscopic precipitation observed.

As discussed briefly in Chapter 3 a reduction in pH is associated implicitly with an increase in dissociated hydrogen or hydronium ions. Crans *et al.*[2] and Baruah[3] discuss the effects of both the introduction of an acid and alkali into a reverse microemulsion medium. Crans inferred that H_3O^+ may preferentially reside at the interface as a result of partial positive charge destabilising the O-H interactions particularly when there is little free water.[2-3]

4.4.1.3 Effect of varying the pH and the dispersed phase volume.

For small dispersed volumes of ~ 10 µl/g only minor changes occur to the pH upon the addition of HCl. (see Table 4.5) In addition, Figure 4.13 shows representative quartz nanoparticles, where a comparable quantity and size of precipitate irrespective of the HCl addition is seen. The particles are analogous to those observed in Chapter 3.

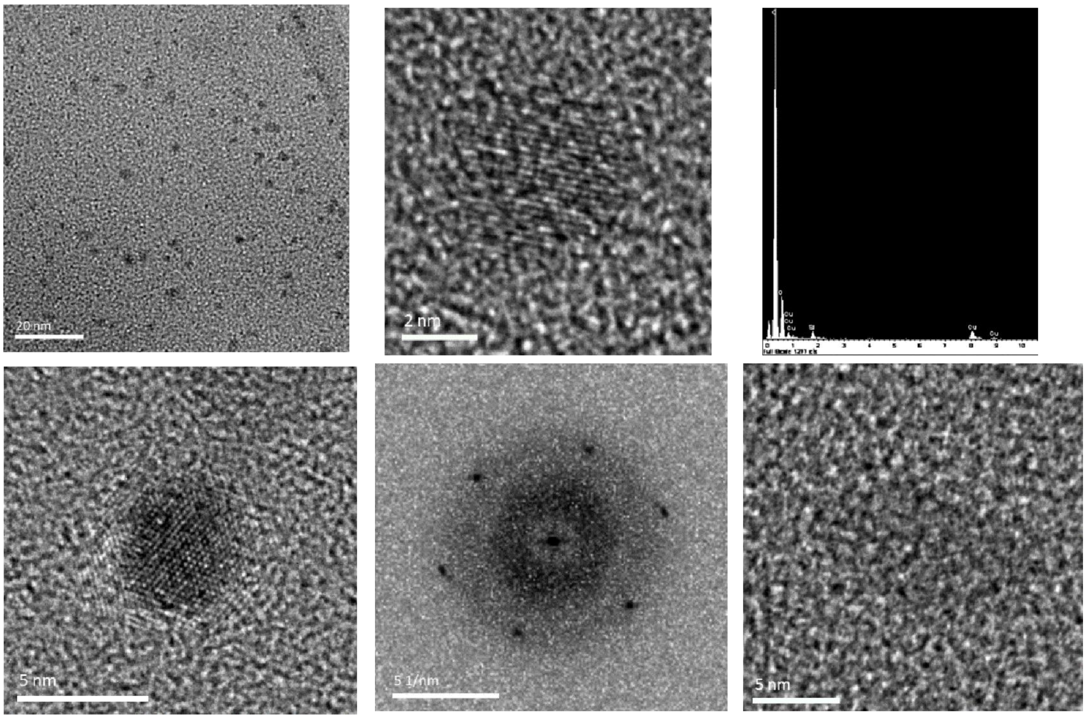

Figure 4.13: a BF image of representative material from a 1:1 Span80/Brij30/heptane microemulsion with 10 µl/2g 5 wt % SMS, b and c: HREM of nanoquartz, with EDX spectra illustrating elemental composition of sample from a 1:1 Span80/Brij30/heptane microemulsion with 10 µl/2g 5 wt % SMS + and 10 µl/2g 0.3 M HCl, d and e: HREM and corresponding FFT - [212] zone axis of nanoquartz from 10 µl/2g 5 wt % SMS + 10 µl/2g 1.5 M HCl sample and f: HREM of nanoquartz from 1:1 Span80/Brij30/heptane microemulsion with 10 µl/2g 5 wt % SMS + 10 µl/2g 2.2 M HCl sample

The effect of the varying the pH can be carried out with a larger dispersed phase volume of 100 µl/2g, where from Table 4.5 a pH range of ~1-7 is measured for a 1 wt % SMS 100 µl/2g samples with a 1:1 mixed 2.2 M, 1.5 M, 0.3 M and 0 M HCl microemulsion respectively. Thus, one can document and analyse the effect of pH and volume of dispersed phase concomitantly through comparison of Figures 4.13-4.17.

4.4.1.3.1 No HCl addition : pH ~ 7

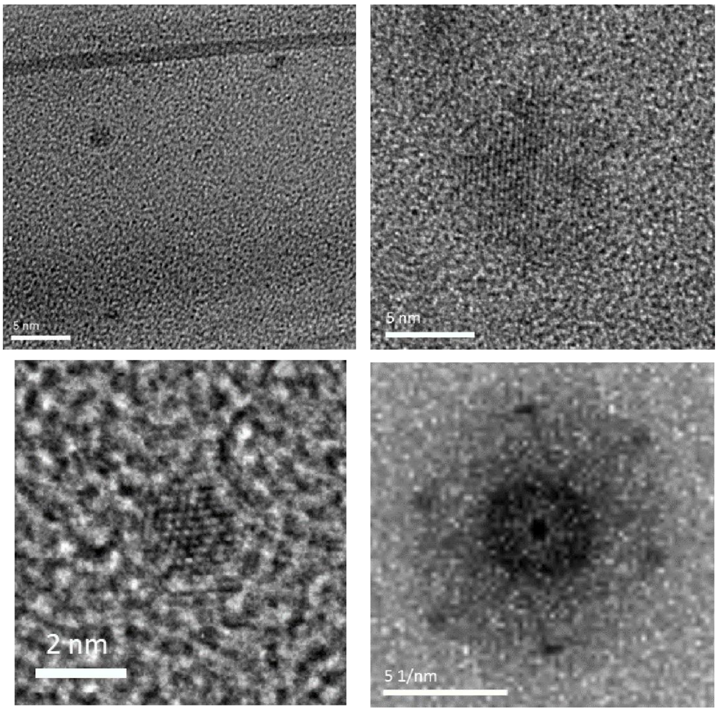

Figure 4.14 a, b and c: BF and HREM images of representative material, with corresponding d: FFT of a representative quartz nanocrystal indexed to be the [212] zone axis of quartz for a 1:1 Span80/Brij30/heptane microemulsion with 100 µl/2g 1 wt % SMS sample with a pH of 6.5.

4.4.1.3.2 0.3 M HCl addition: pH ~ 5

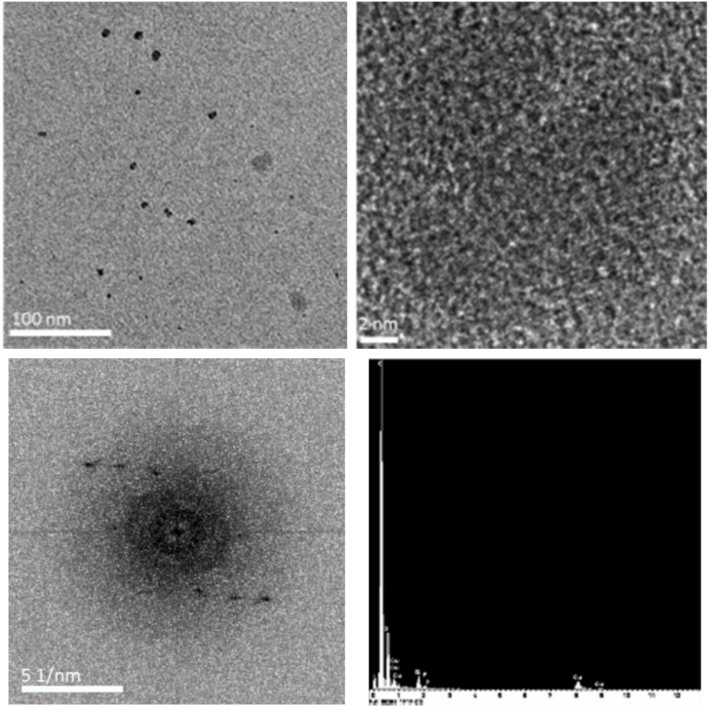

Figure 4.15 a and b: BF and HREM image of representative material, with corresponding c: FFT of a representative cristobalite nanocrystal of 1:1 Span80/Brij30/heptane microemulsion with 100 µl/2g 1 wt % SMS + 100 µl/2g 0.3 M HCl sample with a pH of 4.8

4.4.1.3.3 1.5 M HCl pH ~ 2

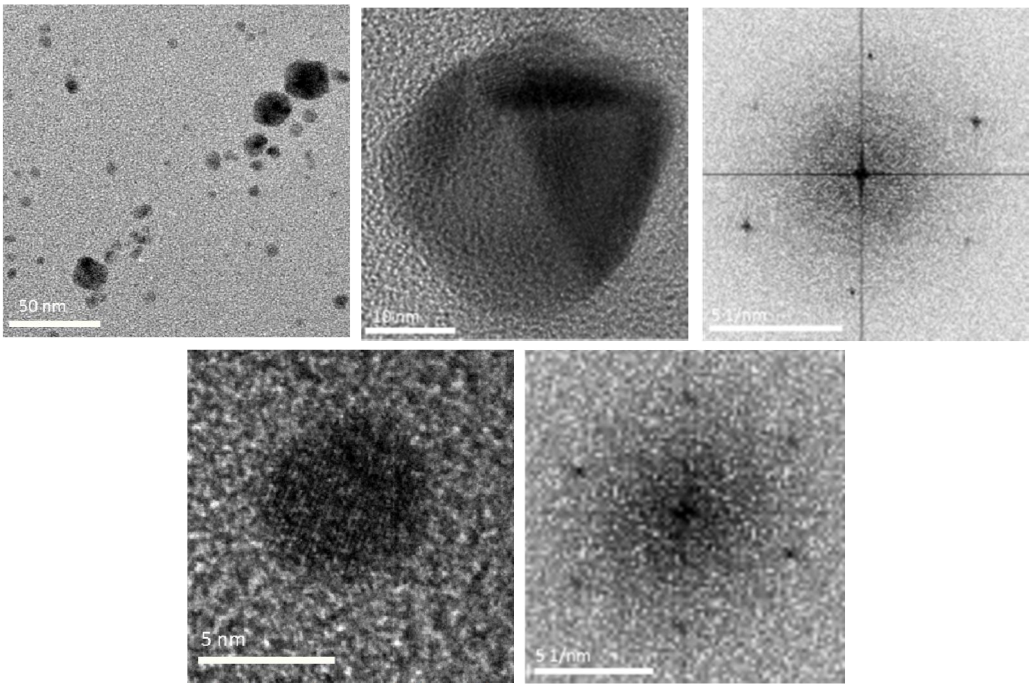

Figure 4.16 a BF images of sample, b and d: HREM image of representative material, with corresponding c and e respectively: FFT of a representative quartz nanocrystal indexed to be the [-1-10] and [212] zone axis respectively, of 1:1 Span80/Brij30/heptane microemulsion with 100 µl/2g 1 wt % SMS + 100 µl/2g 1.5 M HCl sample with a pH of 1.6.

4.4.1.3.4 2.2 M HCl addition: pH < 1

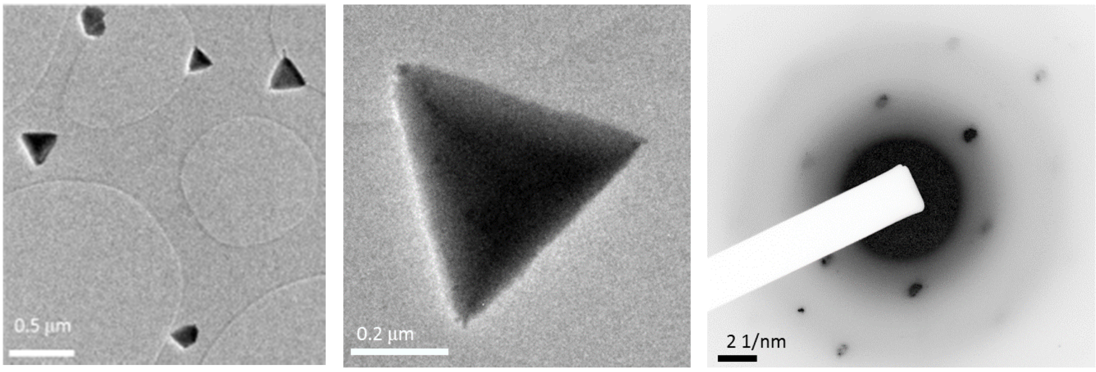

Figure 4.17 a and b: BF images of representative material, with corresponding c: DP of a representative quartz nanocrystal indexed to be the [001] zone axis of 1:1 Span80/Brij30/heptane microemulsion with 100 µl/2g 1 wt % SMS + 100 µl/2g 2.2 M HCl sample with a pH of 0.8.

Figure 4.7 presents a graphical view of the effect of varying the aqueous fraction upon the phase stability of the 1:1 Span80:Brij30/heptane system, whilst Table 4.5 documents the pH of the equivalent systems.

The effect of pH particularly upon the condensation and oligomerisation process of silica phases in addition to the ability for a microemulsion to induce a pH shift towards neutrality compared to the bulk phase has been discussed in Chapter 3. For the four aforementioned samples of 1 wt % SMS 100 μl/2g with 0 M, 0.3 M, 1.5 M and 2.2 M HCl the pH is measured to be 6.5, 4.8, 1.6 and 0.8 respectively, with the comparable bulk aqueous phase to be 12.4, 2.0, 1.1 and 0.3 respectively. For this large dispersed phase, it can be expected that the pH should be more comparable to the bulk phase, given the reduced pH shifting ability of the microemulsion at these larger dispersed volumes, and it is indeed observed that the strong acidity of HCl overwhelms the pH shift capabilities of the microemulsion.

Relating Figures 4.14 - 4.17 to the phase diagrams in Section 4.4.1.1 the microemulsions incorporating no HCl have a pH close to neutral and solely precipitate small 2 - 5 nm quartz nanocrystals. The 0.3 M HCl addition reduced the pH to that of a weak acid ~5, which predominantly precipitates small 2-5 nm quartz crystals in addition to a metastable silica polymorph: cristobalite. As the acid concentration is increased to 1.5 M and 2.2 M for large dispersed phase volumes, the pH rapidly declines to around or below 1. These changes are accompanied by a change in the size and morphology of the precipitate, moving from 2-5 nm nanocrystals to 100-500 nm triangular crystalline quartz. (See Figure 4.17) This change in crystal size arises both from an increased droplet size and decreased pH which raises the supersaturation, since both these factors provide more SiO_2 to grow the nanoquartz to larger dimensions. Additionally, the extreme pH conditions may disrupt any adsorption of surfactant upon the quartz surface, by the production of charges through the protonation of OH/SiOH groups under the extreme pH conditions, thus removing any surfactant stabilisation of smaller nanoquartz particles.[13] Upon aging of the samples, no significant difference in the size or morphology of the precipitate was observed from 24 hours onwards, with reasons discussed in Chapter 3.

4.4.1.4 SAXS Analysis and geometric droplet sizes

4.4.1.4.1 Electron density

The electron density of the dispersed phase may be estimated entirely by the relative concentrations of its components. For the SMS concentrations considered in this study, there is only a minor change to the electron density of the aqueous phase. The electron densities of each of the components or phases are displayed in Table 4.6.

Component	**Electron density / Å^{-3}**	**Electron density relative to the heptane continuous phase / Å^{-3}**
Water	0.33	0.09
HCl	0.44	0.20
SMS	0.30	0.06
Span 80 head groups	0.32 – 0.35	0.08 – 0.11
Span 80 tail groups	0.24 – 0.27	0.00 – 0.03
Brij 30 head groups $(OCH_2CH_2)_4OH$	0.32 – 0.37	0.08 – 0.13
Brij 30 tail groups $(C_{12}H_{25})$	0.24 – 0.27	0.00 – 0.03
Average head groups	0.31 – 0.36	0.07 – 0.12
Average tail groups	0.24 – 0.27	0.00 – 0.03
Heptane	0.24	0

Table 4.6: The electron densities of the components of the microemulsion A range is given upon different densities of components being adopted.

If the baseline electron density is taken to be that of the heptane continuum, one can see that taking the centre of the micellar core as an arbitrary point and moving radially outwards towards the continuum, no change in sign of the relative electron density contrast is observed. Thus the pair-distance distribution function, p(r), will show a single maximum. Also, there is very little electron density contrast in the system so that analysing the SAXS data using the GIFT software is prone to larger errors. To gain a more detailed perspective, the geometric prediction and GIFT prediction from the experimental SAXS data were computed to estimate the droplet size within the system upon the addition of 10, 50 and 100 µl/2g of surfactant and heptane continuum for the addition of 0.3 M, 1.5 M and 2.2 M HCl as previously described. The scattering and pair-distance distribution functions obtained from the raw data and GIFT analysis, espectively, from SAXS experiments are presented in Graph 4.3.

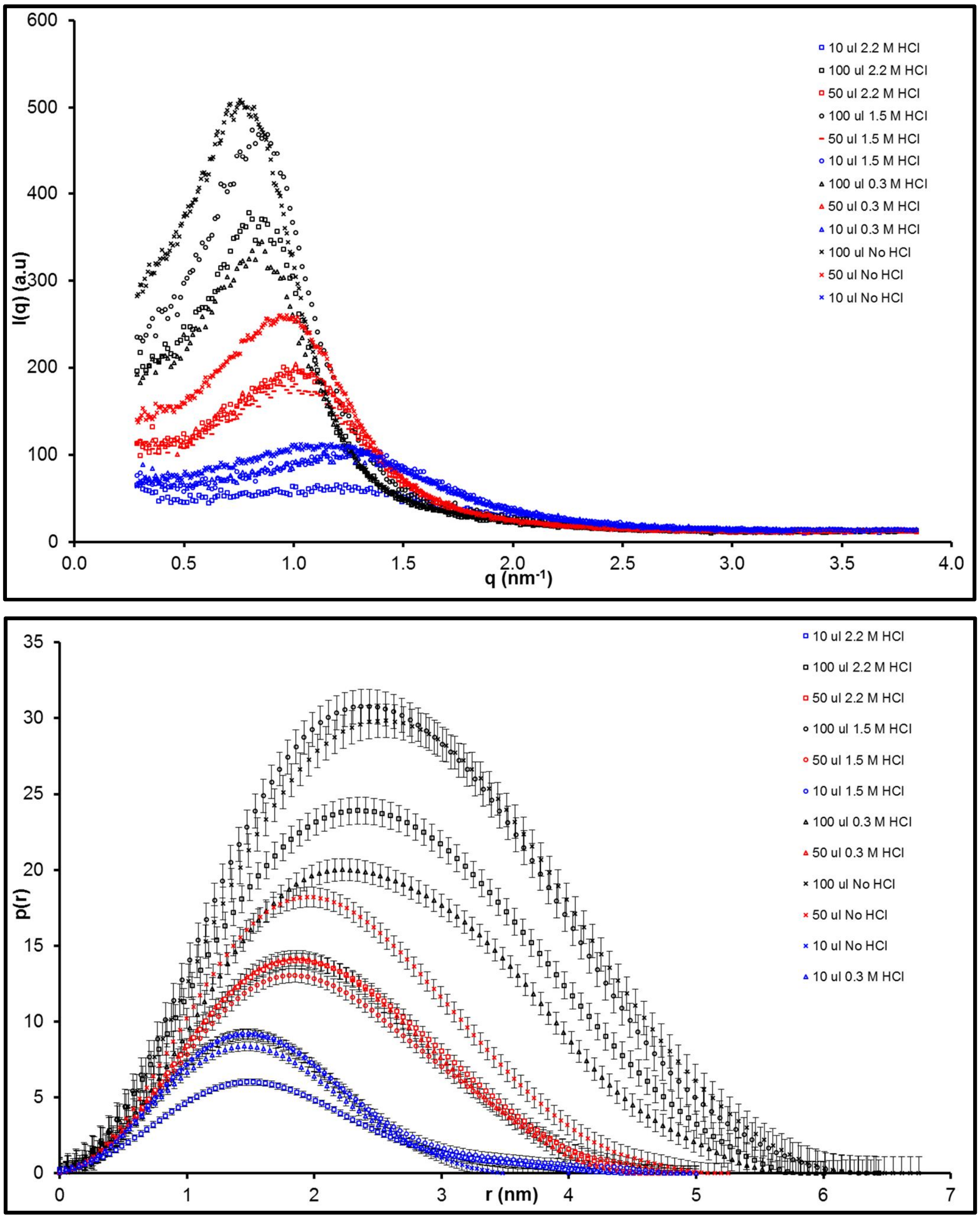

Graph 4.3 a and b: a SAXS scattering function and b: b: Pair distribution function for dispersed 1 wt %. aqueous sodium metasilicate nonahydrate

within a 40 wt %. Span 80/Brij 30/heptane system. Blue: 5 µl/g, red: 25 µl/g and black: 50 µl/g

The pair distance distribution, p(r), curves generated from the scattering data in Graph 4.3 a are obtained after the incorporation of a hard sphere structure factor in the GIFT analysis. This is included in order to account for the interdroplet interactions. This p(r), distribution function can be interpreted as a measure of the probability of the distances inside the droplet, summing over all sizes, and hence provides further information regarding the size, shape and inner structure. However note that the surfactant tails have essentially the same electron density as the heptane continuous phase, and hence only the size of the microemulsion droplets hydrophilic core can be reliably determined, particularly since heptane can penetrate into the hydrocarbon tail region to reduce the electron density contrast still further. From Graph 4.3b, an apparent increase in droplet size is seen to accompany an increase in the volume of dispersed phase, as would be expected.

The introduction of HCl appears to induce a small reduction in the measured hydrophilic core and hence whole droplet size for the cases of 50 µl/2g and 100 µl/2g dispersed volumes, though no effect is seen for the 10 µl/2g dispersed volumes. However, given the experimental error of ± 0.3 nm, the effect of acid addition upon droplet sizes is not significant and may be negligible.

Dispersed volume / µl/2g		**10**	**50**	**100**
$R_{\mathrm{GIFT-core}}$ / nm (± 0.3 nm)	**0 M HCl**	1.5	2.1	2.7
	0.3 M HCl	1.5	1.9	2.4
	1.5 M HCl	1.5	1.9	2.4
	2.2 M HCl	1.5	1.9	2.4

Table 4.7: Comparison of the droplet size of 1:1 Span80:Brij30 microemulsion with aqueous, 0.3 M, 1.5 M and 2.2 M HCl dispersed phase at various dispersed volumes.

4.4.1.5 Water perturbation

It has been previously highlighted that the outcome of the crystallisation can depend on the droplet size, particularly the water pool size. For small or negligible free water pools, crystallisation may be forced to occur close to the surfactant interface and thus templating by surfactant may dominate. Furthermore at high surfactant:water ratios, a high supersaturation may lead to rapid nucleation and less-organised nanocrystals. Thus one must calculate the quantity of water within the aqueous phase that is structurally perturbed by the surfactant interface. Numerous values have been reported regarding the number of water molecules perturbed due to ethylene oxide groups in PEO structures such as Brij 30. However, Caldararu suggested in support of Zhu and Schelly[14-16] that although variations were observed in the degree of hydration of PEO chains, beyond W = 2.5 a free water pool is observed, suggesting a Brij 30 molecule can bind to 2.5 water molecules.[14] Thus the calculation of the depth of the hydration layer is based on Caldararu's value. Table 4.8 shows how the amount of free water varies with a change in microemulsion core droplet size. One must note that a 1:1 combination of Span80:Brij 30 surfactant was employed.

4.4.1.5.1 No HCl addition

Dispersed volume / µl/2g	**10**	**50**	**100**
$R_{GIFT - core}$ / nm (± 0.3 nm)	1.5	2.1	2.7
Number of droplets per gram of microemulsion (x 10^{18})	24	9.7	5.1
Number of water molecules per droplet	14	173	650
Number of surfactant molecules per droplet	26	62	112
Number of Brij 30 surfactant molecules per droplet	13	31	56
Water taken by Brij 30 per droplet	≥14	77.5	140
Fraction of water bound to Brij 30	1.00	0.4	0.2

Table 4.8: Estimation of perturbed water molecules by surfactant from GIFT radii upon no HCl addition.

4.4.1.5.2 0.3 M HCl addition

Dispersed volume / µl/2g	**10**	**50**	**100**
$R_{GIFY - core}$ / nm (± 0.3 nm)	1.5	1.9	2.4
Number of droplets per gram of microemulsion (x 10^{18})	24	13	7.3
Number of water molecules per droplet	14	128	456
Number of surfactant molecules per droplet	26	46	79
Number of Brij 30 surfactant molecules per droplet	13	23	40
Water taken by Brij 30 per droplet	≥14	57.5	100
Fraction of water bound to Brij 30	1.00	0.45	0.22

Table 4.9: Estimation of perturbed water molecules by surfactant from GIFT radii upon 0.3 M HCl addition.

4.4.1.5.3 1.5 M and 2.2 M HCl addition

Dispersed volume / µl/2g	**10**	**50**	**100**
$R_{GIFT - core}$ / nm (± 0.3 nm)	1.5	1.9	2.4
Number of droplets per gram of microemulsion (x 10^{18})	24	13	7.3
Number of water molecules per droplet	14	128	456
Number of surfactant molecules per droplet	26	46	79
Number of Brij 30 surfactant molecules per droplet	13	23	40
Water taken by Brij 30 per droplet	≥14	57.5	100
Fraction of water bound to Brij 30	1.00	0.45	0.22

Table 4.10 Estimation of perturbed water molecules by surfactant from GIFT radii upon 2.2 M HCl addition

As shown in each table, for the various acid concentration additions above, when the dispersed phase is increased from 10-100 µl/2g and the core radius increases from 1.5 to 2.7 nm, the percentage of water molecules perturbed by the surfactant layer decreases from ~100 % to ~ 20 %. This reveals, as expected, an increase in the free-water pool size with dispersed phase volume. This may result in a greater degree of self-organisation, thus making the resultant crystals that are uniform as the size of the droplet increases as observed in Section 4.4.1.4.

4.4.1.6 Effect of varying the SMS precursor concentration.

SMS concentrations between 1 and 5 wt %. were employed in the microemulsion system. Little macroscopic precipitate was observed for any concentration of SMS, thus TEM was utilised to image any nanoscopic material.

4.4.1.6.1 No HCl addition

The analysis of samples with no HCl addition was completed in Chapter 3. An associated increase in the quantity of nanoparticles precipitated with increasing precursor concentrations is observed; however no change in the morphology or size (2-5 nm) of the aforementioned particles is observed. Each of the representative nanoparticles are indexed to be the [201] zone axis of quartz.

4.4.1.6.2 0.3 M HCl addition

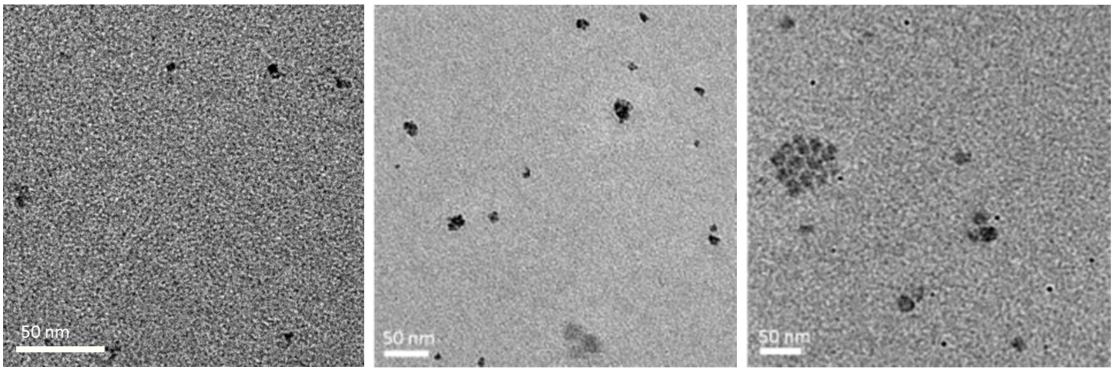

Figure 4.18 a - c, BF images for 0.25 wt %, 1 wt % and 5 wt % SMS respectively of 1:1 Span80/Brij30/heptane microemulsion with 10 µl/2g SMS + 10 µl/2g 0.3 M HCl sample.

4.4.1.6.3 1.5 M HCl addition

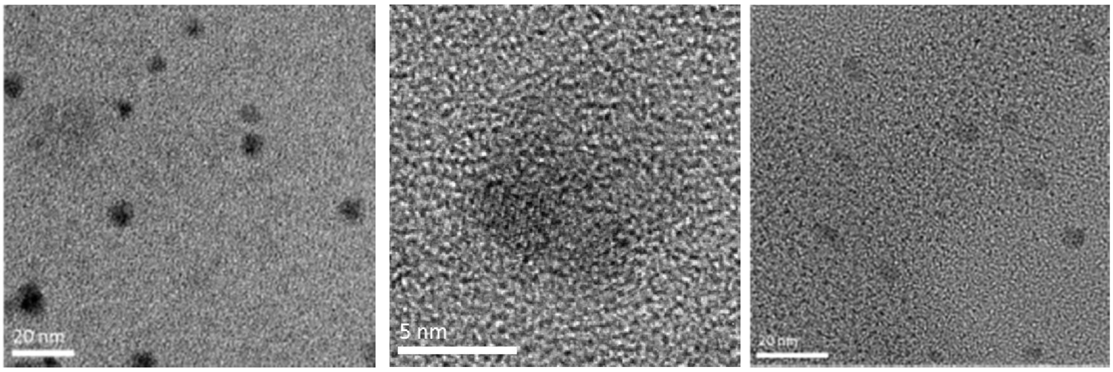

Figure 4.19a, and c: BF or b: HREM images of representative material for 0.25 wt %, 3 wt % and 5 wt % SMS respectively of 1:1 Span80/Brij30/heptane microemulsion with 10 µl/2g SMS + 10 µl/2g 1.5 M HCl sample.

4.4.1.6.4 2.2 M HCl addition

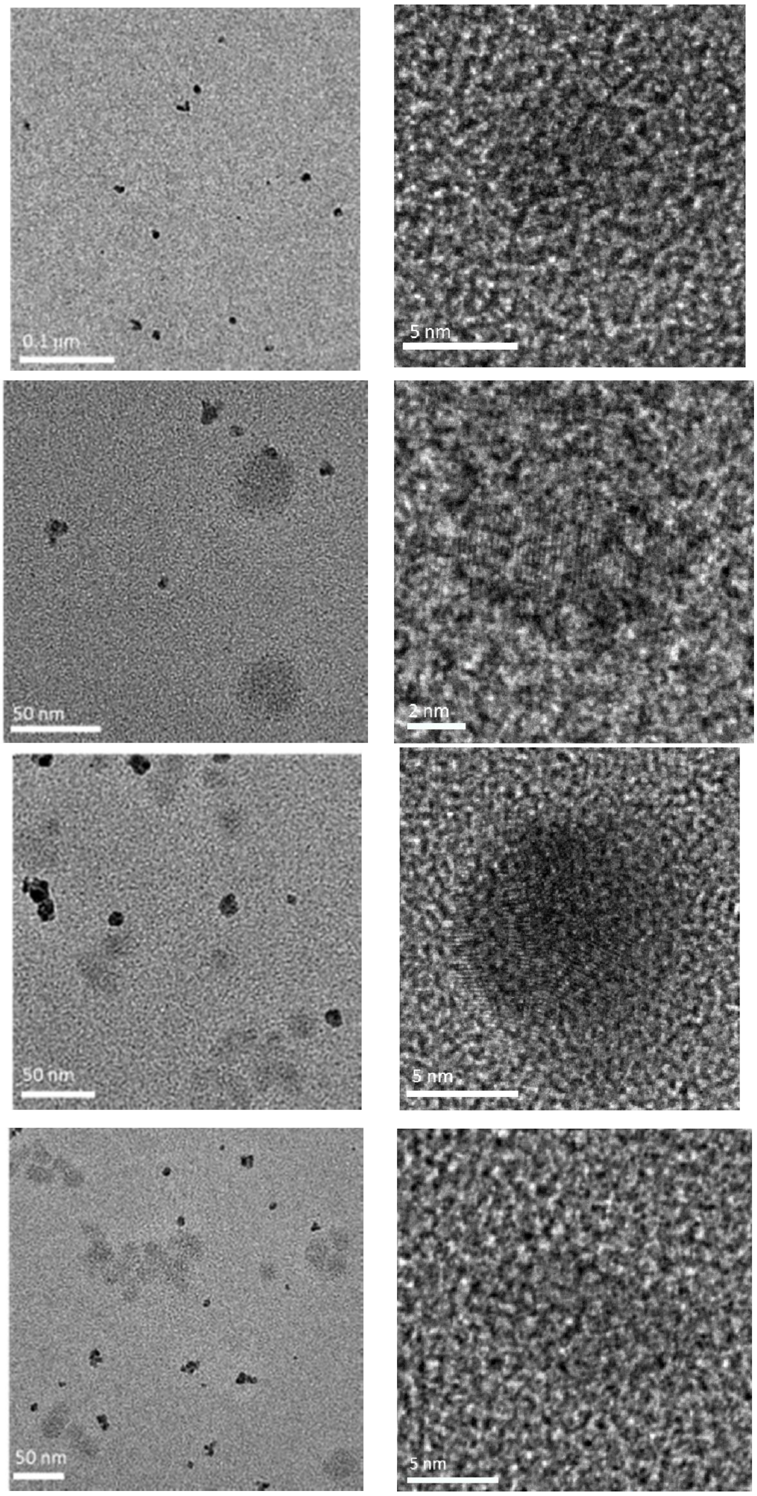

Figure 4.20 a, c, e and g: BF images of representative material for 0.25 wt %, 1 wt %,3 wt % and 5 wt % SMS respectively and b, d, f and I: HREM images of representative material of 1:1 Span80/Brij30/heptane microemulsion with 10 µl/2g SMS + 10 µl/2g 2.2 M HCl sample.

For 0 M, 0,3 M, 1.5 M and 2.2 M HCl additions to microemulsions containing 10 µl/2g dispersed phase volumes, varying SMS concentrations between 1 and 5 wt% were analysed. Varying the SMS concentration from 1 to 5 wt %. had no effect on the probe measured pH value. In particular: for 10 µl/2g dispersed phase volumes, the pH of 0.3 M HCl added microemulsions was 5.6-5.8, for 1.5 M HCl added microemulsions the pH was 5.1-5.7 and for 2.2 M HCl added microemulsions the pH was 5.2-5.4. Note the significant shift towards neutrality for these small dispersed phase volumes. The precipitate was found to be nanoquartz in all cases, with no evidence of other silica polymorphs being found. Comparisons of the bright field (BF) images in Figures 4.18-4.20 show an associated increase in the quantity of nanoparticles precipitated with increasing precursor concentration irrespective of the concentration of HCl added; however no major change in the morphology or size of the aforementioned particles is observed with respect to an increase in SMS precursor concentration.

4.4.1.7 Estimated silica concentration within the droplet

SAXS measurements were performed to determine an approximate droplet size via GIFT analysis. Assuming the droplet size remains independent of the SMS precursor concentration, one can estimate the average number of silica molecules per droplet to be expected for a completely mono-disperse system, see Table 4.11.

Only the aqueous case is discussed as it has been highlighted that the addition of acid makes negligible difference to the droplet size.

Dispersed volume / µl/2g		**10**	**50**	**100**
$R_{GIFT - core}$ / nm (± 0.3 nm)		1.5	2.1	2.7
Number of droplets per gram of microemulsion (x 10^{18})		24	9.7	5.1
Mean number of silica molecules per droplet	**1 wt % SMS**	0.008 ± 0.005	0.10 ± 0.04	0.4 ± 0.1
	2 wt % SMS	0.016 ± 0.005	0.20 ± 0.04	0.8 ± 0.1
	3 wt % SMS	0.025 ± 0.005	0.31 ± 0.04	1.2 ± 0.1
	4 wt % SMS	0.033 ± 0.005	0.41 ± 0.04	1.6 ± 0.1
	5 wt % SMS	0.041 ± 0.005	0.51 ± 0.04	1.9 ± 0.1
	6 wt % SMS	0.049 ± 0.005	0.61 ± 0.04	2.3 ± 0.1

Table 4.11 Estimation of silica molecule number in each droplet

This approximation indicates that most droplets contain no silica molecules so there appears to be insufficient precursor present to allow the precipitation of silica within any one droplet based on the solubility of silica phases. One can rationalise the observation of crystalline nanomaterial being observed by TEM, primarily by the degree of polydispersity among the droplets within the microemulsion, with further suspected contributing factors. Larger droplets are expected to contain a larger number of silica molecules so that the largest may support quartz nucleation. Secondly, the exchange of material to promote further growth beyond the nucleation stage is supported by the occurrence of transient dimer formation between energetic colliding droplets as detailed in Chapter 1 and Chapter 3.

4.5 Triton X-100 system

4.5.1 Microemulsion preparation

The same method as described in Chapter 3 was adopted to prepare the microemulsions. The 2.2 M HCl was added in a 1:1 vol. with respect to the SMS aqueous dispersed phase, via both a mixed microemulsion methodology as described in Chapter 2, Section 2.2.1 and via direct addition to the SMS containing microemulsion. Microemulsions were left for varying degrees of time (1 hour – 3 years) before analysis was performed.

4.5.2 Microemulsion experiments

Using the 3D nanoconfinement of microemulsion droplets, the following variables are to be investigated: the effect of the addition of HCl both via a direct addition and mixed microemulsion method has upon the process of nucleation, precipitation and crystal growth or aggregation.

4.6 TX-100/hexanol/cyclohexane: Results and discussion

To determine the range over which 3D confinement within the microemulsion is maintained, a series of systematic experiments, varying the concentration of aqueous SMS alongside the droplet size of the dispersed phase were completed. The range of concentrations and volumes stabilised are illustrated in Section 4.6.1.

Despite SMS being readily soluble in water, from initial studies, supersaturated solutions often initiated immediate destabilisation of the microemulsion. This may be due to a number of factors including: perturbation of water molecules by the surfactant or elevated pH levels within the dispersed phase.

4.6.1 55 wt % (2.2) Triton X-100 : (1) 1-hexanol in cyclohexane microemulsion system

In addition to the phase diagrams presented in Section 4.4.1, the macroscopic observations of this TX100/hexanol/cyclohexane microemulsion systems are documented, to show both the dependency on the concentration of the SMS precursor, the concentration of HCl and the volumes of dispersed phase. The effects will be discussed further.

4.6.1.1 Effect of acid addition upon the phase diagram stability

4.6.1.1.1 No HCl addition

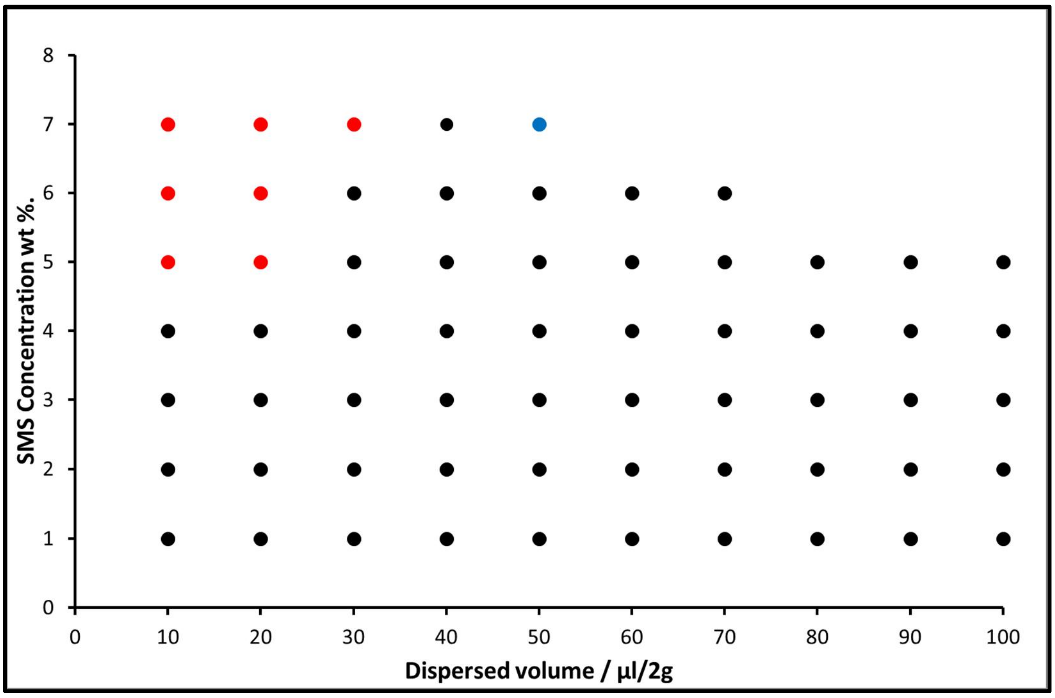

Figure 4.21 Graphical display of microemulsion compositions with varying SMS concentration and dispersed volume, and the effect upon the stability. Black = microemulsion, red = immediate precipitation of amorphous silicate phase and blue = unstable

As one would expect the material synthesised from the microemulsion is dependent upon a combination of both the SMS precursor concentration, the dispersed volume, in addition to the concentration of HCl added. SMS concentrations between 1 and 7 wt %. were employed in the microemulsion system, however beyond 4 wt % SMS for small dispersed volumes stable microemulsions could not be obtained. Similarly, little macroscopic precipitate was observed for any precursor concentration, hence TEM was utilised to image any nanoscopic material.

4.6.1.1.2 2.2 M HCl - Direct addition

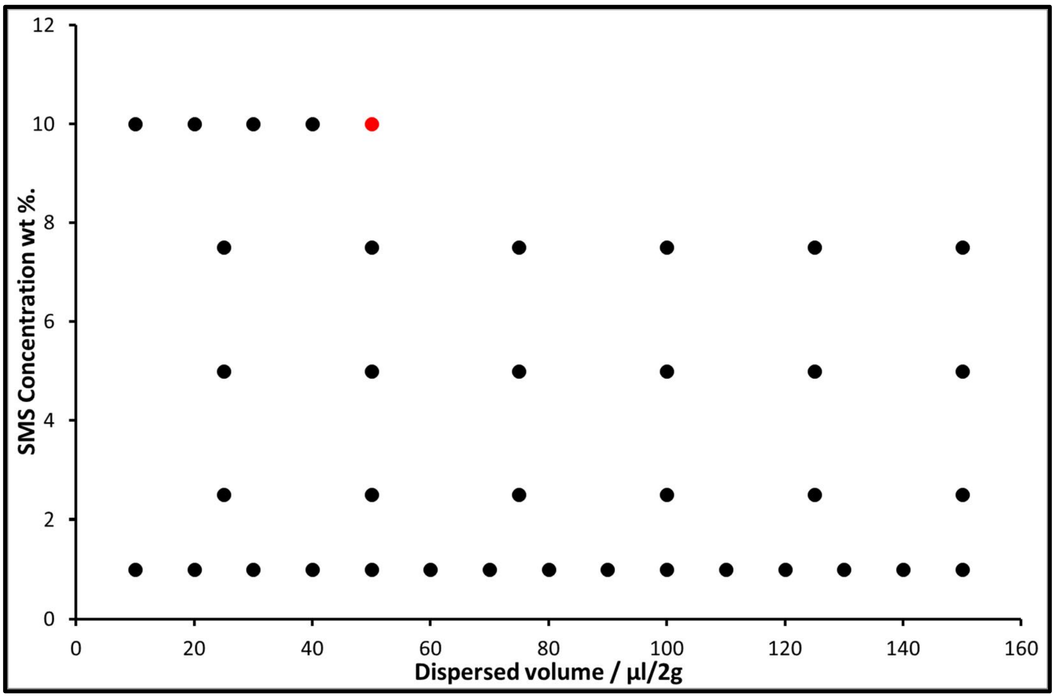

Figure 4.22 Graphical display of microemulsion compositions with varying SMS concentration and dispersed volume, and the effect upon the stability upon the direct addition of 2.2 M HCl. Black = microemulsion, red = immediate precipitation of amorphous silicate phase.

In comparison to the case where no HCl is added, larger dispersed volumes are capable of being stabilised along with higher SMS precursor concentrations. SMS concentrations between 1 and 10 wt %.SMS. were employed in the microemulsion system, with only dispersed phases above 50 µl/2g unstable for 10 wt %. SMS precursor concentrations. Similarly, little macroscopic precipitate was observed for any precursor concentration, hence TEM was utilised to image any nanoscopic material.

4.6.1.1.3 2.2 M HCl - Mixed microemulsion addition

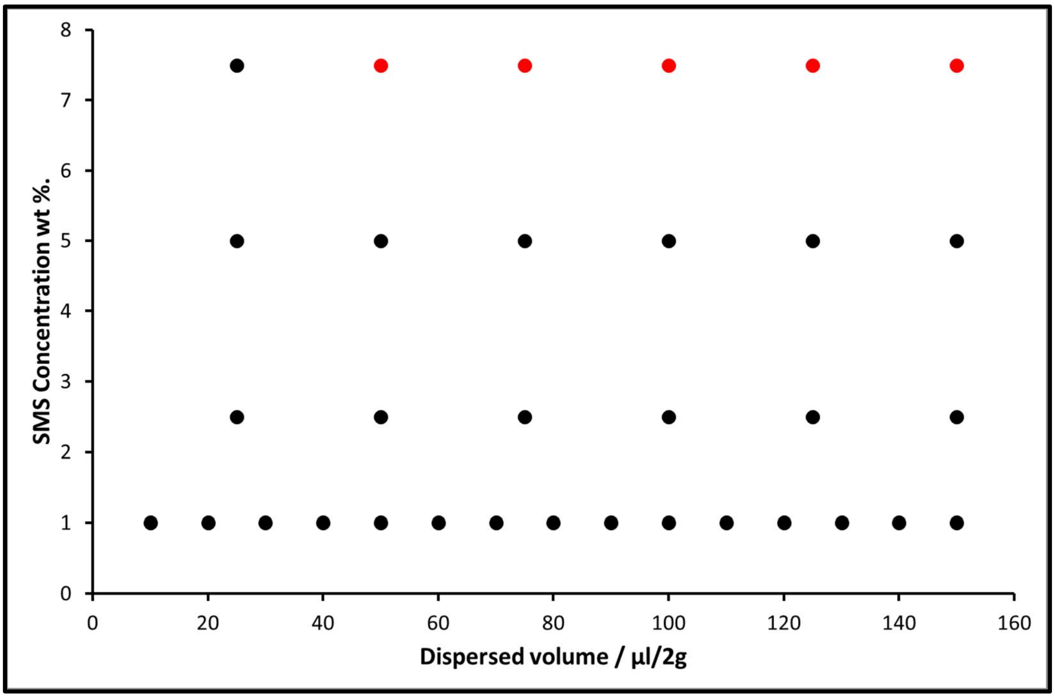

Figure 4.23 Graphical display of microemulsion compositions with varying SMS concentration and dispersed volume, and the effect upon the stability upon the mixed microemulsion addition of 2.2 M HCl. Black = microemulsion, red = immediate precipitation of amorphous silicate phase and blue = unstable

In comparison to the direct addition of 2.2 M HCl, lower SMS precursor concentrations are capable of being stabilised, i.e. < 5 wt % SMS. SMS concentrations between 1 and 7.5 wt %. SMS were employed in the microemulsion system for a similar range of dispersed phases to the direct addition. Stability was generally lost for SMS concentrations above 5 wt %. SMS. Similarly, little macroscopic precipitate was observed for any precursor concentration, hence TEM was utilised to image any nanoscopic material.

4.6.1.2 pH

SMS (% wt.)	Dispersed volume (µl/2g)	Addition of 2.2 M HCl	pH	SMS (% wt.)	Dispersed volume (µl/2g)	Addition of 2.2 M HCl	pH
1	25	No HCl	9.2 ± 0.1	5	25	No HCl	9.6 ± 0.1
		Direct	0.8 ± 0.1			Direct	1.7 ± 0.1
		Mixed	0.3 ± 0.1			Mixed	0.4 ± 0.1
	100	No HCl	9.4 ± 0.2		100	No HCl	9.7 ± 0.1
		Direct	1.0 ± 0.1			Direct	1.0 ± 0.2
		Mixed	0.7 ± 0.1			Mixed	0.7 ± 0.1
2.5	25	No HCl	8.6 ± 0.1	7.5	25	No HCl	10.4 ± 0.1
		Direct	1.1 ± 0.1			Direct	1.9 ± 0.1
		Mixed	0.1 ± 0.1			Mixed	0.4 ± 0.1
	100	No HCl	10.1 ± 0.2		100	No HCl	10.9 ± 0.1
		Direct	1.0 ± 0.1			Direct	1.0 ± 0.1
		Mixed	1.0 ± 0.1			Mixed	0.9 ± 0.2

Table 4.12 : pH measurements of 55 wt % (2.2) Triton X-100 : (1) 1-hexanol in cyclohexane microemulsion system with variation of both dispersed volume and SMS precursor concentration and 2.2 M HCl added by a direct addition and a mixed microemulsion method.

Similar to prior measurements the pH within microemulsion confinements was measured using a pH probe. The values are documented in Table 4.12 above. Note, that the pH of the comparable microemulsion system with a UHQ water dispersed phase is ~ 7.5, for the range of dispersed phase employed, whereas the pH of the unconfined aqueous metasilicate solutions ranges between 12-13, with the pH of the HCl microemulsion being ~0.3. Considering the data from Table 4.12, one can infer, that for all dispersed phases a move towards neutrality is observed with respect to the unconfined aqueous silicate and acid solutions.

For all dispersed phases, upon the addition of 2.2 M by both direct HCl addition and HCl microemulsion addition methods, the resultant microemulsion is very acidic, however there is a slightly greater shift towards neutrality for the smaller dispersed phases of 25 µl/2g for most SMS precursor concentrations compared to the larger dispersed phases of 100 µl/2g, which are more comparable to the unconfined bulk system of a pH ~ 0.3. As for previous experiments, one can suggest that this is due to the degree of pH shifting being dependent upon the dispersed volume, in addition to the strong acidity of the HCl overwhelming the pH shift of the microemulsion for larger dispersed phase volumes.

Conversely to the Span80:Brij30 system, the addition of acid to the TX-100 surfactant system widens the stable region of the phase diagram. As noted previously the addition of an acid in particular and thus the pH, is known to have a varied effect upon emulsion formation which is largely dependent on the surfactant utilised.[5-7]

4.6.1.2.1 Effect of varying the pH for a given dispersed phase volume.

4.6.1.2.1.1 No HCl addition

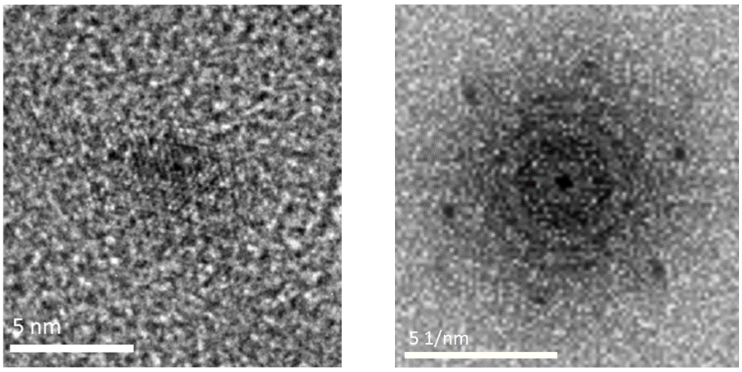

Figure 4.24 a HREM image of representative material, and b: corresponding FFT indexed to be the [00-1] zone axis of 55 wt % (2.2) Triton X-100 : (1) 1-hexanol in cyclohexane microemulsion with 25 µl/2g 5 wt % SMS sample. pH = 9.6

4.6.1.2.1.2 2.2 M HCl – Direct addition

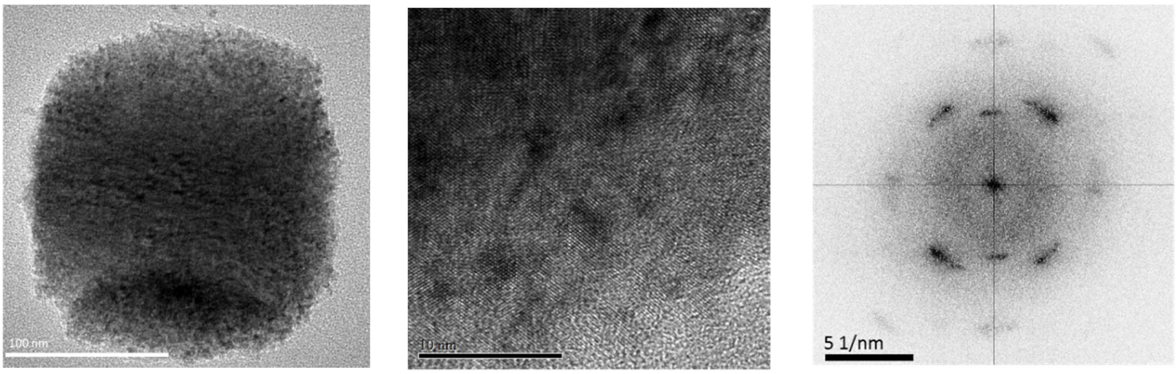

Figure 4.25 a: BF, b: HREM image of representative material, and c: corresponding FFT indexed to be the [1-1-4] zone axis from a 55 wt % (2.2) Triton X-100 : (1) 1-hexanol in cyclohexane microemulsion with 25 µl/2g 5 wt % SMS + 1:1 2.2 M HCl direct addition sample. pH = 1.7

4.6.1.2.1.3 2.2 M HCl – Mixed microemulsion addition

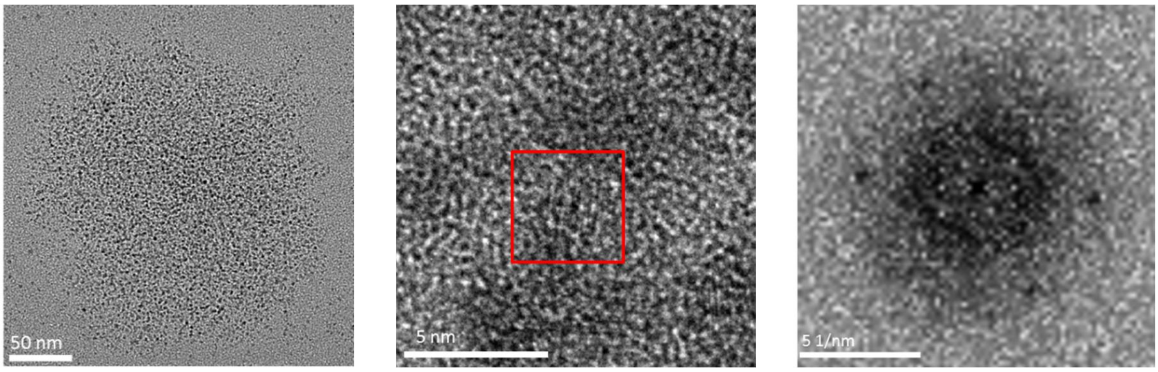

Figure 4.26 a: BF, b: HREM image of representative material, and c: corresponding FFT indexed to be the [001] zone axis of quartz from a 55 wt % (2.2) Triton X-100 : (1) 1-hexanol in cyclohexane microemulsion with 25 µl/2g 5 wt % SMS + 1:1 2.2 M HCl mixed microemulsion addition sample. pH = 0.4

There is an observed decrease in pH from 9.6 with no HCl, to 1.7upon the addition of HCl through direct addition, to 0.4 for the addition of HCl via a mixed microemulsion method. One can note a change in the morphology, ordering and level of aggregation in the precipitate. For the addition of no HCl only small 2-5 nm quartz nanoparticles which are comparable to the size of the microemulsion droplets are obtained. Moving passed neutrality to a pH of 1.7, large ordered square shaped structures of the order of 50-200 nm in dimension are observed, where each structure consists of many smaller nanoparticles. The HREM indicates regions of varying electron densities, both FFTs and DPs of the region reveal quartz single crystal-like properties, instead of polycrystalline properties, suggesting these crystals are of similar nature to mesocrystals or iso-oriented crystals. One can postulate the small nanoparticles observed when no HCl is added are the building blocks to the large nanoaggregate structures.

As the pH recedes further to 0.4, the nanoaggregates appear less complete, however the initial stages of the structures can be observed. One can see the gradual addition of the quartz nanoparticles to form the larger ordered nanoaggregate structures.

This indicates that the presence of an acid, with an excess of hydrogen ions encourages the formation of the nanoaggregates structures, possibly indicating that hydrogen bonding is involved in their formation. However upon the acid receding to below ~ 1, poorly aggregated structures are obtained both for the direct addition of HCl, but particularly for the mixed microemulsion addition.

4.6.1.3 Effect of varying the SMS precursor concentration.

As observed from Section 4.6.1.1, SMS concentrations between 1 and 10 wt %. SMS were employed in the microemulsion system. Little macroscopic precipitate was observed for any concentration of SMS, thus TEM was utilised to image any nanoscopic material which is documented below.

4.6.1.3.1 No HCl addition

Figures 4.27 and 4.28 show TEM data for a constant dispersed phase of 10μl/2g in a (2.2) Triton X-100 : (1) 1-hexanol surfactant continuum with no HCl added; images are presented for SMS concentrations of 5 and 15 wt %. respectively.

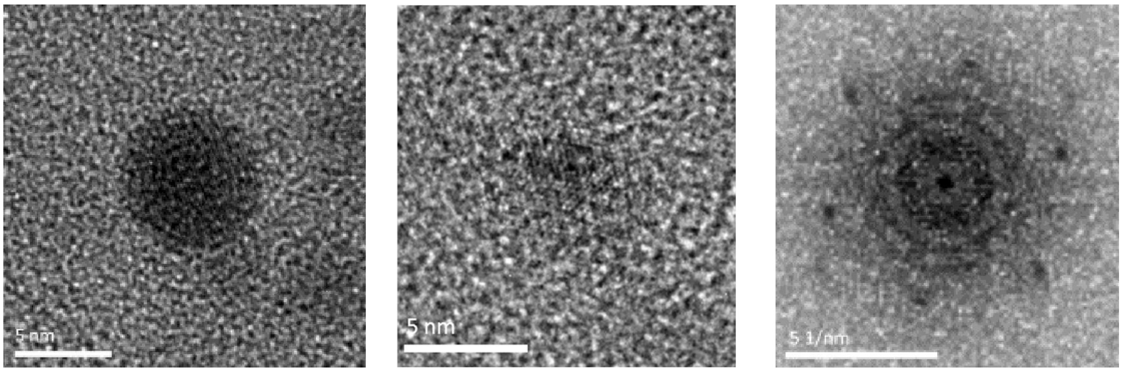

Figure 4.27 a: BF, b: HREM image of representative material, and c: corresponding FFT indexed to be the [00-1] zone axis of quartz from a 55 wt % (2.2) Triton X-100 : (1) 1-hexanol in cyclohexane microemulsion with 10 µl/2g 5 wt % SMS. pH ~ 9.6

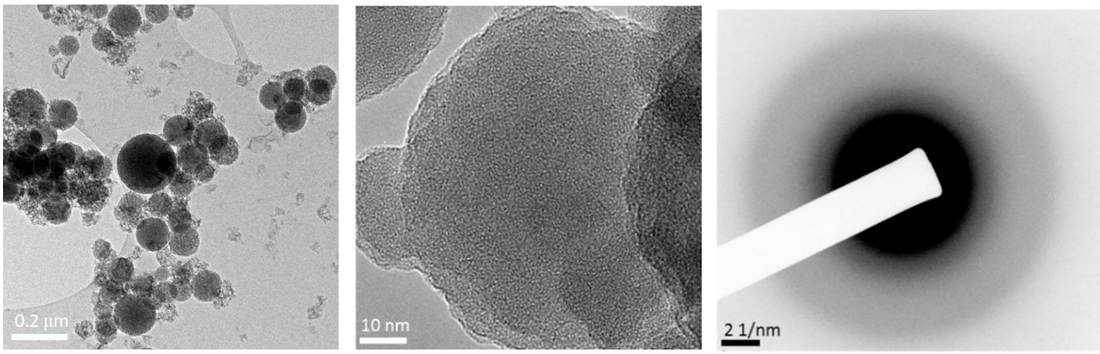

Figure 4.28a and b: BF, and c: corresponding DP highlighting the material to be an amorphous silica phase of 55 wt % (2.2) Triton X-100 : (1) 1-hexanol in cyclohexane microemulsion with 10 µl/2g 15 wt % SMS. pH > 11.

As per observations made in Chapter 3 the increase in the concentration of precursor has resulted in a different polymorphic outcome. As the concentration has increased from 5 to 15 wt %. SMS a shift in the majority polymorph from the stable crystalline quartz form to the metastable amorphous phase, confirmed by the broad halos is observed. Precipitation of the most stable form is favoured when crystallisation is just deemed possible, i.e. when there is only just sufficient material present to form near-stable nuclei of the thermodynamically most stable form. Increasing the supersaturation beyond this point allows metastable forms to also produce near-stable nuclei, and at a greater rate. Thus despite the nanoconfinement, the surplus material helps promote kinetic control, hence thermodynamic control is lost, allowing the formation of metastable nanocrystals and amorphous phase.

4.6.1.3.2 2.2 M HCl - Direct addition

The same analysis is to be completed for the direct addition of 2.2 M HCl to the microemulsions. From Figure 4.29 for a constant dispersed phase of 25 µl/2g in a (2.2) Triton X-100 : (1) 1-hexanol surfactant continuum with 2.2 M HCl added via direct addition; images are presented for SMS concentrations of 2.5, 5 and 7.5 wt %.

25 µl 2.5 wt % SMS + 1:1 2.2 M HCl Direct addition

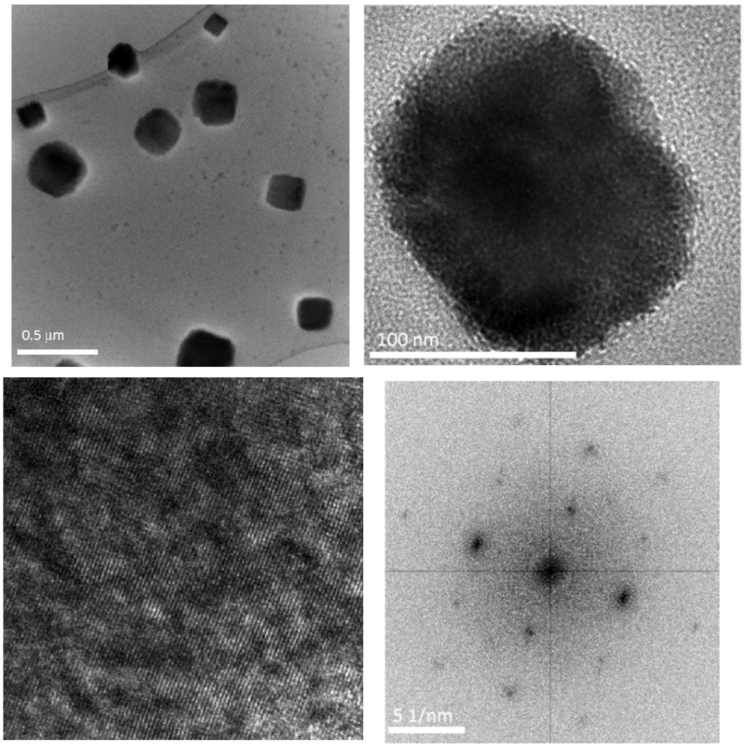

Figure 4.29 a: BF, b and c: HREM image of representative material, and d: corresponding DP indexed to be the [1-1-4] zone axis of quartz from a 55 wt % (2.2) Triton X-100 : (1) 1-hexanol in cyclohexane microemulsion with 25 µl/2g 2.5 wt % SMS + 1:1 2.2 M HCl direct addition sample. pH = 1.1

25 µl 5 wt % SMS + 1:1 2.2 M HCl Direct addition

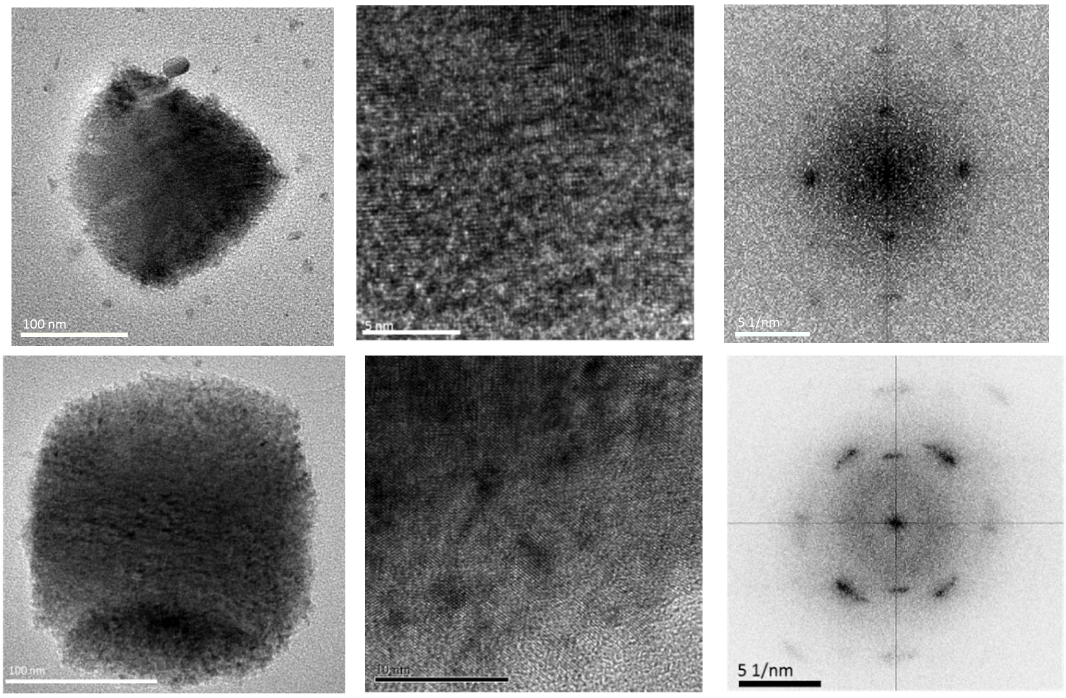

Figure 4.30 a and d: BF, b and e: HREM image of representative material, and c and f: corresponding FFT and DP indexed to be the [1-1-4] zone axis of quartz from a 55 wt % (2.2) Triton X-100 : (1) 1-hexanol in cyclohexane microemulsion with 25 µl/2g 5 wt % SMS + 1:1 2.2 M HCl direct addition sample. pH = 1.7

25 µl 7.5 wt % SMS + 1:1 2.2 M HCl Direct addition

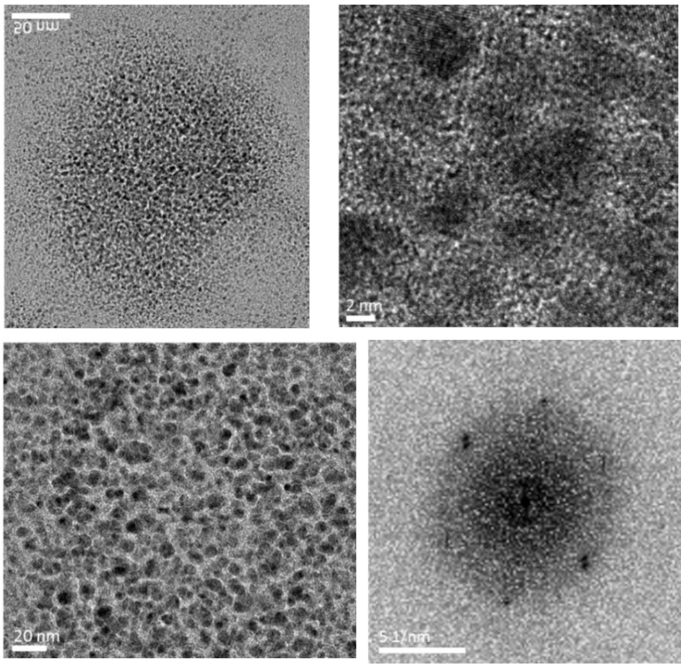

Figure 4.31 a and c: BF, b: HREM image of representative material, and d: corresponding FFT of the individual nanoparticles indexed to be the [1-1-4] zone axis of quartz for 55 wt % (2.2) Triton X-100 : (1) 1-hexanol in cyclohexane microemulsion with 25 µl/2g 7.5 wt % SMS + 1:1 2.2 M HCl direct addition sample. pH = 1.0

Figures 4.29-4.31 reveal the TEM data from three samples with a dispersed phase of 25 µl/2g and 1:1 2.2 M HCl direct addition with differing SMS concentrations of 2.5, 5 and 7.5 t % SMS precursor. As the concentration of SMS precursor is increased, instead of a change in the polymorphic outcome, there is a change in the morphology, particularly the level of nanoparticle aggregation. A gradual decrease in the degree of organisation of the nanoaggregates with an increase in SMS precursor concentration is observed. A large contrast can be seen between the 2.5 and 7.5 wt % SMS samples from Figures 4.29 and 4.31. For 2.5 wt % SMS a well-defined single crystal-like DP is generated, however for 7.5 wt % SMS no agglomeration or partial agglomerated material is seen. For 5 wt. % SMS partial agglomeration is exhibited, in Figure 4.30a, with poor alignment of the nanoparticles resulting in arcing of the DP pattern in Figure 4.30c.

4.6.1.3.3 2.2 M HCl - Mixed microemulsion addition

For the addition of HCl via mixed microemulsions no trends in morphology of precipitate were observed. Both small quartz nanocrystals and initial stages of nanoaggregates were observed as seen in Section 4.6.1.3 for 2.5 and 5 wt %. SMS precursor concentrations. No further organised nanoaggregate structures were observed.

4.6.1.4 Effect of varying the dispersed phase volume

The Figures below reveal TEM data obtained from microemulsion samples of 2.5 and 5 wt % SMS precursor, with differing volumes of dispersed phases (25 µl and 100 µl/2g) for 2.2 M HCl addition, by direct and mixed microemulsion methods.

4.6.1.4.1 2.2 M HCl - Direct addition

TEM data from 2.2 M HCl direct addition are shown in Figures 4.32-4.35. Figures 4.32-4.33 reveal the TEM data from two samples with a SMS precursor concentration of 2.5 wt % SMS with dispersed phases of 25 μl/2g and 100 μl/2g with 1:1 2.2 M HCl direct addition respectively. As the droplet size is increased there are two apparent changes in the precipitate. As the dispersed volume is increased from 25 to 100 μl/2g, firstly there is a change in the morphology, particularly the level of nanoparticle aggregation with a decrease in the degree of organisation of the nanoaggregates and secondly a change in the polymorphic outcome from the stable quartz phase to a metastable amorphous silica phase

25 μl 2.5 wt % SMS + 1:1 2.2 M HCl Direct addition

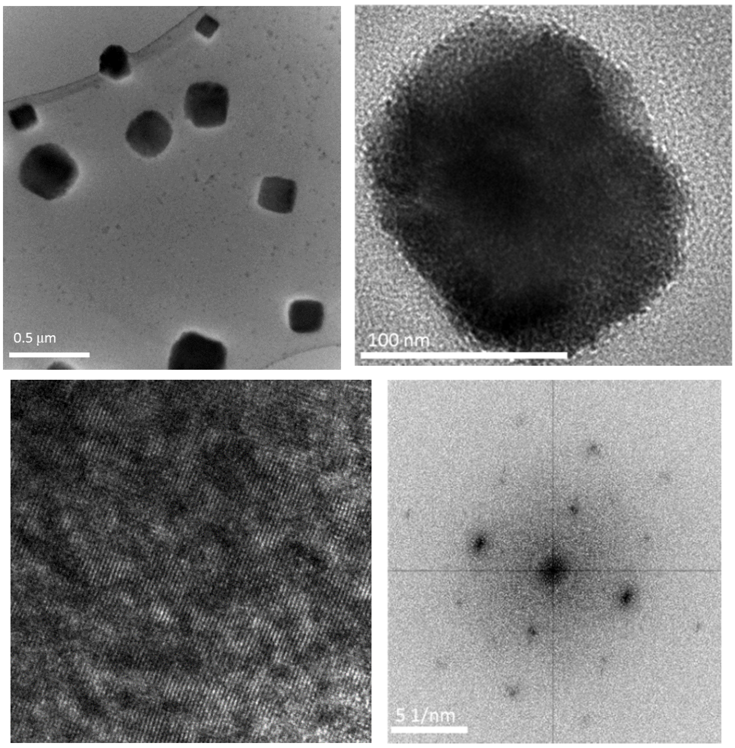

Figure 4.32 a and b: BF, c: HREM image of representative material, and d: corresponding FFT indexed to be the [1-1-4] zone axis of quartz from a 55 wt % (2.2) Triton X-100 : (1) 1-hexanol in cyclohexane microemulsion with 25 μl/2g 2.5 wt % SMS + 1:1 2.2 M HCl direct addition sample. pH = 1.1

100 µl 2.5 wt % SMS + 1:1 2.2 M HCl Direct addition

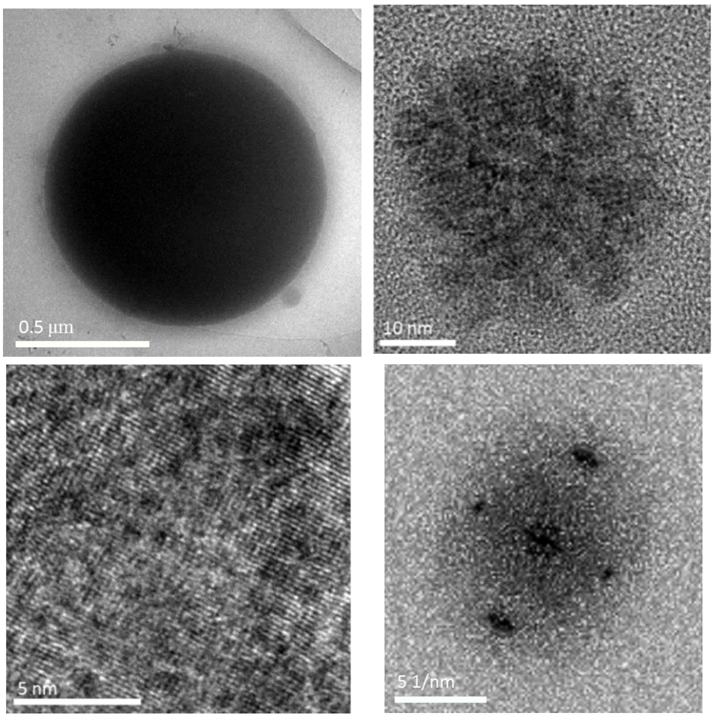

Figure 4.33 a and b: BF, c: HREM image of representative material, and d: corresponding FFT indexed to be the [1-1-4] zone axis of quartz from a 55 wt % (2.2) Triton X-100 : (1) 1-hexanol in cyclohexane microemulsion with 100 µl/2g 2.5 wt % SMS + 1:1 2.2 M HCl direct addition sample. pH = 1.0

The decline in the level of aggregation with increased dispersed phase volume is comparable with that observed for an increase in SMS precursor concentration documented in Section 4.7.2.2. The structures are incomplete with partial agglomeration exhibited, and slight arching is seen in the corresponding DP of the material suggesting poor alignment of the nanoparticles. Figures 4.34-4.35 illustrate the TEM data from two samples with a SMS precursor concentration of 5 wt %. SMS with dispersed phases of 25 µl/2g and 100 µl/2g and 1:1 2.2 M HCl direct addition respectively. They reveal a similar pattern in precipitate to the 2.5 wt % SMS case above. As the droplet size is increased again two changes in the precipitate are apparent. As the dispersed volume is increased from 25 to 100 µl/2g, firstly there is a change in the morphology, particularly the level of nanoparticle aggregation with a decrease in the degree of organisation of the nanoaggregates and secondly a change in the polymorphic outcome from the stable quartz phase to a metastable amorphous silica phase.

25 µl 5 wt % SMS + 1:1 2.2 M HCl Direct addition

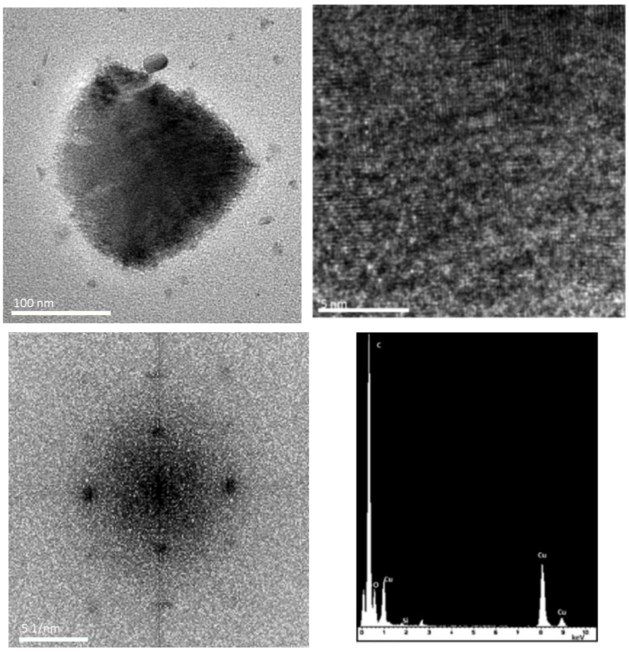

Figure 4.34 a: BF, b: HREM image of representative material, c: corresponding FFT indexed to be the [1-1-4] zone axis of quartz and d: EDX spectrum highlighting the elemental composition for 55 wt % (2.2) Triton X-100 : (1) 1-hexanol in cyclohexane microemulsion with 25 µl/2g 2.5 wt % SMS + 1:1 2.2 M HCl direct addition sample. pH = 1.7

100 µl 5 wt % SMS + 1:1 2.2 M HCl Direct addition

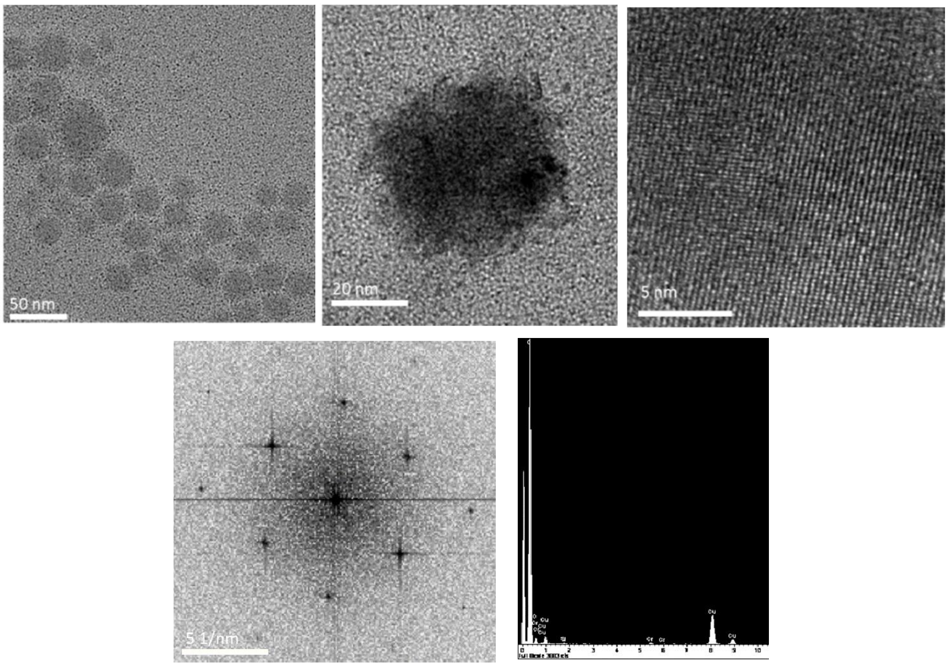

Figure 4.35 a BF: amorphous silica b: BF, c: HREM image of representative crystalline material, d: corresponding FFT indexed to be the [110] zone axis of quartz and e: EDX spectrum highlighting the elemental composition of 55 wt % (2.2) Triton X-100 : (1) 1-hexanol in cyclohexane microemulsion with 25 µl/2g 2.5 wt % SMS + 1:1 2.2 M HCl direct addition sample. pH = 1.7

The decline in the level of aggregation with increased dispersed phase is comparable with that observed for an increase in SMS precursor concentration documented previously. The structures are incomplete with partial agglomeration exhibited.

Comparisons of the data for the two samples shows a change in the majority polymorph produced from the microemulsion, from the stable quartz to a metastable amorphous phase, with an increase in dispersed volume from 25 to 100 µl/2g. Upon the addition of 25 µl of dispersed phase, nanoparticles of quartz and nanoaggregates are the sole precipitate, whilst for the 100 µl case the metastable amorphous silica phase dominates in the form of much larger spheres, together with a minority of quartz nanoparticles and reduced ordering of the nanoaggregates.

4.6.1.4.2 2.2 M HCl - mixed microemulsion addition

Figures 4.36-4.37 illustrate the TEM data from two samples with a SMS precursor concentration of 2.5 wt % SMS with dispersed phase volumes of 25 µl/2g and 100 µl/2g and 1:1 2.2 M HCl mixed microemulsion addition respectively

25 µl 2.5 wt % SMS + 1:1 2.2 M HCl mixed microemulsion addition

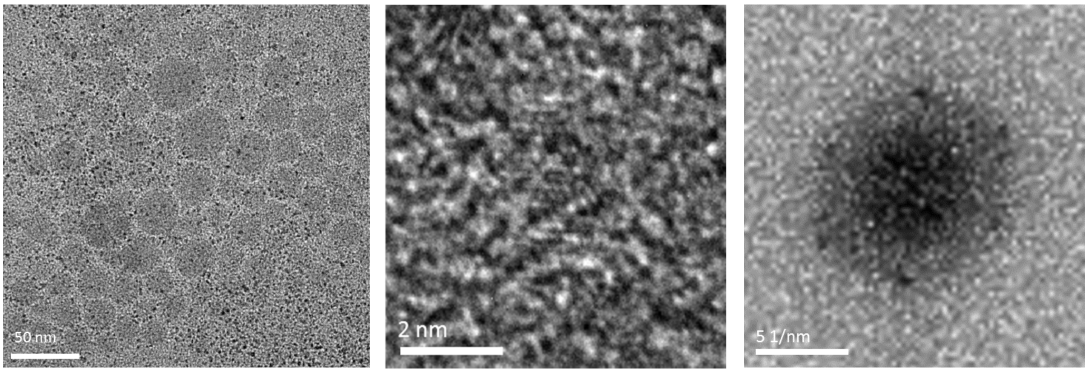

Figure 4.36 a BF, b: HREM image of representative material, c: corresponding FFT indexed to be the [201] zone axis of quartz from a 55 wt % (2.2) Triton X-100 : (1) 1-hexanol in cyclohexane microemulsion with 25 µl/2g 2.5 wt % SMS + 1:1 2.2 M HCl mixed microemulsion addition sample. pH = 0.1

100 µl 2.5 wt % SMS + 1:1 2.2 M HCl mixed microemulsion addition

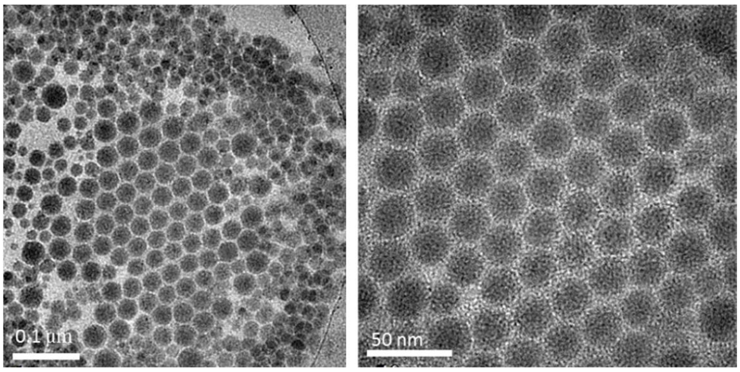

Figure 4.37 a BF, b: HREM image of representative material from of 55 wt % (2.2) Triton X-100 : (1) 1-hexanol in cyclohexane microemulsion with 100 µl/2g 2.5 wt % SMS + 1:1 2.2 M HCl mixed microemulsion addition sample. pH = 1.0

No nanoaggregate structures are observed for the mixed microemulsion method, however similarly to previous cases, as the droplet size is increased there is a change in dominating polymorphic outcome from the stable quartz phase to a metastable amorphous silica phase. This is expected be a result of the possible loss of confinement to precipitate the metastable form. In this way Ostwald's rule of stages dominates and thermodynamic control is lost and the precipitation of metastable forms is possible in addition to the stable form.

4.6.1.5 SAXS analysis and geometric droplet size

4.6.1.5.1 Electron density

The particular droplet structure for a given aqueous/surfactant/oil system can be deconvoluted and evaluated using the program DECON to produce a radial electron density profile provided the droplets are sufficiently spherical and monodisperse. However simply calculating and comparing the electron density of the neighbouring components of the micelle allows the shape and internal structure to be predicted. The electron densities of each of the components or phases are displayed in Table 4.13.

Component	**Electron density / Å^{-3}**	**Electron density relative to the cyclohexane continuous phase / Å^{-3}**
Water	0.33	0.06
HCl	0.44	0.17
SMS	0.30	0.03
TX-100 Head groups	0.35	0.08
TX-100 tail groups	0.24 – 0.29	-0.03 – 0.02
Hexano-1-ol - OH portion	0.32	0.05
Hexan-1-ol - hexane portion	0.23 – 0.28	-0.04 – 0.01
Cyclohexane	0.27	0

Table 4.13 The electron densities of the components of the microemulsion. A range is given upon different densities of components being adopted.

The electron density of the dispersed phase may be determined entirely by the relative concentrations of its components.

If the baseline electron density is taken to be that of the cyclohexane continuum, one can see upon moving radially outwards towards the continuum, the electron density alternates from positive to negative relative to the cyclohexane with an electron density ~0.27 Å^{-3}. Thus the pair-distance distribution function, p(r), in Graph 4.4 has two distinct maxima and a minimum suggesting that the best fit for the TX100 surfactant system is the core shell model. It consists of a high electron density core consisting of the dispersed phase, hydrophilic head group of the surfactant and the OH portion of the hexane-1-ol co-surfactant and a hydrophobic shell comprised of the surfactant tail groups and the co-surfactant hexane tail which have a lower electron density than the surrounding cyclohexane.

Here there is significant contrast in the electron density of the core and the shell meaning that the hydrophilic core radius is subject to less error.

To gain a more detailed perspective, the geometric prediction and GIFT prediction from the experimental SAXS data were computed to estimate the droplet size within the system upon the addition of 10 and 100 µl/2g of surfactant and oil continuum. The scattering and pair-radial distribution functions obtained from the raw data and GIFT analysis, respectively, from SAXS experiments are presented in Graph 4.4.

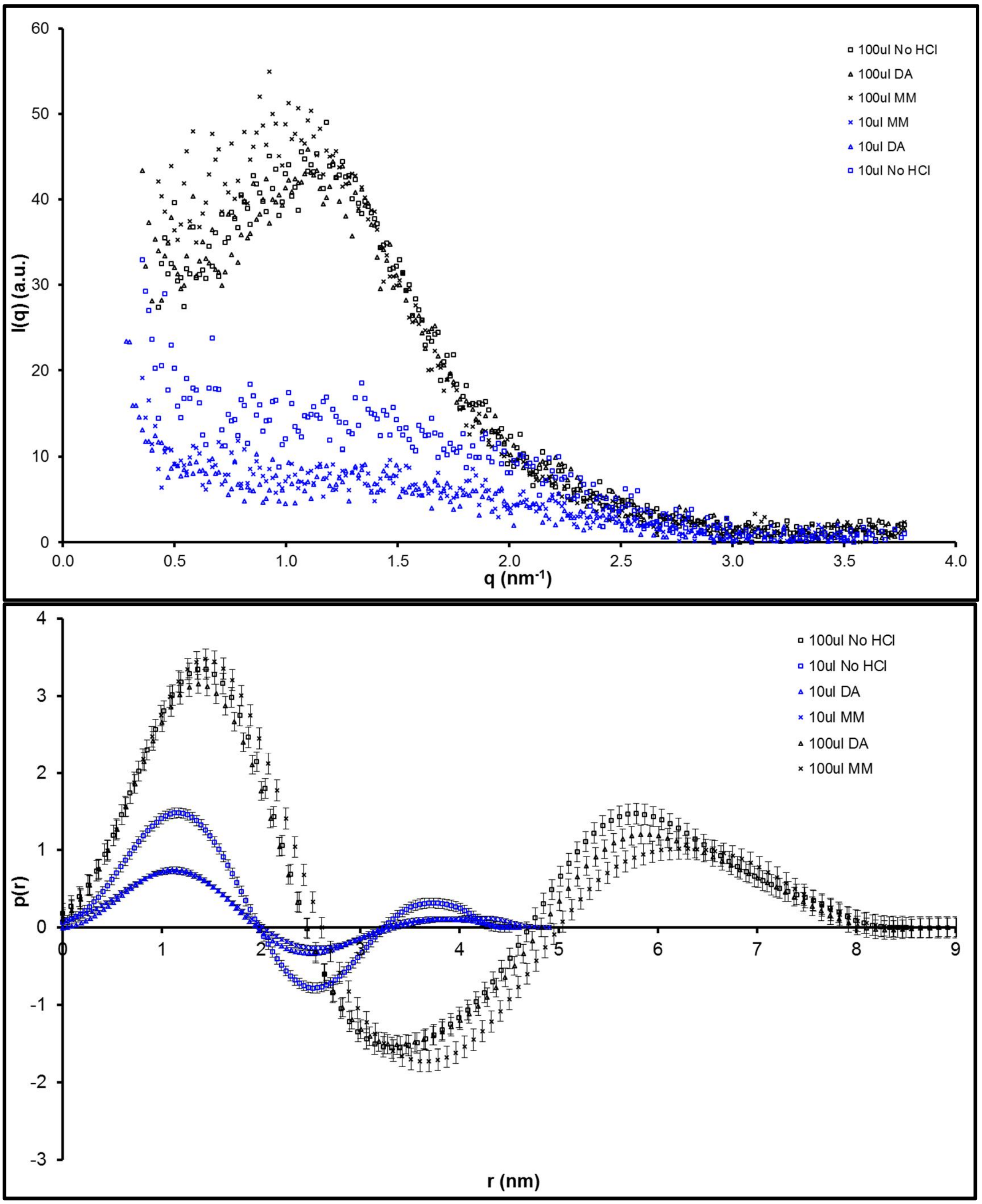

Graph 4.4. a SAXS scattering function and b: Pair distribution function for dispersed 1% aqueous sodium metasilicate nonahydrate within a TX100/Hexanol/cyclohexane system

Consistently the core droplet sizes are much smaller than predicted from the geometric predictions. Such is rationalised by the lack of hexanol being incorporated in to the geometric calculations. Hexanol is known to act as a cosurfactant to reduce the droplet size due to its ability to increase the interfacial area.

The surfacant tails are estimated to have an average length of 0.8 nm based on the TX-100 chain length determined from the CH_3, CH_2 and benzene components, The dimensions of these are taken to be: 0.15, 0.1265[17] and 0.44 Å based on Eastoe[18] approximation of the length of benzene being approximately 3.5 carbons long. Summing up, the extended length of the surfactant chain is ~ 1 nm implying the actual length to be ~ 80 % or 0.8 nm. The GIFT estimation agrees strongly for small dispersed phase volumes of 10 µl for the hydrophobic shell, with an average value of 0.8 nm, determined approximately from the p(r) curve, by finding half the diffrence between the second inflexion point and the point where p(r) falls to zero. For the geometric predictions one adopted the area per molecule found for TX-100 to be 0.643 nm^2 [19], which correspond to hydrophilic core radii values of 3.0 to 4.3 nm for the dispersed volumes of 10 – 100 ul/2g, for all methods employed. Further reported values of the TX-100 surface area are much greater at 0.77 nm^2.[20] Substituting the higher value gives better agreement for the core sizes, leading to hydrophilic core radii of 2.4 – 3.4 nm which is more in line with the GIFT values. Moreover, adopting a larger surface area per surfactant induces a larger degree of freedom, particularly at higher droplet sizes, thus allowing for a greater degree of penetration by the cyclohexane. One expects the lengthening of the surfactant tails for larger droplet sizes to be partially accounted for by a reduction in the sharpness between the hydrophobic and hydrophilic portions due to hexanol penetration.

4.6.1.6 Water perturbation

It has been previously highlighted that the outcome of the crystallisation can depend on the micellar size, particularly the water pool size. For small or negligible free water pools, crystallisation may be forced to occur close to the surfactant interface and thus templating by surfactant may dominate, furthermore at high surfactant:water ratios a high supersaturation will be lead to rapid nucleation and less-organised nanocrystals. Thus one must calculate the quantity of water within the aqueous phase that is structurally perturbed by the surfactant interface. For TX100, Qi and Ma's[21] value of 5.3, is adopted to determine the depth of the hydration layer. Tables 4.14-4.16 shows how the amount of free water varies with a change in radial size of the micelles.

4.6.1.6.1 No HCl addition

Dispersed volume / µl/2g	**10**	**100**
$R_{GIFT-core}$ / nm (± 0.3 nm)	1.5	2.4
Number of droplets per gram of microemulsion (x 10^{18})	32	9.3
Number of water molecules per droplet	10	358
Number of surfactant molecules per droplet	11	36
Water taken by TX100 per droplet	≥10	191
Fraction of water bound to TX100	1.00	0.53

Table: 4.14 Estimation of perturbed water molecules by surfactant from GIFT radii upon no HCl addition.

4.6.1.6.2 2.2 M HCl - Direct addition

Dispersed volume / µl/2g	**10**	**100**
$R_{GIFT-core}$ / nm (± 0.3 nm)	1.5	2.4
Number of droplets per gram of microemulsion (x 10^{18})	32	11
Number of water molecules per droplet	20	593
Number of surfactant molecules per droplet	11	29
Water taken by TX100 per droplet	≥20	154
Fraction of water bound to TX100	1.00	0.26

Table 4.15 Estimation of perturbed water molecules by surfactant from GIFT radii upon direct addition of HCl.

4.6.1.6.2 2.2 M HCl - Mixed microemulsion addition

Dispersed volume / µl/2g	10	100
$R_{GIFT - core}$ / nm (± 0.3 nm)	1.6	2.3
Number of droplets per gram of microemulsion (x 10^{18})	26	11
Number of water molecules per droplet	12	309
Number of surfactant molecules per droplet	13	32
Water taken by TX100 per droplet	≥12	170
Fraction of water bound to TX100	1.00	0.55

Table 4.16: Estimation of perturbed water molecules by surfactant from GIFT radii upon mixed microemulsion addition of HCl.

As shown in each table for the various acid additions above, when the dispersed phase is increased from 10-100 µl/2g and the hydrophilic core radius from 1.5 to 2.4 nm, the percentage of water molecules perturbed by the surfactant layer decreases from ~100 % to ~ 25 %. This reveals an increase in the free-water pool size. As the free water pool increases with droplet size the ordering within the nanoaggregates declines.

4.6.1.7 Estimated silica concentration within the droplet

At larger dispersed phases the individual precipitation sites tend to be larger. From Tables 4.14-4.16 one can see there are fewer droplets for a given sample size, thus indicating there are most likely fewer nucleation sites. Thus estimating the number of SiO_2 units that could potentially exist upon synthesis in the droplet may provide greater understanding of the formation of the quartz crystals observed. Only the aqueous case is discussed as it has been highlighted that the addition of acid makes negligible difference to the droplet size.

		No HCl		**DA HCl**		**MM HCl**	
Dispersed volume / µl/2g		**10**	**100**	**10**	**100**	**10**	**100**
$R_{GIFT - core}$ / nm (± 0.3 nm)		1.5	2.4	1.5	2.4	1.6	2.3
Mean number of silica per droplet	**2.5 wt %**	0.016 ± 0.004	0.56 ± 0.08	0.016 ± 0.004	0.45 ± 0.07	0.010 ± 0.003	0.24 ± 0.04
	5 wt %	0.033 ± 0.004	1.12 ± 0.08	0.032 ± 0.004	0.91 ± 0.07	0.020 ± 0.003	0.48 ± 0.04
	7.5 wt %	0.049 ± 0.004	1.67 ± 0.08	0.048 ± 0.004	1.36 ± 0.07	0.030 ± 0.007	0.72 ± 0.04
	10 wt %	0.066 ± 0.004	2.23 ± 0.08	0.064 ± 0.004	1.81 ± 0.07	0.040 ± 0.003	0.96 ± 0.04
	15 wt %	0.099 ± 0.004	3.35 ± 0.08	0.096 ± 0.004	2.69 ± 0.07	0.060 ± 0.003	1.44 ± 0.04

Table 4.17 Estimation of the nominal mean number of silica units residing in the microemulsion droplets (based upon the GIFT-determined droplet radius)

This approximation indicates that most droplets contain no silica units so there appears to be insufficient precursor present to allow the precipitation of silica within any one droplet based on the solubility of silica phases. One can rationalise the observation of crystalline nanomaterial being observed by TEM, primarily by the degree of polydispersity among the droplets within the microemulsion, with further contributing factors. Larger droplets and higher SMS precursor concentrations are expected to contain a larger number of silica molecules so that they may support quartz nucleation. Secondly, the exchange of material to promote further growth beyond the nucleation stage is supported by the occurrence of transient dimer formation between energetic colliding droplets as detailed in Chapter 1.

In addition to the actual number of silica per droplet, one is aware that surfactant:silica ratio can have a significant effect upon the morphology of the product obtained.

4.6.1.7.1 Effect of varying the silica to surfactant ratio.

The variation in surfactant to silica ratio is known to have a significant effect in silica precipitation processes, particularly in surfactant-templated materials through self-assembly mechanisms to generate nanoscale structures. Such work was summarised by Edler. K[22], whereby the mechanism of silica nanoparticles is highlighted for both ionic and non-ionic surfactants, in addition to acidic and alkaline environments.[18] Work of particular interest is that of the silica syntheses through the use of non-ionic surfactants, particularly those with PEO head groups, in acidic environments. Boissiere *et al.*[23-34] utilised a surfactant with a PEO head group to synthesise silica-coated surfactant micelles, whereby the pH was maintained at 2.

It is suggested that the silica polymers form, before they insert themselves in to the PEO head group. The counter effect is observed in this system whereby instead of the micelles becoming coated with silica, one would expect that the silica form becomes coated with surfactant head groups. Blin *et al.*[25] noted that the ratio of the hydrophilic to the hydrophobic portion of surfactant was critical to the synthesis of these type of structures.

Nevskaia *et al.*[26] adds to this with a study of the effect of the PEO length through the adsorption of the Triton surfactant series on to pre-made quartz structures with varying surfaces, suggesting that adsorption occurs via hydrogen bonding interactions or hydrophobic attraction between the ether groups of oxyethylenic chains and surface hydroxyl groups residual from the orthosilicic acid intermediate. Consequently the adsorption of PEO groups is dependent upon the hydroxyl component upon the surface, and thus the pH and free-water pool of the system that work to bind hydrogen with the hydroxyl group or compete to form hydrogen bonds with the quartz surface respectively. The optimised pH noted for acidic syntheses was 2, to slow precipitation with an increase in pH required for precipitation. Such would be in agreement for the adsorption of TX-100 on to a quartz surface. For too low a pH with a significant free hydrogen ion presence, one would suspect that the hydroxyl groups would become hydrogen bound to the free hydrogen ions, limiting the adsorption of PEO groups. Once bound the PEO residual surfactants are expected to assist the formation of the nanoaggregates observed through hydrophobic interactions between the hydrophobic tail groups encouraging aggregation of the nanoparticles. This is possibly supported by the increased presence in oxygen on the EDX spectrum for the nanoaggregate structures. If the surfactant molecules were to adsorb evenly across the quartz structures, one would expect that the nanoaggregates would not appear as ordered, producing a more polycrystalline structure. Thus one must speculate that the surfactant preferentially adsorbs to one particular face of the quartz nanoparticles leading to oriented attachment.

		No HCl		**DA HCl**		**MM HCl**	
Dispersed volume / µl/2g		**10**	**100**	**10**	**100**	**10**	**100**
$R_{GIFT\text{ - }core}$ / nm (± 0.3 nm)		1.5	2.4	1.5	2.4	1.6	2.3
No of surfactant		11	36	11	29	13	32
Ratio of surfactant: silica	**2.5 wt %**	733	67	715	64	1363	135
	5 wt %	367	34	357	32	681	68
	7.5 wt %	220	22	238	21	454	45
	10 wt %	183	17	178	16	341	34
	15 wt %	122	11	119	11	227	22

Table 4.18 : Estimation of surfactant:silica molecule number in each droplet

One can estimate the ratio of surfactant:silica necessary for the formation of the nanoaggregate structures. From prior observations in combination with Table 4.18 it can be seen that fully nanoaggregate structures, are preferred when the surfactant: silica ratio is high at ~700:1. As the ratio reduces, one observed a decrease in the level of aggregation, and an increase in the polycrystallinity within the structures. One can thus rationalise the reduction in the completion of nanoaggregate formation at higher SMS precursor concentrations and larger droplet sizes, whereby there are significantly more silica molecules available to contribute to the formation of nanoparticles, however a reduction in a surfactant:silica ratio means that the nanoparticles are unable to undergo oriented attachment and thus remain as individual nanoparticles.

4.6.1.8 Proposed formation mechanism

The growth of the nanoparticles of dimensions up to the size of the microemulsion dimensions are explained by transient dimer formation which promotes material exchange. For the formation of the nanoaggregate structures no clear methodology is understood, however at present one can speculate that the following factors may contribute to their formation:

- Surfactant:silica ratio
- pH

Quartz can be considered an uncharged, polar surface. For adsorption to occur, typically one of the following mechanisms is observed: hydrogen bonding or dispersion force interactions between the solid surface and the surfactant molecule.[27] For hydrogen bonding or acid-base interactions to occur, the substrate must have a suitable surface group to participate. Noting quartz's' formation mechanism and elemental composition, silanol OH groups can be assumed to be pervasive across the surface, making it suitably easy for EO groups of a PEO type surfactant to hydrogen bond to the quartz silanol groups, as the hydroxyl group acts as the hydrogen donor to the EO group. PEO surfactants are known to adsorb on solid surfaces to form complete monolayers assuming sufficient hydroxyl groups are considered free.[26] The data in Table 4.18 highlights a necessary surfactant:silica ratio of ~700:1 must be reached or is desirable to promote complete aggregation of the individual quartz nanoparticles. One believes that 'full' aggregation occurs at high surfactant:silica ratio, as the nanoparticles are to be covered with a complete monolayer which supports the attractive hydrophobic interactions, which are existent between the non-polar surfactant tail groups, to lead to nanoparticulate aggregation.[28-29] In addition to the hydrophobic interactions, there are forces between the individual nanoparticles, where when in close proximity the nanoparticles can orient themselves until identical faces are in register with each other.[29] Thus as the ratio of surfactant : silica reduces, one observed a decrease in the level of aggregation, and an increase in the polycrystallinity within the structures. This rationalises the reduction in the completion of nanoaggregate formation at higher SMS precursor concentrations and larger droplet sizes.

pH is not expected to have a pronounced affect upon adsorption for a non-polar surface and a non-ionic surfactant, however at extreme pH there is a possibility of producing charges through the protonation of OH or SiOH groups.[27] Indeed, such is observed, when the pH of the acid recedes to below ~ 1, producing a very acidic system, poorly aggregated structures dominate. Such findings supports the mechanism of adsorption highlighted by Nevskaia *et al.*[26] who suggest adsorption occurs via hydrogen bonding interactions or hydrophobic attraction between the ether groups of oxyethylenic chains and surface hydroxyl groups. Thus if the pH is too low, the hydroxyl groups will become protonated and restrict the surfactant species from adsorbing. However, it was noted that nanoaggregate structures appear only upon the addition of sufficient acid, indicating the presence of some excess of hydrogen ions (within reason) encourages the formation of the nanoaggregates structures.

4.7 Conclusion

This chapter concludes the addition of HCl acid of various concentrations and various methods to the Span80/Brij30 and TX-100/hexan-1-ol surfactant systems. The purpose was based on prior experimentation whereby hydrochloric acid is noted to catalyse the hydrolysis of sodium metasilicate to silicon hydroxide/silicic acid. In addition C.Chen *et al.*[1] crystallised an organic dipicolinic acid phase in microemulsions and observed nanoaggregate structures, thus one wondered what affect a similar system would have upon an inorganic silica phase.

The Span80:Brij 30 microemulsion system was seen to produce quartz nanoparticles, typically of the order of the droplet size, in addition to larger single crystals at larger dispersed volumes upon the addition of HCl. Metastable polymorphs were also observed upon substantial supersaturation levels being achieved. A summary of the conditions for the different silica precipitates is summarised in Table 4.19.

Identity of precipitates	**Nanoquartz (2-5 nm)**	**Cristobalite**	**Larger triangular quartz structures**
Image	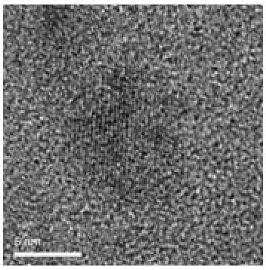	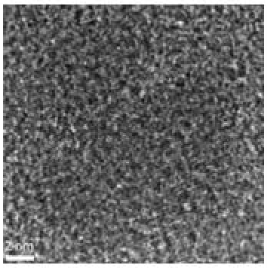	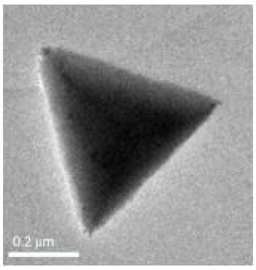
pH	**~ 7**	**~ 5**	**< 1**
Mean radius of droplets hydrophilic core	**1.5 - 2.7 nm**	**~ 2.4 nm**	**~ 2.4 nm**
Bound water percentage	**20 – 100 %**	**22 %**	**22 %**
Mean number of silica per droplet	**0.01 – 2.3**	**0.4**	**0.4**

Table 4.19 : Summary of precipitate conditions for the 30 wt % 1:1 Span 80:Brij 30: heptane microemulsion system.

The TX-100 surfactant system precipitated comparable quartz nanocrystals to those obtained without the addition of HCl to the Span80: Brij 30 and the TX-114 (Chapter 3) systems. Upon the addition of HCl, nanoaggregate formation in the order of 50-200 nm is possible via oriented attachment of the 2-5 nm primary nanoparticles previously observed. Typical conditions to produce 'complete' nanoaggregates are with a pH ~ 1 - 2, the incorporation of HCl and a high surfactant:silica ratio of ~700:1. Deviation from such conditions produces incomplete agglomerations or simple individual nanocrystals. Such formation of nanoaggregates is suspected to be a result of surfactant adsorption at the hydroxyl groups upon the silica resulting in ordering due to hydrophobic interactions between the surfactant tail groups. Such suggestions are preliminary and further work would be required to confirm the formation mechanism. A summary of the conditions for the different silica precipitates is summarised in Table 4.20.

Identity of precipitates	**Nanoquartz (2-5 nm)**	**Amorphous**	**Complete aggregation**	**Partial aggregation**
Image	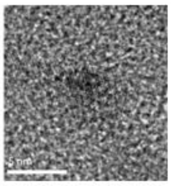	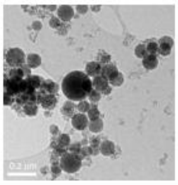	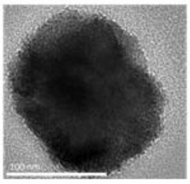	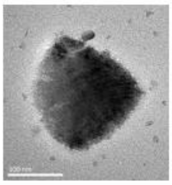
No HCl, direct or mixed microemulsion addition	**No HCl, direct addition and mixed microemulsion addition**	**No HCl, direct addition and mixed microemulsion addition**	**Direct addition**	**Direct addition and mixed microemulsion addition**
pH	**0 - 9.6**	**~ 1 - 11**	**~ 1 - 2**	**~ 0 - 1**
Mean radius of droplets hydrophilic core	**1.6 - 2.5 nm**	**2.2 – 2.4 nm**	**~ 1.6 nm**	**~ 1.6 – 2.5 nm**
Bound water percentage	**26 – 100 %**	**26 – 53 %**	**~ 100 %**	**~ 26 – 100 %**
Mean number of silica per droplet	**0.02 – 3.22**	**0.24 – 3.22**	**0.04**	**0.02-0.45**
Surfactant : silica ratio	**All**	**~ 60 – 10 :1**	**~700:1**	**~20 – 400 :1**

Table 4.20 : Summary of precipitate conditions for the 55 wt % 2.2:1 Triton X-100:1-hexanol:cyclohexane microemulsion system.

References

1. C.Chen, C.E. Nicholson, H.E. Ramsey and S.J. Cooper, *Cryst. Growth. Des',* 2015, 15, 1060-1066;C. Chen, Crystallisation of glycine and dipicolinic acid from microemulsions', 2012. Thesis
2. D.C. Crans and N.E. Levinger, *'The accounts of chemical research',* 2012, 45 (10), 1637-1645
3. 8.D.C. Crans and N.E. Levinger and B. Branuah, '*Langmuir'*, 2007, 23, 6510-6518
4. D.C. Crans, A.M. Trujil, S. Bonetti, C.D. Rithner, B. Baruah and N.E. Levinger, *'The Journal of Organic Chemistry',* 2008, 73, 9633-9640
5. F. Peral and E. Gallego, *'Spectrochim. Acta A,'* 2001, 56, 2149-2155
6. Yang, P. Roonasi and A. Holmgren, '*Journal of Colloid and Interface Science',* 2008, 328-1, 41-47
7. J. L. Chai, J. L. Li, *Colloid J*, 2009, **71**, 257-262.
8. S. Kosmella and J. Koetz, *Curr. Opin. Colloid Interface Sci.*, 2012, **17**, 261-265.
9. X.-Q. Li, J.-l. Chai, S.C Shang, H.-l. Li, J.-j. Lu, B. Yang and Y.-t. Wu, *J. Chem. Eng',* 2010, **55**, 3224-3228
10. Yaghmur. A, Aserin. A, Tiunova. I and Garti. N, *'Journal of Thermal Analysis and Calorimetry',* 2002, **69**, 163-177
11. R. Zhang, Y. Wang, L. Tan, H.Y. Zhang and M. Yang, 'J.Chromatogr Sci,' 2012, 598-607
12. Qiong. G, Surfactants in nonpolar oils: agents of elecric charging and nanogel templates', 2012. Thesis. Georgia Institute of Technology.
13. Myers. D, 'Surfactant Science and Technology', John Wiley & Sons, 2005
14. H. Caldararu, A.Caragheorgheopo1, M. Vasilescu, I. Dragutan, and H. L. Caldararu, '*J. Phys. Chem'.* 1994, 98, 5320-5331
15. Zhu, D.-M.; Schelly, Z. A. Lungmuir 1992, **8**, 48.
16. Zhu, D.-M.; Wu, X.; Schelly, Z. A, '*J. Phys. Chem'.* 1992, **96**, 7121.
17. K. Esumi and M. Ueno, 'Sturcture- Performance Relationships in Surfactants', CRC Press, 2003
18. Eastoe. J, 'Aggregation and adsorption at interfaces;, Unpublished work, available at: http://www.chm.bris.ac.uk/eastoe/Surf_Chem/2%20Aggregation%20and%20adsorption%20at%20interfaces.pdf. accessed 30/03/16
19. B. Janczuk, J. M. Bruque," M. L. Gonzalez-Martin, and C. Dorado-Calasanz,' *Langmuir*' 1996,11, 4515-4518
20. M. Almgren, J. van Stam, S. Swarup, J.E. L¨ofroth, '*Langmuir'*, 2, 986. 432.
21. L.Qi and J. Ma, *J. Colloid Interface Sci'* 1998, **197,** 36-42
22. Edler. K, *'Australian Journal of Chemistry',* 2005, **58(9**), 627-645
23. C. Boissiere, A. Larbot, C. Bourgaux, E. Prouzet, C.A. Bunton, *'Chem Mater',* 2001**, 13**, 3580
24. 20. C. Boissiere, M.A.U. Martines, M. Tokumoto, A. Larbot, E. Prouset, *Chem Mater'*, 2003, **15**, 509
25. J. Blin, A. Léonard, Y. Zhong-Yong, L. Gigot, A Vantomme, A. K. Cheetham, B.L Su, *Angewandte Chemie,* 2003, **45(25**), 2872-2875

26. D. M. Nevskaia, A. Guerrero-Rutz, A. Lopez-Gonzalez, '*Journal of Colloid and Interface Science',* 1996, **181**, 571–580
27. Myers. D, 'Surfactant Science and Technology', John Wiley & Sons, 2005
28. Mittal. K.L and Shah. D.O, *Adsorption and Aggregation of Surfactants in Solution,* CRC Press, 2002
29. Song. R-Q and Colfen. H, *'Advanced Materials',* 2010, **12**, 1301 – 1330.

Chapter 5 - Nano-graphite crystallisation

5.1 Introduction

Carbon is an extremely abundant and versatile element. It is the fourth most abundant element by mass in the universe, whilst additionally acting as the building block for > 95% of known chemical compounds.[1] Carbon's versatility stems from its unrivalled ability to bond to itself, in addition to both electronegative and electropositive species.[2] Isolated carbon atoms have the following electronic configuration: $1s^2 2s^2 2p^2$, with the $1s^2$ electrons confined to the core, the remaining 4 valence electrons participate in the three hybridized bonding states: sp^1, sp^2 and sp^3. These hybridized states govern the atomic arrangement and as such carbon is known to exist as a number of allotropes with a diverse range of physical and chemical properties.[3]

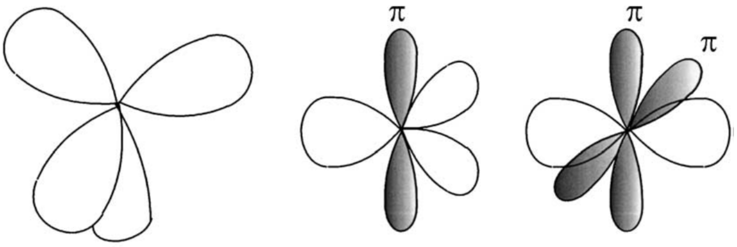

Figure 5.1: Hybridized states of carbon[3] Reprodcued (adapted) with permission from Robertson. J, *'Materials Science and Engineering: R Reports',* 2002, 37(4-6)129-281. Copyright © 2002 Elsevier Science B.V.

There are three 'parent' allotropes: diamond, graphite and fullerenes (See Figure 5.2) which can be extended to include: carbon nanotubes (CNTs), nano-onions, graphene and amorphous carbons (amorphous carbon (a-C) and tetrahedral amorphous carbon (ta-C)

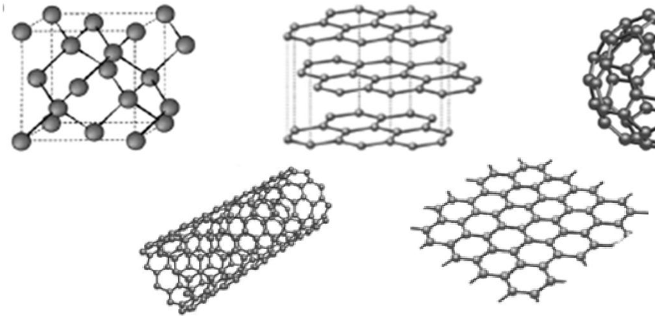

Figure 5.2: Allotropes of carbon: a: diamond, b: graphite, c: buckyball, d: carbon nanotubes and e: graphene.[4] Reproduced with permission from M Scarselli, P Castrucci and M De Crescenzi, *'J. Phys.: Condens. Matter',* 2012, 24, 313202. As licensed by Creative Commons Attribution CC BY licence 3.0.

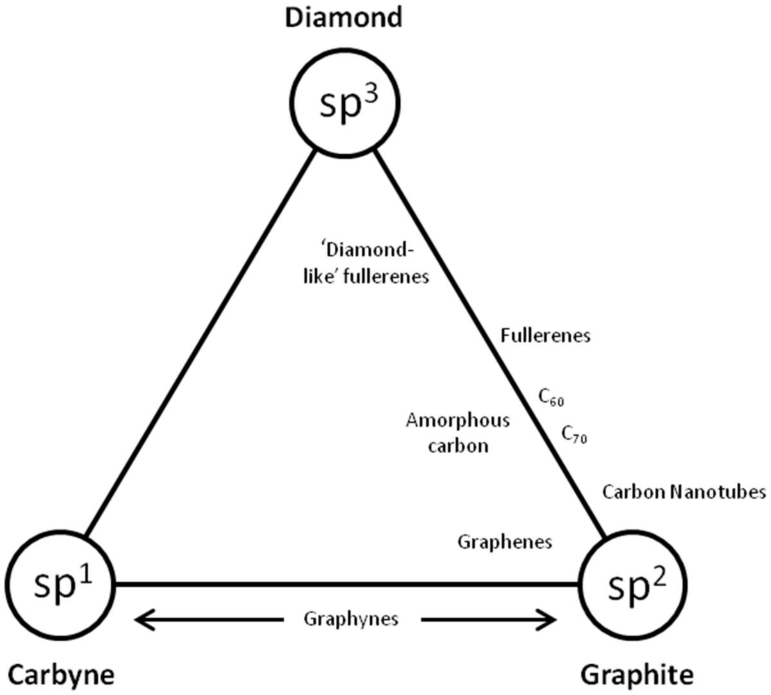

Figure 5.3: Simplified ternary "phase" diagram of carbon allotropes. [5] Reprinted (adapted) with permission from O.A. Shenderova,1,2 V.V. Zhirnov,1,3 and D.W. Brenner, '*Critical Reviews in Solid State and Materials Sciences*', 27(3/4):227–356 (2002). Copyright © 2002 Taylor & Francis

Diamond, a crystalline allotrope consisting purely of sp^3 hybridized carbon, exists commonly with a cubic structure, but rarely, may also exhibit a hexagonal structure. Each of the sp^3 carbon atoms forms strong covalent bonds to four adjacent carbon atoms to generate a 3-dimensional rigid tetrahedral structure. Diamond can be obtained via both natural and synthetic methods.[6-8] Terrestrial diamonds develop primarily from kimberlite and lamproite host rocks in igneous and metamorphic environments within the Earth's upper mantle (150-200 km below the surface) at temperatures >1300 K and pressures of >40 kbar.[9] Diamond synthesis was first attempted by Hannay in 1880, through heating and compression of nitrogenous hydrocarbons. Despite apparent verification of this method by Londsale and Bannister (1943) using X-ray analysis, doubts remain due to poor reproducibility.[6] The basis for the first accepted synthesis was reported in 1955 by Bundy *et al*,[8] which utilised the now familiar high pressure, high temperature (HPHT) approach of >50 kbar pressures and temperatures exceeding 1800 K. These conditions mimic the natural process.

Unique properties of diamond include its exceptional natural hardness and thermal conductivity;[10] it is electrically insulating and chemically inert[6-7], whilst being aesthetically pleasing due to its high refractive index and optical dispersion. Thus diamond has a number of direct industrial applications including; acting as a heat sink for electronic systems, as an abrasive or to provide protective coatings for optics.[9]

Diamond is indeed a metastable allotrope relative to graphite under ambient conditions, (Figure 5.4) $C_{diamond} \rightarrow C_{graphite}$ having a small negative associated free energy of reaction, $\Delta G^o = - 2895$ J g atom^{-1} at 25 °C and 1 atm pressure.[6] This indicates that diamond will convert to graphite spontaneously over time, with an energy difference between the two phases ~ 0.02 eV/atom. However this occurs at a negligible rate due to the high activation energy in the order of 0.4 eV/atom.[3]

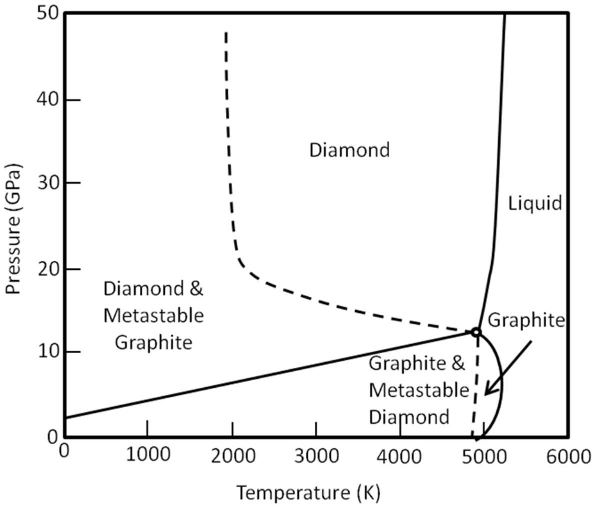

Figure 5.4: The thermodynamic phase diagram for the various high pressure and high temperature polymorphs of carbon.[6] Reproduced (adapted) with permission from Ferro. S, '*J. Mater. Chem'*, 2002, 12, 2843–2855. Copyright © 2002, Royal Society of Chemistry

Crystalline graphite, the thermodynamically stable form of elemental carbon, contains 2D planar layers of hexagonally bonded sp^2 carbon atoms, i.e. graphene. Each of the sp^2 carbon atoms forms a covalent bond with three adjacent carbon atoms. This in-plane structure is stabilised further by the overlap of the remaining perpendicular non-hybridized p-orbitals to form mobile delocalised π-orbitals between the graphene layers. Thus the layers are arguably bound weakly by a Van der Waals type force,[11] which leads to the anisotropic behaviour of graphite.

For natural graphite, the graphene layers are known to stack in a number of orientations: hexagonal (AA), Bernal (AB) and rhombohedral (ABC).[12] See Figure 5.5.

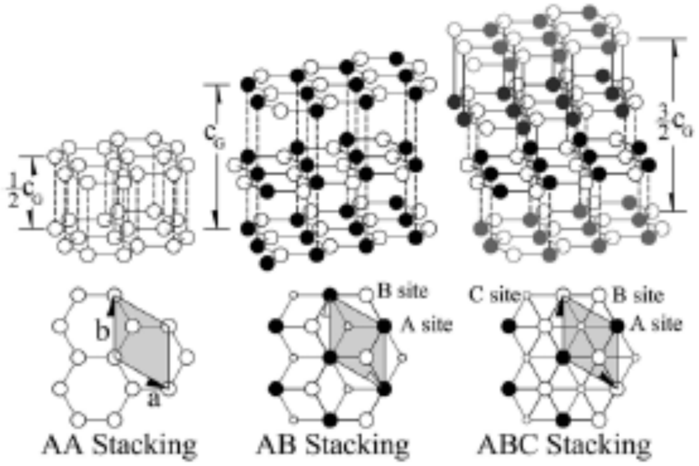

Figure 5.5: Three common orientations of stacking arrangements of graphene layers. [12] Reproduced with permission from Hass. J, W.A. de Heer and E.H. Conrad, ‘J. Phys. Condens. Matter’, 2008, 20. As licensed by Creative Commons Attribution CC BY licence 3.0.

Bernal stacking (AB) has the lowest associated energy and hence is the most common stacking arrangement (~80% of single crystal graphite), formed by stacked graphene sheets with a relative perpendicular rotation of 60º. This reveals a unit cell with four atoms; A and B and A’ and B’, with two sub-lattices of atoms where A/A’ lies above A’/A respectively, and B/B’ lies above a vacancy. Bernal[13], in collaboration with Bragg (1924) proposed and confirmed the structure and graphite lattice, in addition to the Bernal AB stacking.[13-14] Hexagonal (AA) stacking is the least common orientation, consisting of two aligned graphene layers. This orientation is markedly unstable due to steric hindrance leading to reduced delocalisation effects and thus, is only expected to exist upon intercalation of alkali metal ions.[15] A detailed explanation for the poor stability is given by Charlier. J.C *et al.* (1994)[15]. Briefly, the proximity of the atoms results in an increased repulsion, in addition to a lack of electron transfer between A and B atoms. Hence, the delocalisation of electrons which would act to stabilise the AB structure is not observed.[15] The final stacking orientation is rhombohedral graphite with three rotated or translated graphene layers; A, B and C. Both A and B lie as in Bernal stacking, whilst C is in the same orientation as B, but is translated in parallel to the plane,[12] such that an inequivalent atom in C lies above an atom in B. Grinding is known to introduce rhombohedral stacking.[16]

Further, disordering via rotations or translations of adjacent graphene sheets give rise to stacking faults, where sheet curvature and fluctuations of the interlayer spacing may be observed. This is known as turbostratic graphite; a representation is shown in Figure 5.6 [2,17]

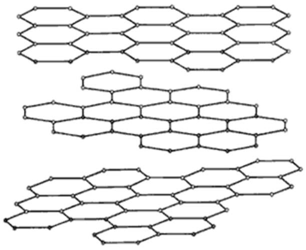

Figure 5.6: Representative image of turbostratic graphene sheets.[18] Reproduced (adapted) with permission from A. N. Kolmogorov and V. H. Crespi, '*Phys. Rev. B'*, 2005, 71.235415. Copyright © 2005, American Physical Society

Similarly to diamond, graphite can be formed by both natural and synthetic routes. As defined by Kwiecinska *et al*,[19] natural graphite is essentially the end product of the graphitisation of organic matter, coals and anthracite and thus relates to a high metamorphic grade. It is believed to be derived by two major routes: metamorphic evolution of dispersed carbonaceous material or precipitation from carbon saturated fluids, under conditions of metamorphism, in addition to pressure and shear strain. The graphitisation conditions are estimated to range between: 600- 800 K, and 2 – 6 kbar.[19]

A brief summary of the routes to which graphite has been achieved is provided by Kwiecinska and Peterson as detailed below.[19]

Natural graphite is essentially the end product of metamorphic and tectonic processes upon carbonaceous material present in sedimentary, igneous and metamorphic rocks. Metamorphism is the change in structure of minerals present in rocks with the aid of heat and pressure. For graphite formation, the process may be broken in to numerous steps, however for simplicity these can be summarised as: carbonisation, polymerisation and graphitisation.[20] Carbonisation is the process describing the formation of amorphous carbon from complex carbon containing compounds. This may proceed by a variety of routes, with a number detailed below, however, it can be summarised as the removal or loss of volatile matter such as H, N and O at relatively low temperatures.[21] The middle step is essentially the formation of graphitic planar sheets, whilst the latter step of graphitisation can be defined as the progressive arrangement of disordered regions to form highly ordered graphitic structures from amorphous carbon structures when subjected to progressively increasing temperatures.**[22]**

Further to metamorphism via heating and application of pressure, graphite has been proven to form in environmentally parallel synthetic reactions of the type:[19]

$$CaCO_3 + 4H_2 \rightarrow CH_4 + H_2O + Ca(OH)_{2.}$$

Giardini *et al.*[23] (1968) undertook the reaction of calcite and hydrogen over a range of temperatures, pressure and time scales, noting that the reaction was highly temperature dependent: in particular only initiating at temperatures greater than 800 K. Graphite formation occurred under specific reaction conditions in agreement with the graphite phase boundary predicted by Eck *et al.*[24] However, the absence of graphite at low pressures, within the metamorphic temperature range, implicates additional abiotic reaction conditions are necessary to overcome a notoriously high activation energy barrier.

Salotti *et al.*[25] extended the above mechanism, further pyrolysing the emitted methane gas to larger hydrocarbons and infinite graphitic structures.[25] The sole pyrolytic dissociation of methane: $CH_4 \rightarrow C + 2H_2$, has been further investigated using a number of substrate materials including transition metals[26] and graphite electrodes.[27]

Several works utilising the decomposition of carbon monoxide, in preference to methane provided a basis for the work in references [26-27]. Davis *et al.* (1953 and 1957)[28], Hofer *at al.* (1955)[29] and Walker *et al.* (1958)[30] undertook catalytic deposition of carbon via carbon monoxide decomposition over transition metals. With similar experimental design, Davis maintained the temperature in the furnace at 723 K, Hofer at 623 K with Walker varying the temperature in the range 723 – 923 K. However each attempt produced a polycrystalline carbon, with no clear evidence of graphite. Karu and Beer (1966)[31] among others, noted the importance of a high purity, defect free substrate. The former prepared a graphite film via the pyrolysis of methane over a heated nickel single crystal held at 1173 K, whilst the latter pyrolysed acetylene over films of nickel or platinum at 1273 K to produce three-dimensionally ordered graphite. Furthermore, publications such as that by Hirai and Yajima (1966)[32] raised the dependence of deposition on factors, such as pressure, substrate, gas flow rate and methods of heating, further to temperature.

Based on the findings of these previous works, Robertson (1969) undertook a low temperature (925 – 1025 K) pyrolysis of methane in a static atmosphere over vacuum annealed thin foil catalysts of iron, cobalt and nickel to deposit ordered graphite 'flakes' or single crystal structures.[26]

For the last century, proposed reaction conditions and mechanisms for natural routes of graphitisation have provided a basis for the laboratory synthesis of graphite and other carbon allotropes. It is clear that there are many variables such as: temperature, time, applied pressure, partial pressures of certain gaseous components, the presence of a catalyst and the nature of the reactants affect the character of the carbonaceous material.

It is apparent that there has been consistently a high level of interest in understanding the origin and mechanism behind graphite formation, with numerous modifications to the reactants, reaction conditions, experimental set-up, understanding of physical properties and with great effort to synthetically reproduce comparable graphite structures throughout the 20th Century as documented and discussed previously. However, ultimately such work has been driven by diversity of physical properties and their potential industrial applications of the material such as graphite acting as a solid lubricant additive, working to increase the life of mechanical systems such as pumps, grinding and metal forming dies.[33-35] Further; pencils consist of pencil 'lead', where graphite (natural or synthetic), but preferably a ground powder with a fine particle size, is blended with a clay binder, with the addition of water, before being extruded and dried at 1250 K before being oil-immersed.[36]

Graphene is a two-dimensional single atomic plane or monolayer, of hexagonally packed sp^2 carbon atoms, which acts as the basic building block of a number of graphitic materials: 3D graphite, 1D carbon nanotubes (CNTs) and 0D fullerenes, buckyballs or carbon nano-onions. Top down synthesis routes have included the exfoliation of graphite intercalated compounds (GIC) via rapid heating;[20,37] solvent-mediated exfoliation of natural flake graphite via sonication and centrifugation;[38] exfoliation of graphene oxide,[39] the 'unzipping' of carbon nanotubes[40] and within colloidal suspensions.[41] Despite the potential to produce high purity, defect-free material, these 'top-down' methods rely on the availability of natural or highly orientated graphite, in addition to producing low yields and the requirement of numerous processing steps. Conversely, 'bottom-up' synthesis typically produces larger quantities of material, however existing synthesis routes result in a higher proportion of defects or impurities. 'Bottom-up' attempts have included: epitaxial growth on electrically insulating surfaces via thermal decomposition of SiC; thermal and plasma enhanced chemical vapour deposition (CVD) (growth on metals or support free)[42] or totally organic approaches from polyacyclic hydrocarbons (PAHs) or sugars.[43-44] Irrespective of the diverse carbon sources available, the synthesis methods reported to date require either elevated temperatures or pressure relative to ambient conditions, to ensure a sufficient degree of graphitisation.

5.2 Project outline

Previous research regarding the synthesis of carbon from carbohydrate precursors has been documented. Graphene and luminescent carbon dots were both synthesised, however elevated temperatures were necessary.[45-46] Sucrose has been dehydrated at room temperature in the presence of sulfuric acid to produce luminescent carbon dots. To isolate, the particles were refluxed with nitric acid, treated with 4,7,10-trioxa1,13-tridecanediamine and heated to 393 K under a nitrogen atmosphere for 72 hours.[45] The 5 nm particles had a mean interlayer spacing of 3.4 Å, similar to graphite, but lacked 3D crystalline order.

Glucose, a smaller carbohydrate has been used as a precursor to graphene, through treatment with dicyandiamide during calcination at 873 K on a carbon nitride template.[46] Numerous top-down approaches for the reduction of graphene – oxide to graphene used lithium aluminium tetrahydride with phosphorous tribromide[47] and zinc with mineral acid.[48] However, in this project one aims to demonstrate how nanographitic particles can be produced at room temperature for the first time by a bottom-up synthesis route using microemulsions.

Using a derivation of the 'carbon snake experiment', our research employs a carbohydrate, sucrose, in an acidified 3D-nanoconfinement of the droplets of a w/o microemulsion in an attempt to gain thermodynamic control of the dehydration and thus crystallisation of carbonaceous material (graphene and graphite) at room temperature.

5.3 Formation mechanism

The dehydration of sucrose by concentrated sulfuric acid in bulk solution is documented by Caratzoulas[49] to undergo rapid polymerisation producing carbonaceous products of the humin type, which can be viewed as highly-defective, furan-rich sheets. The synthesis proceeds via the intermediate 5-

hydroxymethylfurfural (HMF) which is then either polymerised to give humins or split and reopened to levulinic acid and formic acid as depicted in Figure 5.7.

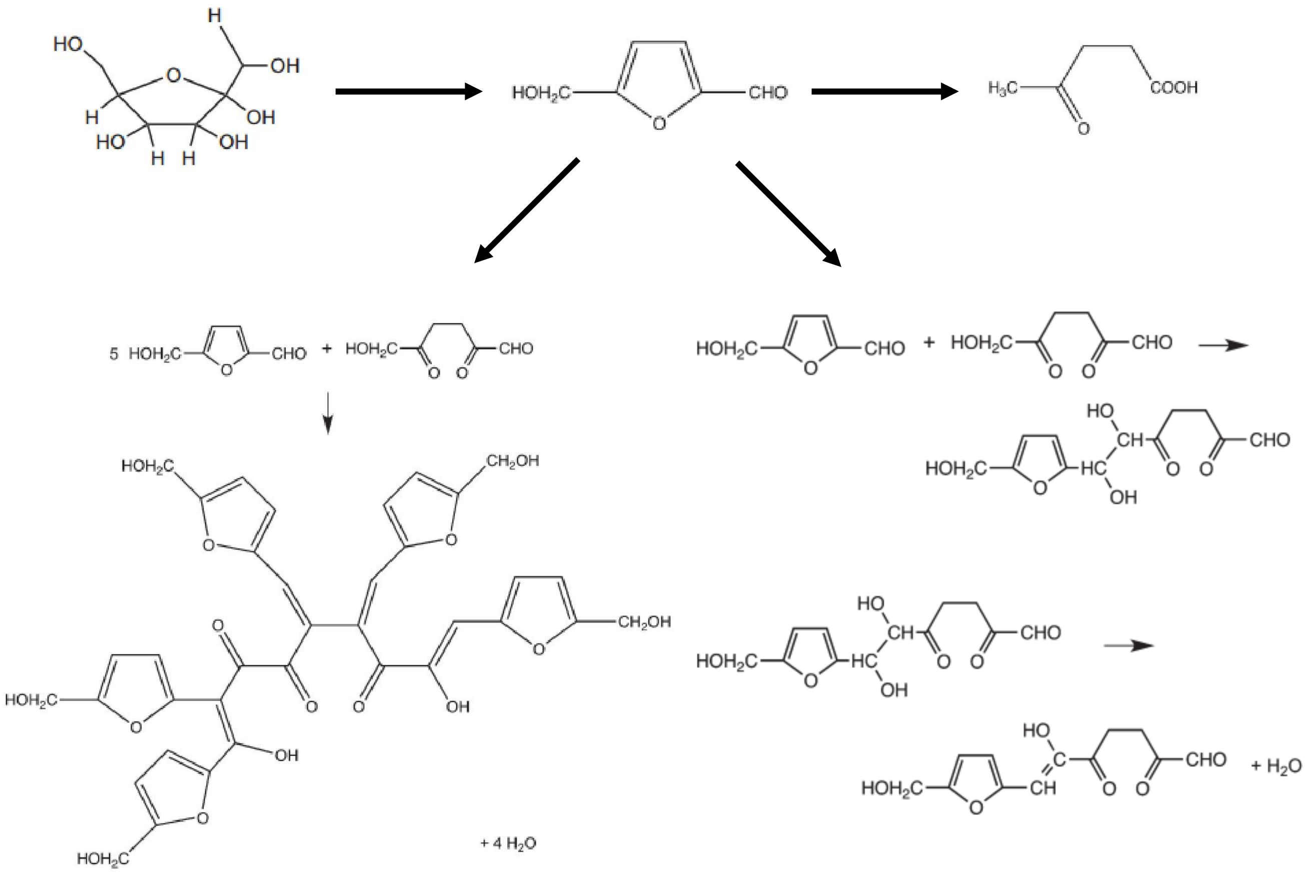

Figure 5.7 Illustration of the potential overview for the dehydration of sugars to humin type structures.[49-50] Reproduced (adapted) with permission from S. Caratzoulas and D.G. Vlachos, '*Carbohydrate Research',* 2011, 346, 664-672 Copyright © 2011 Elsevier Ltd and S.K.R. Patil and C.R.F. Lund, '*Energy Fuels',* 2011, 25, 4745-4735. Copyright © 2011, American Chemical Society.

However, one expects that within the microemulsion the growth rate of carbonaceous sheets will be significantly reduced, due to a lack of precursor material, thus forcing the carbonaceous material to remain within the droplets subjected to a huge excess of sulfuric acid. The hypothesis is that this will promote complete dehydration, and thus the formation of pristine graphene sheets, which only then stack irreversibly, depicted in Figure 5.8.

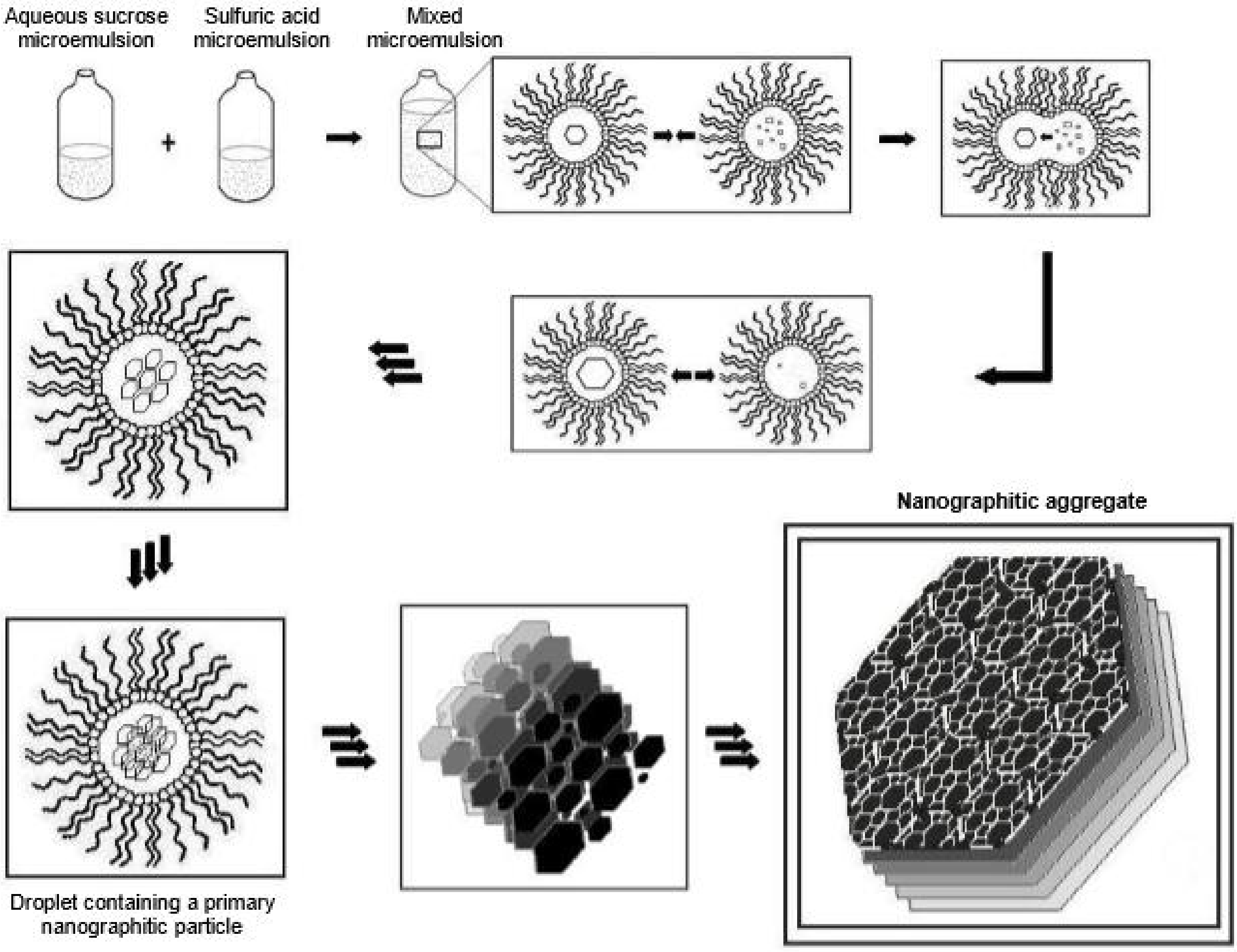

Figure 5.8 Schematic diagram depicting the nanographite synthesis mechanism.[51]

5.4 Thermodynamic control

This approach is similar to the microemulsion-synthesised nanoquartz documented in Chapters 3 and 4, and the crystallisation of stable polymorphs of organic molecules documented in the literature.[52] In these systems, the thermodynamic control was gained over materials by recrystallisation or a simple synthesis mechanism, requiring a rotation of bonds, a change in torsion angle or a varied degree of hydrogen bonding to gain polymorphic control. Such thermodynamic control is typically achieved through the pre-requisite of reversibility, which ensures that the less stable, but typically quicker growing nuclei readily dissolve, thus enforcing an equilibrium nuclei population dominated by the most stable form to be achieved. The dehydration of sucrose can be deemed essentially irreversible, thus one must think about reversible processes, such as the carbonaceous sheet stacking. Essentially, the bathing of the sheets in sulfuric acid means that only pristine graphene sheets will stack irreversibly. Defective sheets containing polyfurans and other oxygen containing functionalities will not stack irreversibly as the interactions between the defective sheets will be too weak. Instead these defective sheets will remain in contact with the sulfuric acid until they are fully dehydrated to (near) pristine graphene. This can be rationalised by looking at the effective overlap of stacking layers, which is a function of their size, shape, chemical and structural purity and the strength of the surrounding acid. This is presented in the Introduction to Chapter 5. Natural graphitic material is known to stack in a number of orientations as depicted in Figure 5.5: Hexagonal (AA), Bernal (AB) and rhombeherdal (ABC), with Bernal packing being the most common.[12]

Further, disordering of graphene sheets through rotation and translations of graphene sheets results in turbostratic stacking and thus possible rotation, translation, curvature, fluctuations of the interlayer spacing and 'normal' atomic positions are observed.[17] For turbostratic stacking one only observes (002l) reflections (notably the (002)) and (hkl) reflections with l=0, i.e. the (100) and the (110); and (hkl) reflections with l>0 are absent, since this would indicate 3 dimensional order, i.e. ordered stacking.

Thus a parallel to the thermodynamic control of crystallisation in microemulsions relying on the formation of a near stable nucleus can be drawn. If one takes the example of polyfuranic defective carbonaceous sheets and turbostratic/AA/ABC stacked graphite, weak inter-layer Van der Waals forces are expected to be experienced – these can be deemed metastable phases. However when efficient stacking occurs, AB, whereby relatively strong interlayer interactions are experienced between pristine graphene sheets that stack irreversibly in comparison to defective sheets, this can be deemed to be the thermodynamic stable form. This is, for example, exemplified by graphite oxide dispersing rapidly in water via sonication,[53] whereas graphite requires 2 days of stirring in chlorosulfonic acid to produce graphene.[54]

5.5 Experimental

5.5.1 Control experiments

Unconfined bulk experiments were performed to investigate the solubility of sucrose in relevant solvents, in addition to determining the potential for dehydration by sulfuric acid and to allow comparisons with the microemulsion route.

5.5.2 Solubility tests

Bulk solubility tests of sucrose were performed to determine the level of saturation in water at room temperature. Incremental increases in the mass of sucrose were added to 1 g of water, placed in a constant temperature oven at 25 °C and left to equilibrate. Similar studies were performed using cyclohexane and pentan-1-ol to ensure sucrose was sufficiently insoluble in the desired continuous phase. Sucrose solubility was found to be ~65 wt% in water, with < 0.01 wt% in cyclohexane and <0.01 wt% in pentan-1-ol.

5.5.3 Unconfined bulk experiments

Control experiments were carried out in the bulk phase to investigate the product obtained from the reaction outside the confinement of the microemulsion droplets.

5.5.3.1. Visual observations

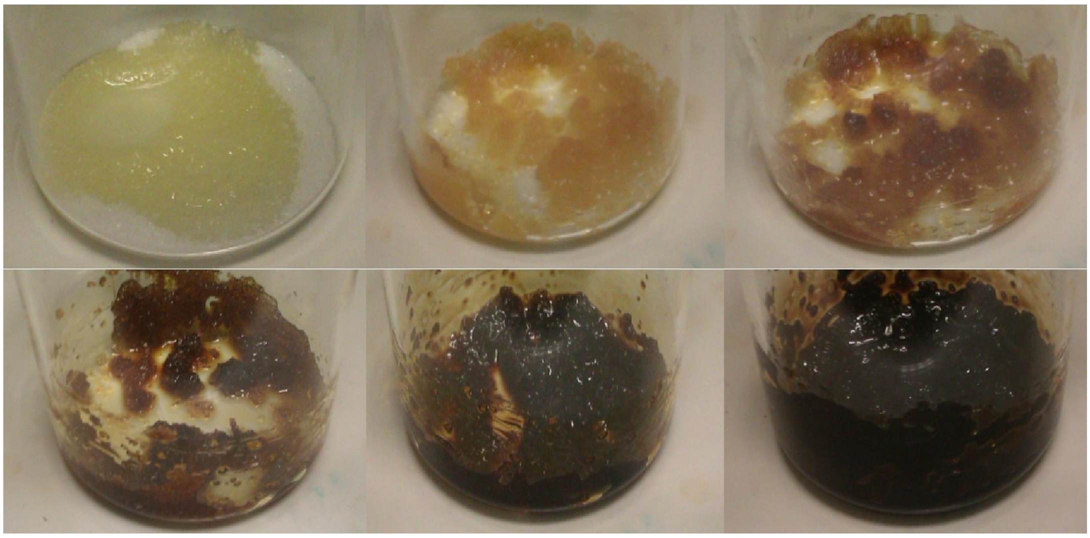

Figure 5.9: Images of the progression of the 'black carbon snake' experiment using sucrose and concentrated sulfuric acid.

Various volumes of concentrated sulfuric acid were added dropwise to sucrose, with continuous stirring. Colour changes were observed as pictured in Figure 5.9 above.

As expected the sucrose initially gained a yellow colouring, followed by a red tint, before gaining a black colouring; indicating the formation of carbonaceous product. The overall chemical reaction can be generally simplified to:

$$C_{12}H_{22}O_{11} \rightarrow 12C + 11H_2O$$

Although of course the carbonaceous product is not pure carbon; rather it also contains significant quantities of oxygen and hydrogen since the dehydration of sucrose does not go to completion. The sulfuric acid is hydrated by the released H_2O as follows: $H_2SO_4.nH_2O + mH_2O \rightarrow H_2SO_4.n_1H_2O$, where $\boldsymbol{n}$ is determined from the density of the acid used, $\boldsymbol{m}$ is equal to (11*n), and $\boldsymbol{n_1=n+m}$.[60] However, one may still expect residual H_2SO_4 along with gaseous CO_2 and SO_2 as by-products upon the oxidation of carbon in the presence of sulfuric acid.

$$C_{12}H_{22}O_{11} \rightarrow 12C + 11H_2O \rightarrow CO_2 + SO_2$$

Note that if pure carbon was obtained, a distinct lack of peaks would be observed in the infra-red spectrum of the product. As can be observed from the presence of the peaks in Figure 5.10 various other by-products are created.

5.5.3.2 IR

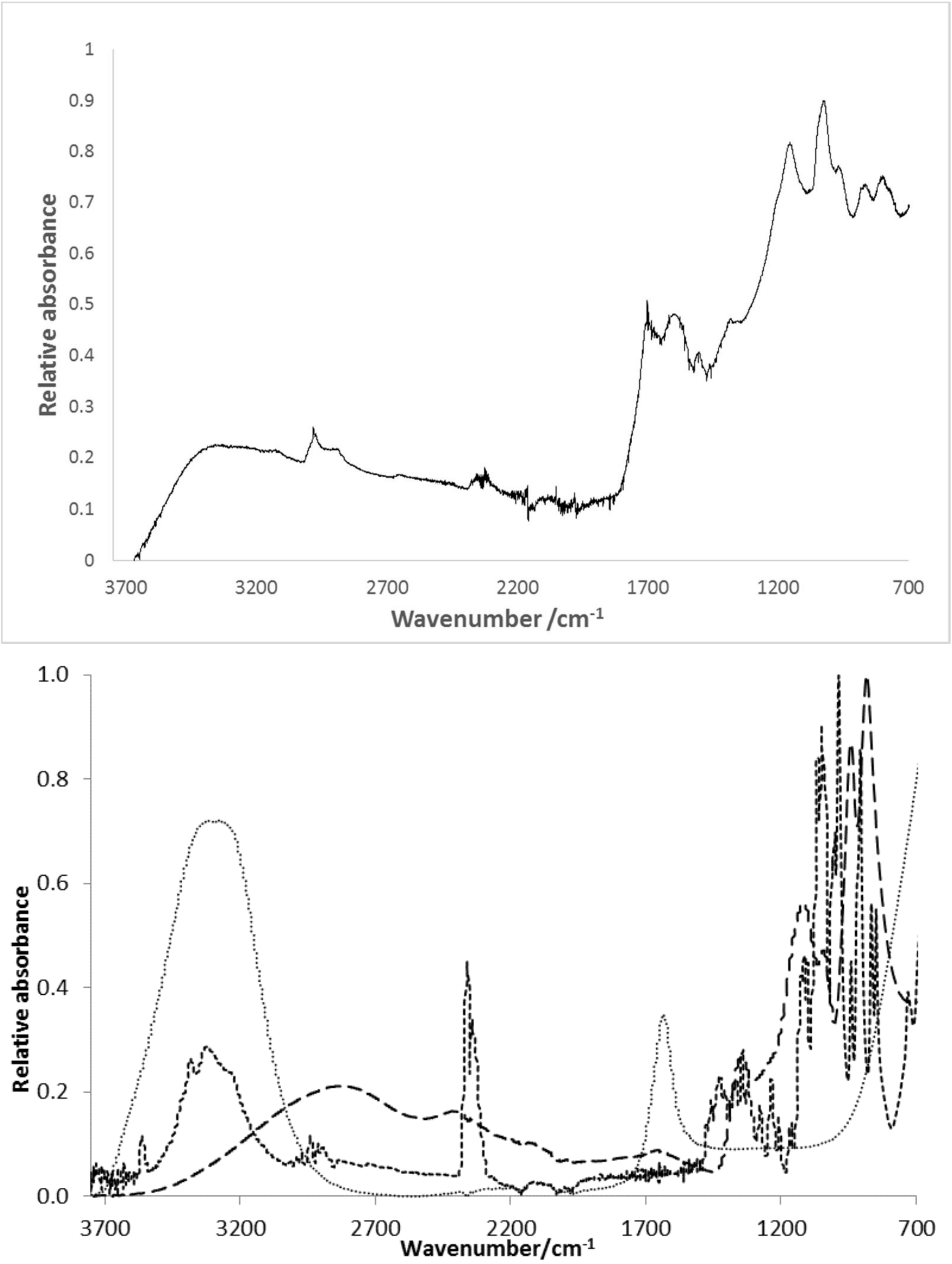

Figure 5.10 a and b:a:Infra-red spectrum of the (black) carbonaceous material produced from the reaction of granulated sugar and sulfuric acid in the bulk, b : Infra-red spectrum of the (long dash) concentrated sulfuric acid, (star) water and (short dash) sucrose.

Upon analysis of Figure 5.10 in parallel with Table 5.1 few peaks are visible. A broad, weak stretch is observed in the 3300 cm^{-1} region, attributed to hydrogen bonded O-H stretches. Two non-negligible peaks occur at 2846 cm^{-1} and 2913 cm^{-1}, characteristic of aliphatic sp^3 C-H (CH and CH$_2$) stretches, with a supporting shoulder at ~1480 cm^{-1}. A further doublet observed in the region of 2300-2400 cm^{-1} indicates the presence of the asymmetric stretch of gaseous O=C=O, attributable to gaseous CO_2 within the surrounding air of the instrument. A further significant peak can be found centred at 1665 cm^{-1} (with peak broadening due to merging with the carbonyl peak at 1700 cm^{-1}, resulting in stretching over the 1550cm^{-1} – 1900cm^{-1} region). A number of vibrations are known to contribute to this stretch. Firstly, the H-O-H bend occurs at ~1635 cm^{-1}, with the sp^2 C=C bond being found between 1500-2200 cm^{-1}, depending on substituent groups. Given the high carbon content of the product, the peak is mainly due to C=C stretches. Three major peaks remain: 1144cm^{-1}, 1020cm^{-1} and 870cm^{-1}. Upon further comparisons to the overlaid spectra, the first can be attributed to C=O, with the others to vibrations ($\upsilon_{as(}$HOSO$_3$), $\upsilon_{s(}$HOSO$_3$) and υ(S-OH) originating from the sulfuric acid or more accurately hydrated sulfuric acid (monohydrate).[55] The FTIR data confirms that the product is a carbonaceous one containing oxygen and hydrogen chemical functionalities (primarily, C=O, C-O, C-OH and C-H) and residual hydrated sulfuric acid.

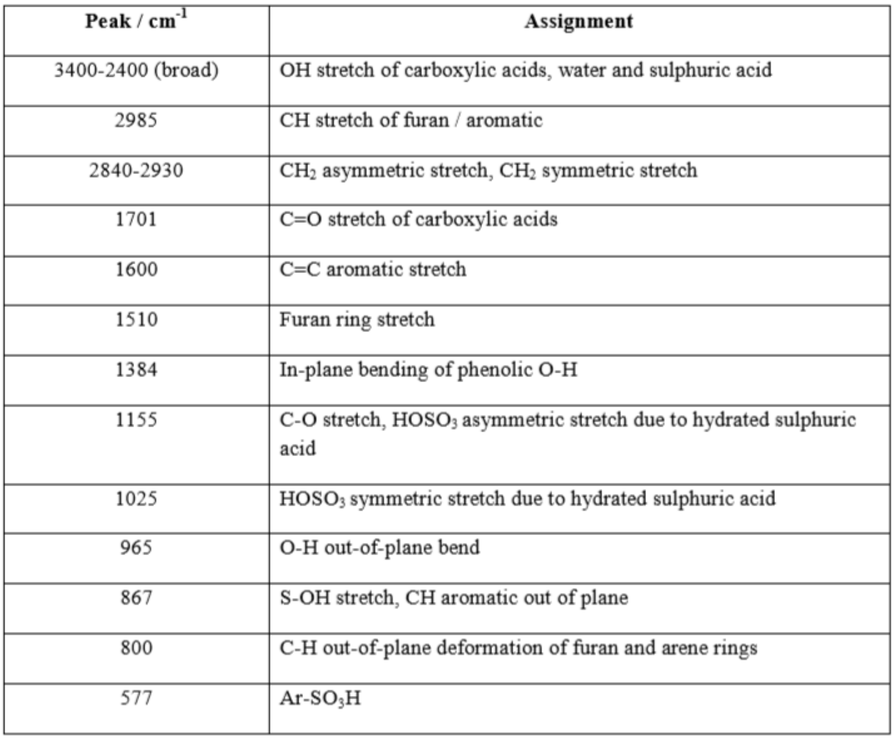

Peak / cm^{-1}	Assignment
3400-2400 (broad)	OH stretch of carboxylic acids, water and sulphuric acid
2985	CH stretch of furan / aromatic
2840-2930	CH_2 asymmetric stretch, CH_2 symmetric stretch
1701	C=O stretch of carboxylic acids
1600	C=C aromatic stretch
1510	Furan ring stretch
1384	In-plane bending of phenolic O-H
1155	C-O stretch, $HOSO_3$ asymmetric stretch due to hydrated sulphuric acid
1025	$HOSO_3$ symmetric stretch due to hydrated sulphuric acid
965	O-H out-of-plane bend
867	S-OH stretch, CH aromatic out of plane
800	C-H out-of-plane deformation of furan and arene rings
577	Ar-SO_3H

Table 5.1: Assignment of IR peaks of carbonaceous material[50,56]

5.5.3.3.XRD

A brief analysis of the bulk product by x-ray diffraction (Figure 5.11) upon completion of the reaction yields only an amorphous type band, centred at 2θ ~21 °, when compared to the literature, shown in Figure 5.12. However, nano-crystallites of sucrose were evident if analysed prior to the reaction going to completion.

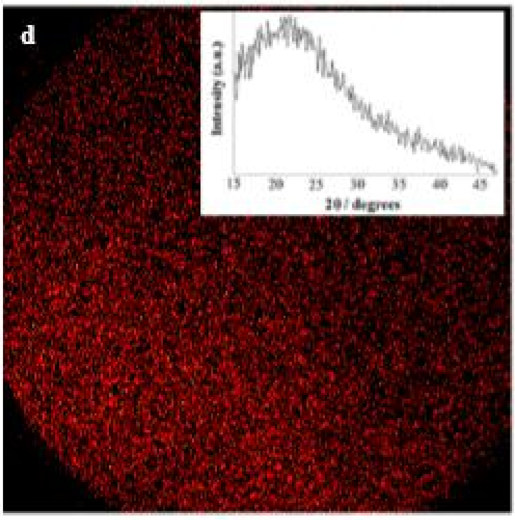

Figure 5.11: Experimental pXRD of the bulk product of sulfuric acid and sucrose. XRD showing only a broad amorphous peak centred at 2θ ~ 21^0. The main picture shows the 2D image; the inset shows the integration across a $\chi = 30^0$ angular range.

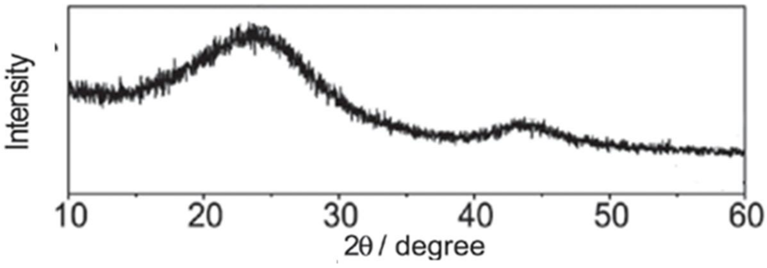

Figure 5.12: Literature pXRD of amorphous carbon[57] Reprinted (adapted) with permission from C.de Almeida and A.J.G. Zarbin, *'J. Braz. Chem. Soc',* 2006, 17(6), 1151–1157. Copyright © 2006 Elsevier Ltd

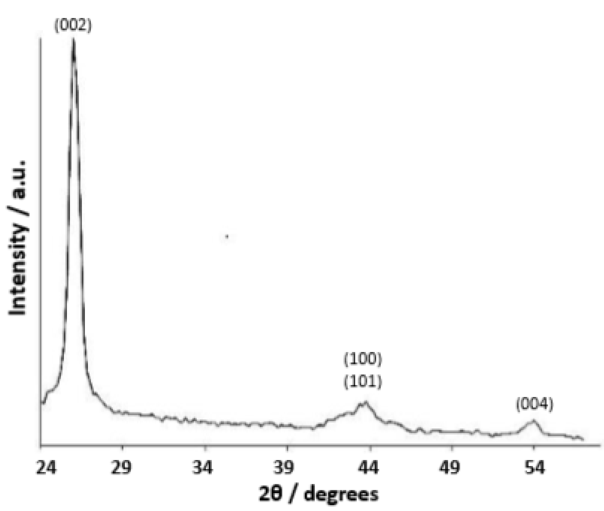

Figure 5.13 XRD data from a commercial multi-layer (12 nm flake) graphene sample purchased from Graphene Supermarket.

The lack of graphitic peaks at 2θ = 42.4 ^{0}and 44.6 ^{0} due to graphite (100) and (101) planes, see Figure 5.13, shows that a graphitic product has not been produced.

5.5.3.4 Raman spectroscopy

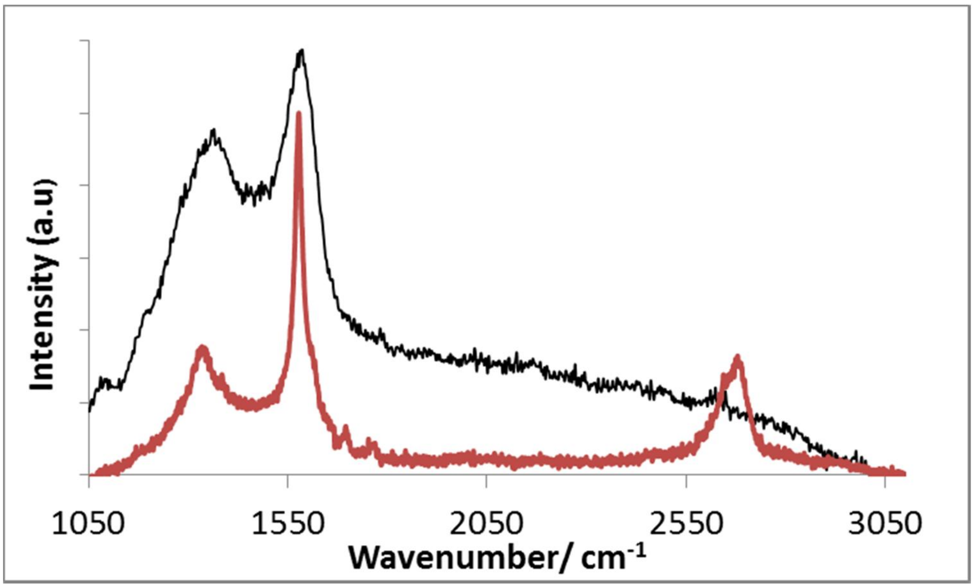

Figure 5.14: Raman spectra of material precipitated from the bulk reaction of sucrose with sulfuric acid (black) and a commercial multi-layer (12 nm flake) graphene sample purchased from Graphene Supermarket (red)

Comparing the two spectra of our product and the commercial 12 nm sized graphene flakes, our product has a significantly increased D peak ~ 1350 cm^{-1}, both in breadth and intensity. The origin of the D peak arises from defects including the presence of disordered systems, finite crystal size and the presence of terminating groups, as would be expected for carbonaceous materials precipitated from the 'carbon-snake experiment'.

5.5.3.5 TEM

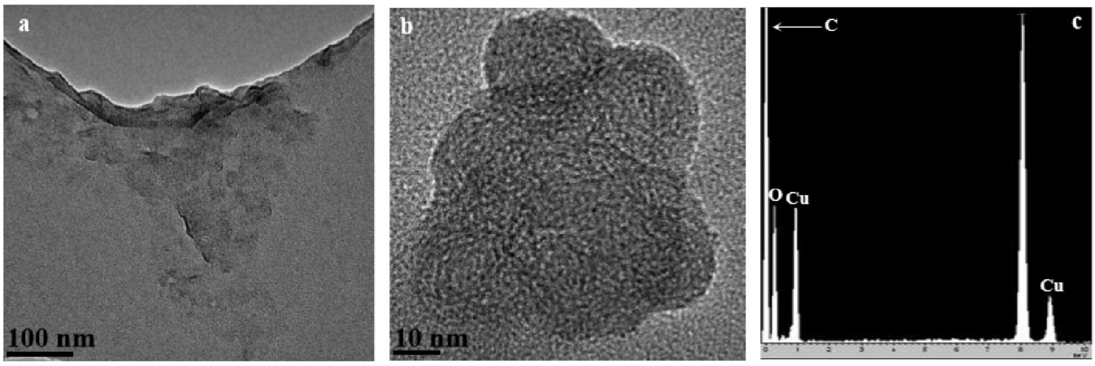

Figure 5.15 TEM images showing the humins amorphous carbon product that arises from the reaction of sulfuric acid with sucrose in the bulk. (a) Bright field TEM image, (b) HREM image and (c) Energy-dispersive X-ray (EDX) spectra of the region displayed in (b). Note the relatively large oxygen peak in (c) showing that a significant proportion of oxygen remains in the amorphous carbonaceous product.

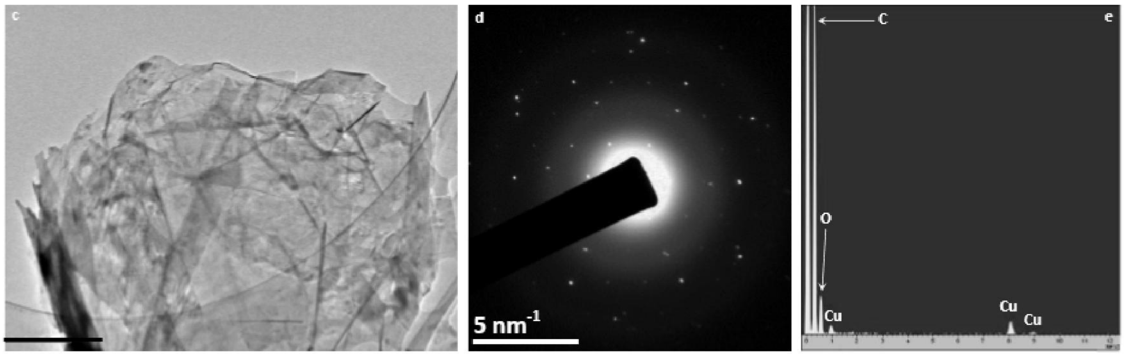

Figure 5.16. TEM data from a commercial multi-layer (12 nm flake) graphene sample purchased from Graphene Supermarket. (c) TEM bright field image, (d) electron diffraction pattern from region (c) and (e) EDX spectrum from region (c).

The TEM images in Figure 5.15 highlight the lack of order in the carbonaceous material produced from the bulk experiments of sucrose with sulfuric acid.

Metastable nano-onions can also be seen to be present. The elemental analysis from the EDX shows a relatively large oxygen peak revealing that a significant proportion of oxygen remains in the amorphous carbonaceous product. This is expected for humin-type amorphous carbon product that arises from the reaction of sulfuric acid with sucrose in the bulk; the elemental composition of humins is typically ~55-65% carbon, 5% hydrogen and 30-40% oxygen.[50] Humins are polyfuranic-based, rather than consisting of benzene rings but they still contain a significant proportion of sp2 carbons. In comparison the commercial multi-layer graphene (Figure 5.16) is seen to produce ordered folded layers of crystalline material, with a much reduced level of oxygen residing in the graphene layers.

5.5.4. Phase diagrams

A phase diagram is an essential pre-requisite to identify a suitable microemulsion composition within a ternary or quaternary system comprised of an aqueous, organic (oil) and surfactant or co-surfactant component. The phase diagram allows the homogeneous single phase microemulsion region to be recognized effectively.

The choice of microemulsion system is dependent on the chemical properties and the solubility of the precursors, in addition to the possible products. The solubility data presented in Section 5.5.2, combined with known solvent immiscibility with both water and sulfuric acid, highlights cyclohexane as a potential microemulsion continuum. A cationic surfactant has been chosen based on its ability to confine concentrated sulfuric acid within the microemulsion droplets. Previous experimental studies highlight the ability of cationic surfactants, in conjunction with an alcohol co-surfactant to provide such confinement.[58-60] Hexadecyltrimethylammonium chloride (CTAC) was chosen preferentially to CTABr, due to its reduced Krafft point, aiding work at ambient temperatures.[61] Pentan-1-ol was chosen after a range of alcohols were tested to determine the optimum co-surfactant. The chemical structures of each component can be seen below in Figure 5.17. It is clear that CTAC has a large hydrophobic tail with its large saturated hydrocarbon chain, adjoined to a small hydrophilic trimethylammonium chloride head group.

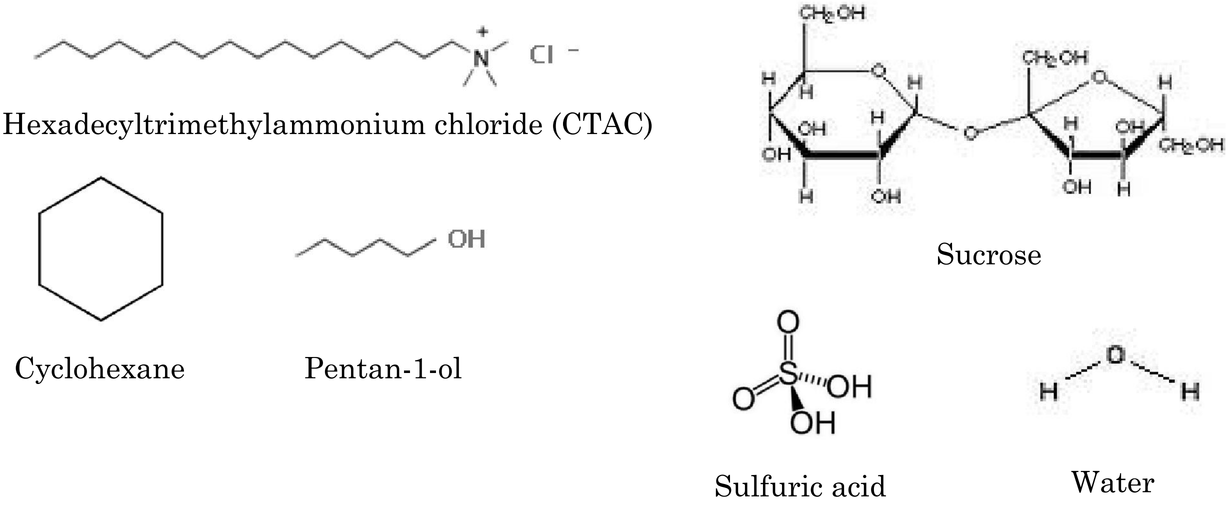
Hexadecyltrimethylammonium chloride (CTAC)

Sucrose

Cyclohexane

Pentan-1-ol

Sulfuric acid

Water

Figure 5.17: Structure of the microemulsion components clockwise from top: Hexadecyltrimethylammonium chloride (CTAC), sucrose, water, sulfuric acid, pentan-1-ol and cyclohexane.

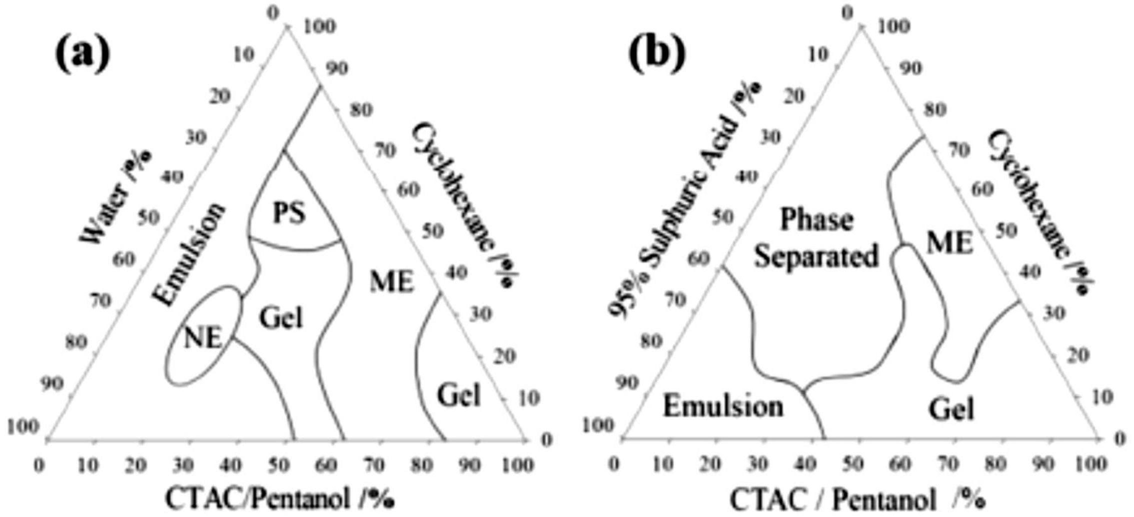

Figures 5.18 a and b: Phase diagrams for the CTAC/pentan-1-ol and cyclohexane system with water and sulfuric respectively.

Phase diagrams, depicted in Figures 5.18a and b, were generated for the specified system, via the creation of 36 compositions, at each of the mass fraction intersection points. The designated cyclohexane:surfactant:co-surfactant ratio 39:5:10, corresponds to a point with ~70 % oil and ~25 % surfactant, when the dispersed phase is added. This composition was chosen as it was found to have the greatest ability to form stable microemulsions.

5.6 CTAC/Pentan-1-ol/cyclohexane system

5.6.1 Microemulsion preparation using a mixed microemulsion methodology

Two different microemulsion methodologies were adopted in the synthesis of graphitic material. The first used a mixed microemulsion methodology. Aqueous sucrose was dissolved in UHQ water at various concentrations between 0.25-70 wt %. Individual acid and aqueous microemulsions were made as follows: the aqueous sucrose or sulfuric acid (10-60 μl) was added to a standard 1 g homogeneous continuous phase of 1:2:7.8 CTAC:pentan-1-ol: cyclohexane, before being dispersed using a vortex shaking machine. The individual acid and sucrose microemulsions were mixed immediately Microemulsions were left for varying degrees of time (1 hour – 3 years). A second method was adopted in an attempt to provide more material for detailed analysis. In this method, termed the sugar crystal dissolution method, sulfuric microemulsions were created as before, however sucrose crystals were added to the acidified microemulsion rather than via a mixed microemulsion method. The vials were left for a month during which time black material deposited on the bottom of the vials.

5.6.2 Microemulsion experiments

Using the 3D nanoconfinement of microemulsion droplets, the following variables were investigated: the effect of the concentration of sugar and sulfuric acid and the droplet size.

5.7 Mixed microemulsion method: Results and discussion

Initial investigations were carried out by varying both the concentration of sucrose (0.25-70 wt %) and droplet sizes, whilst maintaining the acid concentration at ≥95 % and a volume ratio of 1:1 with respect to the volume of the sucrose dispersed phase. In brief, the maximum volume of sulfuric acid dispersed phase which could be added to a 1 g scale was 60 μl, before the microemulsion destabilised. Thus for each concentration of sucrose solution, between 0.1 wt % and 70 wt %, 10 μl increments were added (10-60 μl).

5.7.1 Effect of varying the sucrose precursor concentration.

As mentioned in Section 5.6.1, sucrose concentrations of 0.1 to 70 wt % were employed in the microemulsion system. Visual observations over a period of 7 days indicated the microemulsions remain colourless at low sucrose concentrations, but show increased darkening as the dehydration reaction proceeds in sucrose concentrations of >5 wt %.

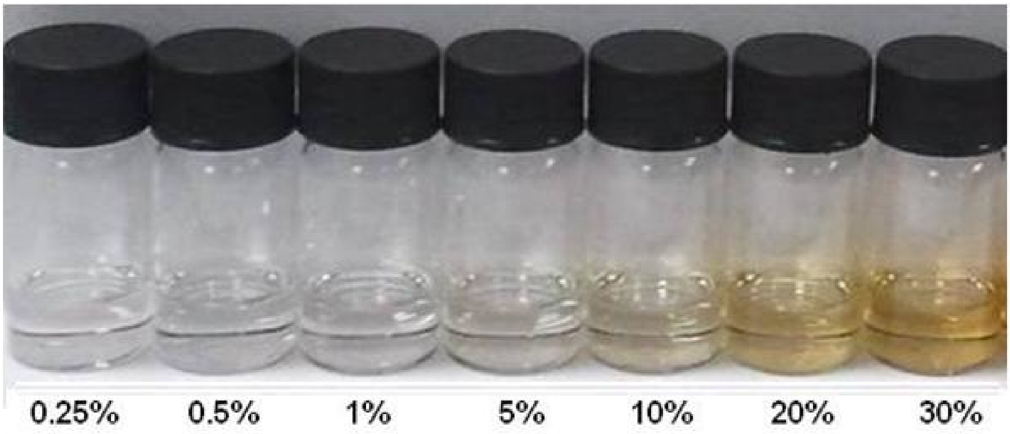

Figure 5.19: Photograph of microemulsions after 7 days under ambient conditions.

5.7.1.1 TEM

No macroscopic precipitate was observed, thus TEM was the primary technique utilised to image nanoscopic product. Results from a consistent dispersed phase volume of 20 µl/g in the surfactant solution are discussed below.

TEM studies revealed a large size differential in our product, ranging from ~2 nm to µm-sized, which is consistent with our proposed mechanism of small graphene sheets stacking to form eventually much larger graphitic material. For a 0.25 wt %. sugar solution, a bright field, high resolution and the corresponding fast Fourier transform (FFT) of the small 2-5 nm particles are presented in Figure 5.20.

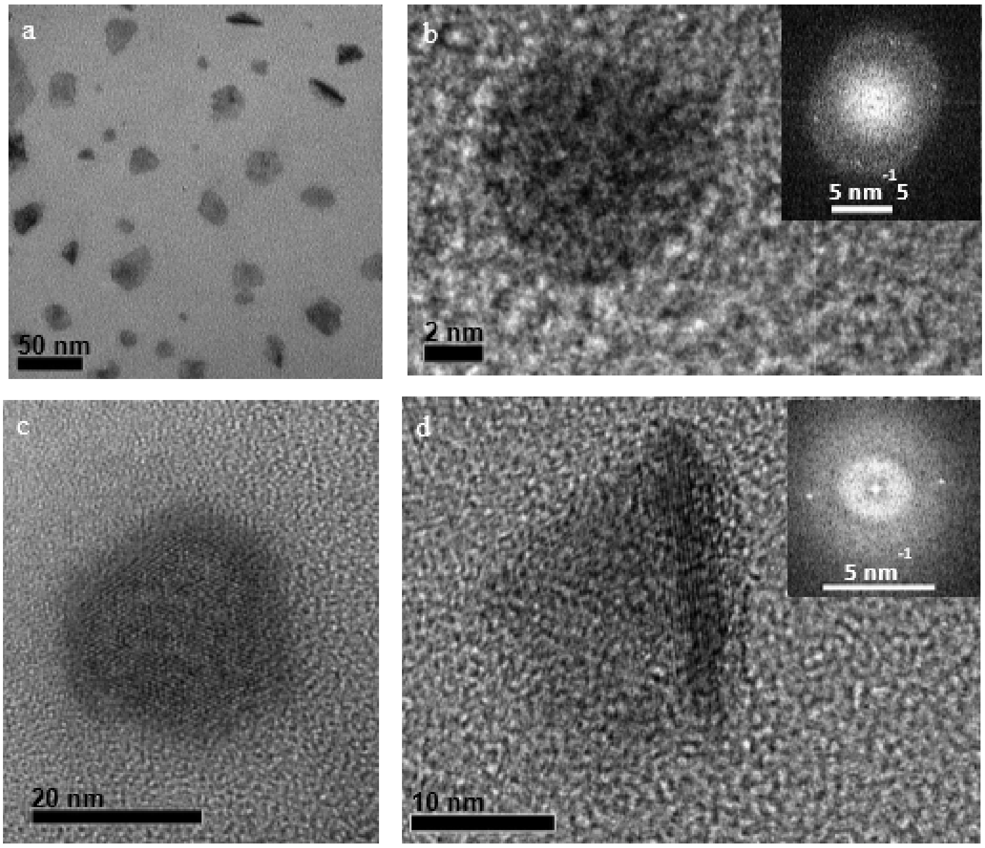

Figure 5.20 a-d: TEM of the primary nanographitic particles synthesised from 0.25 to 1 wt %. aqueous sucrose and sulfuric acid mixed microemulsions. (a) Bright field image of a group of ~3–30 nm particles. (b) High resolution image (HREM) of an 8 nm particle. The FFT (inset) shows the expected graphitic 0.213 nm hexagonal pattern. (c) HREM of a hexagonal ~25 nm particle. (d) A ~15 nm particle folded on the right-hand side, showing 15 layers. The FFT (inset) gives the expected 0.34 nm interlayer graphite spacing.

Note that the Fast Fourier transform (FFT) of the high resolution image is of the primary particle shown in Figure 5.20b shows the 0.213 hexagonal pattern expected for graphite, clearly supporting our hypothesis that the dehydration of sugar can go (virtually) to completion under the nanoconfinement imposed by the microemulsion droplets. In addition, for the folded nanoparticle shown in Figure 5.20d the FFT reveals the expected 0.34 nm graphite interlayer spacing. This also demonstrates the dehydration of sucrose is virtually complete; any residual oxygen must be confined to the sheet edges, where it will not hinder the close stacking of the essentially pristine graphene sheets.

Much of the nanographitic material is larger than these 2-5 nm primary particles and is indeed much larger than the mean expected microemulsion droplet size. This suggests product formation via two different pathways: the material is expelled from the droplet when its size is greater than the droplet size or the droplet size changes to accommodate the dimensions of the product. The former case is similar to what would be expected in Chapter 4, in the oriented quartz nanoaggregates, whereby the quartz nanoparticles, probably with adsorbed surfactant, aggregate to form larger oriented structures. This is unlikely in this case. Expulsion of the 3-30 nm nanoparticles from the droplets as bare particles into the cyclohexane continuous phase would not support crystallographic registry, rather a polycrystalline aggregate of the primary particles would result. This suggests that as the nanoparticles grow, the surrounding sulfuric acid and surfactant film can distort so as to accommodate this growth, with additional sulfuric acid and the surfactant being supplied by impinging and fusing microemulsion droplets.

For the same concentration of sucrose, much larger nanoaggregates of the order of ~250 nm are observed. From Figure 5.21 one can see the original 3-30 nm few-layer graphene primary particles prior and during the stacking process on the surface and edges, confirming the origin of these larger ~250 nm nanoparticles.

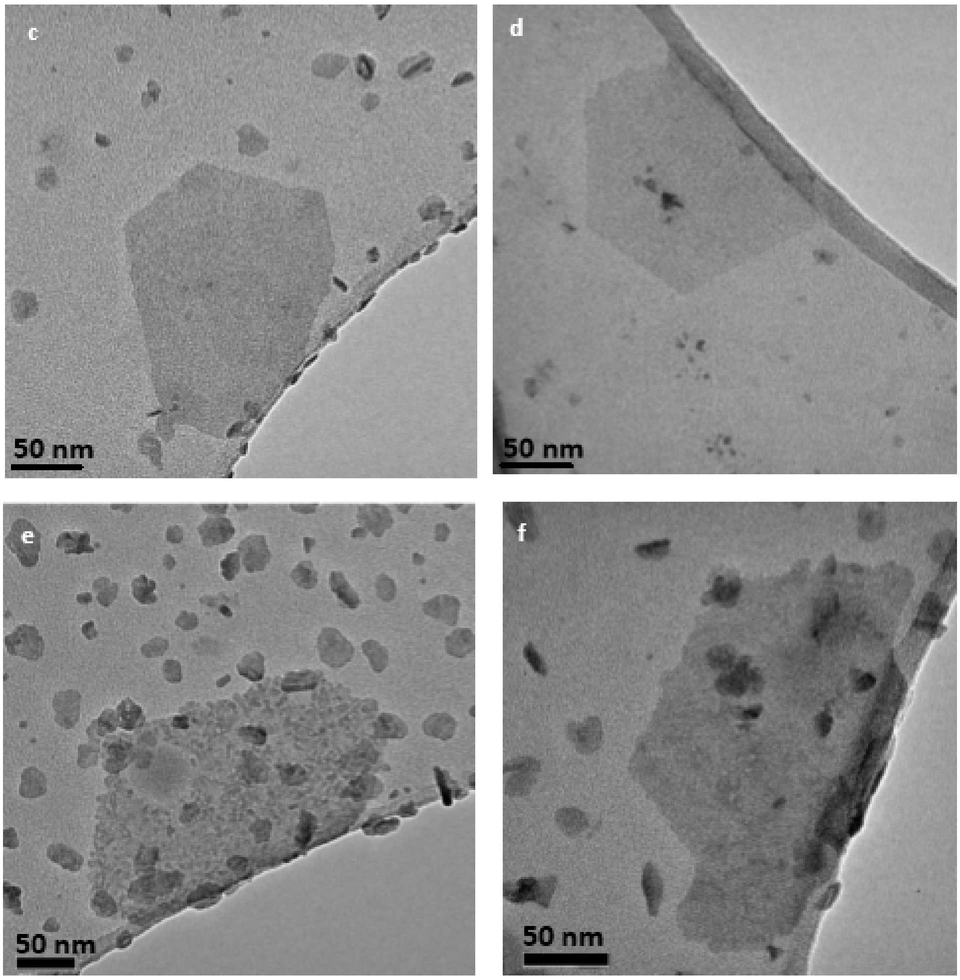

Figure 5.21 c-f: TEM Bright field images of the nanographitic aggregates synthesised from 0.25 to 1 wt.% aqueous sucrose and sulfuric acid mixed microemulsions showing ~ 250 nm particles, surrounded by smaller primary particles.

As per the quartz nanoaggregates in Chapter 4, during formation the structures can appear to have varying electron density across the surface, which is not unexpected given they are composed of smaller 2-30 nm primary particles, however they still produce single crystal-type electron diffraction patterns as shown in Figure 5.22.

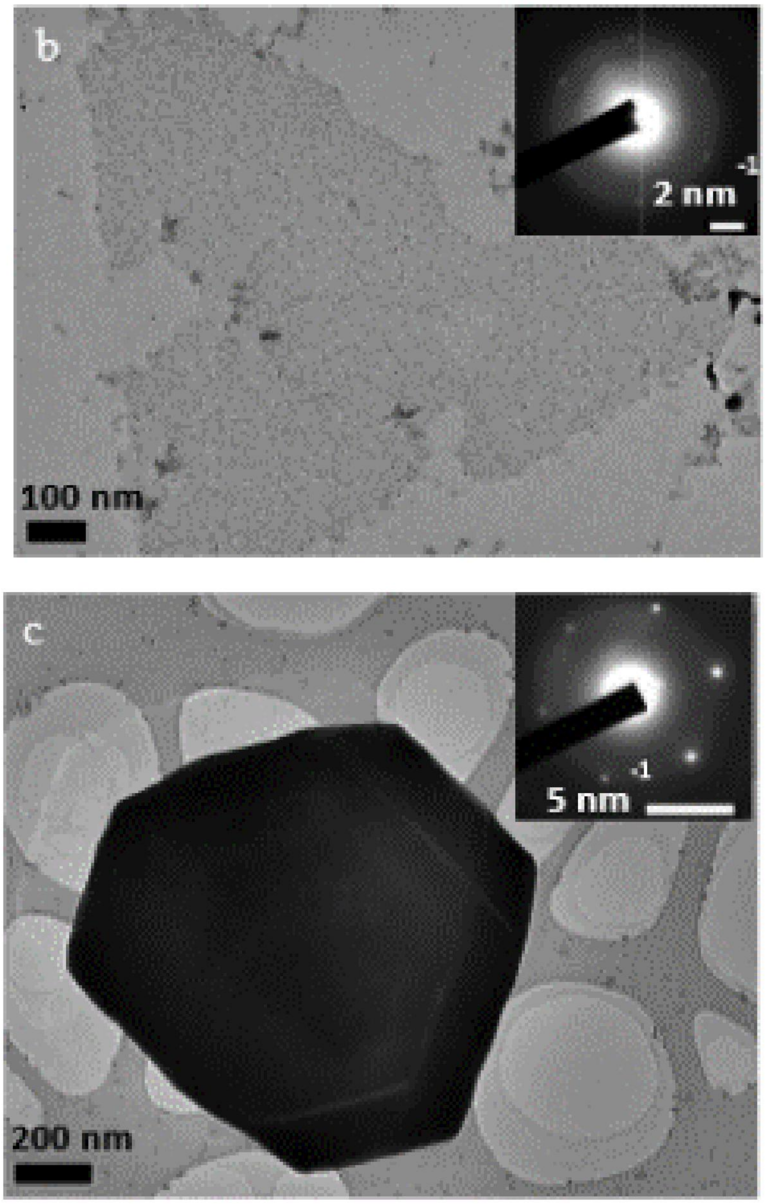

Figure 5.22 b-c: TEM of the nanographitic aggregates synthesised from 0.25 to 1 wt.% aqueous sucrose and sulfuric acid mixed microemulsions. (b) Bright field image of a thin and patchy µm-sized particle. Its weak electron diffraction pattern (inset) shows the expected 0.213 nm hexagon and (c) a µm-sized particle. Its electron diffraction pattern (inset) shows the expected 0.213 nm hexagon.

As the nanoparticles continue to be added onto the aggregates, µm sized crystals are obtained as in Figure 5.22c. In Figure 5.22b and c insets one can see the single crystal diffraction patterns obtained display the 0.213 nm hexagon pattern expected for a graphitic structure constructed with ordered AB Bernal stacking. For turbostratic graphite, one would expect a 0.213 nm ring, rather than 6 60° spaced diffraction spots.

This all supports the accomplishment of thermodynamic control, as the primary nanoparticles of size ~ 2-30 nm have stacked in crystallographic registry, whereby the nanoparticles only stack when their lowest energy stacking arrangement has been attained.

The quantity of the nanographitic product obtained using the mixed microemulsion is limited because the sucrose solutions were restricted to 0.25 to 1 wt%. in the aqueous, thus macroscopic identification techniques proved difficult. However utilising large scale-ups from the original 2 g microemulsion to 50 or 100 g, it was possible to extract sufficient material to perform Raman spectroscopy as an additional technique to identify the product.

5.7.1.2 Raman spectroscopy

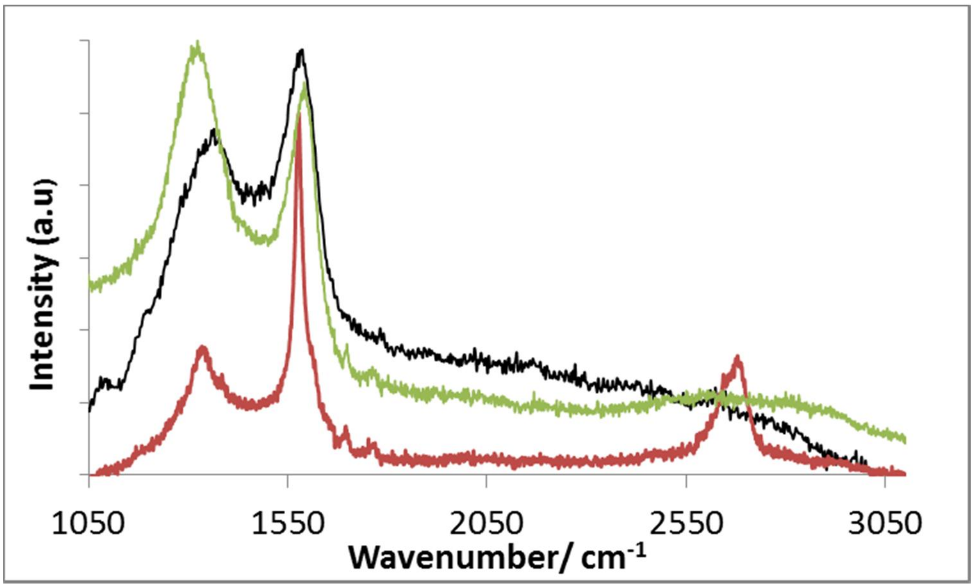

Figure 5.23 Raman spectra of material precipitated from the bulk reaction of sucrose with sulfuric acid (black), a commercial multi-layer (12 nm flake) graphene sample purchased from Graphene Supermarket (red) and spectrum from a 3 μm particle synthesised from a 1 wt.% aqueous sucrose and sulfuric acid mixed microemulsion (green)

For the 3 μm particle from the 1 wt %. sugar microemulsion, there is a G peak at 1580-1600 cm^{-1} and a D peak at 1350 cm^{-1} present. The former is the sole first-order structure present for infinite single crystals of graphitic carbon.[57] The D peak occurs when the carbonaceous product contains defects arising from disordered systems, finite crystal size and the presence of terminating groups. The origin of the Raman D, G and 2D peaks of carbonaceous particles is discussed in greater details in Appendix 2. In brief, the position, relative intensity and FWHM of the Raman D, G and 2D peaks are useful in determining the size of crystalline graphitic domains and defects. Of particular relevance to nanographitic material is the subject of crystalline domain sizes and their influence on the intensity of the D peak, which increases with crystallite size so that $I_D/I_G \alpha L^2$, where L is the domain size. [62,18] The small size of the nanographite obtained led to poor signal to noise, in addition to the third order Si peak of the supporting silicon wafer contributing to the Raman intensity in the region of 1450 cm^{-1}, i.e. around the location of the D peak. Thus a reliable FWHM and peak height for the D peak could not be obtained, but the intrasheet graphitic crystallites are expected to be of mean size of ~2-3 nm in accordance with Ferraris' approximation.[62,18] In comparison to the bulk sample, one can also identify a barely discernible 2D and D+G in the region of 2550 – 3000 cm^{-1}.

5.7.1.3 X-Ray Diffraction (XRD)

Due to no macroscopic precipitate because of the low sucrose concentrations, XRD analysis was not possible.

5.7.1.4 Atomic Force Microscopy (AFM) and Environmental Scanning Electron Microscopy (ESEM)

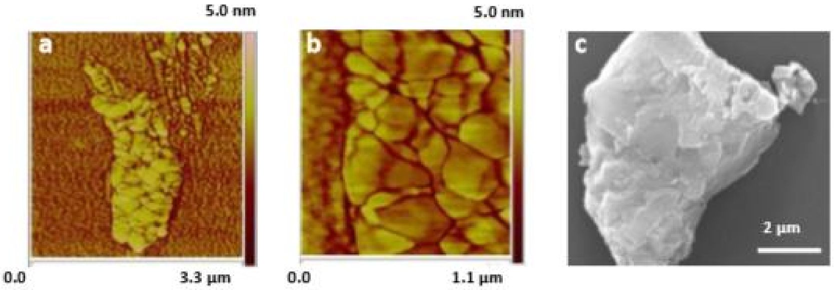

Figure 5.24 a-c: Representative AFM images and ESEM micrograph of the µm-sized graphitic particles synthesised from 0.25 to 1 wt %. aqueous sucrose and sulfuric acid mixed microemulsions. a and b show AFM phase contrast images from a 3 µm graphitic particle and c, shows an ESEM micrograph highlighting multiple steps on the surface of a 10 µm graphitic particle.

Representative AFM images and an ESEM micrograph of the µm-sized graphitic particles synthesised from 0.25 to 1 wt %. aqueous sucrose and sulfuric acid mixed microemulsions are shown in Figure 5.24.

AFM and ESEM were employed to explore the topography of the particles produced from 0.25 – 1 wt %. aqueous sucrose and sulfuric acid mixed microemulsions. The AFM phase contrast images from a 3 µm graphitic particle reveal its constituent nm-sized primary particles, whilst the ESEM micrograph reveals multiple steps and constituent particles on the surface of a 10 µm graphitic particle. The images are in agreement with the formation mechanism and TEM data presented previously, whereby primary 2-30 nm few-layer (near-pristine) graphene particles stack in crystallographic registry to form much larger µm-sized graphitic particles.

5.7.2 Effect of increased variation of sucrose concentration

5.7.2.1 TEM

5 wt %. Sucrose

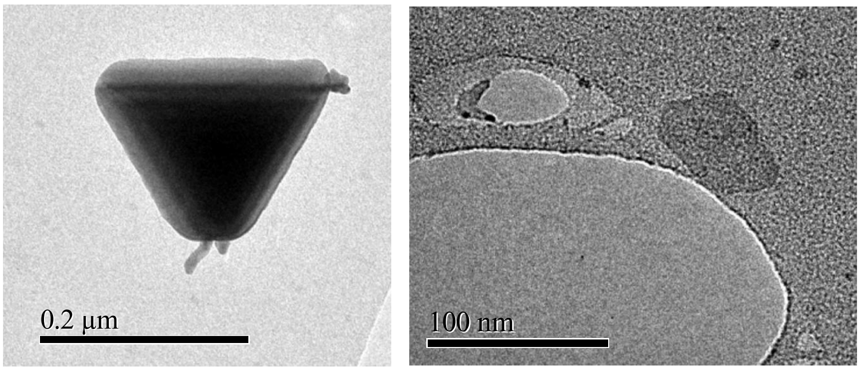

Figure 5.25 a-b: TEM of the nanographitic aggregates synthesised from 5 wt.% aqueous sucrose and sulfuric acid mixed microemulsions. (a) Bright field image of a large µm-sized particle and (b) a µm-sized particle.

As one increases the sucrose concentration above 1 wt % sucrose, there is greater variability in the product quality. When the aqueous sucrose concentration was 5 wt %, the 3-30 nm primary particles are harder to observe. Less frequently, µm sized crystals are seen alongside the thin 50 – 250 nm sheets, see Figure 5.25. In addition, amorphous carbons are observed.

30 wt %. Sucrose

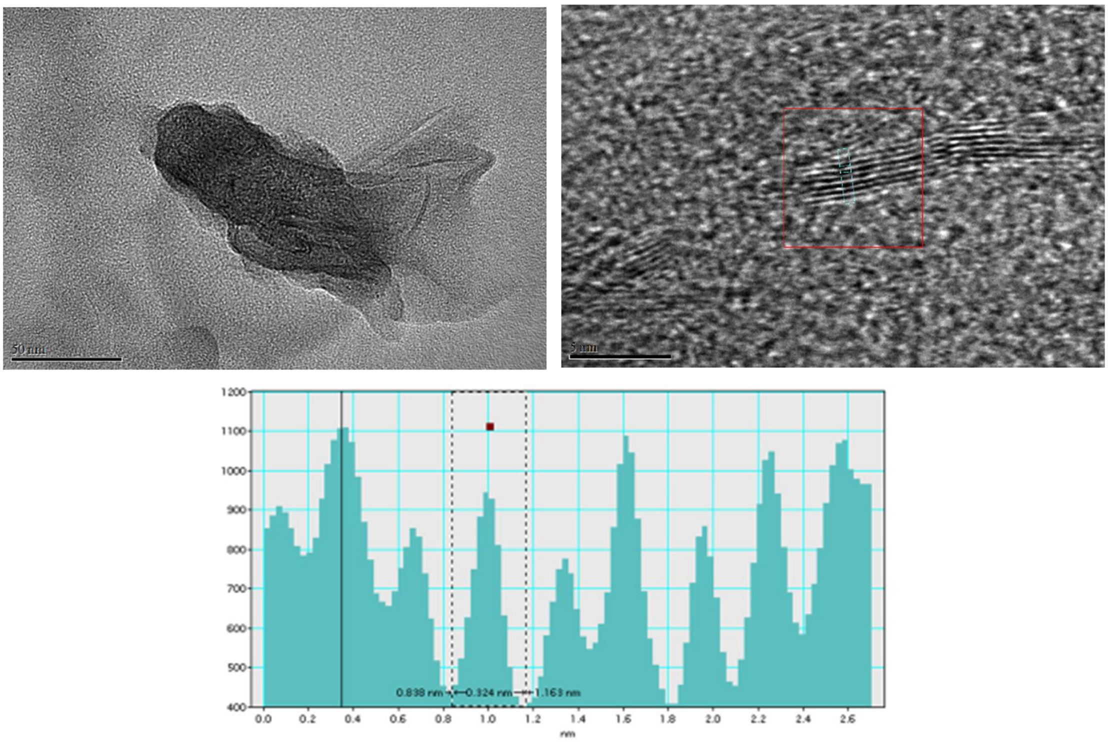

Figure 5.26 a-c : TEM of the nanographitic material synthesised from 30 wt.% aqueous sucrose and sulfuric acid mixed microemulsions. (a) Bright field image of a 150-200 nm sized particle, (b) a HREM imaging revealing a folded edge of graphitic material and (c) a depth profile of the folded material in (b), showing the expected 0.34 nm graphitic interlayer spacing.

For the 30 wt % aqueous sucrose mixed microemulsion an increased degree of disorder can be observed, see Figure 5.26a, in comparison to Figures 5.20-5.21 for the 0.25-1 wt %. sucrose sample. The carbonaceous product no longer exhibits AB Bernal stacking to create the mesocrystal like structures. Instead the material, albeit crystalline is seen to be folded and less-ordered. Figure 5.26b clearly displays the layers within the product, allowing a depth profile (c) to confirm the spacing to be 3.3-3.4 nm as per graphite.

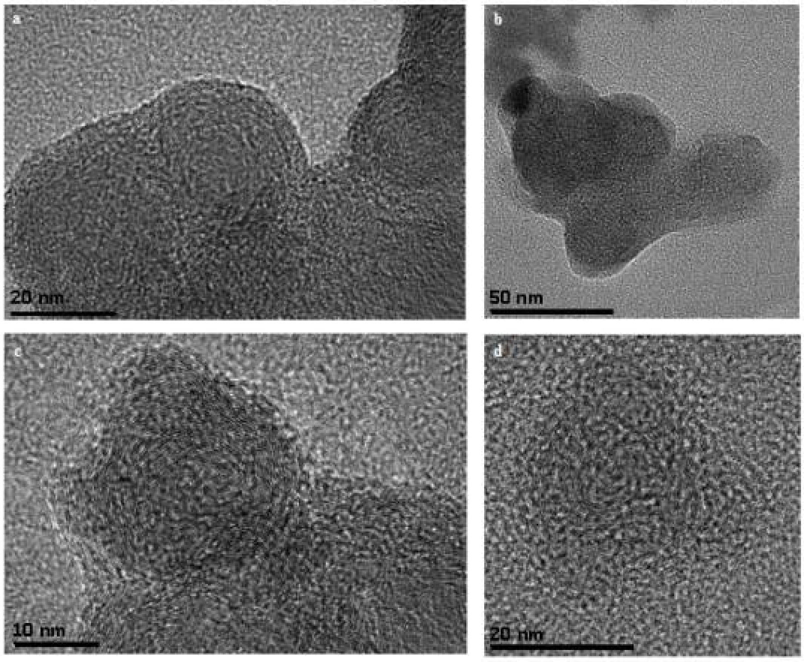

Figure 5.27 a-d: TEM images showing carbon nano-onions synthesised from a 30 wt %. sucrose and 95 wt %. sulfuric acid mixed microemulsions.

As the sucrose concentration increases, most of the product becomes amorphous and humins-like. Carbon nano-onions (see Figure 5.27 a-d) showing the 0.34 nm interlayer spacing also form, as seen in the product from the bulk reaction between sucrose and sulfuric acid. Thus it is important to note that the 3-30 nm nanographitic material and their mesocrystal-like aggregates, the graphitic ~250 nm and μm-sized particles, are only the major product from microemulsions with a low sucrose concentration, typically of 0.25 – 1 wt %.

5.7.2.2 Raman spectroscopy

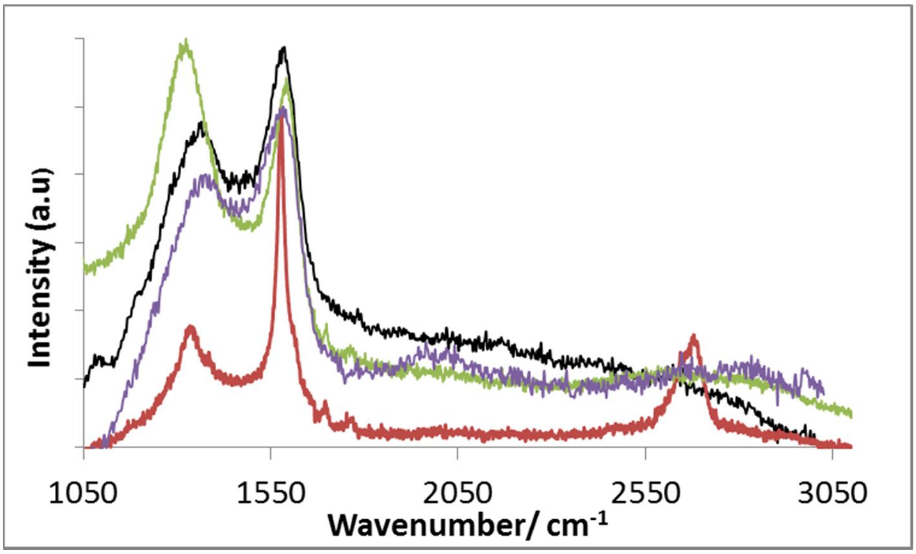

Figure 5.28: Raman spectra of material precipitated from the bulk reaction of sucrose with sulfuric acid (black), a commercial multi-layer (12 nm flake) graphene sample purchased from Graphene Supermarket (red), a spectrum from a 3 µm particle synthesised from a 1 wt.% aqueous sucrose and sulfuric acid mixed microemulsion (green) and spectrum from a precipitate synthesised from a microemulsion ≥ 30 wt.% aqueous sucrose and sulfuric acid mixed microemulsion (purple).

For the ≥ 30 wt %. sucrose microemulsion precipitate, the spectrum is analogous to the bulk sample, with a relatively small D peak ~ 1350 cm^{-1} and no 2D peak, suggesting the presence of disordered carbonaceous product.

5.7.2.3 XRD

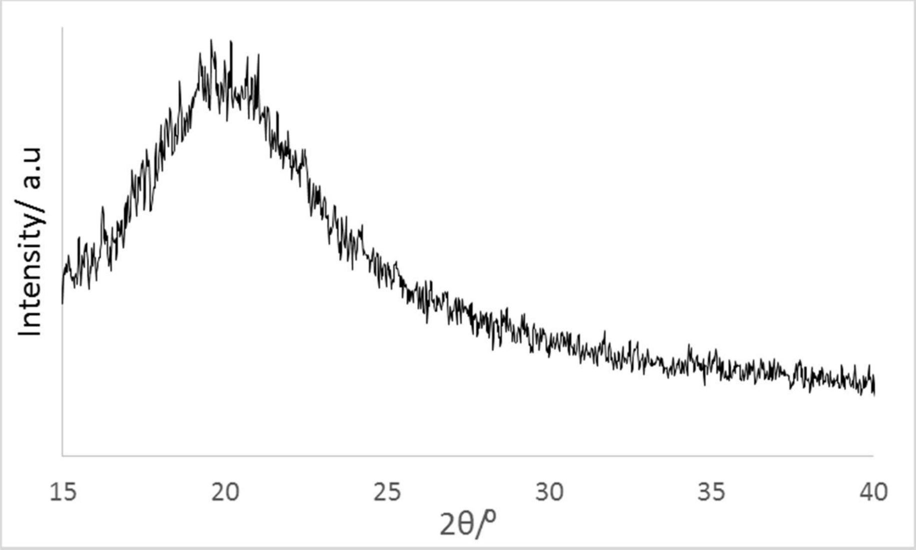

Figure 5.29: Experimental pXRD of the precipitate synthesised from a microemulsion ≥ 30 wt.% aqueous sucrose and sulfuric acid mixed microemulsion. XRD showing only a broad amorphous peak centred at 2θ ~ 21^0.

Analysis of the precipitated product from the 30 wt % sucrose mixed microemulsion by X-ray diffraction (Figure 5.29) yield only an amorphous band, centred at 2θ ~21 °, similarly to that observed in Figure 5.11 for the product of the bulk sugar and sulfuric acid reaction.

5.7.3 Estimation of the amount of carbon within the droplet

SAXs measurements were performed to determine an approximate droplet size. This procedure will be discussed further in Section 5.7.4.2. However, assuming the droplet size remains independent of the sucrose concentration, one can estimate the average number of sucrose molecules per droplet. (Table 5.2)

Sucrose precursor concentration (wt %.)	**Mean number of sucrose molecules per droplet – 20 µl/g (1.9 ± 0.3 nm) (Gift)**
0.25	0.03
1	0.09
5	0.55
10	1.10
30	3.60

Table 5.2: Estimation of the average number of sucrose molecules residing in the microemulsion droplets (GIFT estimation).

This approximation indicates that there is insufficient sucrose present to allow the precipitation of carbon product within any one droplet, without additional sucrose molecules being supplied through colliding droplets that produce a transient droplet dimer, since pristine graphene sheets of size 1-2 nm would require dehydration and polymerisation of ~4-16 sucrose molecules. Hence synthesis of 2 nm-sized carbonaceous particles in the 1 wt % aqueous sucrose mixed microemulsions will occur at a slower rate, so that the particles are bathed in sulfuric acid for sufficient time to become virtually pristine graphene sheets (the primary nanoparticles), thus allowing graphitic particles to eventually develop through further stacking of these primary nanoparticles. However, for a 30 wt % sucrose concentration, the mean number of sucrose molecules per droplets is ~3.6. Thus in this situation, the carbonaceous material can grow relatively rapidly through transient droplet dimer formation, particularly in larger droplets. As such, material can grow to larger dimensions; sufficiently large to stack irreversibly, irrespective of the presence of residual oxygen and hydrogens, and this results in the formation of amorphous humins.

5.7.3.1 Ratio of sulfuric acid: sucrose molecules

Concentration of sucrose (wt%)	**Number of H_2SO_4 molecules per sucrose molecule**
1	584
5	115
10	56
20	27
30	17
40	12
50	10
60	8
70	6

Table 5.3: Estimation of the ratio of sulfuric acid to the sucrose molecules in a droplet, assuming a constant dispersed phase of 20 µl/g (gift estimation).

Table 5.3 reveals that a change in the carbonaceous product occurs increasingly when the ratio of H_2SO_4 molecules: sucrose molecules per droplet decreases below ~100. In the presence of a large excess of sulfuric acid, the carbonaceous material is forced to remain within the droplets subjected to a huge excess of sulfuric acid promoting complete dehydration, thus the formation of pristine graphene sheets which stack irreversibly. Whereas when there is a limited supply of the sulfuric acid, the dehydration does not go to completion, instead the carbonaceous product rapidly becomes insoluble, precipitating as amorphous humins.

5.7.4 Effect of varying the dispersed phase volume

5.7.4.1 TEM

Figure 5.30 reveals TEM data obtained from microemulsion samples of 0.25 -1 wt % aqueous sucrose, but with a larger dispersed volume of 60 µl/g rather than 20 µl/g.

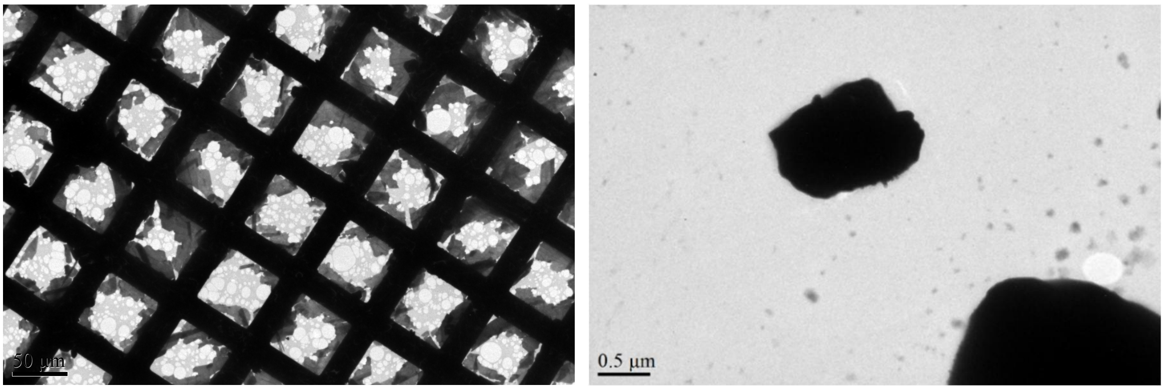

Figure 5.30 a: Low magnitude and b: Bright field images of µm sized amorphous type material from a 60 µl/g 1 wt % aqueous sucrose and sulfuric acid mixed microemulsions.

The TEM images show that amorphous carbon precipitate arises alongside crystalline graphitic material from larger microemulsion droplets. Comparisons of the data from the 0.25-1 wt %. sucrose mixed microemulsion with dispersed volumes of 20 µl/g (Figures 5.20-5.22) and 60 µl/g (Figure 5.30) show a change in the majority polymorph produced from the microemulsion, from the stable nanographite structures for the 20 µl/g microemulsions to metastable amorphous phase for the 60 µl/g microemulsions. This demonstrates that larger droplets have significantly more sucrose molecules to undergo rapid dehydration in the presence of sulfuric acid to produce metastable amorphous carbonaceous material.

5.7.4.2 SAXS analysis and geometric droplet sizes

5.7.4.2.1 Electron density

The electron densities of each of the microemulsion components are displayed in Table 5.4.

Component	**Electron density/Å^{-3}**	**Electron density relative to the cyclohexane continuous phase / Å^{-3}**
Sugar	0.51	0.23
H_2SO_4	0.56	0.28
Water	0.33	0.05
CTAC head groups	0.23	-0.05
Hexadecane CTAC tail groups	0.28	0
Pentanol	0.28	0
Cyclohexane	0.28	0

Table 5.4: The electron densities of the components of the microemulsion

If the baseline electron density is taken to be that of the cyclohexane continuum, one can see that taking the centre of the microemulsion droplet as an arbitrary point and moving radially outwards towards the continuous phase, a change in sign of the relative electron density contrast is observed. Thus the pair-distance distribution function, p(r), in Figure 5.31b has two distinct maxima and a minimum suggesting that the best fit for the CTAC surfactant system is the spherical core-shell model, with a high electron density core consisting of the dispersed phase and the hydrophilic head group of the surfactant and the pentanol co-surfactant, with a hydrophobic shell of hexadecane surfactant tails, with residual cyclohexane between the tail groups. To gain a more detailed perspective, the geometric prediction and GIFT prediction from the experimental SAXS data were computed to estimate the droplet size within the system upon the addition of 20 and 60 µl/g of dispersed phase. The scattering and pair-distance distribution, p(r), functions obtained from the raw data and GIFT analysis, respectively, from SAXS experiments are presented in Figure 5.31a and b.

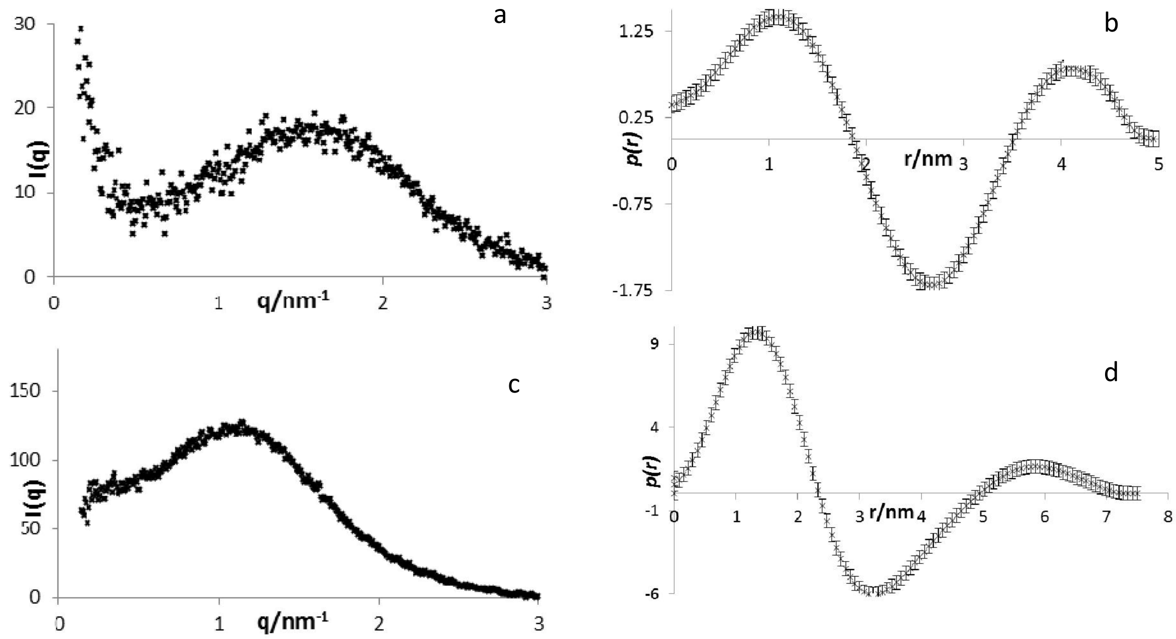

Figure 5.31 a-d: a and b :Scattering curves I(q) vs. q for the mixed microemulsion containing 1 wt.% sucrose, for a: 20 µl/g and b: 60 µl /g. c and d: Pair-distance distribution curves for mixed microemulsion containing 1 wt.% sucrose , for c: 20 µl/g and d: 60 µl /g.

For each case the radius of the inner hydrophilic core phase is established from the value of the point of inflection before the first minimum, which determines the hydrophilic core diameter. Whilst the entire droplet size diameter is accepted to be taken from the point where the pair distribution function returns to zero.

For spherical droplet microemulsions, the mean hydrophilic core radius can be estimated geometrically to be $r = \frac{3\varphi}{NA}$, where φ is the volume fraction of the hydrophilic phase, N is the number of surfactant molecules at the interface and

A is the surfactant area per molecule. For the following geometric calculations a value of 0.65 nm^2 [63] was adopted for CTAC.

Consistently the core droplet sizes are much smaller than predicted from the geometric predictions of 1.84 and 3.14 nm respectively, for the addition of 20 and 60 µl/g of dispersed phase respectively.

This is rationalised by the lack of pentanol being incorporated in to the geometric calculations. Pentanol acts as a cosurfactant to reduce the droplet size due to its incorporation into the microemulsion droplet interface, thus increasing the interfacial area. The extended hydrocarbon chain length for CTAC is 2.174 nm[64], so the thickness of the hydrocarbon tails in the droplets would be expected to have values in the range of ~0.8 x 2.2 = 1.8 nm. Thus, the core radial size may differ by ~1.8 nm. The GIFT-determined values are smaller however, since the cyclohexane penetrates into the CTAC tailgroups, effectively reducing the electron contrast with the continuous phase to near zero before the tailgroup region ends.

5.7.4.3 Estimated carbon concentration within the droplet

One can estimate the average number of sucrose molecule per microemulsion droplet as the dispersed phase volume increases from 20 and 60 µl/g (Table 5.5) using the GIFT-determined hydrophilic core radius size.

Dispersed phase volume µl/g	**Droplet size (nm) GIFT estimation**	**Mean number of sucrose molecules per droplet – 1 wt% sucrose**
20	1.8	0.116 ± 0.006
60	2.1	0.36 ± 0.02

Table 5.5: Estimation of the average number of sucrose molecules residing in the microemulsion droplets (gift estimation).

This approximation illustrates that increasing the dispersed phase volume to 60 µl/g may result in the larger droplets containing enough sucrose for rapid dehydration to occur and lead to the precipitation of amorphous humins. It is also likely that the larger droplets rupture more easily (as outline in Chapter 3, they can change their surface curvature with less energy penalty). Consequently larger droplets are likely to form transient dimers more readily when the droplets collide, and this will also cause the rate of carbonaceous particle growth to increase, making amorphous carbons more likely to be the resulting product.

5.8 Sucrose crystal dissolution methodology: Results and discussion

Insufficient material was attained from the mixed microemulsion method discussed thus far to be able to conduct XRD analysis, so the previous results relied heavily on TEM results. Consequently, a sucrose crystal dissolution methodology was adopted, whereby sugar crystals were added to the bottom of vials containing sulfuric microemulsions. The vials were left for a month during which time black material deposited on the bottom of the vials.

A compromise between two possible mechanisms must be made upon employing this system. Large dispersed volumes (50 – 60 μl/g) are preferred with regards to providing sufficient water and sulfuric acid molecules per droplet to promote the otherwise too slow dissolution of the sucrose crystals via the continuous phase into the sulfuric acid droplets, where the dehydration reaction can then proceed. However, as discussed in Chapter 3, larger droplets tend to undergo changes to the curvature with ease in comparison to smaller droplets. This scenario would recreate a micro bulk sucrose and sulfuric acid reaction where one would expect a carbonaceous material consisting of humins or amorphous carbon to result. Evidence for this undesirable reaction is seen when the black coating occurs on as yet-undissolved sugar crystals. As such, one must note that this sucrose crystal dissolution methodology was only employed to produce sufficient material for further analysis to corroborate the observations from the mixed microemulsion methodology.

5.8.1 Effect of varying the dispersed phase

5.8.1.1 Visual observations

Upon precipitation over the period of 1 month, the quantity of precipitate observed from the for 2 mg/g sucrose crystals in 45 µl/g sulfuric acid microemulsion was significantly less than that produced by a 2 mg/g sucrose crystals in 50 µl/g sulfuric acid microemulsion. However the microemulsion still turns black indicating nanographitic material must remain dispersed throughout the microemulsion, but has not yet reached a size where it will precipitate.

Figure 5.32: Black precipitate observed from sucrose crystal dissolution methodology for 2 mg/g sucrose crystals in 50 µl/g sulfuric acid microemulsion.

5.8.1.2 Raman Spectroscopy

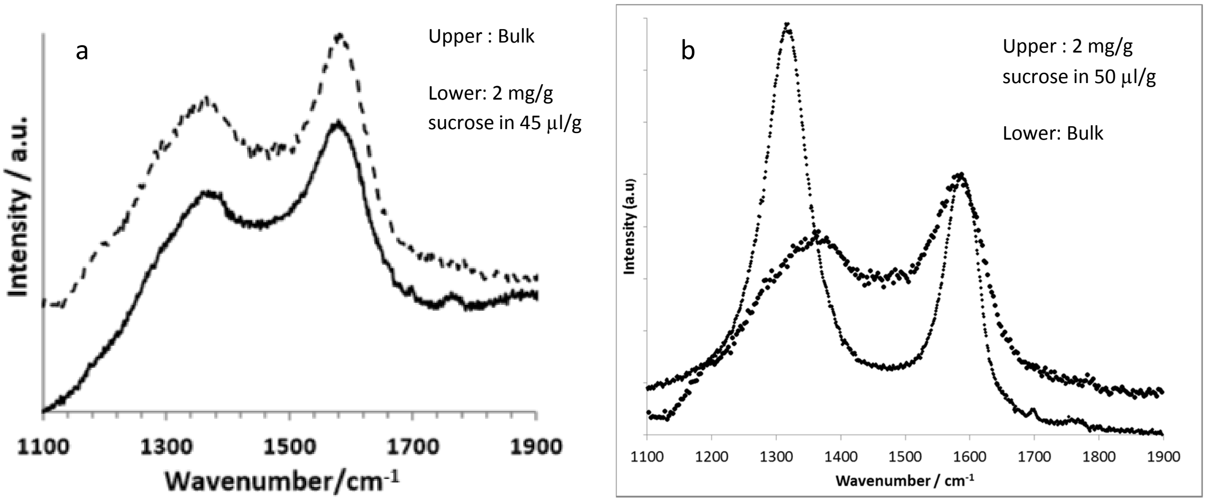

Figure 5.33 a-b: a: Raman spectra of material precipitated from the sucrose crystal dissolution methodology for 2 mg/g sucrose crystals in 50 µl/g sulfuric acid microemulsion quantities of sucrose addition. b: 2 mg/g sucrose crystals in 45 µl/g sulfuric acid microemulsion quantities of sucrose addition. The bulk reaction of sucrose with sulfuric acid Raman spectrum is included on both for comparison. (Bold markers)

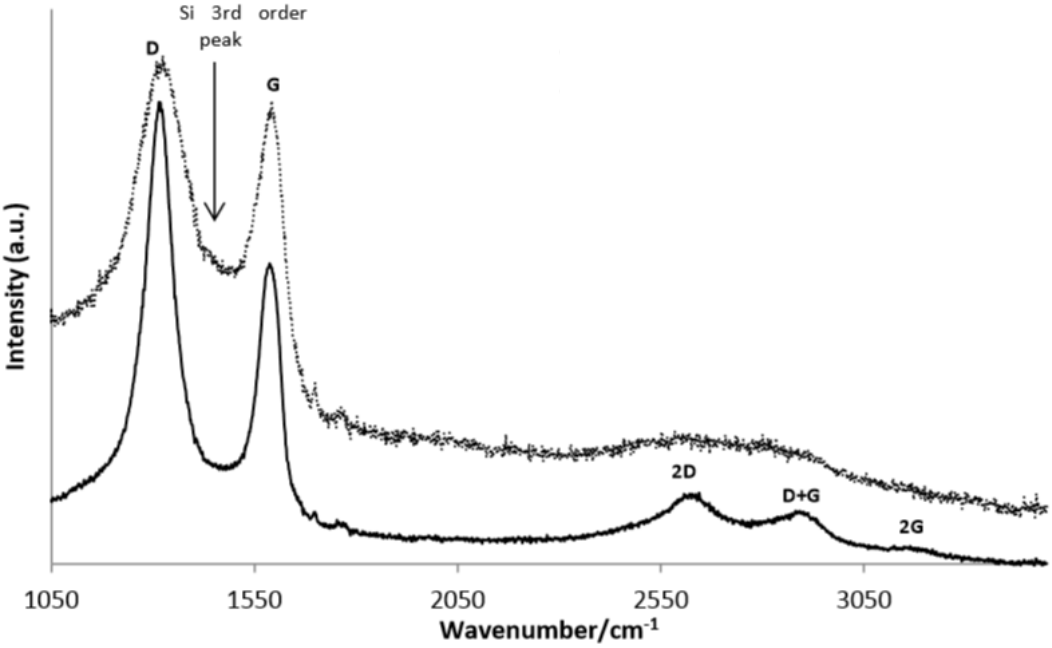

Figure 5.34: Expansion of Figure 5.33 b - Raman spectra of the nanographitic aggregates. Spectrum from a 3 µm particle synthesised from a 1 wt.% aqueous sucrose and sulfuric acid mixed microemulsion (dashed curve). The D peak at ~1350 cm-1 also contains a significant contribution from the silicon wafer 3rd order peak at ~1450 cm-1. The black curve shows the spectrum of the black precipitate from the microemulsion containing 45 µl g^{-1} sulfuric acid with 2 mg g^{-1} added sucrose and has D, G, 2D, D+G and 2G peaks.

In the Raman spectrum of the 50 µl/g sulfuric acid microemulsions case, one can see significant overlap and broadening of both the D and G bands at 1370 cm^{-1} and 1680 cm^{-1}. By reducing the dispersed phase to 45 µl/g in the sulfuric microemulsion, with the same quantity of added sucrose, the D and G peaks are at 1316 and 1585 cm^{-1}, respectively with a 2D peak which is clearly visible at 2630 cm^{-1}, along with the D+G peak (2900 cm^{-1}) and a weak 2G (3170 cm^{-1}) peak (see Figure 5.34). The FWHM of the G peak is narrower at ~70 cm^{-1}, a values representative of nanographitic particles.[65-66] In combination with the width and the relative height of the D peak, one can estimate the graphene domain sizes within the particles to be of the order ~2-3 nm; i.e. a size commensurate with our primary few layer graphene particles seen in the TEM data on the product from the mixed microemulsion synthesis route.

5.8.1.3 XRD

The XRD of the black product obtained in a month by using 50 µl and 45 µl of sulfuric acid per gram of surfactant solution to form the microemulsion, and then adding 2 mg/g of sucrose by the sucrose crystal dissolution method is shown in Figure 5.35.

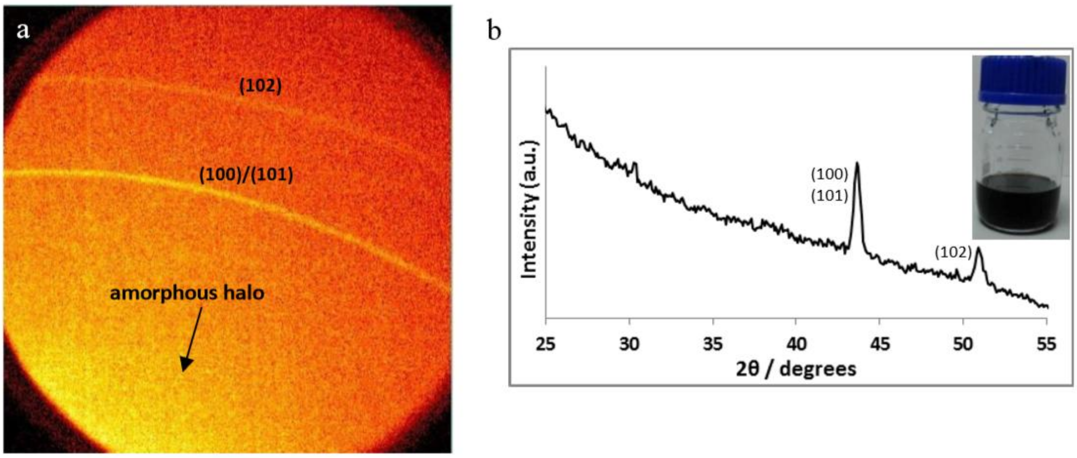

Figure 5.35 a-b: XRD data from <0.1 mg of graphitic nanoaggregates precipitated in 1 month from a 50 µl g^{-1} sulfuric acid microemulsion with 2 mg/g added sucrose. (a) 2D XRD detector image obtained after two hours showing a the graphite (100)(101)(102) peaks and a very weak amorphous halo and b: Chi integration of the data shown in (a).

In Figure 5.35 the graphite (002) peak is not discernible above the broad amorphous peak centred at $2\theta \sim 21^{\circ}$, but the graphite (100)/(101) peaks are clearly visible at $2\theta = 43.8^{\circ}$, with a weaker (102) peak at $2\theta = 51.0^{\circ}$, corresponding to a mean spacings of 0.207 nm and 0.179 nm respectively. Both peaks are relatively sharp, providing a low FWHM of 0.4° and 0.6° for the (100)/(101) and the (102) peak respectively. The (102) peak clearly establishes that graphitic AB stacking has occurred. Applying the Scherrer equation the crystallite domains can be determined to be a minimum of ~15 nm in this direction, corresponding to ~8 nm in the intersheet c-direction and, thus equating to ~23 stacked graphene sheets. The presence of further non-graphitic carbonaceous material may have led to broadening of the XRD peak, thus indicating this to be a minimum value. The 15 nm crystallite size reveals that the primary nanographite building blocks, which have intersheet sizes of only ~

3 nm, must have stacked with crystallographic registry, thus corroborating the observations made in the TEM images.

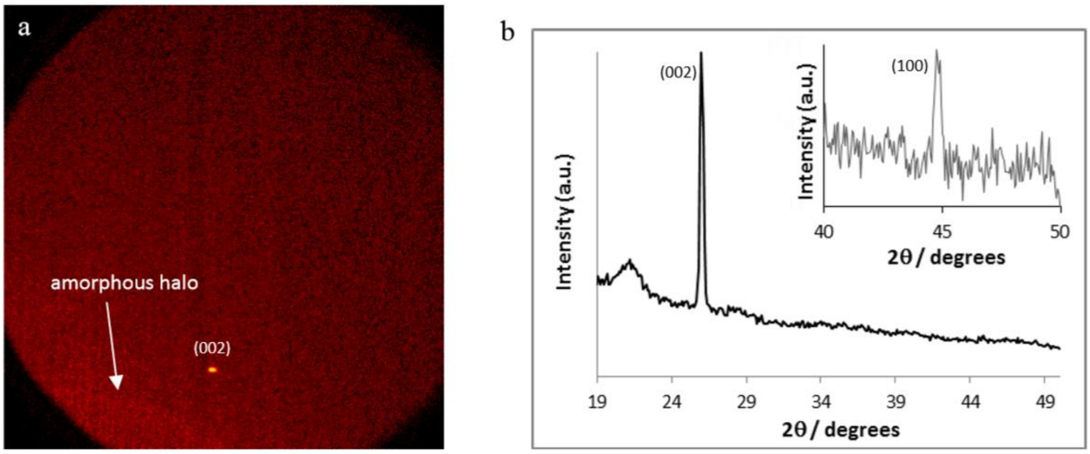

Figure 5.36 a-b: XRD data from <0.1 mg of graphitic nanoaggregates precipitated in 1 month from a $45\ \mu l\ g^{-1}$ sulfuric acid microemulsion with 2 mg/g added sucrose. (a) 2D XRD detector image obtained after two hours showing a the graphite (002) peak and a very weak amorphous halo and b: Chi integration of the data shown in (a).

By reducing the volume of sulfuric acid to 45 µl/g in the microemulsion, whilst maintaining the added sucrose quantity of 2 mg/g; substantially less precipitate is produced, though the microemulsion still turns black showing the presence of much nanographitic primary particles remain dispersed throughout the microemulsion. One would not expect a significant change to the core droplet size, however one can expect the inclusion of less pentanol, making the interfacial film less flexible[67-68] and less susceptible to transient droplet dimer formation, rupturing of the droplets onto the sucrose crystal and the diffusion of the sucrose across the cyclohexane continuous phase into the droplets. Thus the rate of formation of nanographite is significantly slowed, with the formation of amorphous material partially circumnavigated.

Figure 5.36 displays the increased quantity of nanographitic material in the form of the (002) peak at $2\theta = 25.9^{\circ}$, with a much weaker amorphous halo at $2\theta = 21.2^{\circ}$. The limited amount of precipitate means only a single spot rather than a continuous ring is observed, due to limited orientations. The $2\theta = 25.9^{\circ}$ value corresponds to a mean interplanar spacing of 0.344 nm, which is analogous to the 0.335 nm value for graphite. Applying the Scherrer equation the crystallite domains can be determined to be a minimum of ~25-30 nm, supporting that the primary nanographite building blocks, which have intersheet sizes of only ~ 3 nm, must have stacked with crystallographic registry, thus corroborating the observations made in the TEM images.

5.8.1.4 TEM

The TEM of the 50 µl g^{-1} sulfuric acid microemulsion with 2 mg/g added sucrose, in Figure 5.36 shows a mixture of amorphous carbonaceous materials alongside nanographitic particles similar to those observed from the mixed microemulsion method.

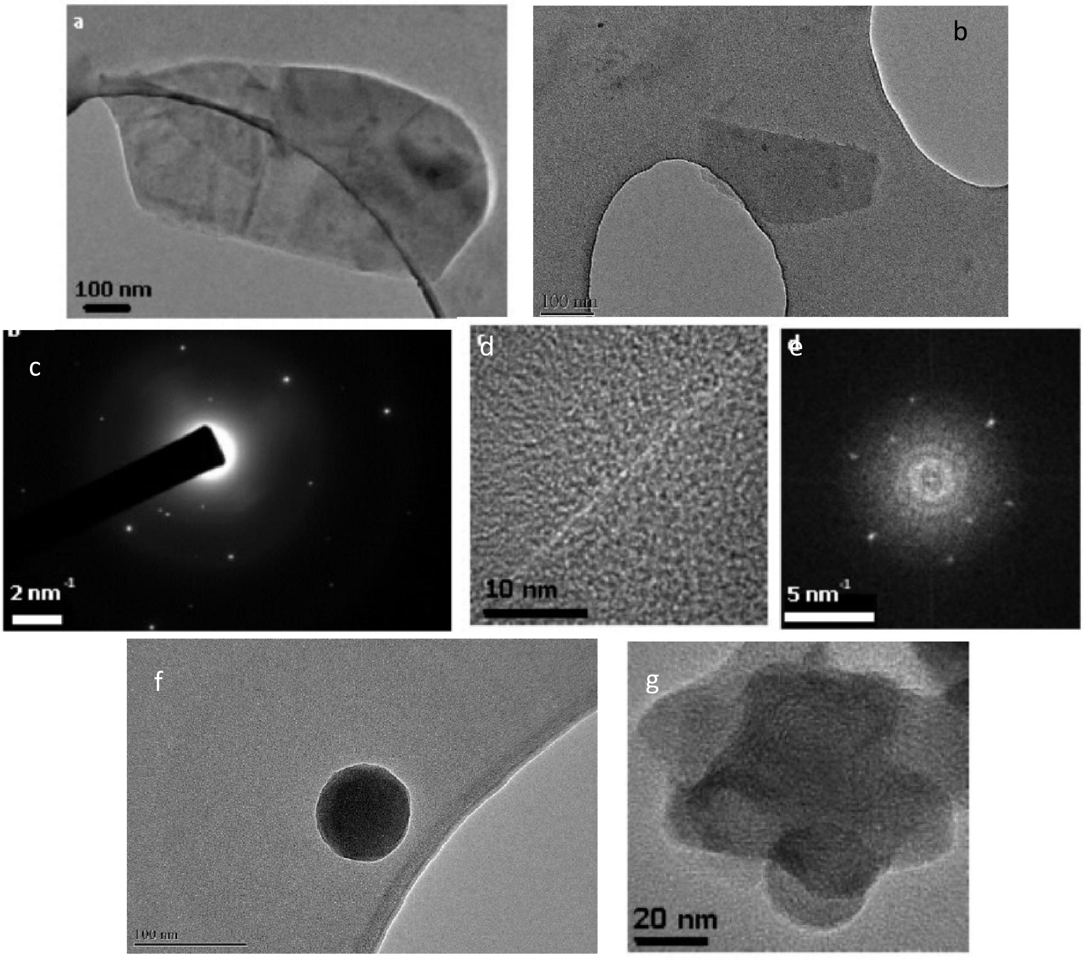

Figure 5.37a-g: a and b. TEM Bright field images of the nanographitic material comparable to the nanoparticle observed by the mixed microemulsion method, c: corresponding DP to b, with expected 0.213 nm hexagon, d: HREM image of part of the aggregate shown in a, encompassing a folded region, eLFFT of the region around this HREM image, showing the 0.213 nm hexagonal spacing and the 0.34 nm interlayer spacing arising from the folded region, f and g: TEM bright field image showing amorphous carbons that comprised the majority of the precipitate along with a minority of the nanographitic particles.

Although not apparent from Figure 5.37, TEM analysis confirmed that the sample consisted primarily of amorphous carbons, suggesting that although one would expect minimal change (see Figure 5.39) in the droplet size between the two cases, the slightly larger droplet results in a significant reduction in the free energy associated with a change in the film curvature, thus enabling the droplets to rupture on the sucrose crystals. This induces the formation of a significant proportion of amorphous carbons rather than the formation of nanographite.

5.8.1.5 SAXS analysis and geometric droplet sizes

5.8.1.5.1 Electron density

The electron densities of each of the microemulsion components are displayed in Table 5.6.

Component	**Electron density/Å^{-3}**	**Electron density relative to the cyclohexane continuous phase / Å^{-3}**
Sugar	0.51	0.23
H_2SO_4	0.56	0.28
CTAC head groups	0.23	-0.05
Hexadecane CTAC tail groups	0.28	0
Pentanol	0.28	0
Cyclohexane	0.28	0

Table: 5.6: The electron densities of the components of the microemulsion

If the baseline electron density is taken to be that of the cyclohexane continuum, one can see that taking the centre of the microemulsion droplet as an arbitrary point and moving radially outwards towards the continuous phase, a change in sign of the relative electron density contrast is observed. Thus the pair-distance distribution function, p(r), in Figure 5.39 has two distinct maxima and a minimum suggesting that the best fit for the CTAC surfactant system, with a sole sulfuric acid dispersed phase is also a spherical core-shell model as described in Section 5.7.4.2. However, substitution of the water phase increases the electron density of the aqueous phase significantly, thus increasing the electron density contrast between the confined phase and the oil continuum phase. One would expect the 1st maximum of the p(r) to be more pronounced in comparison to the mixed microemulsion case, as indeed can be seen from Figure 5.39.

To gain a more detailed perspective, the geometric prediction and GIFT prediction from the experimental SAXS data were computed to estimate the droplet size within the system upon the addition of 20, 45 and 60 µl/g of sulfuric acid dispersed phase. The scattering and pair-distance distribution, p(r), functions obtained from the raw data and GIFT analysis, respectively, from SAXS experiments are presented in Figures 5.38-5.39.

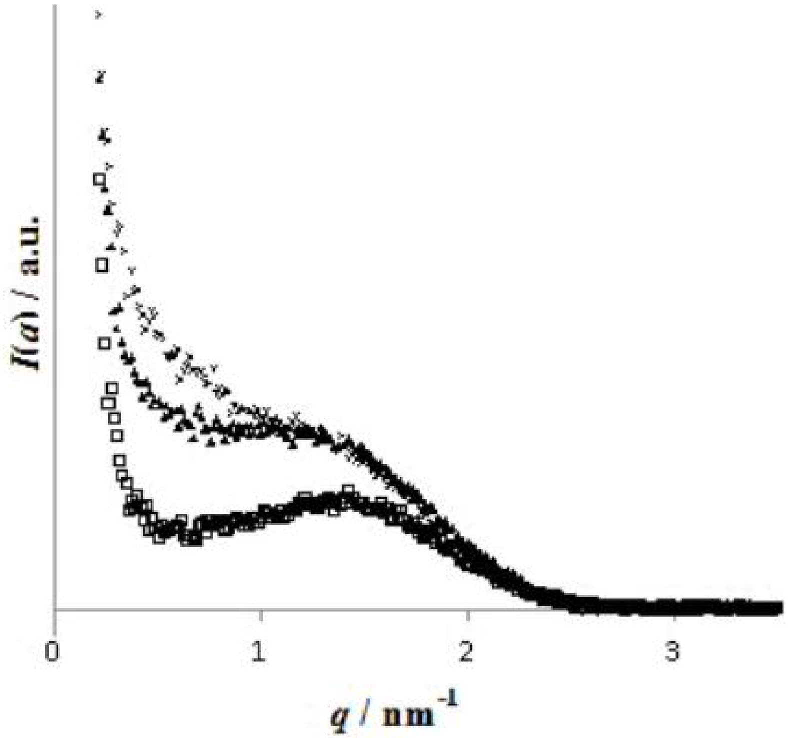

Figure 5.38: Scattering curves I(q) vs. q for the sulfuric acid microemulsion with 20 µl/g (squares), 45 µl /g(triangles) and 50 µl /g (crosses) dispersed phase volume.

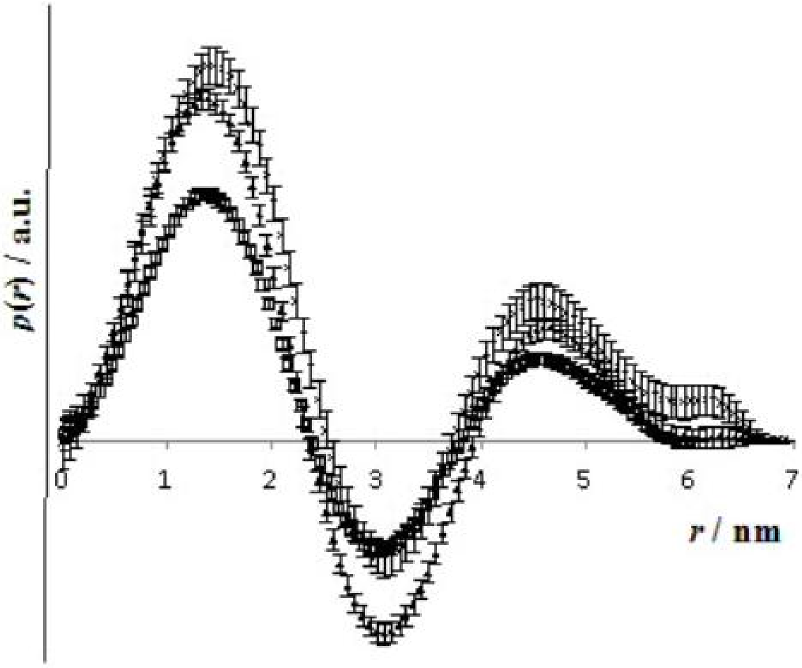

Figure 5.39: Pair-distance distribution curves for the sulfuric acid microemulsions with 20 µl/g (squares), 45 µl /g(triangles) and 50 µl /g (crosses) dispersed phase volume.

The same approach is applied as in Section 5.7.4.2 is employed to determine both the geometric and GIFT droplet size estimations. The GIFT estimation determined the hydrophilic core radii to be ~ 1.8, 1.9 and1.9 nm, respectively for the 20 µl/g, 45 µl/g and 50 µl/g. The analogous geometric determined values are: 1.45, 1.94 and 2.03 nm respectively. The minor differences between the two estimations may originate from the pentanol cosurfactant, which acts to reduce the droplet size due to its incorporation into the microemulsion droplet interface, thus increasing the interfacial area. The participation of pentanol in the surfactant interface, particularly at larger volumes, will result in increased flexibility in the interfacial layer. This makes the droplet more susceptable to transient droplet dimer formation, rupturing of the droplets onto the sucrose crystal and the diffusion of the sucrose across the cyclohexane continuous phase into the droplets, thus increasing the rate of reaction between the sucrose crystal and the sulfuric acid. The whole droplet sizes are determined to be 2.9, 3.0 and 3.3 nm respectively for the 20 µl/g, 45 µl/g and 50 µl/g from the GIFT estimation, implying the CTAC hexadecane tails to be ~0.9 -1.4 nm, which is slightly lower than the expected value of 1.8 nm, based on an extended hydrocarbon chain length of 2.174 nm for CTAC. One must note the similar electron densities for the CTAC hexadecane tails and the pentanol, in addition to the cyclohexane which is subject to penetration, making the determination of the droplet value difficult. However, the hydrophilic core radius is subject to less error, due to a much greater electron density contrast between the core and the shell.

5.9 Conclusions

The microemulsion methodology provides a simple room temperature route for the synthesis of the thermodynamically stable nanographite. Nanographitic particles can be synthesised within the confinement of a microemulsion, albeit at extremely low sucrose concentrations to ensure a majority nanographite product. As expected, this hinders the quantity of material yielded. The nanographite formation proceeds via an oriented stacking of nanographene sheets, which are the primary particles. This oriented stacking eventually results in larger ~250 nm to µm-sized nanographite, with a mesocrystals-like structure. The larger particles are achieved through pristine nanographene sheets stacking irreversibly in the lowest energy formation. These findings challenge traditional ways of thinking, whereby it is assumed that the synthesis of graphitic material from a bottom-up method always required significant temperature and/or pressure. A summary of the material presented from various microemulsion compositions is presented in the table below.

Identity of precipitate	Nanographite	Larger graphitic material.	Poorly organised graphitic material	Nano-onions	Amorphous humin-like carbon
Image	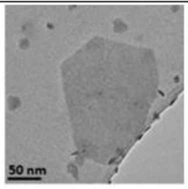	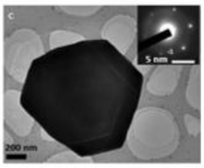		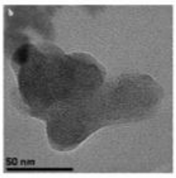	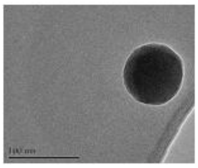
Sucrose precursor concentration wt %	1 - 25 wt %.	1 – 25 wt %.	> 3 wt %.	> 30 wt %.	> 30 wt %.
Mean radius of droplets hydrophilic core	1.8 – 2.1 nm	1.8 – 2.1 nm	1.8 – 2.1 nm	1.8 – 2.1 nm	1.8 – 2.1 nm
Mean number of sucrose per droplet	0.03 – ~2.5	0.003 - ~2.5	> ~3.5	> ~3.5	> ~0.55
Ratio of sucrose: acid	1: 25 - 600	1:25 - 600	1 - <17	1: <17	1: <115

Table 5.7: Summary of carbonaceous precipitate synthesised from various microemulsion compositions.

Note nanographitic is most typically observed in the majority for 0.25 – 1 wt %. sucrose precursor concentrations, however it is present as the minority product for higher sucrose precursor concentrations.

References

1. Z. Ren et al., Aligned Carbon Nanotubes, NanoScience and Technology, 2013, Springer-Verlag Berlin Heidelberg.
2. E. HL Falcao and F. Wudl, 'J Chem Technol Biotechnol', 2007, 82, 524–531.
3. Robertson. J, *'Materials Science and Engineering: R Reports',* 2002, 37(4-6)129-281
4. M Scarselli, P Castrucci and M De Crescenzi, '*J. Phys.: Condens. Matter',* 2012, 24, 313202
5. O.A. Shenderova,1,2 V.V. Zhirnov,1,3 and D.W. Brenner, '*Critical Reviews in Solid State and Materials Sciences*', 27(3/4):227–356 (2002)
6. Ferro. S, '*J. Mater. Chem'*, 2002, 12, 2843–2855
7. R. C. De Vries, '*Ann. Rev. Mater. Sci'*, 1987, 17, 161
8. F.P. Bundy, H.T. Hall, H.M. Strong and R.F. Wentorf', *Nature* 176, 51-54 (1955).
9. G.P. Bulanova, '*Journal of Geochemical Exploration'*, 53 (1995) 1-23
10. Lanhua Wei, P. K. Kuo, and R. L. Thomas, T. R. Anthony and W. F. Banholzer, *'Phys. Rev. Lett',* 1993, 70(24), 3764
11. M. C. Schabel and J. L. Martins, *'Phys. Rev. B',* 1992, 46(11)
12. Hass. J, W.A. de Heer and E.H. Conrad, ' J. Phys. Condens. Matter', 2008, 20, 323202
13. J.D. Bernal, *Proceedings of the Royal Society of London. Series A, Containing Papers of a Mathematical and Physical Character*, 1924, 106, 740
14. A. Goetz, A. B. Focke, and A. Faessler, Phys. Rev. 1952, 39, 168
15. J.-C. Charlier, X. Gonze and J.-P. Michenaud, '*Europhys. Lett'*, 28 (6), pp. 403-408 (1994) Graphite Interplanar Bonding: Electronic Delocalization and van der Waals Interaction
16. D.D.L.Chung, *; Journal of Mat. Sci',* 2002, 37, 1475–1489
17. D J Johnson and C N Tyson, Journal of Physics D: Applied Physics, 1969, 6(2), 787
18. A. N. Kolmogorov and V. H. Crespi, '*Phys. Rev. B',* 2005, 71.235415
19. B. Kwiecinska and H.I. Peterson, 'International Journal of Coal Geology, 2004, 57, 99–116
20. S. Malak, A. Vijaraghavan, R. Erni, K. Ariga, I. Khalakhan and J.P. Hill, 'Nanoscale', 2010, 2, 2139–2143
21. J. Robertson, 'Current Opinion in Solid State 6 Materials Science', 1996, 1, 557-561
22. L. C. Blackman, G. Saunders and A. R. Ubbelohde *Proceedings of the Royal Society of London. Series A, Mathematical and Physical Sciences*, 1961, 364(1316), 19-40

23. A. A. Giardini, C. A. Salotti and J. F. Lakner, Science, New Series, 1968, 159(3812, 317-319
24. R. V. Eck, E. R. Lippincott, M. O. Dayhoff and Y. T. Pratt, Science, New Series, 1966, 153(3736), 628-633
25. Salotti. C.A, E.W. Heinrich and A.A. Giardini, Economic Geology, 1971, 66(6), 929-932
26. Robertson. S.D, *'Nature',* 1969, 221, 1044-1046
27. Zaikovskii. A.V, Mal'tsev. V.A, Novopashin. S.A, Sakhapov. A.Z and Smovsh. D.V, *'Nanotechnologies in Russia',* 2012, 7(11), 654-657
28. Davis. W.R, Slawson. J.R and Rigby. G.R, 'Nature', 1953, 171, 756
29. Hofer. J.E, Sterling. E and McCartney. J.Y, *'J. Phys. Chem',* 1955, 59(11), 1153-1155
30. Walker. P.L, Rakszawaski. J.F, Imperial. G.R, *'Journal of Physical Chemistry',* 1959, 63(2), 133-149
31. Karu. A.E and Beer. M, *'J. Appl. Phys',* 1966, 37, 2179
32. T. Hirai and S. Yajima, *'J. Mat. Sci',* 1967, 2, 18-27
33. W.J. Bartz, Wear, 17 (1971) 421-432
34. Venu Gopal. A and Venkateswara Rao. P, *'Materials and Manufacturing Processes',* 2004, 19(2), 177-186
35. Jeong. D.J, Kim. D.J, Kim. J.H, Kim. B.M and Dean. T.A, *'Journals of Materials Proecessing Technology',* 2001, 113(1-3),544-550
36. Ishida et al, *'Pencil lead and manufacturing method of the same ',* 1977, Patent No: US4107451
37. M. A. Pimenta, G. Dresselhaus, M. S. Dresselhaus, L. G. Cancadoza, A. Jorioa and R. Saitoe, *'Phys. Chem. Chem. Phys'.,*2007, 9, 1276–1291
38. Khan. U, O'Neill. A, Lotya. M, D. Sukanta, Coleman. J.N, *'Small',* 2010, 6(7), 864-871
39. Stankovich. S, Dikin. D.A, Piner. R.D, Kohlhass. K.A, Kleinhammes. A, Jia. Y, Wu. Y, Nguyen. ST. and Ruoff. R.S', *'Carbon',* 2007, 45, 1558-1565
40. Kosynkin. D.V, Higginbotham. A.L, Sinitski. A,Lomeda.J.R, Dimiev. A, Price. K and Tour. J.M, *Nature,* 2009. 458, 872-876
41. Nethravathi. C and Rajamathi. M, Carbon, 2008, 46(14), 1994-1998
42. Obraztsov. A.N, Obraztsova. E.A, Tyurnina. A.V, Zolotukhin. A.A, 'Carbon', 2007, 45(10), 2017-2021
43. Zhu. C, Guo. S, Fang. Y and Dong. S, *ACS* Nano, 2010, 4(4), 2429-2437
44. Li. X, Kurasch. S, Kaiser. U and Antonietii. M, *Angewandte* Chemie' 2012, 51(38), 9689-9692
45. Peng, H.; Travas-Sejdic, J. Chem. Mater. 2009, 21, 5563–5565
46. Li, X.-H.; Kurasch, S.; Kaiser, U.; Antonietti, M. Angew. Chem. Int. Ed. 2012, 51, 9689 –9692.
47. Liu, H.; Miao, C.; Tang, Z.; Zheng, X.; Qin, X.; Zhang, X. Mat. Lett. 2012, 83, 62–64.

48. Dey, R. S.; Hajra, S.; Sahu, R. K.; Raj, C. R.; Panigrahi, M. K. Chem. Commun. 2012, 48, 1787–1789.
49. S. Caratzoulas and D.G. Vlachos, *'Carbohydrate Research',* 2011, 346, 664-672
50. S.K.R. Patil and C.R.F. Lund, *'Energy Fuels',* 2011, 25, 4745-4735
51. Hargreaves. N and Cooper.S. J, *Cryst. Growth and Des',* 2016 To be published ASAP.
52. C. Chen, O. Cook, C.E. Nicholson and S.J. Cooper, 'Cryst. Growth Des', 2011, 11(6), 2228-2237
53. Shao, G.; Lu, Y.; Wu, F.; Yang, C.; Zeng, F.; Wu, Q. J. Mater. Sci. 2012, 47, 4400-4409.
54. Behabtu, N.; Lomeda, J. R.; Green, M. J.; Higginbotham, A. L.; Sinitskii, A.; Kosynkin D.V, Tsentalovich D, Parra-Vasquez. A.N, Schmidt. J, Kesselman. E, Cohen. Y, Talmon. Y, Tour.J.M, Pasquali. M, *'Nat. Nanotechnol',* 2010 Jun;5(6):406-11
55. K.L. Nash, K.J. Sully and A.B. Horn, *'J. Phys. Chem. A',* 2001, 105, 9422-9426
56. P. Innocenzi, 'Journal of Non-Crystalline Solids', 2003, 316, 309–319
57. C.de Almeida and A.J.G. Zarbin, *'J. Braz. Chem. Soc',* 2006, 17(6), 1151–1157
58. Palazzo, G.; Lopez, F.; Giustini, M.; Colafemmina, G.; Ceglie, A. J. Phys. Chem. B 2003, 107, 1924-1931.
59. Giustini, M.; Palazzo, G.; Colafemmina, G.; Monica, M. D.; Giomini, M.; Ceglie, A. J. Phys. Chem. 1996, 100, 3190-3198.
60. Mills, A. J.; Wilkie, J.; Britton, M. M. J. Phys. Chem. B 2014, 118, 10767−10775.
61. M.S. Dresselhaus and G. Dresselhaus, 'Advances in Physics', 2002, 51(1), 1-186
62. A.C. Ferrari, S.E. Rodil and J. Robertson, *'Physical Review B',* 2003, 67, 155306
63. Knock, M. M., Bain, C. D. Langmuir 2000, 16, 2857-2865
64. Tanford, C. J. Phys. Chem. 1978, 76, 3020-3024.
65. M.S. Dresselhaus, A. Jorio, and R.Saito, *'Annual Review of Condensed Matter Physics',* 2010, 1, 89-108
66. F. Tuinstra[1] and J. L. Koenig, J. Chem. Phys., 1970, 53, 1126
67. Eastoe, J.; Hollamby, M. J.; Hudson, L. Adv. Colloid Interface Sci. 2006, 128-130, 5-15.
68. López-Quintela, M. A.; Tojo, C.; Blanco, M. C.; Garćia Rio, L. G.; Leis, J. R. Curr. Opin. Colloid Interface Sci. 2004, 9, 264–278.
69. Reich. S and Thomsen. C, *'Phil. Trans. R. Soc. Lond.A'* (2004)362, 2271–2288

70. Wang. Y, Alsmeyer. D.C and McCreery. R.L, *Chem. Mater.*, 1990, *2* (5), pp 557–563
71. Kostic, R.; Miric, M.; Radic, T.; Radovic, M.; Gajic, R.; Popovic, Z. V.Acta Physica Polonica A, 2009, vol. 116, Issue 4, p.718
72. P.K. Chu and L.Li, *'Materials Chemistry and Physics',* 2006, 96, 253-277
73. Vidano, R., Fishbach, D., *Solid State Comm,* 39. 341-344. 1981.
74. Istvan Pócsik[a,] , Martin Hundhausen[b], Margit Koós[a], Lothar Ley[b], Journal of Non-crystalline solids, 1998, 227-230 (2), 1083-1086
75. M. J. Matthews, M. A. Pimenta, G. Dresselhaus, M. S. Dresselhaus, and M. Endo, Phys. Rev. B 59, R6585(R) , 1999
76. Maultsch. J, Reich. S, Thomsen. C, Requardt. H and Ordejon. P, *'The American Physical Society – Physical Review Letters',* 2004, 92(7), 075501
77. R. Saito, A. Jorio, A. G. Souza Filho, G. Dresselhaus, M. S. Dresselhaus, and M. A. Pimenta Phys. Rev. Lett. 2001, 88, 027401

Chapter 6 - Conclusions and further work

6.1 Overview of this project

The synthesis of silica from a sodium metasilicate precursor (SMS) was detailed in Chapter 3, with the aim to investigate the effect of 3D-nanoconfinement over the synthesis process. Both a TX-114 / 60 wt %. cyclohexane microemulsion system and a 40 wt %. 1:1 Span 80: Brij30/heptane microemulsion system were employed. The most stable crystalline quartz form of silica was solely precipitated for low SMS concentrations; < 6 wt %. SMS for the TX-114 / 60 wt %. Cyclohexane system and < 7.5 wt %. SMS for the 40 wt %. 1:1 Span 80: Brij30/heptane system. Above these SMS concentrations the majority polymorph shifts to the metastable forms: cristobalite and amorphous silica spheres, as the increase in supersaturation allows metastable forms to also produce near stable nuclei, and a greater rate. Thus despite the nanoconfinement, the surplus material helps promote kinetic control, hence thermodynamic control is lost, allowing the formation of metastable nanocrystals. Variation of the volume of the dispersed phase of aqueous SMS precursor was also investigated, whereby larger dispersed volumes allowed the precipitation of metastable forms of silica: cristobalite and the amorphous phase, as they are expected to contain sufficient material to produce near stable nuclei of the metastable forms. The pH of the microemulsions, particularly their ability to shift the pH towards a neutrality point, was investigated, particularly due to the importance of pH upon the speciation, and thus oligomerisation and condensation of silica. The microemulsion was noted to cause a move towards neutrality for all dispersed volumes, however a much greater effect over the pH was observed for smaller dispersed volumes, whilst the pH of the higher dispersed phase volumes remains closer to that of the aqueous SMS solutions. As the pH approached that of the aqueous SMS solutions; i.e. for high SMS precursor concentrations and large dispersed phases, lone spherical amorphous structures were produced due to the occurrence of ionic species $Si(OH)_5^-$, adsorption of hydroxyl ions, inducing repulsion between the similarly charges species hindering aggregation of particles, whereas in a more acidic medium, the monomeric $Si(OH)_4$ species is expected to dominate, which bears no charge, thus potentially allowing aggregation of material, particularly at higher SMS concentrations. (See Figure 3.4)[1]

The 'age' of the microemulsion sample also proved of interest, to the morphology of the precipitate, particularly the ability to aggregate. One must note that no significant growth of the 2-5 nm quartz nanoparticles was observed for most of the SMS aqueous and dispersed volumes investigated, which appear confined by the dimensions of the microemulsion droplet. One can speculate the interface of the microemulsion droplets may act as a layer to retard the growth of the nanoparticles beyond the confinement within the acidic medium.[2] However, aging the sample over a period of 7 days, one can see aggregation that is limited to 50-100 nm aggregates, with no further growth of the aggregates beyond the 7 days. (See Figures 3.40 and 3.41). The mechanism is not known, however one can speculate that the process may be driven by surfactant adsorbing onto specific crystal faces of the primary quartz nanoparticles, with hydrophobic interactions between the surfactant tails the supporting agglomeration of primary quartz nanoparticles.[3]

Thus thermodynamic control was exerted over the precipitation of silica from an aqueous SMS solution, via the 3D-nanoconfinement of microemulsion droplets, through careful control of the precursor concentration and volume of aqueous dispersed phase.

Based on the work of Chen *et al,*[4] whereby an organic dipicolinic acid was crystallised within acidified microemulsions, producing nanoaggregate mesocrystal-like structures, it was wondered whether a similar affect would occur for an inorganic quartz phase, if hydrochloric acid was added to SMS aqueous microemulsions.

A summary of the silica phases synthesised from various microemulsion compositions is presented in the following tables.

30 wt %. 1:1 Span 80: Brij 30: heptane

Identity of precipitates	Nanoquartz (2-5 nm)	Cristobalite	Larger triangular quartz structures
Image	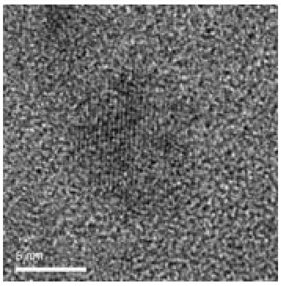	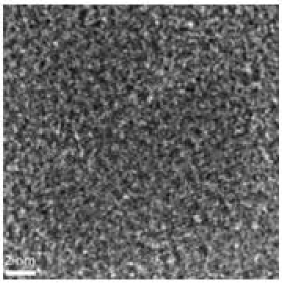	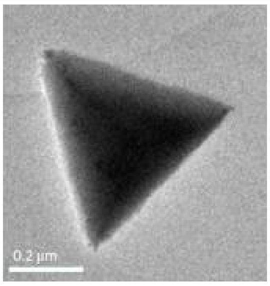
pH	~ 7	~ 5	< 1
Mean radius of droplets hydrophilic core	1.5 - 2.7 nm	~ 2.4 nm	~ 2.4 nm
Bound water percentage	20 – 100 %	22 %	22 %
Mean number of silica per droplet	0.01 – 2.3	0.4	0.4

The Span80:Brij30 microemulsion system was seen to produce quartz nanoparticles of ~ 2-5 nm, in addition to larger triangular crystalline quartz structure of ~200-500 nm. This change in crystal size arises both from an increased droplet size and decreased pH which raises the supersaturation. Both these factors provide more SiO_2 to grow the nanoquartz to larger dimensions. Additionally, the extreme pH conditions may disrupt any adsorption of surfactant upon the quartz surface, by the production of charges through the protonation of OH/SiOH groups under the extreme pH conditions, thus removing any surfactant stabilisation of smaller nanoquartz particles.[13] Further, metastable polymorphs were observed upon substantial supersaturation levels being achieved.

55 wt %.2.2:1 TX-100:hexanol:cyclohexane

Identity of precipitates	Nanoquartz (2-5 nm)	Amorphous	Complete aggregation	Partial aggregation
Image	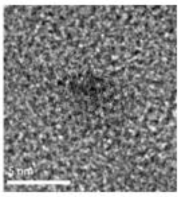	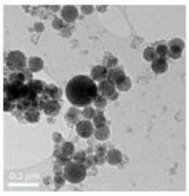	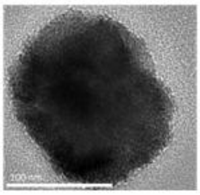	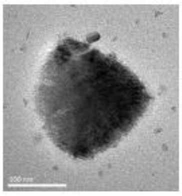
No HCl, direct or mixed microemulsion addition	No HCl, direct addition and mixed microemulsion addition	No HCl, direct addition and mixed microemulsion addition	Direct addition	Direct addition and mixed microemulsion addition
pH	0 - 9.6	~ 1 - 11	~ 1 - 2	~ 0 - 1
Mean radius of droplets hydrophilic core	1.6 - 2.5 nm	2.2 – 2.4 nm	~ 1.6 nm	~ 1.6 – 2.5 nm
Bound water percentage	26 – 100 %	26 – 53 %	~ 100 %	~ 26 – 100 %
Mean number of silica per droplet	0.02 – 3.22	0.24 – 3.22	0.04	0.02-0.45
Surfactant : silica ratio	All	~ 60 – 10 :1	~700:1	~20 – 400 :1

The TX-100:hexanol surfactant system was seen to produce primary quartz nanoparticles of ~2-5 nm, in addition to nanoaggregate mesocrystals-like structures in the order of 50-200 nm, via oriented attachment of the 2-5 nm primary nanoparticles previously observed. The primary nanoquartz particles were observed under most conditions discussed, as can be seen in the table above. The 'complete' formation of the nanoaggregates typically occurred when the pH was ~1 - 2, with the incorporation of HCl and a high surfactant:silica ratio of ~700:1. Deviation from such conditions produces incomplete agglomerations or simple individual nanocrystals as can be seen from the table above. The formation of nanoaggregates is suspected to be a result of surfactant adsorption at the hydroxyl groups upon the silica resulting in ordering due to hydrophobic interactions between the surfactant tail groups. Such suggestions are preliminary and further work would be required to confirm the formation mechanism.

Moving away from inorganic species, the same microemulsion methodology was employed to target the study of thermodynamic control over the synthesis and crystallisation of carbonaceous materials. Two microemulsion methodologies were employed: a mixed microemulsion method and a crystal dissolution methods as described in Chapter 2 and Chapter 5. For the mixed microemulsion method, the most stable graphite form of carbon was solely precipitated for low sucrose concentrations; < 30 wt % aqueous sucrose, and preferentially, in small droplets within the CTAC/hexanol system. Primary 2-5 nm nanographite particles were observed at all concentrations < 30 wt % aqueous sucrose. Larger nanoparticles ~ 250 nm were also observed. This nanographite formation is expected to proceed via an oriented stacking of nanographene primary particles. This oriented stacking eventually results in larger ~250 nm to μm-sized nanographite, with a mesocrystals-like structure. The larger particles are achieved through pristine nanographene sheets stacking irreversibly in the lowest energy formation. Above these sucrose concentrations and for larger droplet sizes, the majority polymorph shifts to yield disordered graphitic material and the metastable amorphous carbon spheres and nano-onions. This is expected to be a consequence of an increased number of sucrose, meaning there are sufficient sucrose molecules per droplet that the carbonaceous material can grow relatively rapidly through transient droplet dimer formation. As such, material can grow to larger dimensions; sufficiently large to stack irreversibly, irrespective of the presence of residual oxygen and hydrogens, and this results in the formation of amorphous phases.

However, the mixed microemulsion methodology yielded no macroscopic precipitate, thus a sucrose crystal dissolution method was employed solely to yield sufficient material to corroborate the observations made from the mixed microemulsion experiments. For this method sufficient nanographitic material was extracted after a period of one month for further analytical analysis. However, two competing mechanisms could arise in this sugar dissolution method; the desired mechanism whereby sugar slowly dissolve into the hydrophilic core of the microemulsion droplets and then undergoes reaction, and an undesired route whereby sulfuric acid microemulsion droplets rupture onto the sugar crystals, releasing their sulfuric acid which then reacts with the sugar crystals to produce amorphous carbons. Larger dispersed volumes are preferred with regards to providing sufficient water and sulfuric acid molecules per droplet to promote the dissolution of the sucrose crystals into the droplets.

However, larger droplets tend to undergo changes to the curvature with ease in comparison to smaller droplets, thus enabling the droplets to rupture on the sucrose crystals. This scenario recreates the micro bulk sucrose and sulfuric acid reaction where one would expect a carbonaceous material consisting of humins or amorphous carbon to result. This methodology thus induces the formation of a significant proportion of amorphous carbons rather than the formation of nanographite.

As such, one must note that this sucrose crystal dissolution methodology was only employed to produce sufficient material for further analysis to corroborate the observations from the mixed microemulsion methodology.

A summary of the carbonaceous phases synthesised from various microemulsion compositions is presented in the following table.

1:2:7.8 CTAC:pentanol:cyclohexane

Identity of precipitate	Nanographite	Larger graphitic material.	Poorly organised graphitic material	Nano-onions	Amorphous humin-like carbon
Image	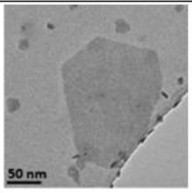	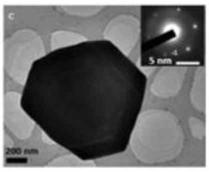		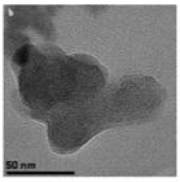	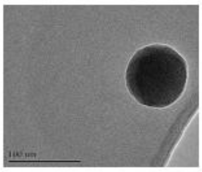
Sucrose precursor concentration wt %	1 - 25 wt %.	1 – 25 wt %.	> 3 wt %.	> 30 wt %.	> 30 wt %.
Mean radius of droplets hydrophilic core	1.8 – 2.1 nm	1.8 – 2.1 nm	1.8 – 2.1 nm	1.8 – 2.1 nm	1.8 – 2.1 nm
Mean number of sucrose per droplet	0.03 – ~2.5	0.003 - ~2.5	> ~3.5	> ~3.5	> ~0.55
Ratio of sucrose: acid	1: 25 - 600	1:25 - 600	1 - <17	1: <17	1: <115

In conclusion, both nano-quartz and graphite have been synthesised within the 3D-nanoconfinement of microemulsion droplets. Both these findings challenge traditional ways of thinking, whereby it has always been assumed that quartz and graphite synthesis typical require elevated temperatures and/or pressure if a bottom-up synthesis method is employed.

6.2 Further work

The two main areas to be developed are: techniques to extract the nanoscopic material and development of the formation mechanism behind the two types of mesocrystals like aggregate structures identified.

Chapter 4 reveals the capabilities of microemulsions to control the morphology and structure of nanoaggregates formed from primary nanoparticles. Thus far, preliminary understanding allows one to speculate that the formation of the nanoaggregates is determined by the pH of the system and the relative concentration of surfactant, however future work to answer the following may provide a more detailed insight:

- What role does the pH of the system have upon the formation of the aggregated structures within non-ionic surfactant systems. Moreover, is the presence of an acid a necessity for the nanoaggregate structures to be observed?
- Confirmation of the role of surfactant in the nanoaggregate formation is required. In particular, how does the concentration of surfactant predetermine the completeness of the aggregate structures?
- How does the method of acid addition to the aqueous microemulsion affect the aggregation of the primary particles?
- Under what condition does the droplet composition restrict the size of the primary nanocrystals to that of the droplet size?
- The growth mechanism of the nanoaggregate and nano-primary particles within the microemulsion droplets requires more investigation as this may provide an understanding regarding the requirements/restrictions of scale-up and extraction of the nanocrystalline materials.

  Is 3D-nanoconfinement of the microemulsion droplets a strict requirement, or can other surfactant phases, such as lamellar systems, be employed to crystallise the most thermodynamically stable phase.

References

1. X. Yang, P. Roonasi and A. Holmgren, *'J. Colloid Interface Sci',* 2008, 382(1), 41-47
2. Rimer J.D, Lobo. R.F and D.G Vlachos, *'Langmuir',* 2005, 21 (19), 8960-71
3. D. M. Nevskaia, A. Guerrero-Rutz, A. Lopez-Gonzalez, '*Journal of Colloid and Interface Science',* 1996, 181,571–580
4. Chen, C.E. Nicholson, H.E. Ramsey and S.J. Cooper, *Cryst. Growth. Des',* 2015, 15, 1060-1066;

Appendix 1

Quartz				Cristobalite				Silicon	
hkl	d-spacing	hkl	d-spacing	hkl	d-spacing	hkl	d-spacing	hkl	d-spacing
100	4.2574	013	1.6593	101	4.040	220	1.756	111	3.13501
011	3.3446	103	1.6593	110	3.530	004	1.736	220	1.91979
101	3.3446	210	1.6091	111	3.138	203	1.692	311	1.63721
110	2.4580	121	1.5423	102	2.845	104	1.642	400	1.3575
012	2.2818	211	1.5423	200	2.489	301	1.612	331	1.24573
102	2.2818	113	1.4532	112	2.468	213	1.604	422	1.10839
111	2.2375	300	1.4191	201	2.342	222	1.574	511	1.045
200	2.1287	122	1.3826	211	2.121	302	1.495		
021	1.9806	212	1.3826	202	2.024	312	1.432		
201	1.9806	023	1.3753	113	1.932	204	1.423		
112	1.8184	203	1.3753	212	1.874				
003	1.8018	031	1.3726						
022	1.6723	301	1.3726						
202	1.6723								

Table 1: Presentation of corresponding d-spacings and hkl miller planes, for the three ambient pressure polymorphs of silicon dioxide; quartz, cristobalite and silicon[1-2]

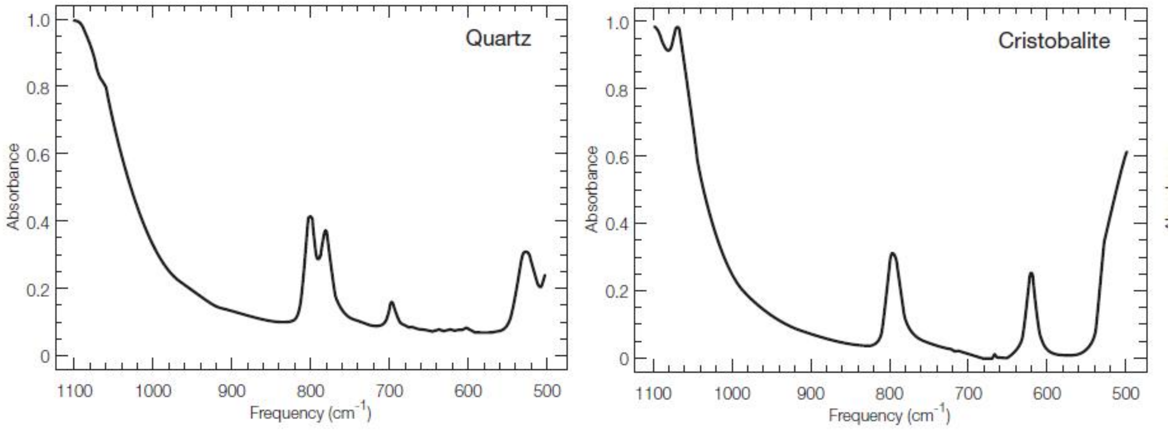

Figure 1: Respective IR of quartz and cristobalite.[3]

Zone axis	d-spacings /Å			Angles/ degrees		
[212]	2.13	1.82	2.28	50.15	55.40	74.45
[-1-10]	2.13	2.28	2.28	57.58	64.83	57.59
[00-1]	2.46	2.46	2.46	60	60	60
[0-4-2]	2.28	2.13	1.81	74.45	50.15	55.40
[1-1-4]	2.46	1.54	1.98	51.14	38.86	90
[110]	3.34	1.92	2.28	59.70	36.09	90
[001]	2.13	2.13	2.13	60	60	60

Table 2: Table to indicate corresponding d-spacing's and angles for zone axes of quartz observed.

References

1. Mindate.org accessed 03/03/16
2. http://newton.umsl.edu/run/nano/known.html accessed 30/03/16
3. E. R. Lippincott, A. Van Valkenburg, C. E. Weir, and E. N. Bunting, '*Journal of Research of the National Bureau of Standards'*, 1958, p61

Appendix 2: Raman spectroscopy

Raman spectroscopy is a vital identification technique for carbon based materials as black opaque graphitic material is virtually impossible to differentiate by observation techniques such as colour and mass (density). Raman spectroscopy can be utilised as a non-destructive, non-intrusive analytical technique which acts as a sensitive probe for the structural characterisation of carbonaceous materials. The existence of the peaks, their relative intensities, breadth and shape can reveal vital information about the structure of the material, such as: finite crystallite size, out-of-plane stacking order, defects and edges, or the presence of heterogeneous atoms.[1]

Graphene and graphite are assembled from hexagonal planes of sp^2 covalently bonded carbon atoms as shown in Figure 5.1.

The unit cell of graphene, a single monolayer, is composed of two inequivalent atoms whilst that of 3D- graphite, i.e. a number of layers stacked in an AB orientation, held via very weak Van der Waals type interactions, consists of four atoms as depicted in Figure A2.1 a&b and c&d respectively.

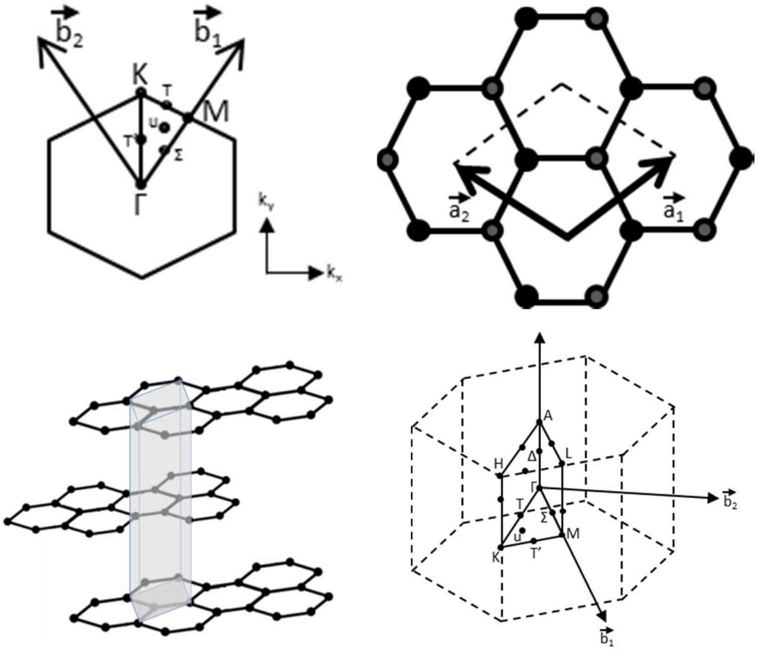

Figure A2.1 Diagrams illustrating the arrangement within graphite. [2-3]

Reproduced with permission from M.S. Dresselhaus, A. Jorio, and R.Saito, *'Annual Review of Condensed Matter Physics'*, 2010, 1, 89-108 Copyright © 2010, Annual Reviews

Graphene and graphite belong to the D_{6h} point group, each with vibrational modes of the type E_{2g}, B_{2g}, A_{2u} and E_{1u} as demonstrated by the point group characterisation table.[4] As graphene has 2 inequivalent atoms per unit cell, it yields 6 phonon modes at q=0 or the zone centre, Γ, hence $\Gamma^{graphene} = A_{2u} + B_{2g} + E_{1u} + E_{2g}$.[5] Three of these modes are acoustic (A) and three are optic (O) phonon modes, with one being out-of plane (oTO and oTA), and two in-plane: longitudinal (LO and LA) and transverse (iTO and iTA).[1] From this vibrational representation of graphene can be deduced by combining the in-phase or out-of-phase normal modes, giving the irreducible representation of graphite is given as $\Gamma^{graphite} = 2A_{2u} + 2B_{2g} + 2E_{1u} + 2E_{2g}$.[5] These are depicted in Figure A2.2 The B_{2g} modes are deemed 'silent' or optically inactive phonons, where, from Figure A2.2, it is clear that the carbon atoms move in the direction of the c-axis, or perpendicular to the graphene plane. The A_{2u} and E_{1u} modes represent translation of the graphene planes and are both IR-active. The former corresponds to motion perpendicular to the graphene plane, whilst the latter represents translation within the graphene plane.[5] For the Raman active modes, which in the case of a single crystal must observe the rule $q \approx 0$, (q is the wave vector of the scattered phonon)[6], it is important to note that the E_{2g} (1) mode is rarely observed via Raman spectroscopy, but instead can be detected by low-frequency neutron scattering. More prominent is the inherent Raman active G peak for graphitic carbon, occurring at 1582 cm^{-1}. This feature originates from the doubly degenerate (iTO and LO) optical phonon modes with E_{2g} (2) symmetry at the Brillouin zone centre, Γ, however the degeneracy disappears at other points within the zone.[6] Moreover, these two modes arise from the in-plane movement of the carbon atoms in or with opposite phase with respect to an adjacent plane.[3] This is depicted in Figure A2.2 [4] Further, this mode is not unique to six-fold hexagonal sp^2 carbon rings and thus occurs for all pairs of sp^2 carbons, i.e. in chain structures.[7] For other sp^2 carbon environments such as: films, nanocrystalline and amorphous, the G peak has been observed to shift between 1500 - 1630 cm^{-1}.[7] This is the sole first-order structure present for infinite single crystals of graphitic carbon.

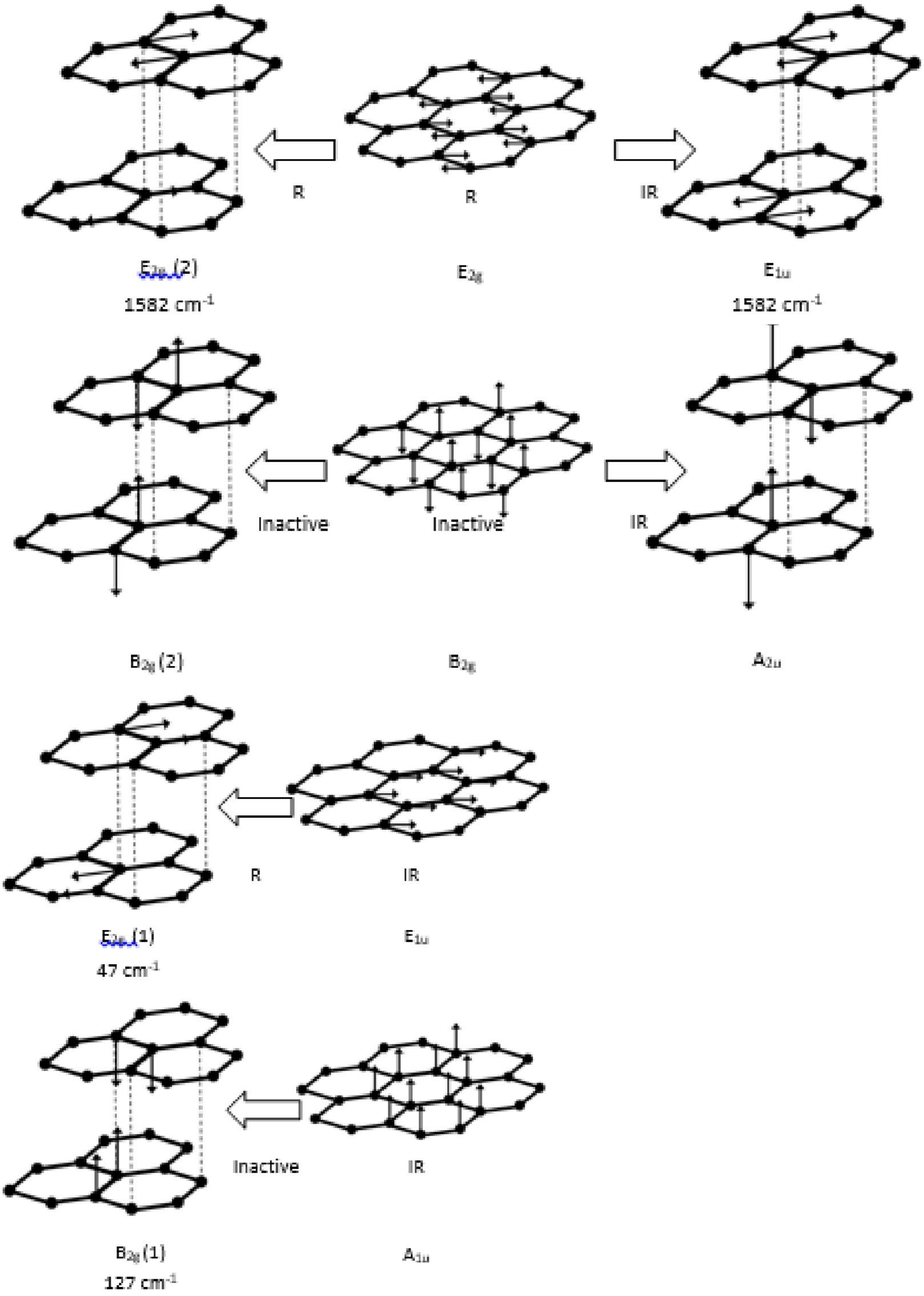

Figure A2.2: 6 phonon modes of graphite.[4] Reprinted (adapted) with permission from Wang. Y, Alsmeyer. D.C and McCreery. R.L, *Chem. Mater.*, **1990**, *2* (5), pp 557–563. Copyright © 1990, American Chemical Society

For nanocrystalline materials, or those with defects or finite crystalline domains (L_a) where L_a < 0.5µm,[3] additional lines are observed. This is due to the q-vector selection rule being relaxed to allow contributions of phonons near the zone centre.[6] This relaxation is known to cause both shifts in position and broadening of observed bands. Now $\Delta q \approx 2\pi/d$, where d is the domain dimension. This relaxation gives rise to a further feature at 1350-1370 cm^{-1}, denoted the D peak, originally named by Tuinstra & Keonig due to its presence in disordered systems. [3] The symmetry origins of the D line have been complex to assign due to a number of conflicting observations. Firstly, Tuinstra & Keonig illustrated the intensity dependence of the D peak on the crystallite size, L_a.[3] Wang et al[4] further attributed the presence of the D peak to any kind or disorder or defect present in the material. A significant number of proposed theories were published in an attempt to explain the observed behaviour and presence of the D peak: Reich and Thomson[8] and Ferrari and Robertson[6] generated three thorough complementary review articles. To address their observations of the D feature, Tuinstra and Koening, suggested that due to a finite crystal size, an A_{1g} breathing mode of the lattice becomes active due to loss of translational symmetry in disordered structures.[3] Moreover, this can be summarised as a result of the breakdown in the q-vector selection rule.

Wang *et al.*[4], sought clarification of the issue regarding defects, disorder and dispersion, with the publication eliminating a number of hypotheses including; that the D feature is solely due to the presence of terminating groups. [4] Wang et al concluded, that the origin and nature of the D peak was ascribed to a high (or a peak in) density of phonon states of graphite.[4] However both of these explanations fail to reason the observations of Vidano et al.[9] A dispersion behaviour of the D peak was noted, i.e. the observed frequency of the line changes upon excitation with differing photon energies. This behaviour is clear from the Raman spectrum in Figure A2.4 where the D peak is shown to shift with excitation energy at a rate of 40-50 cm^{-1}/eV. [10,12] Pocsik[10] and Matthews[11] who attempted to explain, using experimental evidence, the observed dispersion phenomena. It has been proposed that this behaviour was due to selectively coupled resonances between the excited electrons and the scattered phonons, however as stated by Matthews, one would expect a contribution from all phonon branches.[11] Pocsik has worked to eliminate the VDOS/PDOS theory, citing lack of explanation of the dispersion phenomena. In addition there are no zone centre phonon modes observed which correspond to the D peak.[13]

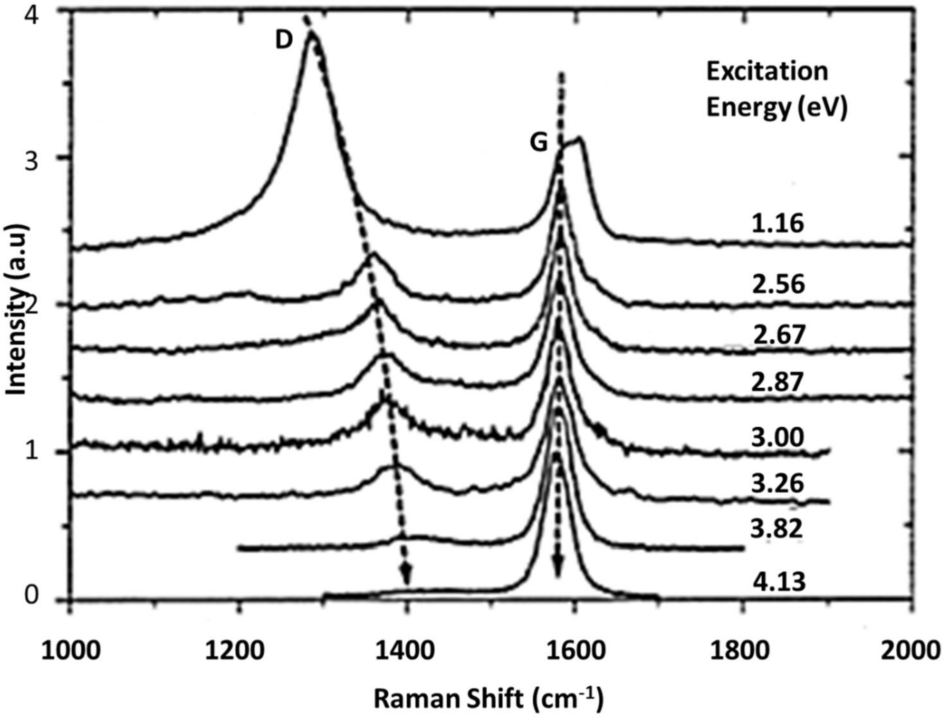

Figure A2.4: Raman spectrum illustrating the G and D position on the excitation energy.[10] Reprinted with permission from I. Pócsik, M. Hundhausen, M. Koós, L. Ley, Journal of Non-crystalline solids, 1998, 227-230 (2), 1083-1086. Copyright © 1998 Elsevier Science B.V.

Combining the observed dispersion of the D peak from Figure A2.4, it is clear that there are three branches around the M and K points with this energy (between the dashed lines).[10] Further, Pocsik draws on the break down of the selection rule, enabling all vibrational modes to be accessed, but stipulates that only those that are resonance-enhanced may contribute to the Raman spectrum, i.e. when the modes have the same wave-vector as the electronic transition ($\pi - \pi^*$).[10] Matthews, continuing on the same theme, narrows the coupling behaviour to overlap between the optic, specifically the TO branch[11] with the transverse acoustic (TA) branch around the K point, with all phonons of the same magnitude contributing to the D feature.[11]

In 2000, Thomson and Reich[8] developed a counter second order double–resonance model, where the initial/final transition, in addition to the elementary excitation make real transitions, to account for all known observations and behaviours of the D mode. The double resonance can be broken in to a number of steps, depicted in A2.5. Initially, an electron absorbs a photon with a given laser energy, $E_{i,}$ to be excited with momentum k, creating an electron-hole combination around the K point. Before recombination with the hole, a number of processes may occur, however here we consider the Stokes processes. The electron is scattered to a state with momentum $k + q,$ via the emission of a phonon with momentum q. The electron is elastically scattered back via lattice defects to return to a state with momentum k and emits a phonon to recombine with the hole.[1,14]

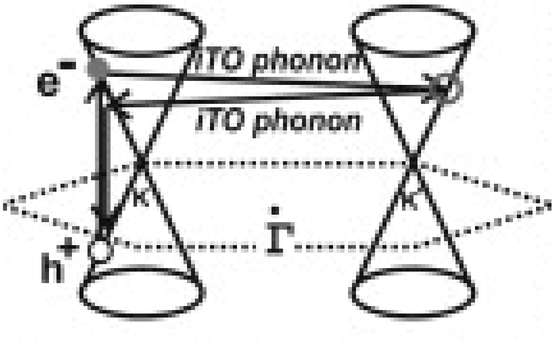

Figure A2.5 :A pictorial image demonstrating the second order double-resonance model.[6] Reprinted with permission from L.M. Malard, M.A. Pimenta, G. Dresselhaus, and M.S. Dresselhaus, '*Physics Reports*', 2009, 473 (5-6), 51-87. Copyright © 2009 Elsevier B.V

Figure A2.5 depicts one possible resonant condition, however in addition to the **k + q** state, either the electron-hole formation or recombination are able to be resonant and therefore there are 4 possible resonant conditions and contributions. [14] It is clear from the representation of Thomsen and Reich's proposed mechanism in Figure A2.5 that for a dispersive mode, a variance in the excitation photon energy, $E_{i,}$ leads to a corresponding change in the momentum and hence energy of the emitted phonon. Saito et al[14] (2002) generalised the double-resonance mechanism, applying to all phonon branches, yielding an explanation for all observed peaks within the Raman of both ordered and disordered graphite.

References

1. M. A. Pimenta, G. Dresselhaus, M. S. Dresselhaus, L. G. Cancadoza, A. Jorioa and R. Saitoe, *'Phys. Chem. Chem. Phys'.,*2007, 9, 1276–1291
2. M.S. Dresselhaus, A. Jorio, and R.Saito, *'Annual Review of Condensed Matter Physics',* 2010, 1, 89-108
3. F. Tuinstra and J. L. Koenig, J. Chem. Phys. 53, 1126 (1970)
4. Wang. Y, Alsmeyer. D.C and McCreery. R.L, *Chem. Mater.*, **1990**, *2* (5), pp 557–563
5. Kostic, R.; Miric, M.; Radic, T.; Radovic, M.; Gajic, R.; Popovic, Z. V.Acta Physica Polonica A, 2009, 116(4), p.718
6. A.C. Ferrari, S.E. Rodil and J. Robertson, *'Physical Review B',* 2003, 67, 155306
7. P.K. Chu and L.Li, *'Materials Chemistry and Physics',* 2006, 96, 253-277
8. Reich. S and Thomsen. C, '*Phil. Trans. R. Soc. Lond.A'* (2004)362, 2271–2288
9. Vidano, R., Fishbach, D., *Solid State Comm,* 39. 341-344. 1981

10. I. Pócsik, M. Hundhausen, M. Koós, L. Ley, Journal of Non-crystalline solids, 1998, 227-230 (2), 1083-1086
11. M. J. Matthews, M. A. Pimenta, G. Dresselhaus, M. S. Dresselhaus, and M. Endo, Phys. Rev. B 59, R6585(R) , 1999
12. Robertson. S.D, *'Nature',* 1969, 221, 1044-1046
13. Maultsch. J, Reich. S, Thomsen. C, Requardt. H and Ordejon. P, *'The American Physical Society – Physical Review Letters',* 2004, 92(7)
14. R. Saito, A. Jorio, A. G. Souza Filho, G. Dresselhaus, M. S. Dresselhaus, and M. A. Pimenta Phys. Rev. Lett. 2001, 88, 027401
15. L.M. Malard, M.A. Pimenta, G. Dresselhaus, and M.S. Dresselhaus, '*Physics Reports',* 2009, 473 (5-6), 51-87